Atomistic simulations of nano-architectured semiconductors : Thermal and vibrational properties

Paul Desmarchelier

N° d'ordre NNT : 2021LYSEI081

THÈSE de DOCTORAT DE L'UNIVERSITÉ DE LYON
opérée au sein de :
L'Institut National des Sciences Appliquées de Lyon

Ecole Doctorale N° 162
MECANIQUE, ENERGETIQUE, GENIE CIVIL, ACOUSTIQUE

Spécialité/discipline de doctorat :
Thermique Energétique

Soutenue publiquement le 06/12/2021, par :
Paul Matthieu Alexandre DESMARCHELIER

Atomistic Simulations of Nano-Architectured Semiconductors : Thermal and Vibrational Properties

---

Devant le jury composé de :

Bourgeois, Olivier	Directeur de recherche, CNRS	Président
Martin, Evelyne	Directrice de Recherche, CNRS	Rapporteure
Neophytou, Neophytos	Professeur, University of Warwick	Rapporteur
Fugallo, Giorgia	Chargée de Recherche, CNRS	Examinatrice
Lacroix, David	Professeur, Université de Lorraine	Examinateur
Volz, Sebastian	Directeur de Recherche, CNRS	Examinateur
Termentzidis, Konstantinos	Directeur de recherche, CNRS	Directeur de thèse
Tanguy, Anne	Professeure, INSA de Lyon	Co-Directrice de thèse
Alvarez, F. Xavier	Professeur, Universitat Autònoma de Barcelona	Invité
Jacquin, Laurent	Professeur, Ecole Polytechnique	Invité
Merabia, Samy	Directeur de recherche, CNRS	Invité
Nakamura, Yoshiaki	Professeur, Osaka University	Invité

Département FEDORA – INSA Lyon - Ecoles Doctorales

SIGLE	ECOLE DOCTORALE	NOM ET COORDONNEES DU RESPONSABLE
CHIMIE	**CHIMIE DE LYON** **https://www.edchimie-lyon.fr** Sec. : Renée EL MELHEM Bât. Blaise PASCAL, 3e étage secretariat@edchimie-lyon.fr	**M. Stéphane DANIELE** C2P2-CPE LYON-UMR 5265 Bâtiment F308, BP 2077 43 Boulevard du 11 novembre 1918 69616 Villeurbanne **directeur@edchimie-lyon.fr**
E.E.A.	**ÉLECTRONIQUE, ÉLECTROTECHNIQUE, AUTOMATIQUE** **https://edeea.universite-lyon.fr** Sec. : Stéphanie CAUVIN Bâtiment Direction INSA Lyon Tél : 04.72.43.71.70 secretariat.edeea@insa-lyon.fr	**M. Philippe DELACHARTRE** INSA LYON Laboratoire CREATIS Bâtiment Blaise Pascal, 7 avenue Jean Capelle 69621 Villeurbanne CEDEX Tél : 04.72.43.88.63 **philippe.delachartre@insa-lyon.fr**
E2M2	**ÉVOLUTION, ÉCOSYSTÈME, MICROBIOLOGIE, MODÉLISATION** **http://e2m2.universite-lyon.fr** Sec. : Sylvie ROBERJOT Bât. Atrium, UCB Lyon 1 Tél : 04.72.44.83.62 secretariat.e2m2@univ-lyon1.fr	**M. Philippe NORMAND** Université Claude Bernard Lyon 1 UMR 5557 Lab. d'Ecologie Microbienne Bâtiment Mendel 43, boulevard du 11 Novembre 1918 69 622 Villeurbanne CEDEX **philippe.normand@univ-lyon1.fr**
EDISS	**INTERDISCIPLINAIRE SCIENCES-SANTÉ** **http://ediss.universite-lyon.fr** Sec. : Sylvie ROBERJOT Bât. Atrium, UCB Lyon 1 Tél : 04.72.44.83.62 secretariat.ediss@univ-lyon1.fr	**Mme Sylvie RICARD-BLUM** Institut de Chimie et Biochimie Moléculaires et Supramoléculaires (ICBMS) - UMR 5246 CNRS - Université Lyon 1 Bâtiment Raulin - 2ème étage Nord 43 Boulevard du 11 novembre 1918 69622 Villeurbanne Cedex Tél : +33(0)4 72 44 82 32 **sylvie.ricard-blum@univ-lyon1.fr**
INFOMATHS	**INFORMATIQUE ET MATHÉMATIQUES** **http://edinfomaths.universite-lyon.fr** Sec. : Renée EL MELHEM Bât. Blaise PASCAL, 3e étage Tél : 04.72.43.80.46 infomaths@univ-lyon1.fr	**M. Hamamache KHEDDOUCI** Université Claude Bernard Lyon 1 Bât. Nautibus 43, Boulevard du 11 novembre 1918 69 622 Villeurbanne Cedex France Tél : 04.72.44.83.69 **hamamache.kheddouci@univ-lyon1.fr**
Matériaux	**MATÉRIAUX DE LYON** **http://ed34.universite-lyon.fr** Sec. : Yann DE ORDENANA Tél : 04.72.18.62.44 yann.de-ordenana@ec-lyon.fr	**M. Stéphane BENAYOUN** Ecole Centrale de Lyon Laboratoire LTDS 36 avenue Guy de Collongue 69134 Ecully CEDEX Tél : 04.72.18.64.37 **stephane.benayoun@ec-lyon.fr**
MEGA	**MÉCANIQUE, ÉNERGÉTIQUE, GÉNIE CIVIL, ACOUSTIQUE** **http://edmega.universite-lyon.fr** Sec. : Stéphanie CAUVIN Tél : 04.72.43.71.70 Bâtiment Direction INSA Lyon mega@insa-lyon.fr	**M. Jocelyn BONJOUR** INSA Lyon Laboratoire CETHIL Bâtiment Sadi-Carnot 9, rue de la Physique 69621 Villeurbanne CEDEX **jocelyn.bonjour@insa-lyon.fr**
ScSo	**ScSo*** **https://edsciencessociales.universite-lyon.fr** Sec. : Mélina FAVETON INSA : J.Y. TOUSSAINT Tél : 04.78.69.77.79 melina.faveton@univ-lyon2.fr	**M. Christian MONTES** Université Lumière Lyon 2 86 Rue Pasteur 69365 Lyon CEDEX 07 **christian.montes@univ-lyon2.fr**

*ScSo : Histoire, Géographie, Aménagement, Urbanisme, Archéologie, Science politique, Sociologie, Anthropologie

Résumé

À l'échelle nanométrique, les propriétés thermiques et vibratoires sont intimement liées et dépendent de la forme et de la composition des matériaux. Grâce à la nanostructuration, les nanocomposites permettent un meilleur contrôle du transport thermique. Ceci permet notamment d'améliorer les performances des générateurs thermoélectriques en offrant de meilleurs isolants, mais aussi une meilleure gestion de la chaleur dans les composants électroniques. Dans ce travail, les propriétés thermiques de quelques nanocomposites sont étudiées en utilisant des calculs à l'échelle atomiques, par le biais de la modélisation de Dynamique Moléculaire.

Dans un premier temps, l'accent est mis sur des nanocomposites constitués d'une matrice amorphe et de nano-inclusions cristallines. L'approche développée pour les amorphes, séparant la partie balistique du transfert thermique qui prend la forme d'onde plane se propageant dans le matériau et la partie diffusive repartissant lentement l'énergie dans le matériau, est mise à profit. La séparation de ces contributions a montré que si la structuration affecte systématiquement la partie balistique, maîtriser l'impact sur le transport diffusif est plus complexe. Celui-ci peut notamment être réduit par la présence de pores ou d'inclusions plus molles que la matrice, mais dans des proportions variables.

Une deuxième partie est consacrée à l'étude des nanofils de silicium, et à l'impact de l'amorphisation de ceux-ci. Pour cela, le transport d'énergie en fonction de la fréquence dans des nanofils avec une âme cristalline et une coque amorphe est étudié. La coque amorphe provoque l'apparition d'un transport diffusif et une baisse de transmission aux basses fréquences. Ensuite, la dynamique moléculaire est couplée aux équations hydrodynamiques du transport de chaleur. Ce couplage est mis à profit pour étudier la distribution radiale du flux de chaleur en régime établie dans les nanofils cylindriques avec une couche amorphe régulière. Cette analyse suggère que la réduction de la conductivité thermique due à l'ajout de la coque n'est pas uniquement liée aux changements des propriétés de l'interface, mais plutôt à un effet global de la coque amorphe sur le libre parcours moyen.

Finalement, la structuration en cône de la couche amorphe est utilisée pour induire une rectification thermique, c'est-à-dire une asymétrie spatiale dans le transport thermique. Cette rectification semble être due à la perturbation de la propagation des porteurs de chaleur à basses fréquences.

Mots-clés : Nanocomposite, Nanothermique, Matériaux Amorphe, Transport Balistique, Nanofils, Simulations Atomistiques, Rectification Thermique

Abstract

At the nanoscale, thermal and vibrational properties are intimately linked and depend on the shape and composition of the material. Thanks to the nanostructuration, nanocomposites allow a better control of the heat transfer. This can be used to improve the performances of thermoelectric generators through a better insulation, but also to improve the heat management in microelectronics application. In this work, the thermal properties of some nanocomposites are studied using atomistic level simulations, thanks to molecular dynamics.

In a first part, the focus is laid on nanocomposites composed of an amorphous matrix and crystalline nano-inclusions. The approach separating the propagative and diffusive contribution, developed for amorphous materials, is used. The ballistic contribution where the heat is propagated by plane waves is systematically impacted by the nanostructuration. Whereas affecting the diffusive contribution, that spreads the heat slowly at the nanoscale, is more challenging. This can be done, for instance, through pores or inclusions softer than the matrix but in variable proportions.

A second part is dedicated to the study of silicon nanowires, and the impact of amorphization. For this, the transport of energy as a function of frequency in crystalline core amorphous shell nanowire is studied. An amorphous shell causes the apparition of diffusive transport and the decrease in transmission at low frequencies. Then, molecular dynamics are coupled to hydrodynamic heat equations to study the radial distribution of flux in those nanowires. This analysis suggests that the reduction of the thermal conductivity upon the addition of shell cannot be linked solely to modified interface properties, but are rather due to a global effect of the shell on the mean free path of heat carriers.

Finally, it is shown that structuration of the amorphous layer in a conical shape can be used to obtain thermal rectification, that is, a spatial asymmetry in thermal transport. This rectification appears to be caused by the perturbation of transmission at low frequencies.

Keywords: Nanocomposite, Nanoscale Thermal Transfer, Amorphous Materials, Ballistic Transport, Nanowires, Atomistic Simulations, Thermal Rectification

Remerciements

En premier lieu, j'aimerais remercier mes directeurs de thèse : Konstantinos Termentzidis et Anne Tanguy. Avoir deux directeurs de thèse, c'est profiter d'un accompagnement régulier et complémentaire. Merci à eux d'avoir pris le temps m'écouter tout au long de ma thèse. J'aimerais aussi remercier les différentes personnes ayant aidé à la réalisation de ce travail : V. Gioradano, S. Merabia, Y. Beltukov, J. Kioseoglou, toute l'équipe MiNT du CETHIL et ceux qui y sont passé et en particulier W. Gonclaves. Merci aussi à mes co-doctorants Haoming Luo et Xiaorui Wang pour les conseils et échanges. Merci aux differents membres du CETHIL et du LaMCoS qui m'ont aidé, avec une pensée particulière pour L. Guilmard, B. Govehovitch qui m'ont assisté dans mes errances informatiques. C'est aussi pour moi l'occasion de remercier les étudiants avec qui j'ai travaillé, Alice, Matthias et Peng, pour leur implication et leur patience avec mes explications. Merci également, aux doctorants du CETHIL avec qui j'ai pu échanger, en particulier avec toute l'équipe de feu la pause café. Je voudrais également adresser un remerciement particulier à Aline Bel-brunon et Christian Brandl[1] sans qui ce travail n'aurait jamais pu commencer. Merci Alexandra pour ton aide précieuse pour la bibliographie. Merci à Louise pour son soutient sans faille durant toute l'aventure qu'est le doctorat. Les circonstances particulières de ces dernières années m'amène à remercier également mes compagnons de confinement Federico et Jeroen grâce à qui un mini-laboratoire à vu le jour à Lyon 3 durant quelques semaines. Merci également à tous mes autres camarades doctorants ou non qui m'ont écouté râler et fourni à l'occasion de précieux conseils, notamment Loan et Vincent qui m'ont accompagné tout le long de mes longues études. Je voudrais aussi remercier ma famille et mes proches qui m'ont soutenu et encouragé pendant ces trois ans.

———

[1] Danke sehr, deine Einführung in die Molekulardynamik hat meine letzten vier Jahre (und vielleicht noch mehr) bestimmt.

Contents

List of Acronyms

List of Symbols

Vector quantities are shown in **bold**

$\bar{\bar{\sigma}}$	Stress tensor
ΓX	$\langle 100 \rangle$ direction in the reciprocal space
$\hbar$	Planck Constant
κ	Thermal Conductivity
Λ	Mean Free Path
$\mathbf{j}$	Heat Flux
$\mathbf{q}$	Wave Vector
$\mathcal{F}\{\}$	Fourier Transform
∇	Nabla Operator
ν	Frequency
ω	Pulsation $2\pi\nu$
ρ	Mass Density
τ	Phonon lifetime
a	Lattice Constant of a Crystal
C_p	Heat Capacity at Constant Pressure
C_{latt}	Heat Capacity of the lattice
D	Diffusivity
E	Energy
E_k	Kinetic Energy
E_p	Potential Energy
k_b	Boltzmann Constant
m	Atomic mass
N	Number of atoms
T	Temperature
v_g	Phonon group velocity
V	Volume

List of Figures

List of Tables

Introduction

Thermal management, has always been crucial and is an increasingly hot topic. Avoiding freezing or overheating is fundamental for human survival. This objective has driven the development of the earliest technologies and continues to do so. This involves the understanding and the mastering of heat transfer. In particular, conserving or dissipating heat is a key point of many applications since the last two centuries with the development of modern technologies. It is in the 19^{th} century that Joseph Fourier proposed a formal relation between a temperature difference and the transfer of heat [Fourier 1822]. This development was parallel to the apparition and improvements of heat engines. With the heat engines came the thermodynamic theory. Interestingly, the second principle of thermodynamics, discovered at that time, pushed L. Boltzmann to propose a microscopic interpretation of entropy, together with the fundamental microscopic equations for out-of-equilibrium heat transfer [Boltzmann 1903]. Since then, the understanding of the composition of the matter at a microscopic level has evolved, and heat transfer is now described at the nanoscale, as well as at the atomic and even sub-atomic scales [Zenji *et al.* 2020]. This improved knowledge of physics at a nanoscale participated greatly in the development of microelectronics [Riordan 2004].

The development and miniaturization of microelectronic components, has created new needs. Two of them are particularly relevant for this work: a better management of waste heat and the powering of autonomous devices. As 72 % of the energy ends up wasted as heat [Forman *et al.* 2016], energy recovery at any scale represents an important opportunity. For instance, this heat can be used to generate the energy necessary to power small devices [Kishore & Priya 2018]. In parallel, through better thermal management, the impact of mass computing could be reduced, by reducing the need for cooling [Oltmanns *et al.* 2020]. These two applications, have in common to require semiconductors with tailored thermal properties. However, a precise knowledge of the heat propagation is also useful in many other fields and applications. For instance, the thermal properties of a material affect the mechanical properties through thermo-mechanical coupling [Allen 1991, Chrysochoos & Peyroux 1997]. A popular use of this effect is in shape memory alloys [Lester *et al.* 2015]. Another example, is crack propagation, as it is an energy activated process, an efficient thermal management could help to prevent brittle failure [Vincent-Dospital *et al.* 2020].

As the microchips get smaller and smaller, the power density and thus joule heating are increased [Schelling *et al.* 2005]. This means that the heat has to be efficiently managed, this happens through a good coupling with heat sinks [Zheng *et al.* 2021]. For this, a good thermal design at the nanoscale is crucial. To understand the length and timescale it concerns, it is useful to have in mind the size of transistors. The first 5 nm transistors were available to the public in 2020 and the 3 nm are already in mass production test mid-2021 [Lily 2021]. The timescale is set by

the processor frequency, that is around 2 to 10 GHz, this results in subnanosecond cycles. This is not the only link between thermal management and information processing. An advanced mastering of thermal transfer at the nanoscale could render possible the processing of information through heat transport (thermal computing) [Sklan 2015]. To achieve this, one should not only be able to guide heat but also to have thermal switches and thermal diodes [Wang & Li 2007, Wehmeyer *et al.* 2017, Kasprzak *et al.* 2020].

A good control of the thermal properties is also required for thermoelectric generation. It relies on the Seebeck effect, linking an electric potential difference and a thermal gradient. In order to use it to generate electricity, semiconductors with a good electrical conductivity to transport the charges and a low thermal conductivity to sustain the thermal gradient are needed. These two properties, with the Seebeck coefficient and the temperature, are used to measure the performance of thermoelectric materials through the figure of merit [Rowe 2018]. A way to increase the efficiency is to take advantage of an appropriate nanostructuration [Haras & Skotnicki 2018]. These applications give the scope of this work: the study of thermal transfers in semiconductors. More precisely, the focus will be laid on the lattice contribution to thermal conductivity at the nanoscale.

With the decrease in the size of the objects, the macroscale models start to be less and less accurate. In the case of thermal transfer, this means that the Fourier law does not give an accurate representation anymore. At the nanoscale, the heat transfer is often described by pseudo-particle (or heat carrier) exchanged between hot and cold zones. The lattice heat carriers (*phonons*), are described as vibrations of the atoms around their equilibrium positions. These vibrations are transmitted through the atomic network. In this aspect, phonons are very close to sound waves, but they differ by one important factor: the frequency. To carry a substantial energy amount, very high frequencies, and thus low wavelength, are needed. This renders the phonon much more sensitive to obstacles or collisions with another vibration than the sound waves. This frequent scattering distributes slowly the heat through the material. Such a representation gives an accurate prediction for the simple cases, for crystalline semiconductors for instance. It can even take into account the role of defects on the thermal conductivity. However, the usual solid mechanics description, initially developed for crystals [Ashcroft *et al.* 1976, Kittel 1976], relies on the periodicity of the material. So, that, it starts to fail when disorder goes from the exception to the norm. The simplest high disorder materials for which the model fails are glasses. But the nanostructuration of the material can also disturb the crystalline lattice enough to render this picture ineffective and require more complex models.

Glasses and nanostructured materials not only render the simplest thermal transfer model ineffective, but they also usually have a reduced thermal conductivity. These are, thus, materials of choice for the applications of interest. Glasses are the simplest low thermal conductivity materials, they do not rely on pores nor on nanostructuration to have a low thermal conductivity. Rather, their low thermal conductivity stems from the lack of structural periodicity, preventing the ballistic

transport of energy above a few nanometers [Allen & Feldman 1993]. However, this structural disorder also prevents the circulation of electrons, rendering their use for electronic applications complicated. Nanocomposites can be used to circumvent this problem.

Nanostructured materials or nanocomposites cover a wide range of materials with features of characteristic dimension below the hundred of nanometers. The modern fabrication methods allow the creation of structures at this scale. The dimensions reached are small enough to change the propagation properties of heat carriers [Sledzinska *et al.* 2020]. One popular example are superlattices, where very thin layers of two different phases are alternated. This pattern alters the thermal transport in two ways: by introducing interfaces that scatter the heat carriers and by introducing a periodicity that can change the transport properties [Ravichandran *et al.* 2014]. Other popular nanostructures also include nanowires or nanotubes that force the heat flux in one dimension [Rurali 2010]. However, the simplest nanostructures consist of inclusions of nanometric dimensions in a host matrix. In these nanometerials the nanoinclusions act as scatterers for the heat carriers, slowing their propagation and the transport of heat. Interestingly, the nanostructuration tends to impact the heat transport more than the electrical conductivity. The average distance traveled by an electron before scattering is much smaller than for phonon. As a result, the nanostructuration needs to be much smaller to affect the electrons than the heat carriers. This can be used, notably in amorphous crystalline nanocomposites, where the crystalline structure insures the electrical conductivity and the amorphous matrix provides the thermal insulation.

The nanostructures used for the reduction of thermal conductivity often take advantage of the resonant frequency of the material to attenuate the transmission of energy. In this aspect, they are very close to materials designed for sound attenuation, and principle and design can be transferred from one field to the other [Maldovan 2013]. This is notably the idea behind metamaterials [Kishore *et al.* 2021].

There are multiple ways to circumvent the shortcomings of the usual theory of transport at the nanoscale. One of them is to consider each atom individually. This allows to get rid of the hypothesis about the short scale periodicity of the structures. By building a model based on a simple fundamental element, a point mass interacting with others, it is possible to model the heat transfer in complex nanostructures. This thesis is based on this principle: using molecular dynamics, the vibrational and thermal properties of nanocomposites are studied. Such an approach not only allows to represent explicitly arbitrary microstructures. But it can also be used to compare, understand and improve continuous theories. The direct access to the different quantities that MD simulations provide, can also be used to improve continuum medium heat transfer model [Tong *et al.* 2019]. For instance, thermomechanical coupling at the macroscale couples two different quantities, temperature and displacement, at the nanoscale, these quantities are both linked to the movements of the atoms [Jabbari *et al.* 2017].

This thesis will start with a brief overview of the theory of thermal transfer at the

nanoscale, a special attention will be devoted to the distinction between continuum and discrete method. The length and timescale limitation of the methods will be discussed. It entails a more detailed description of the molecular dynamics methods used to describe heat transfer.

In the second chapter, the thermal properties of several bulk nanocomposites will be studied. The effect of the size, stiffness and interconnection of the nanoinclusions will be analyzed. Going through the chapter, the systems go from spherical scatterers in an amorphous matrix to a percolating crystal mesh embedded in a crystalline or amorphous matrix.

The third chapter will focus on the thermal transport in composite nanowires. In a first step, the properties of constant diameter core shell nanowires will be analyzed thanks to wave-packet propagation. This will be the occasion to study, the role of an interface parallel to the flux through the analysis of heat flux radial distribution in core/shell nanowires. This analysis is led using hydrodynamic heat transfer equations to give perspective on the obtained profiles.

Finally, it is shown that an asymmetric amorphous shell can induce thermal rectification in silicon nanowires.

At the end of each chapter, there is a small conclusion and synthesis recalling the key points mentioned in it. Moreover, to ease the reading of the manuscript the central results, and argumentation are outlined by black boxes.

Chapter 1

Theoretical Background and Methods

Contents

Before getting to the results obtained in this thesis, the theoretical background and methods of analysis of the heat transfer are presented. In particular, this chapter focuses on thermal transfer through lattice vibrations. It starts with a short recall of the equations used to describe thermal transport at the macroscale, then, the theoretical modeling of thermal transport is introduced. This introduction starts with thermal transfer in crystals and is then extended to glasses. After this, two continuous approaches of thermal transfer are presented: Monte-Carlo for phonons and the hydrodynamic heat equations. This is followed by a presentation of some atomistic models. Among those, Molecular Dynamics (MD), a method that is used through-out this monograph, is presented more in depth. At this occasion, the different concepts used to study the thermal and vibrational properties of nanomaterials are presented.

1.1 Nanoscale Thermal Transport

In this section, the fundamentals of heat transfer are recalled, starting with the Fourier law and its limits. After this, the concept of phonon is introduced and its role in thermal conductivity explained.

1.1.1 From Macro to Nanoscale

Before getting to the explanation of the theoretical foundation of the modern understanding of lattice thermal conductivity, it is useful to recall how heat transfer is modeled at the macroscale.

Let's start by recalling what heat is, thermodynamically. One of the first definition of heat, appears in the first principle as defined by Joule in 1843: heat is a way energy can be exchanged, as is work [Joule 1851]. It corresponds to a variation of the fast degree of freedom, whereas work corresponds to a slow degree of freedom. Heat is also tightly linked to entropy: a heat transfer induces an entropy increase. The second principle infers that in an isolated system, the heat has to flow from the hot to the cold subsystem [Diu & Guthmann 1989].

The founding relation of the thermal transfer science is the Fourier law. It links the heat flux ($\mathbf{j}$) going through a material to the temperature gradient (∇T) across the material, using an intrinsic property of the material, the thermal conductivity (κ):

$$\mathbf{j} = -\kappa \nabla T, \tag{1.1}$$

This relation can be used directly to model heat transfer in the steady state. To get the evolution as a function of time, it can be combined with the energy conservation

relation:

$$(\frac{\partial E}{\partial t}) + \nabla \cdot \mathbf{j} = 0, \tag{1.2}$$

with E the energy in the absence of heat source. If the energy variations are due only to temperature variations, it can be rewritten as:

$$\rho C_p(\frac{\partial T}{\partial t}) + \nabla \cdot \mathbf{j} = 0 \tag{1.3}$$

with ρ the density of the material and C_p the heat capacity. Combining the equations (1.1) and (1.3) the usual equation governing the diffusion of heat for constant κ at the macroscale is obtained:

$$(\frac{\partial T}{\partial t}) = \frac{\kappa}{\rho C_p} \nabla \cdot (\nabla T) \tag{1.4}$$

This is a typical diffusion equation. It can be solved analytically for simple initial conditions. Interestingly, the concept of Fourier series was created to solve this equation. It can also be solved using numerical methods, as finite or discrete elements.

However, being a phenomenological equation, established on empirical observations in 1822, it has its limits. It is an accurate description of thermal transfer in solids at the macroscale. The main shortcoming of this model is that, it assumes that the temperature gradient is instantaneously felt across the system. In other terms, the response time of the system is neglected [Volz 2007]. If this approximation is reasonable for relatively long timescales, it starts to fail for shorter timescales.

To explain this shortfall and other limitations of this theory, the way heat is transported at the microscopic level must be considered.

1.1.2 Lattice Thermal Conductivity

As stated in the introduction, the scope of this work is the study of heat conduction, the radiative and convective heat transfer are thus neglected. Moreover, in this section, a supplementary hypothesis is made, that is, that atoms do not move significantly away from their equilibrium position. As a consequence, there are only two possibilities left to carry heat, through electrons or through mechanical wave propagation. The thermal conductivity due to the vibration of the atoms is called *lattice thermal conductivity*, it is the main contributor to heat transfer in insulators and in most semi-conductors. In this section, the theoretical modeling of this lattice thermal conductivity is presented through the concept of phonons.

One Dimensional Atomic Chain The vibrational modes of a periodic discrete system, such as a crystal lattice, can be quantified. These discrete modes are called *phonons*. A quick example can be given for an atomic chain such as the one represented in figure 1.1 [Kittel 1976]. In this model, the atoms are point masses linked by springs with their first neighbors.

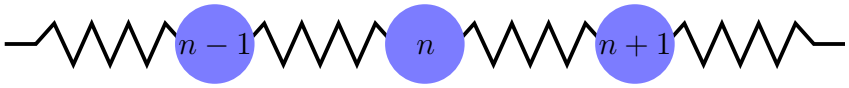

Figure 1.1: Representation of a 1D atomic chain as point masses linked by springs.

For this simple system, the equation of motion of the atom i can be written as:

$$m\frac{\partial^2 u_n}{\partial t^2} = k(u_{n+1} - u_n) + k(u_n - u_{n-1}), \tag{1.5}$$

with u_n the displacement of the atom n, k the spring constant. Solutions for this equation can be found in the form of a plane wave $u_n = u_0 \exp(i[\omega t - qna])$, with a the interatomic distance at equilibrium, ω the eigenfrequency of the mode and q its wave vector (reduced to a scalar in the case of the 1D chain). Injecting this solution in equation (1.5) gives the relation between ω and q:

$$\omega = 2\sqrt{\frac{k}{m}}\left|\sin\frac{qa}{2}\right|, \tag{1.6}$$

this relation is called the dispersion relation. To complete the solution, boundary conditions must be set, here periodic boundary conditions are used to model an infinite crystal [Ashcroft *et al.* 1976]. For N atoms, the atom N is linked with the atom $N-1$ on the left and the first atom on the right. Using this, one finds $q_n = \frac{2\pi n}{Na}$ with n labeling the mode number. In most applications, N is sufficiently large for q to be considered continuous. In periodic lattices, q has a maximal value. Indeed, due to the discreteness of the lattice, multiple wave vectors can describe the same mode ($u_n = u_0 \exp\{i[\omega t - qna]\}$ is the same if q is increased by $2\pi/a$). All possible vibrational modes can then be defined with [Ashcroft *et al.* 1976]:

$$-\frac{\pi}{a} < q < \frac{\pi}{a}. \tag{1.7}$$

This space of uniquely defined modes is called the Brillouin zone. The group velocity of phonons can be derived from the dispersion relation with $v_g = \frac{\partial\omega}{\partial q}$. The modes so described are called acoustic phonons. If two types of atoms with different masses or stiffness constants are introduced, other modes appear. The two different atoms can now move in phase as described earlier, or out of phase. The out of phase solution, concerning higher frequencies, gives the optical phonons [Kittel 1976].

Three Dimensional Lattice The concepts given for a one dimensional atomic chain can be extended to a three-dimensional crystal lattice [Kittel 1976]. This increases the number of degree of freedom to three per atom. There are now $3N$ modes, for each mode described earlier: there are three possible branches, one longitudinal corresponding to a movement parallel to the propagation direction akin to compression (see figure 1.2a) and two transverse for the two directions perpendicular to the propagation akin to shear modes (see figure 1.2b). $\mathbf{q}$ is now a three-dimensional

wave vector. The different directions possible for **q** correspond to the different lattice directions [Dove 1993]. The notion of Brillouin zone is now extended in each direction, depending on the periodicity of the lattice in these directions.

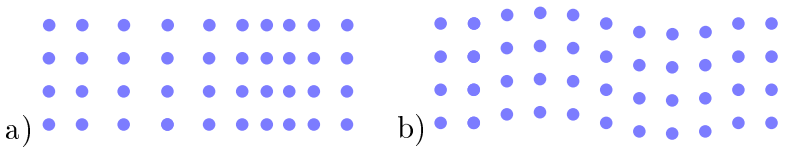

Figure 1.2: Example of a longitudinal/compression (a) and a transverse/shear (b) modes.

The description of the crystal laid out in this section corresponds to the vision of lattice dynamics, a fundamental field for the understanding of vibrational and thermal properties at the microscale. It is presented shortly in section 1.7.1.

Phonon Distribution Each quantified vibration, called a *phonon* is characterized in crystals by its wave vector **q**. The energy carried by each phonon depends on its frequency and is given by $\omega\hbar$, with $\hbar$ the Planck constant. The phonons are indistinguishable quasi-particles, occupying discrete states and not concerned by the Pauli exclusion principle. As such, they obey Bose-Einstein distribution [Ashcroft *et al.* 1976]:

$$f_{BE} = \frac{1}{\exp\left(\frac{\omega\hbar}{k_b T}\right) - 1}, \tag{1.8}$$

with k_b the Boltzmann constant. This gives pulsation distibution of phonons at a given temperature T. This distribution function as a function of frequency and temperature implies that at low temperature the high frequency phonons have a very low probability of existence, or equivalently, a very low impact on the physical properties of the system. The temperature below which the quantum nature of phonons matters is called the Debye temperature Θ_D. In other words, below Θ_D, not all the modes are allowed, the high frequency modes are "frozen", that is there probability of existence are very low as described by the Bose-Enstein distribution of modes (equation [1.8]) [Ashcroft *et al.* 1976]. Above this temperature, the Bose-Einstein distribution starts to be equivalent to the Maxwell-Boltzmann distribution for indistinguishable classical particles. This distribution is given by:

$$f_{MB} = \frac{1}{\exp\frac{\omega\hbar}{k_b T}}. \tag{1.9}$$

Up to this point, the phonons have been described as waves, however, within the wave-particle duality picture, they can also be seen as particles. This particle picture is useful to describe their contribution to the thermal conductivity.

1.1.3 Phonon Scattering

In the model introduced in this section, with a perfect lattice and a harmonic potential (interatomic forces represented by springs) phonons do not interact with each other, and there is nothing limiting their propagation. As phonons are the lattice heat carriers, this translates into an infinite thermal conductivity [Dove 1993]. In reality, the lifetime of the vibrational modes is limited either through damping (anharmonicity of the interaction potential) or through imperfections that break the lattice periodicity. Using the particle picture, the anharmonicity can be understood as a collision between phonons. The most commonly described type of collisions, are the "three phonon processes" where two phonons collides to create a third or one phonon splits in two. Among those collisions, two types are distinguished, the elastic collisions that conserve the overall crystal momentum (sum of the wave vectors) and the inelastic collisions or Umklapp processes that do not conserve it. In all cases, the conservation of energy imposes that:

$$\omega_1 + \omega_2 = \omega_3 \tag{1.10}$$

with ω_1 and ω_2 the frequency of the incident phonons, ω_3 the frequency of the resulting one.

Normal Scattering The elastic collisions are called *normal scattering*. The conservation of wave vector in the case of normal scattering can be written as:

$$\mathbf{q_1} + \mathbf{q_2} = \mathbf{q_3}, \tag{1.11}$$

with $\mathbf{q_1}$ and $\mathbf{q_2}$ the wave vectors of the two incident phonons, and $\mathbf{q_3}$ the wave vector of the resulting phonon (see figure 1.3a). This kind of scattering does not change the overall direction of the phonon flow: the resulting phonon direction corresponds to the sum of the direction of the two incidents phonons. Consequently, it does not affect the overall transport of heat [Kittel 1976].

Umklapp Scattering However, due to the periodicity of the lattice, phonon/phonon scattering does not necessary conserve the wave vector sum. If the wave vector of the created phonon exceeds the maximum value allowed (defined in 1D by equation [1.7]), the equation (1.11) becomes:

$$\mathbf{q_1} + \mathbf{q_2} = \mathbf{q_3} + \mathbf{G}, \tag{1.12}$$

with $\mathbf{G}$ a reciprocal lattice vector, corresponding to the inverse of the lattice distance in the 1D case. These processes change the orientation of the wave vector sum (see figure 1.3) and thus slow the propagation of heat, inducing a reduction of the thermal conductivity [Kittel 1976].

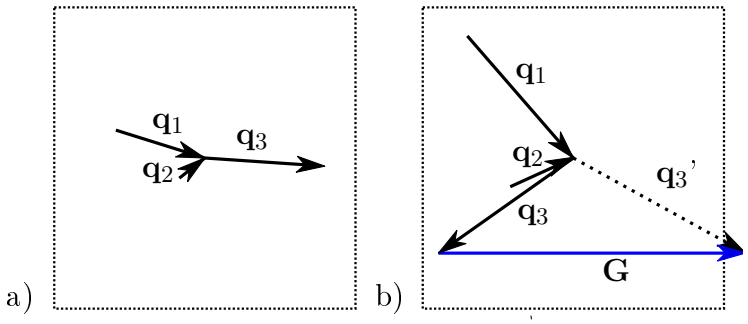

Figure 1.3: Schematic representation of Normal (a) and Umklapp scattering (b), $\mathbf{q_i}$ represents the phonon i through its wave vector. The square in dashed line represents the first Brioullin zone, $\mathbf{G}$ is a reciprocal lattice vector represented by the blue arrow.

"Geometrical" Scattering In real crystals, there are defects that breaks the periodicity of the lattice, this perturbs the propagation of phonons. Different defect types have a diverse impact on phonons. The first kind are point defects, that is crystalline vacancies or interstitial, impurities or isotopes. These point defects interact mostly with high frequency phonons, that have a wavelength comparable to the size of the defect [Tritt 2005]. The second kind are unidimensional defects, typically dislocations. The dislocations affect the transport through the distortion of the lattice they induce. Again, this perturbs mostly the high frequency phonons due to the reduced size of the dislocation core [Ziman 1960]. The third types of defect are surface defects, typically grain boundaries or 2D lattice imperfections (twins or stacking faults). This kind of defects usually induces a partial reflection of the phonons, distributing the energy of the incident phonon between the two side of the boundary (reflection and transmission) [Ziman 1960]. The effect of interfaces on the thermal transport is a very active subject [Termentzidis 2017]. The last type of defects are volume imperfections, typically inclusions of another phase. Their effect depends on their size and composition, these defects are the subject of chapter 2.

So far, it has been shown that the phonons can be seen as particles whose trajectories are modified by collisions, either with other phonons or defects. This picture is called the phonon gas model. The evolution of the distribution of particles and thus heat transfer within this picture can be described using the Boltzmann Transport Equation (BTE).

1.1.4 Boltzmann Transport Equation

The BTE is an equation describing the evolution of the distribution function of particles. It was derived originally to describe atomic diffusion in monoatomic gases. It supposes that in these gases, the collisions between atoms are rare, conserve momentum and happen instantaneously[1].

[1] Or at least, that the duration of a collision is negligible in front of the relaxation time of the system [Kittel 1976].

It is derived from the Liouville theorem [Pottier 2007] describing the time evolution of a distribution function with an additional collision term. The original equation for a distribution $f(\mathbf{r}, \mathbf{v}, t)$ of moving particles with positions $\mathbf{r}$ and velocity $\mathbf{v}$ is [Kittel 1976]:

$$\frac{\partial f}{\partial t} + \mathbf{v}\nabla_{\mathbf{r}} f + \alpha \nabla_{\mathbf{v}} f = (\frac{\partial f}{\partial t})_{coll}. \tag{1.13}$$

The $(\frac{\partial f}{\partial t})_{coll}$ is the collision term, it describes the variation of the distribution due to collisions between particles. $\mathbf{v}\nabla_{\mathbf{r}} f$ is the advection term and $\alpha \nabla_{\mathbf{v}} f$ the force term coming from the Liouville theorem. In the case of a monoatomic gas, f is the Maxwell-Boltzmann distribution (see equation [1.9]). In this case, the collision term is derived using the effective section of the atoms to estimate the probability of collision [Diu & Guthmann 1989].

Before going on, it is worth mentioning that, the exact form of equation (1.13), including every kind of non-linear interactions between coupled particles (and not only the collisions), is a set of coupled equations, each involving higher order terms forming the BBGKY hierarchy [Kreuzer 1981]. The form given here is a simplification for independent particles, the correlation between pairs of particles being hidden in the collision term.

In the case of phonons, the equilibrium distribution function is the Bose-Einstein distribution (see equation [1.8]). And the equation (1.13) is simplified by neglecting the force term, considering that there is no external field acting on the phonons. The $\mathbf{v}$ in the advection term corresponds to the group velocity of acoustic phonons.

The collision term is often estimated thanks to the relaxation time approximation:

$$(\frac{\partial f}{\partial t})_{coll} = \frac{f - f^0}{\tau} \tag{1.14}$$

with τ the relaxation time and f^0 the equilibrium distribution function. The relaxation time is a parameter describing the time needed to return to equilibrium once the system is perturbed. In the case of phonons, τ corresponds to the lifetime of phonons, that is the average time between two collisions [Kittel 1976].

By using these approximations, the equation (1.13) reduces to:

$$\frac{\partial f}{\partial t} + \mathbf{v}\nabla_{\mathbf{r}} f = \frac{f - f^0}{\tau}, \tag{1.15}$$

and in the steady state, the first term is null. This particular form of the BTE used for a rarefied phonon gas is the Peierls-Boltzmann equation [Pottier 2007].

The distribution function and group velocity can be used to compute the heat flux due to phonons [Ziman 1960]:

$$j = \frac{1}{3} \sum_{\mathbf{q}} f_{\mathbf{q}} \omega_{\mathbf{q}} \hbar v_{\mathbf{q}}, \tag{1.16}$$

with $\sum_{\mathbf{q}}$ a sum over each mode labeled by its wave vector $\mathbf{q}$ and $f_{\mathbf{q}}$ the probability density attributed to a particular mode. If the deviation to the equilibrium

distribution is caused by a thermal gradient, equation (1.16) can be transformed in [Ziman 1960]:

$$j = \frac{1}{3}\nabla T \sum_{\mathbf{q}} \omega_{\mathbf{q}} \hbar \frac{\partial f_{\mathbf{q}}}{\partial T} v_{\mathbf{q}}^2 \tau_{\mathbf{q}}, \tag{1.17}$$

with $\tau_{\mathbf{q}}$ the relaxation time of the mode $\mathbf{q}$. By dividing the equation (1.17) by ΔT the kinetic theory results can be recognized:

$$\kappa = \frac{1}{3} \sum_{\mathbf{q}} C_{latt} v_{\mathbf{q}}^2 \tau_{\mathbf{q}}, \tag{1.18}$$

with $C_{latt} = \omega\hbar\frac{\partial f_{\mathbf{q}}}{\partial T}$ the lattice heat capacity [Ashcroft *et al.* 1976]. The equation (1.18) is useful to understand the role of time/length scale in the shortcoming of the Fourier law. For this, the Mean Free Path (MFP) $\Lambda = v_{\mathbf{q}}\tau_{\mathbf{q}}$ is introduced, it corresponds to the average distance traveled by a phonon before a scattering event. If this distance is small in front of the system size (as represented in figure 1.4 b), κ does not depend on size and geometry and the Fourier law (equation [1.1]) is valid. If Λ is of the order of the size of the system, the transport is ballistic (as represented in figure 1.4 a). In this case, the value of κ depends on the size and geometry of the system.

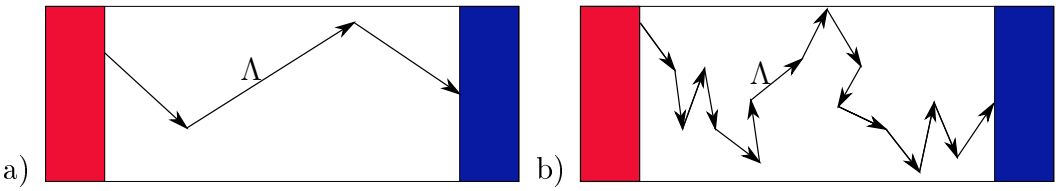

Figure 1.4: Schematic representation of ballistic (a) and diffusive transport (b). The blue region represents the cold and the red the hot thermal bath, each arrow represent the trajectory of a phonon between scattering events.

The BTE is a very useful tool to model thermal transport. It is widely used to estimate the thermal conductivity at the nanoscale using a continuous model, some of those models are presented in section 1.2.

1.1.5 Thermal Transport in Amorphous Material

The development of section 1.1.4 relies on the phonon gas picture. This representation of lattice thermal conductivity assumes that the lattice vibrations that carry heat, are moving in a straight line at a given velocity with a given frequency, wave vector and polarization. The distance traveled by these phonons being limited by collisions with other phonons or crystal defects [Ashcroft *et al.* 1976]. This model was designed for perfect crystals, and is still effective for crystals with defects, but breaks down for disordered systems. Indeed, in disordered systems, like amorphous materials, phonons with a well defined eigenvector are no more eigenmodes of the system.

The vibrational modes in amorphous materials have been extensively described by Tanguy *et al.* [Tanguy *et al.* 2002, Tanguy 2015, Beltukov *et al.* 2016]. Three types of vibrations were identified: plane waves (*propagons*), vibrations with a rotational structure (*diffusons*), and multifractal modes (*locons*).

The breakdown of the phonon gas model was introduced earlier by Allen and Feldmann [Allen & Feldman 1993]. They have shown that for disordered solids, the BTE cannot be applied. In these solids, the mean free path of some plane waves excitations is of the order of the interatomic distance. Due to the small propagation length, these excitations do not have a well-defined group velocity and wave vector. Therefore, their contribution to the thermal conductivity can not be estimated through equation (1.18). However, those vibrations still contribute to the heat transport. To take those contributions into account, a new model was developed.

For this, they have introduced an intermediary transport regime between the localization and the propagation of vibrations: the diffusive regime [Allen & Feldman 1993, Allen *et al.* 1999]. They have extended the notion of phonon as heat carriers and established a distinction between propagative and non-propagative phonons. For the propagative one, the phonon gas model can be applied and the equation (1.18) used to estimate their contribution to the lattice thermal conductivity. In the frequency range of the *propagons*, a plane wave excitation keeps its structure, and wave fronts show a well defined group velocity (see figure 1.5a). Allen and Feldman have called the eigenmodes of the dynamical matrix in this frequency range *propagons*, by analogy with the dynamics of plane wave excitations in the same frequency range [Feldman *et al.* 1999].

On the contrary, for the non-propagative phonons, no proper wave vector/velocity can be defined. The non-propagative phonons can be decomposed into two categories of eigenmodes: the locons and the diffusons. Locons are localized modes, with a low participation ratio[2] as described by Anderson in disordered systems [Anderson 1958, Faez *et al.* 2009] (see figure 1.5c). These vibrations are always supported by the same sites. As such, they do not contribute to the transportation of energy through the system [Beltukov *et al.* 2018].

Diffusons designate the eigenmodes in the frequency range where plane waves are strongly scattered (see figure 1.5b for the dynamical evolution of plane waves with finite extent in the frequency range of *diffusons*). They were originally interpreted as off diagonal terms in the heat current operators [Allen & Feldman 1993]. In the frequency range of diffusons, the vibrational energy is neither transported at finite velocity, neither localized, but it is spread diffusively. This can be shown as resulting from the decomposition of the plane waves on random vibrations that break the front wave [Tanguy *et al.* 2010]. The resulting diffusion is characterized by a diffusivity coefficient D_i [Feldman *et al.* 1993]. The contribution of the vibrations to the thermal conductivity in this frequency range is written as:

[2]The participation ratio describes the proportion of atoms participating to a vibrational mode. The definition is given by equation 1.43 in the following of this chapter.

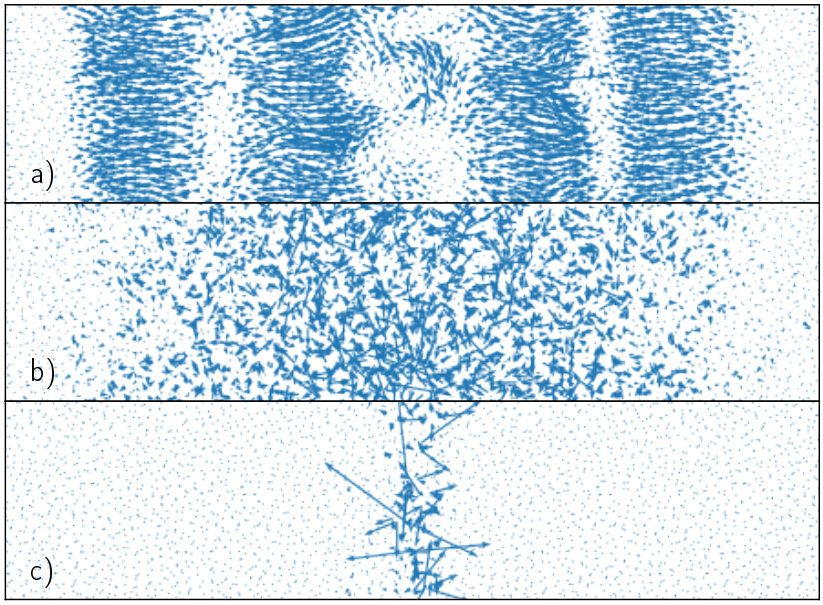

Figure 1.5: Illustration[a] of the velocity fields in the different regimes: propagative (a), diffusive (b) or localized (c) the blue arrows represent the velocity of the atoms.

[a]Obtained by exciting a slice of Amorphous Silicon (a-Si) at 1 (a), 12 (b) and 19 THz (c) with a longitudinal force excitation at a given frequency on a finite temporal window (see section 1.5.3), the first image is obtained 1.7 ps after the excitation, the others 12 ps after it.

$$\kappa = \sum_i C_{latt} D_i. \tag{1.19}$$

These regimes being described, a difficulty arises: how to distinguish them and compute the different contributions to the thermal conductivity. This difficulty was circumvented in the seminal paper of Allen and Feldman by considering the contributions of the different regimes using a Matthiessen rule [Feldman *et al.* 1993]. Multiple authors have simply used a frequency limit to discriminate between propagative and diffusive modes [Beltukov *et al.* 2013, Larkin & McGaughey 2014]. The used frequency limit is set by the Ioffe-Regel criterion. This criterion relies on the comparison between the MFP and the wavelength [Feldman *et al.* 1993]. It reflects that for a MFP lower than the wavelength, no group velocity nor wave vector can be defined. However, both propagative and diffusive regimes coexist around this frequency hence, the diffusons progressively take-over the propagons and there is no sharp limit. The distinction between locons and diffusons is based on the participation ratio [Feldman *et al.* 1993, Beltukov *et al.* 2016], but also on their contribution

to energy transport [Beltukov *et al.* 2018]. In amorphous silicon, most of the heat transfer appears to be diffusive, one of the latest approximation gives only 30 % of propagative contributions [Tlili *et al.* 2019].

Some authors use a different definition of diffusons. For instance, Seyf and Henry have developed a method to distinguish the propagons and diffusons systematically based on the periodicity of the eigenmode [Seyf & Henry 2016]. However, Tanguy *et al.* have already shown that all eigenmodes in amorphous materials can be described as superposition of plane waves [Tanguy *et al.* 2002]. The propagative or diffusive nature of the propagation depends on the number and orientation of these plane waves.

1.2 Continuous models

In the section, continuous medium models relying on the equation (1.18) are presented: starting with the direct use of equation (1.18), it continues with a stochastic approach to solve BTE (the Monte-Carlo method) and concludes with the hydrodynamic heat equations that uses the BTE to rederive a heat equation taking boundaries and relaxation time effects into account.

1.2.1 Model Based on Kinetic Theory of Gases

The equation (1.18) is used in many models to predict the thermal conductivity of solids. These models have been first described by Callaway [Callaway 1959], and Klemens [Klemens 1955]. They contain estimations of the lifetime due to different scattering processes. These lifetimes are then summed using the Matthiessen rule:

$$\tau_T^{-1} = \sum_i \tau_i^{-1}. \tag{1.20}$$

This approach is valid if the scattering phenomena are independent of each others. For example, Klemens gives an estimation of the lifetime reduction due to the different scattering sources named in section 1.1.3 depending on the temperature range [Klemens 1958].

This kind of method have been widely used since the sixties [Slack & Galginaitis 1964], and continue to be popular [Yang & Dames 2013]. However, the determination of the coefficient often requires fitting to experimental data of the thermal conductivity as a function of the temperature, and the method thus appears to be mainly phenomenological.

1.2.2 Monte-Carlo Resolution of the Boltzmann Equation

In general, Monte-Carlo methods refer to approaches using a random sampling from a distribution to compute an approximation of a numerical quantity by averaging over numerous inputs. In the context of thermal transport, it can be used to compute an approximate solution of the BTE [Lacroix *et al.* 2006]. The idea is to create two

thermal baths, each one sampling phonons from the Bose-Einstein distribution, and to let the phonons, represented by particles, propagate in the structure (see figure 1.6). The phonons' energy, velocity, and direction are chosen to represent the physical distribution of the phonons in the structure. This depends on the temperature set for the thermal baths and material being modeled. The system is

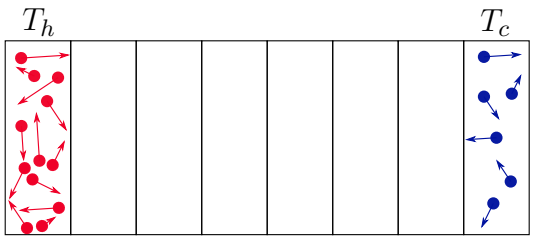

Figure 1.6: Schematic view of the starting point of a MC simulation, the phonons (dots) are generated in the hot (T_h) and cold (T_h) heat baths and have a velocity distribution taken from equation (1.8).

discretized in volume elements. These elements have distinct properties depending on their temperature, and material composition. Then the movement of the phonons across the material (phonon drift) is simulated iteratively. At each time step, the position of the phonons are updated, by multiplying their velocity vector by the time step. During this propagation step, it is checked that the phonons do not interact with boundaries or interfaces. The eventual collisions result in either a specular reflection or a diffusion, depending on the surface properties. After the phonon drift phase, the phonons have a set probability to be scattered by different mechanisms (atomic defects, phonon-phonon processes, *etc.*). The probability of each scattering mechanism is determined by the temperature and some material properties of the volume elements. The temperature of each volume element is determined by the energy of the phonons inside the volume at the given time step. After a certain number of time steps, a steady state is reached. At this point, the heat flux and thermal conductivity can be computed, using the phonons velocity and energy [Termentzidis 2017].

This method is particularly useful to compute the thermal properties of nanocomposites in the steady state. Contrary to the method described in the previous section, it can be used to model arbitrary complex geometries. The size limitation is given by the number of time steps needed to reach steady state. This amounts to a few micrometers. Given that the Bose-Einstein distribution is respected, provided that the different scattering probabilities are adapted to the conditions, this method is valid from 0 K up to the melting point [Termentzidis 2017].

1.2.3 Hydrodynamic Heat Transport Equations

The BTE can also be used to obtain a continuous medium equation describing the heat transport at the microscale. This is the idea behind the hydrodynamic

heat equations. For this, equation (1.15) is used to derive the balance equation of energy [Sendra *et al.* 2021]:

$$\frac{\partial e}{\partial t} + \nabla \cdot \mathbf{j} = 0, \tag{1.21}$$

and of momentum:

$$\frac{\partial \mathbf{p}}{\partial t} + \nabla \cdot \mathbf{\Pi} = \int \hbar \mathbf{q} C(f_{\mathbf{q}}) d\mathbf{q}, \tag{1.22}$$

with $e = \int \hbar\omega_{\mathbf{q}} f_{\mathbf{q}} d\mathbf{q}$ the energy density $\int d\mathbf{q}$ being the sum over the modes, $\mathbf{j} = \int \hbar\omega_{\mathbf{q}} f_{\mathbf{q}} v_{\mathbf{q}} d\mathbf{q}$ the heat flux, $\mathbf{p} = \int \hbar\mathbf{q} f_{\mathbf{q}} d\mathbf{q}$ the momentum density, $\mathbf{\Pi} = \int \hbar\mathbf{q} v_{\mathbf{q}} f_{\mathbf{q}} d\mathbf{q}$ the flux of crystal momentum and $C(f_q)$ the linearized collision operator.

By linking the energy density variation and the heat flux, equation (1.21) ensures the energy conservation. By expending the distribution $f_{\mathbf{q}}$ around the equilibrium Bose Einstein distribution and combining equations (1.21) and (1.22) one can obtain [Guyer & Krumhansl 1966b, Guyer & Krumhansl 1966a, Sendra *et al.* 2021]:

$$\mathbf{j} + \kappa \nabla T + \tau \frac{\partial \mathbf{j}}{\partial t} = l^2 [\nabla^2 \mathbf{j} + \alpha \nabla (\nabla \cdot \mathbf{j})], \tag{1.23}$$

where ℓ is the non local length, τ the heat flux relaxation time and α a non local coefficient. These parameters depend on the dispersion relations and lifetimes of the different phonon branches [Sendra *et al.* 2021]. The non-local length ℓ characterizes the distance over which the flux is affected by the boundary, and it can be understood as a length over which the flux is self correlated. This depends, in the derivation this work relies on, on the dispersion relation in the crystal and the relaxation time Sendra *et al.*:

$$\ell^2 = \frac{1}{5} \frac{\langle v_{g,\mathbf{q}}^3 / v_{p,\mathbf{q}} \tau_{\mathbf{q}}^2 \rangle}{\langle v_{g,\mathbf{q}} / v_{p,\mathbf{q}} \rangle} \tag{1.24}$$

where $\langle x_\lambda \rangle = \int \hbar\omega_\lambda \partial_T f_\lambda^{eq} d\lambda / C_v$ refers to the average over each wavelength weighted by the contribution of each mode to the thermal capacity, v_g is the group velocity, v_p is the phase velocity and $\tau_{\mathbf{q}}$ is the relaxation time of the mode. The heat flux relaxation time τ is defined by:

$$\tau = \frac{\langle v_{g,\mathbf{q}}^2 \tau_{\mathbf{q}}^2 \rangle}{\langle v_{g,\mathbf{q}}^2 \tau_{\mathbf{q}} \rangle}. \tag{1.25}$$

In the same way, the thermal conductivity is recovered:

$$\kappa = \frac{1}{3} C_v \langle v_{g,\mathbf{q}}^2 \tau_{\mathbf{q}} \rangle, \tag{1.26}$$

which is equivalent to equation (1.18). This description assumes that the material is isotropic. The relaxation time and velocities are usually extracted from *ab initio* simulations.

The first two terms of equation (1.23) correspond to the usual Fourier law. The last term in the left-hand side introduces the thermal inertial effect, this term is important when the timescale is close to the phonon lifetime. The terms in the right-hand side introduce non-local effects that appear when the size of the system

is of the order of the mean free path. This last term is analogous to a viscous term. This equation has some similarity with the Navier-Stokes equation (NSE). The heat flux here corresponds to the flow velocity in the NSE, the temperature gradient correspond to the pressure gradient and the non local length to the viscous term. For these reasons, equation (1.23) is called the phonon hydrodynamic equation. Moreover, it is to be noted that the NSE can be derived from the BTE applied to atoms [Diu & Guthmann 1989].

If the original derivation was made for low-temperature applications for specific materials where N-processes dominate like graphene [Guyer & Krumhansl 1966b, Cepellotti *et al.* 2015, Lee *et al.* 2015], it has been shown that it can be generalized for other materials at room temperature [Beardo *et al.* 2021a, Alajlouni *et al.* 2021, Beardo *et al.* 2020, Guo *et al.* 2018].

The equations (1.23) and (1.21) can be solved for complex geometries using the finite element method. For this, boundary conditions are needed, the slip (Neumann) boundary condition for the tangential heat flux $\mathbf{j_t}$ is often used:

$$\mathbf{j_t} = -C\ell\nabla\mathbf{j_t}\cdot\mathbf{n}, \tag{1.27}$$

with $\mathbf{n}$ the normal vector pointing toward the exterior, and C the slip coefficient. C is determined as a function of the specular and diffusive phonon-boundary reflections [Beardo *et al.* 2019]. C sets the heat flux at the boundary.

It is also worth to note that the applicability of the hydrodynamic heat transport model derived in [Sendra *et al.* 2021] is limited to small enough Knudsen numbers. A limit of validity is given by the fact that the effect of the boundaries should not overlap that is $\ell < L/2$ with L characteristic length. This method, implemented using finite elements, has already successfully modeled the thermal relaxation of nanostructured heat sources on Si substrate [Beardo *et al.* 2021a, Alajlouni *et al.* 2021] or thermoreflectance experiments [Beardo *et al.* 2020]. Alternatively, the method can be used more phenomenologically to provide an interpretation of mesures obtained with MD [Melis *et al.* 2019]. This approach will be used in chapter 3 in conjunction with molecular dynamics to study the radial heat flux distribution in nanowires.

1.3 Molecular Dynamics (MD)

The thermal and vibrational properties at the nanoscale are dictated by the microstructure. To reflect this, many methods that consider the atomic structures explicitly were developed. One of them is MD, in this section, the basic concepts of this method are reviewed.

1.3.1 Movement of Particles

Molecular Dynamics is a simulation method in which the movement of each atom constituting the matter is modeled. It was developed in the fifties at the very beginning of computer simulation [Alder & Wainwright 1959]. The idea is rather simple,

the movement of each atom is derived from the newtonian equation of motion. The forces acting on each atom are computed from an interatomic potential:

$$m_i \frac{d^2\mathbf{r}_i}{dt^2} = -\frac{\partial U}{\partial \mathbf{r}_i}, \tag{1.28}$$

where $\mathbf{r}_i$ is the position of the atom i, m_i its mass, and U the interaction potential. This equation is then solved by a stepwise integration scheme, giving the evolution of the position and the velocity of each atom. The most commonly used integration scheme is the Verlet velocity scheme [Swope *et al.* 1982]:

$$\mathbf{r}_i(t+\Delta t) = \mathbf{r}_i(t) + \mathbf{v}_i(t)\Delta t + \frac{1}{2}\mathbf{a}_i(t)\Delta t^2 \tag{1.29}$$

with t the time, Δt the integration timestep, $\mathbf{a}_i = \frac{d^2\mathbf{r}_i}{dt^2}$ the acceleration, the velocity $\mathbf{v}_i(t)$ is computed with:

$$\mathbf{v}_i(t+\Delta t) = \mathbf{v}_i(t) + \frac{\mathbf{a}_i(t) + \mathbf{a}_i(t+\Delta t)}{2}\Delta t. \tag{1.30}$$

This integration scheme has the advantage of being simple, stable, and time reversible [Frenkel & Smit 2001]. The time step used depends on the simulation, but has to be short enough to insure energy conservation. For the systems studied in this work, the time step is 1 or 0.5 fs. From this time step, the time and length scale limitations of MD are easy to understand, 1×10^6 times steps are needed to reach a 1 ns. Thus, on modern monoprocessor computers it takes a few hours to compute the trajectories of 1×10^4 atoms over 1 ns. However, MD simulations are easily parallelizable, and thus the simulations can be performed on massive compute-nodes.

Because it uses a classical equation of motion, MD is fully classical and deterministic. There is no quantization of energy states, and the same initial state of the simulated system, same initial positions and velocities, leads to the same evolution (if the integration errors are neglected).

To carry out the different MD simulations described in this manuscript, the open-source software LAMMPS [Plimpton 1995] is used.

1.3.2 Interaction Potential

At the length and time scales of MD the effect of gravity is negligible. The only forces considered are the interatomic forces, computed from the potential U. In classical MD, the electronic structure of the atoms is not considered. The interactions are estimated through an interatomic potential that depends solely on the positions of the atoms relative to each other. The simplest way to design an interaction potential is to have atoms that attract each other when far apart and repel each other when too close. This is the idea behind early interatomic potentials such as the Lennard-Jones potential:

$$U(r_{ij}) = 4\varepsilon\left(\left(\frac{\sigma}{r_{ij}}\right)^{-12} - \left(\frac{\sigma}{r_{ij}}\right)^{-6}\right), \tag{1.31}$$

with r_{ij} the distance between atom i and j, ε setting the interaction energy and σ setting the equilibrium interatomic distance. Equation (1.31) represents the interaction between atoms i and j; the force acting on one atom is simply the sum of all the forces due to atoms surrounding it. While basic, this potential can model relatively accurately the behavior of solid Argon [Ashcroft *et al.* 1976]. To reduce the computational cost, each atom only interacts with the atoms within a cutoff radius (see figure 1.7).

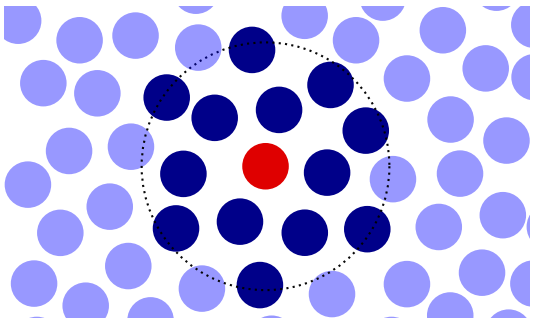

Figure 1.7: Schematic representation of the cutoff radius: the force on the red atom results from the sum of the interaction forces due to every atom within the cutoff radius (in dark blue). The circle in dotted line represents the interaction range (cut-off distance) of the central atoms. The interaction with the other atoms in light blue are ignored.

However, these simple pair potentials are limited to a few practical applications. For instance, the energetically favored structure is systematically a close-packed structure. The attraction/repulsion between the atoms organizes them as hard spheres would. To obtain other crystallographic structures, other interactions have to be introduced. These interactions are classified by the number of simultaneously interacting atoms they involve [Stillinger & Weber 1985]:

$$U(1,\ldots,N) = \sum_i u_1(i) + \sum_{i,j} u_2(i,j) + \sum_{i,j,k} u_3(i,j,k) + \cdots + u_N(1,\ldots,N) \quad (1.32)$$

with N the total number of atoms, u_n the part of the potential involving n atoms. u_1 represents the interaction of one atom with an external field, u_2 a two body interaction where only the distance between the particle i and j matters, u_3 a three body interaction involving the angle formed by the particles (or any combination of the three distances). In most cases, there is no external field (u_1 is null). Also, as n increases the contributions get smaller, so that usual potentials rarely use terms above u_4. In the case of Si, a commonly used potential is the Stillinger-Weber (interatomic potential) (SW) [Stillinger & Weber 1985], it is based on a two and a three body terms:

$$u_2(r_{ij}) = A_{ij}\varepsilon_{ij}\left(B_{ij}\left(\frac{\sigma_{ij}}{r_{ij}}\right)^{p_{ij}} - 1\right)\exp\left(\frac{\sigma_{ij}}{r_{ij} - a_{ij}\sigma_{ij}}\right) \quad (1.33)$$

$$u_3(r_{ij}, r_{ik}, \theta_{ijk}) = \lambda_{ijk}\varepsilon_{ijk}(\cos\theta_{ijk} - \cos\theta^0)^2 \exp\left(\frac{\gamma_{ij}\sigma_{ij}}{r_{ij} - a_{ij}\sigma_{ij}}\right) \exp\left(\frac{\gamma_{ik}\sigma_{ij}}{r_{ik} - a_{ik}\sigma_{ik}}\right) \tag{1.34}$$

with A, B, ε, σ, λ, a, θ^0, γ and p a set of parameters fitted to reproduce the properties of Si, especially the directionality of the covalent bonding. These parameter are set to insure that the diamond phase is the most stable, and that the melting point, the frequency of different modes and the elastic properties are in range with the experimental values. To model amorphous/crystalline nanocomposites, in this thesis, the parameters described by Vink *et al.* [Vink *et al.* 2001] particularly adapted for crystalline and amorphous Si [France-Lanord *et al.* 2014a] are used.

For the simulation of SiO_2 and the melt-quench procedure of Si the Tersoff potential is also used [Tersoff 1988]. The formalism is different, but also includes two body (distance) and 3 three body (angle) dependencies:

$$u_{ij} = f_C(r_{ij})[f_R(r_{ij}) + b_{ij} f_A(r_{ij})] \tag{1.35a}$$

$$f_R(r) = A\exp(-\lambda_1 r) \tag{1.35b}$$

$$f_A(r) = B\exp(-\lambda_2 r) \tag{1.35c}$$

$$f_C(r) = \begin{cases} 1, r < R - D \\ \frac{1}{2} - \frac{1}{2}\sin\left(\frac{\pi}{2}(r - R)/D\right), R - D < r < R + D \\ 0, r > R + D \end{cases} \tag{1.35d}$$

$$b_{ij} = (1 + \beta^n + \zeta_{ij})^{-1/2n} \tag{1.35e}$$

$$\zeta_{ij} = \sum_{k(\neq i,j)} f_C(r_{ik}) g(\theta_{ijk}) \exp\left(\lambda_3^3 (r_{ij} - r_{ik})^3\right) \tag{1.35f}$$

$$g(\theta) = 1 + \left(\frac{c}{d}\right)^2 - \frac{c^2}{d^2 + (h - \cos\theta)^2} \tag{1.35g}$$

$$\eta_{ij} = \sum_{k(\neq)i,j} f_C(r_{ik}) \exp\left(\lambda_3^3 (r_{ij} - r_{ik})^3\right), \tag{1.35h}$$

with A, B, λ_1, λ_2, λ_c, β, n, c, d and h a set of parameter. R and D are cut-off radii. For the simulations of this work, the set of parameter of Munetoh *et al.* [Munetoh *et al.* 2007] was used.

The last potential type that is used in this work is the van Beest, Kramer and van Santen (inter-atomic potential) (BKS) [van Beest *et al.* 1990]. It does not include a three body term. However, it considers long-range Coulomb interactions. Although simple, this potential allows a better modeling of SiO_2 during the melt-quench procedure than the Tersoff potential (see section 2.1). This potential is defined as:

$$U(r_{ij}) = \frac{q_i q_j}{r_{ij}} + A_{ij}\exp(-b_{ij} r_{ij}) - \frac{c_{ij}}{r_{ij}^6}, \tag{1.36}$$

with q_i and q_j the charges of the atoms, A, b, c other bond parameters. The particular implementation of Carré *et al.* was used [Carré *et al.* 2007].

Different interatomic potential are useful in different conditions, for instance the Tersoff potential describes well the liquid phase of Si and the Stillinger Weber describes better the melting point.

1.3.3 Boundary Conditions

Despite the limitation in the number of atoms, MD is not limited to the simulation of nano-objects and can be used for the study of bulk properties. To circumvent the size limitation, periodic boundary conditions are used. With periodic boundary conditions, the atoms do not only interact with atoms in the simulation box, but also with atoms on the other side of the boundary. That is, in figure 1.8 the atoms near the boundary at $x = L$ interact with the atoms near the boundary at $x = 0$. Everything happens as if the system interacted with an image system, a copy of itself, located behind the periodic boundary conditions. As a result, in the direction where periodic boundary conditions are used, the system is "infinite" but with a periodicity given by the box size. On the contrary, at fixed boundary condition

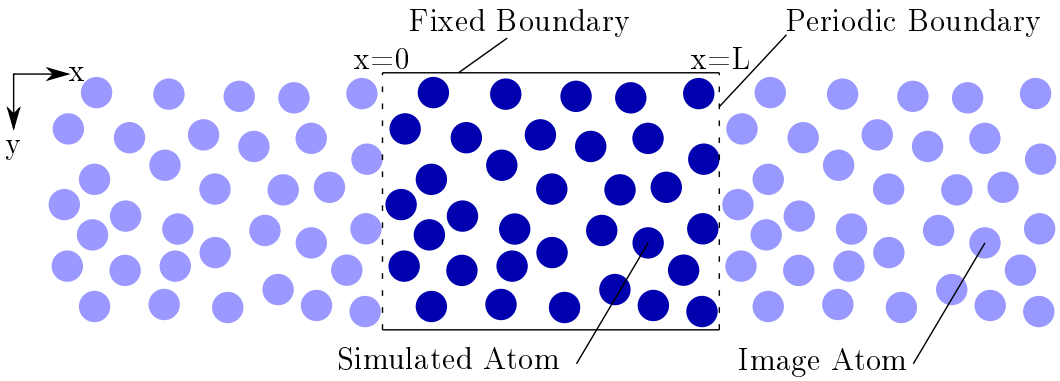

Figure 1.8: Schematic representation of boundary conditions in 2D with periodic conditions in x and fixed boundary conditions in y direction.

the system ends up with free surfaces, because the atoms only interact with atoms within the simulation domain. As a consequence, in a 3D simulation, if periodic boundary conditions are set in the three cartesian coordinate directions, there are no surface effects and this approximates a bulk material. If periodic boundaries are used in two directions thin film properties can be simulated, and if it is used in only in one direction an infinite nanowire can be modeled.

It is to be noted that the artificial periodicity introduced by periodic boundary conditions has a consequence in terms of maximum wave length allowed. Indeed the wave-length cannot be larger than the simulation box length. This has repercussions on the computation of the dynamical structure factor that are discussed in section 1.5.2.

1.3.4 Microstructure Relaxation

An important step in MD simulations is the structural relaxation. Most applications require creating or modifying the microstructure of the object simulated. This implies that the atoms are put in arbitrary positions, without taking into account whether the position is energetically favorable or not. If the position of the atoms are not energetically favorable, too close to another atom for instance, this can create instabilities. If constant energy simulations are performed right away, some atoms could be submitted to large forces and be ejected out of the simulation box. To avoid this, once the geometrical construction is done, the position of the atoms are usually relaxed, with the objective of finding a local energy minimum. This is usually done thanks to a Conjugate Gradient (CG) method [Polak & Ribiere 1969]. This is a stepwise optimisation method that uses the force gradient as well as information from the previous iterations for a quicker convergence. As most iterative optimisation methods, it can be stuck in a local minimum.

If the minimization procedure is successful, the atoms should be in a local minimum of potential energy and the movement of atoms at the beginning of a simulation should be due to their initial velocity only.

1.3.5 Energy, Thermostats, and Barostats

With the methods described up to this point, it is possible to set up a simulation of a nano-object or of bulk material. For this, the geometry (position of the atoms) must be set, the appropriate interaction potential chosen, and the structure relaxed. And only then the integration scheme can simulate the evolution of the system at constant energy. In MD simulations, the energy is expressed as:

$$E = \sum_i U(\mathbf{r}_i) + \sum_i \frac{\mathbf{v}_i^2 m_i}{2}, \tag{1.37}$$

the first term being the potential energy depending on the position and interaction potential, and the second one the kinetic energy depending on the velocity of the atoms. During constant energy simulations, energy conservation implies that the evolution of the system is due to potential energy being transformed in kinetic energy and vice versa. The global energy of the system is thus set by the initial conditions (positions and velocities of the atoms). The number of particles and volume of the simulation cell being fixed at the beginning of the simulation, it reproduces the microcanonical thermodynamical ensemble [Allen & Tildesley 2017]. This ensemble is also called NVE, for fixed number of particle N fixed volume V and fixed energy E. It represents the possible evolutions of an isolated system, without interactions with the environment.

However, practically, it is useful to be able to simulate a system that interacts with the environment. In particular, one may want to set the temperature of the system, this is the role of thermostats. In MD simulations, the instantaneous temperature T of a volume V is defined thanks to the mean kinetic energy of the atoms

inside the volume if the average velocity of each atom is zero (otherwise it is given by the velocity fluctuations [Diu & Guthmann 1989]):

$$T(V) = \sum_{i \in V} \frac{\mathbf{v}_i^2 m_i}{3nk_B}, \tag{1.38}$$

where the sum runs over the n atoms in the volume V. Thus, the temperature can be controlled through the regulation of the velocity of the atoms. This is the idea behind the simplest thermostat: the velocity rescaling thermostat. This thermostat works by changing homogeneously the velocities of some atoms at regular intervals to obtain the chosen temperature. However, this approach is crude and introducing random velocity changes can have a strong influence on the dynamic of the system. To avoid this, other thermostats have been developed, the most popular one is the Nosé-Hoover thermostat [Nosé 1986]. This thermostat uses a reformulation of the equations of motion of the atoms to include the coupling to a thermal bath [Allen & Tildesley 2017]. Such a thermostat allows performing simulations in the canonical ensemble or NVT (fixed number of atoms, volume and temperature).

Alternatively, for other applications, one may wish to monitor and control the pressure. This is useful in particular to avoid thermal stresses when the temperature is modified. In MD, the pressure in a 3D system is computed through [Frenkel & Smit 2001]:

$$P = \frac{Nk_bT}{V} + \sum_{i \in V} \frac{\mathbf{v}_i \cdot \mathbf{f}_i}{3V}, \tag{1.39}$$

with $\mathbf{f}_i$ the forces on atom i. Usually, the control of the pressure is done in simulations where the temperature is also controlled, or NPT simulations (fixed number of atoms, pressure, and temperature). The control of the pressure is mainly achieved through the variation of the volume. The modern barostats, similarly to thermostats, work by introducing new terms in the equation of motion. The barostat used in the simulations of this work is a Nosé-Hoover barostat [Martyna *et al.* 1994].

1.4 Configurations and Structural Characteristics (MD)

This work focuses on solid state nanocomposites, and in particular on nanocomposites with both a crystalline and an amorphous phase. In this section, the elaboration methods of the amorphous phase is presented before getting to the method used to assemble the phases. After this, the monitored structural properties and their evaluation methods are presented.

1.4.1 Elaboration of Amorphous Samples

Crystalline structures are rather simple to create, one only needs to lay out the atoms following the wished crystallographic structure. The creation of an amorphous structure with realistic structural properties is less obvious. There

are two main approaches: either start with atoms in random positions and then relax the positions to get a meta-stable structure, or imitate the experimental procedure: melt a crystalline structure and then quench it to obtain a glass [Ishimaru *et al.* 1997, Guénolé *et al.* 2013]. Both methods have their limitations, for instance the random position based method is sensitive to the initial position, and the melt quench method is sensitive to the quenching parameters [Vollmayr *et al.* 1996, Lee *et al.* 2006, Fusco *et al.* 2010]. In this work, the choice has been made to use melt-quench method, that can been seen as closer to the real procedure used to obtain amorphous material obtained[3]. More practically, this worked is based on earlier works that used the melt-quench approach. In the following, the melt quench methods used in this work are described.

Amorphous Silicon The amorphous silicon sample used in this work are the same as in the publication [Tlili *et al.* 2019]. This was elaborated in the following manner [Fusco *et al.* 2010]:

1. A crystalline silicon structure is created
2. The system is heated at 3500 K using a Tersoff potential
3. The system is equilibrated at 3500 K
4. The system is quenched at a rate of $1 \times 10^{14}\,\mathrm{K\,s^{-1}}$
5. The energy is minimized using the CG method
6. The interaction potential is switched to a SW potential
7. The system is annealed at 100 K for 10 ps
8. The energy is minimized using the CG method

This method combines the realistic micro-structure allowed by using the Tersoff potential for the melt-quench procedure and the mechanical properties adequacy of the SW potential at lower temperature [Tlili *et al.* 2019].

Amorphous Silica The amorphous silica configuration was created using the procedure described in [Mantisi *et al.* 2012].

1. A β-Crystoballite crystal is formed
2. The energy is minimized using the CG method with the BKS potential
3. The system is heated up 5200 K in 1 ns at constant volume
4. The system is annealed for 10 ps at this temperature
5. The system is quenched to 300 K with a rate of $5.3 \times 10^{12}\,\mathrm{K\,s^{-1}}$

[3] Although at a much faster quench rate.

6. The interaction potential is switched to a Tersoff potential [Munetoh *et al.* 2007]
7. The structure is quenched to 10 K at the same rate
8. The energy is minimized using a conjugated gradient method and then a Hessian-free truncated Newton algorithm to ensure a better convergence

Figure 1.9 shows a small portion of the sample at step 1 and step 8.

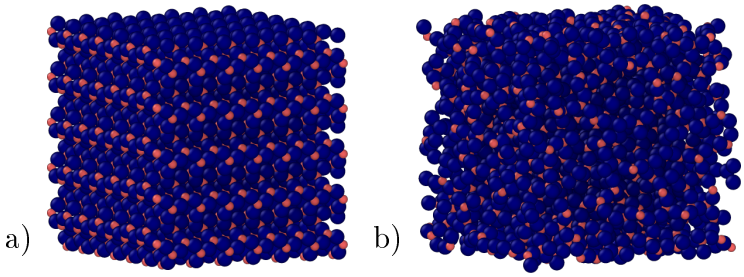

Figure 1.9: β-Crystoballite sample (a) and resulting Amorphous Silica (a-SiO_2) (b), Si atoms are represented by the large blue spheres and O atoms represented by the smaller pink spheres.

1.4.2 Nanocomposites

This work does not focus on the properties of amorphous silicon and silica, but on the properties of nanocomposites involving these materials. The specific nanocomposites are described in the following chapters. However, the basic procedure to obtain them is common to all: a specific shape is cut in the amorphous structure and then the crystalline phase is added inside the hole created. To avoid having overlapping atoms, the hole is either cut slightly larger than the shape of the inclusion (of .1Å) or the overlapping atoms are deleted (that is atoms within less than than 2 Å of each others) The obtained structure is then relaxed using energy/force relaxation methods, to further relax the structure it is also annealed at 100 K for a few thousand time steps. This method was successfully used in previous works [France-Lanord *et al.* 2014a, Termentzidis *et al.* 2018a, Tlili *et al.* 2019], and does not result in unrealistic strains in the structure studied. This point can be verfied using the interfacial energy (see section 3.1.1) or an estimation of the stress/strain fields (see appendix B.4).

1.4.3 Structural Properties

At this point, it is useful to describe the different analysis methods used to evaluate the microstructure of amorphous materials. The different quantities are obtained thanks to the analysis and visualization software OVITO [Stukowski 2009] in conjunction with ASE [Larsen *et al.* 2017].

Radial Distribution Function The RDF represents the probability to find an atom at a distance r from another [Frenkel & Smit 2001]. In MD simulations, it is computed as:

$$g(r) = \frac{3V}{4\pi r^2} \sum_{i \in N} \sum_{j \in N} \langle \delta(r + r_i - r_j) \rangle. \tag{1.40}$$

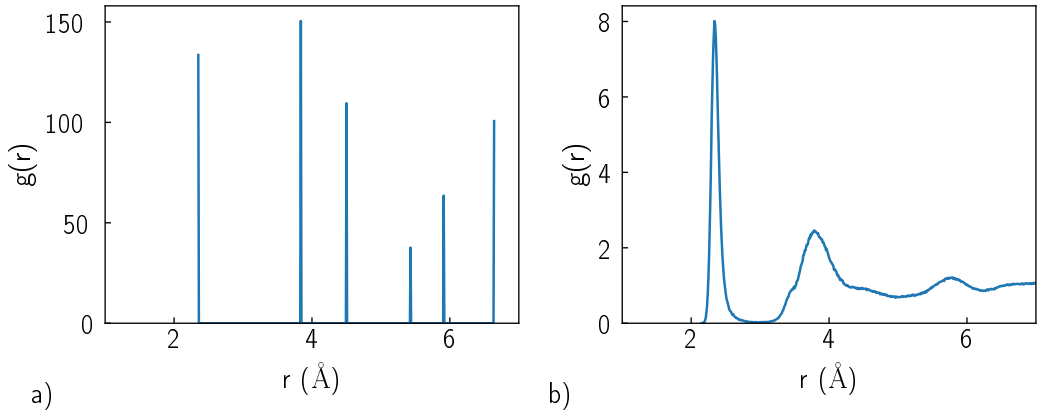

Figure 1.10: RDF of crystalline (a) and amorphous (b) silicon.

Two examples of RDF are given in figure 1.10: the RDF of Crystalline Silicon (c-Si) and a-Si. The RDF of c-Si shows clearly what is expected for a crystal, the atoms are at a set distance from each others, this distance being defined by the crystalline structure. On the other hand, in the glass some peaks corresponding to the average distance to first/second or third neighbor are visible but are less sharp. The atoms are not at a set distance from each others, but distributed around them.

Bond Angle Distribution The Bond Angle Distribution (BAD) gives the distribution of the angles formed by each atom with two first neighbors. For every atom, the angle between each pair of first neighbors is measured, then from the angles list a histogram can be constructed. The first neighbor distance is chosen thanks to the RDF. For instance, in the case of a-Si in figure 1.10 atoms within 3 Å of each other are considered first neighbor. This quantity is useful to verify that the bonding directionality is respected. For instance, for a-Si, the BAD is expected to be around 108° [Fortner & Lannin 1989]. An example of BAD for a-Si is given in the figure 1.11. It shows that the distribution is centered around the expected value and is symmetric around it.

Coordination Analysis The coordination number of an atom corresponds to the number of atoms that are bonded with it. In other words, it is the number of first neighbors. For crystalline structures, it can be deduced from the lattice geometry.

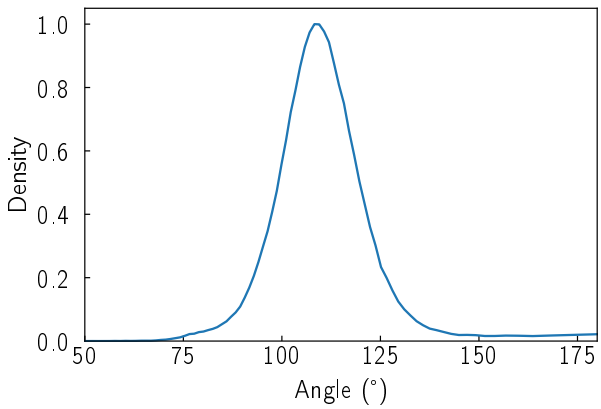

Figure 1.11: Bond angle distribution for a-Si.

For instance, for c-Si in the cubic diamond configuration, it is 4. For amorphous materials, this number has to be computed explicitly. For each particle, the number of atoms within bonding distance are counted. Two atoms can be considered bonded if they are within the maximum distance of the first neighbor deduced from the RDF.

The coordination number distribution can be used as a measure of the quality of a simulated amorphous structure. To analyze it, a histogram, as the one visible in figure 1.12, can be plotted. The figure contains the coordination numbers of the atoms of the a-Si sample used. For a-Si, the coordination number is supposed to be 4, close to the value of c-Si. And this is what is obtained for 94 % of the atoms. There is some over-coordinated atoms and very few under-coordinated atoms, as expected [Fusco *et al.* 2010].

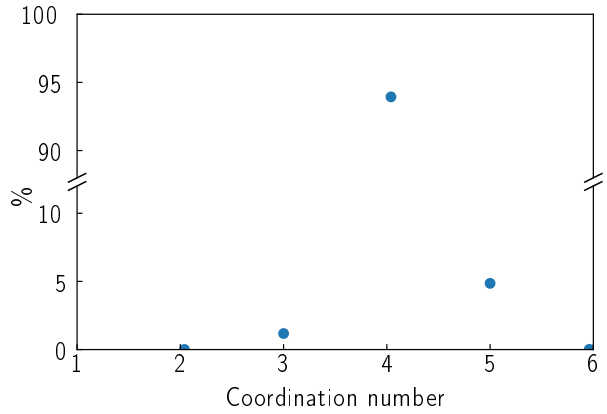

Figure 1.12: Distribution of the coordination numbers for a-Si.

Q-speciation The Q-speciation is a quantity that can be computed for oxide glasses. It corresponds to the number of binding oxygen atoms per silicon atom

in the case of SiO_2. That is, the number of oxygen atoms bonded with a given Si atom that are also bonded to another Si atom. The Q_n notation gives the number of bridging oxygen for a Si atom: a Q_1 Si atom has only one oxygen atom that is also bonded with another Si atom, a Q_2 has two oxygen atoms bonded with other Si atoms and so on. For pure SiO_2, it is expected that the overwhelming proportion of atoms are Q_4, the bonding of O atoms with Si being much more energetically favorable than the others [Sen & Youngman 2003]. Practically, it is computed similarly to the BAD: for every Si atoms, each oxygen atom within bonding range is considered. Then for each oxygen atom the presence of another Si atom with bonding distance is checked, if there is one, the Q number of the atom is increased. This computation is repeated for each Si atom. This is discussed in appendix A.1.

1.5 Vibrational properties (MD)

Not only is MD useful to study the structure of materials and compare it to experimental results, but it can also be used to estimate vibrational properties of structures. This covers a wide range of characteristics: from the eigenfrequency distribution to the damping characteristics. In this section, the different methods used to compute the vibrational properties with MD are reviewed.

1.5.1 Vibrational Density of States

The VDOS of a system describes the spectral distribution of its eigenfrequencies. It is a useful quantity to get an idea of the importance of a particular frequency range, or the allowed vibrational frequencies in a system. More importantly, it is also a useful comparison point with experimental results. For instance, the adequacy between the obtained and experimental VDOS was one of the control point during the definition of the SW potential used for Si in this work [Vink *et al.* 2001]. There are multiple methods that can be used to compute the VDOS, one method relying on a statistical analysis of the movement and two others relying on the dynamical matrix will be described.

Velocity Autocorrelation Function The VDOS can be evaluated thanks to the Fourier transform of the mass weighted Velocity Auto-Correlation Function (VACF) [Dove 1993]:

$$g(\nu) = \frac{N}{k_b T} \mathcal{F}\left\{ \sum_{i \in N} m_i \langle |\mathbf{v}_i(t) \cdot \mathbf{v}_i(0)| \rangle \right\}, \tag{1.41}$$

with $\mathcal{F}\{\}$ the Fourier transform, $g(\nu)$ the VDOS at frequency ν. This quantity can be computed for the whole system or only part of it by selecting the particles over which the sum is performed. As for every quantity computed through a Fourier transform, the maximum frequency is given by the sampling rate $\nu_{max} = (2\tau_{samp})^{-1}$

and the frequency resolution is given by the acquisition time $\nu_{min} = {\tau_{acqu}}^{-1}$. Practically, before recording the VACF, the system is first equilibrated at 50 or 100 K using a Nosé-Hoover thermostat. The VACF is then computed over 100 ps without thermostat. Finally, a Fourier transform of the resulting VACF is performed and then filtered using a Savitzky-Golay polynomial filter [Savitzky & Golay 1964].

Dynamical Matrix The DM is a matrix representing the system through its harmonic interactions, that is, as a point mass linked by spring. Its usage and definition come partially from Lattice Dynamics (see section 1.7.1). The elements of this matrix are defined for any periodical or finite object as:

$$M_{i\alpha,j\beta} = (\sqrt{m_j m_i})^{-1} \frac{\partial U}{\partial r_{i\alpha} \partial r_{j\beta}}, \tag{1.42}$$

with i and j indexing atoms, α and β indexing the spatial directions, m_i the mass of atom i, $r_{j\beta}$ the position of the jth atom in the direction β, and U the potential energy of the system. LAMMPS evaluates the DM by computing the force variation on an atom resulting from a single atomic displacement. The DM reduces the system to a $3N \times 3N$ matrix with N the number of atoms. The eigenvalues of this matrix give the eigenfrequencies squares of the system, and the eigenvectors give the associated vibrational modes (scaled by the square root of atomic masses). The handling of the matrix is facilitated by its sparseness: equation (1.42) reduces to 0 if the atom i lies outside the cutoff radius of atom j. To compute the VDOS, the eigenvalues of this matrix have to be estimated. This can be done with different methods.

Direct Diagonalization For the small systems (below 1×10^4 atoms) the DM can easily be diagonalized explicitly. Many methods and approaches exist to do this, in this manuscript the Implicitly Restarted Arnoldi Method [Lehoucq *et al.* 1998] implemented in Sci Py for Python was used. The direct diagonalization gives eigenmodes together with the frequencies. And thus, by using it, one can easily compute the Participation Ratio (PR) for each mode. The participation ratio indicates the proportion of atoms taking part to a vibrational mode. It is computed as:

$$PR = \frac{1}{N} \frac{(\sum_{i=1}^{N} \|r_i\|^2)^2}{\sum_{i=1}^{N} \|r_i\|^4} \tag{1.43}$$

with r_i the displacement of the ith atom for a given mode and N the total number of atoms. As mentioned before (see section 1.1.5) the participation ratio can be used to identify the localized mode (that have a low participation ratio) and thus complements the VDOS that gives the spectral distribution of the eigenmodes regardless to their contribution to the thermal conducivity.

Kernel Polynomial Method For larger systems, for which the DM can be obtained but not diagonalized explicitly, the eigenvalues are estimated thanks to the Kernel Polynomial Method (KPM) described by Weiße *et*

al. [Weiße *et al.* 2006] and implemented for the computation of the VDOS by Beltukov *et al.* [Beltukov *et al.* 2016]. The VDOS is approximated by series of Chebychev polynomials. By distinguishing the modes that conserve the volume of the Voronoi cell around each atom and those who do not, the transverse and longitudinal modes can be distinguished [Beltukov *et al.* 2015]. The Voronoi cells were computed thanks to the *Voro++* open-source software [Rycroft 2007].

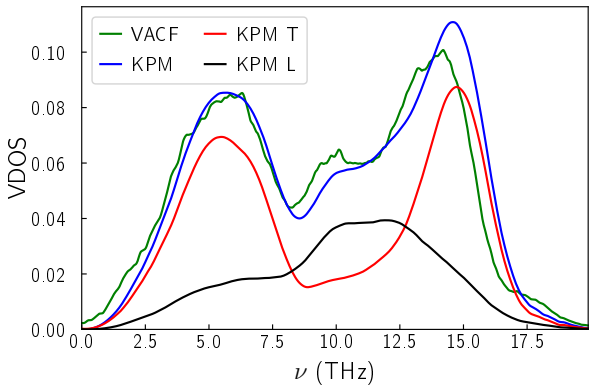

Figure 1.13: VDOS of a-Si estimated using the different methods.

The different results for the DOS of a-Si are represented in figure 1.13. The advantages and drawbacks of the different methods are discussed more in depth in the section 2.1.

1.5.2 Dynamical Structure Factor

The DSF, similarly to the VDOS, is a representation of the vibrational properties of the system. The DSF contains information both about the wave vector and the frequency. It is essentially a spatial and temporal Fourier transform of the atomic displacements. It is used to characterize the vibrational properties of a system, as measured by X-ray or by neutrons scattering experiments [Boon & Yip 1991]. It can be defined as:

$$S_\eta(\mathbf{q},\omega) = \frac{2}{NT}\left|\sum_i^{N_{at}} \exp(-i\mathbf{q}\cdot\mathbf{r_i}) \int_0^\tau \mathbf{u_i}(r_i,t)\cdot\mathbf{m}_\eta exp(i\omega t)dt\right|^2 \tag{1.44}$$

with $\mathbf{q}$ the wave vector, $\mathbf{u_i}$ and $\mathbf{r_i}$ the displacement and position of the i^{th} atom, m_η the polarization vector (parallel or perpendicular to $\mathbf{q}$), T the temperature and N the total number of atoms [Beltukov *et al.* 2013]. The wave vector resolution is given by $2\pi/L$ with L the length of the simulation box in the direction of the wave vector. The direction of the vector $\mathbf{q}$ can be chosen arbitrarily, this allows to sample the dispersion relations in the different directions of the lattice in the case of crystals.

The atomic trajectories used for the computation of $S(\mathbf{q},\omega)$ are obtained as follows: the sample is heated at a finite temperature (in this work 100 K if not otherwise mentioned), equilibrated at this temperature for 5×10^{-3} ns using a Nosé-Hoover thermostat and the atomic trajectories are then recorded during a 1×10^{-2} ns long constant energy simulation.

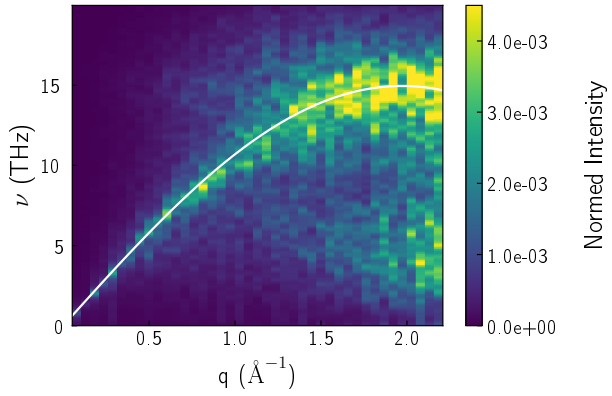

Figure 1.14: Dynamical structure factor of a-Si for longitudinal wave vector, the white lines correspond to the fitted dispersion curve.

From the DSF the phononic dispersion curves can be obtained. To do so, the DSF is first convoluted with a typical energy resolution curve of line-width 1.35 meV (as suggested by Tlili et *al.* [Tlili *et al.* 2019]). Then, the dispersion is estimated from the frequency for which $S(\mathbf{q},\omega)$ has the highest value for each wave vector within the acoustic phonon frequency range. This dispersion is finally fitted to a sine function,$\nu = c_1 \sin(2\pi q c_2)$ with c_1 and c_2 constants (see section 1.1.2), allowing the analytical derivation of the group velocity:

$$v_g = \frac{\partial \nu}{\partial q} = 2\pi c_1 c_2 \cos(\arcsin(\nu/c_1)) \tag{1.45}$$

The DSF for a-Si and the fitted dispersion relation for longitudinal modes is displayed in figure 1.14.[4]

Alternatively, the DSF can be used to extract both the dispersion relation and the lifetime of phonons. To this end, the low frequency region can be fitted with the DHO model [Beltukov *et al.* 2016]:

$$S_\eta(q,\nu) = \frac{A}{4\pi^2 \left((\nu^2 - \nu_\eta^2(q))^2 + \nu^2 \Gamma_\eta^2 \right)} \tag{1.46}$$

with $\Gamma_\eta = 1/\tau_\eta$ the inverse lifetime, $\nu_\eta(q)$ the phonon dispersion, A the amplitude, and η labeling either the longitudinal or transverse polarization. The parameters of equation (1.46) are fitted to match the DSF obtained with equation (1.44) for every wave vector. Thus, this model enables the computation of both the lifetime and the

[4] The result can be compared with what was obtained by Damart *et al.* [Damart *et al.* 2015].

dispersion relation using the DSF only. The fit is performed using a least square algorithm (Levenberg–Marquardt algorithm) from Scipy [Virtanen *et al.* 2020]. The

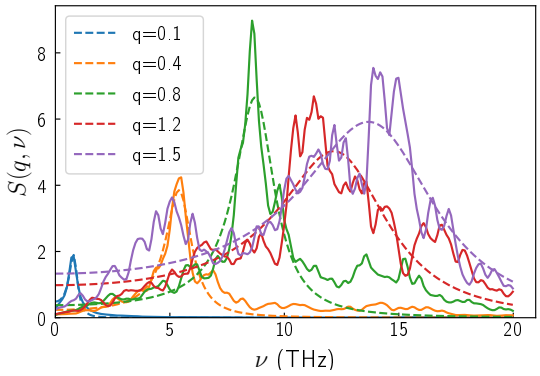

Figure 1.15: $S_\eta(q,\nu)$ as fitted using equation (1.46) for the longitudinal polarization in a-Si.

result of the fitting to a DHO model for a longitudinal polarization for a-Si are displayed in the left panel of Figure 1.15 for a few wave vectors. The expression (1.46) seems to fit to the DSF computed via equation (1.44) reasonably well at low frequencies. However, as the frequency increases the DSF is increasingly noisy, degrading the fit quality.

1.5.3 Wave-Packet Simulations

The vibrational properties of the nanocomposites can also be studied through the analysis of the propagation of a Wave-Packet (WP). For this, an excitation at a given frequency is imposed on a small group of atoms, and the resulting energy propagation is monitored, for this the systems are at very low temperature the only source of energy being the excitation. This gives a frequency resolved insight about the propagation of phonons. The method described here is similar to the one described by Beltukov *et al.* [Beltukov *et al.* 2016]. The WP is generated through a Gaussian windowed sinusoidal force excitation,

$$f = A\sin[2\pi\nu(t-3\tau)]\exp\left[-\frac{(t-3\tau)^2}{(2\tau^2)}\right], \tag{1.47}$$

imposed to the atoms to be excited. The excited slice is generally located in the center of the nanocomposite, at a symmetry plane so that the propagation is the same on each side of the excited plane. The amplitude A is chosen to be sufficiently low to study only the impact of the geometry and microstructure on the wave propagation (typically A$\approx 1\times10^{-4}\,\mathrm{eV\,\AA^{-1}}$). A large amplitude could cause anharmonic effects to appear. The spreading of the Gaussian window τ is chosen to be sufficiently small to offer a compromise between spatial extension of the WP compared to the system length, and the resolution in the frequency space. The

used value is 0.36 ps. The spectral resolution can be defined as the width of the Fourier transform of the window, $\delta\nu \approx 1/2\pi\tau \approx 0.4$ THz. The WP method is thus very similar to pump probe experiments, in which an optically excited transducer induces a mechanical wave, at a frequency of the order of the GHz, in the sample to study [Bartels *et al.* 2006, Dilhaire *et al.* 2011]. In MD the frequency is not limited by the time resolution of the measurement but by the system size.

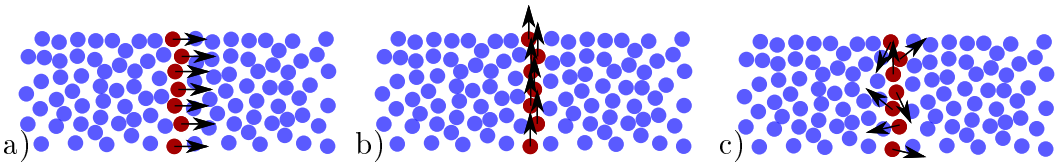

Figure 1.16: Schematic view of a longitudinal (a), transverse (b) or random excitation (c).

Furthermore, contrary to pump probe experiments, MD simulations allow to choose the polarization of the wave created. If the force is applied perpendicularly to the slice, it creates a longitudinal wave (see figure 1.16a). If the force is applied in the direction parallel to the slice, the wave created is transverse (see figure 1.16b). Alternatively, the force can be applied in a random direction, different for each excited atom, as shown in figure 1.16c. This random excitation prevents the apparition of a coherent single plane wave and thus keeps only the diffusive[5] part of the motion [Beltukov *et al.* 2013].

After the excitation, the atomic kinetic energy as a function of the position is recorded every 0.01 ps from the creation of the excitation until the wave reaches the limits of the nanocomposite. This allows studying the spatial and time decay of the wave-packet.

Mean Free Path The analysis of the decay rate of a longitudinal or transverse excitation allows computing its MFP. The amplitude of the wave-packet decreases due geometrical defects (interface/disorder), because of the very temperature the effect of anharmonicity can be neglected. To do so, the envelope of the wave-packet is computed first. The envelope is defined as the maximum amplitude of the wave-packet as a function of the distance from the excitation source (see figure 1.17). Then, the MFP is estimated from the exponential decay rate of the wave-packet envelope [Beltukov *et al.* 2018]. This is very similar to the estimation of an optical MFP with the Beer-Lambert law.

In some occurrences, like at high frequencies in amorphous materials, the exponential decay can be ill-defined. In these cases, the penetration length is used instead of the MFP. The penetration length is defined as the distance to the excitation for which the energy has been divided by $\exp(1)$ [Beltukov *et al.* 2018]. As a consequence, it corresponds to the MFP in the case of a perfect exponential

[5] Diffusive meaning here akin to a diffuson 1.1.5, as opposed to ballistic, here that propagates as a plane wave.

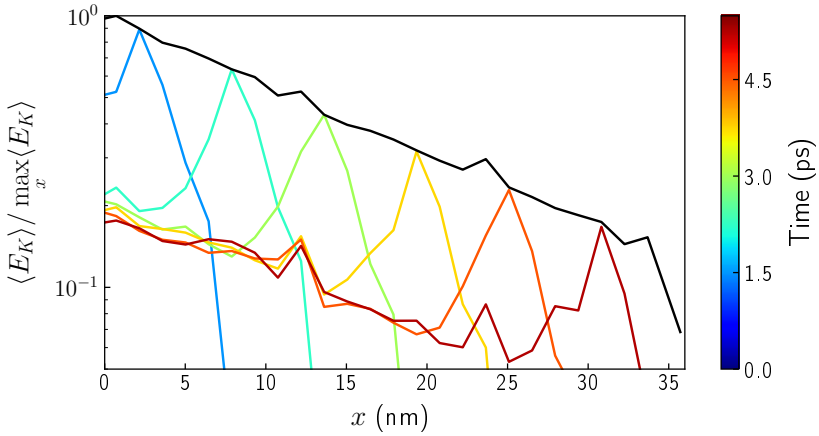

Figure 1.17: The envelope is defined as the maximal amplitude of the wave at a given position (black solid line), the energy distribution for some time steps is represented with different colors. Here, the reference position (0) is the position where the excitation is made, and the initial time corresponds to the 0 in equation (1.47).

attenuation, that is for ballistic propagation[6].

Diffusivity The energy diffusivity is used to estimate the contribution of the non propagating modes (see section 1.1.5) to the thermal conductivity. It is computed thanks to the wave-packet with a random excitation direction [Beltukov *et al.* 2013]. It is derived from the average square distance to the diffusion front:

$$R^2(t) = \frac{1}{E_{tot}} \sum_{i=0}^{N} x_i^2 E_i, \tag{1.48}$$

with N the number of slices, i the slice index, x_i the distance to the excitation, E_i the kinetic energy of the i^{th} slice. The diffusivity is linked to the time dependence of R^2 by the equation of one-dimensional diffusion,

$$R^2(t) = 2D(\nu)t \tag{1.49}$$

$D(\nu)$ is then computed through a least square fit. This can be done for the different excitation frequencies, but it is ill-defined in the purely propagative regime (when the heat carriers travel through the system rather than spread).

1.6 Thermal Conductivity Estimation (MD)

There are numerous methods, that can be used to compute the thermal conductivity using MD. In the following section, the focus is on the non equilibrium

[6] The ballistic regime being defined as the regime where the phonon or propagons dominate heat transport, as a opposed to diffusive dominated by diffusons

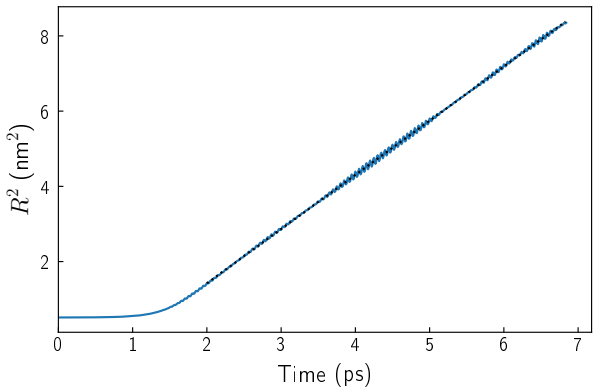

Figure 1.18: Average square distance to the diffusion front as computed with equation (1.48) for a-Si after a random force excitation at 10 THz, the dotted line corresponds to the fit used to compute the diffusivity.

molecular dynamics (NEMD), the equilibrium molecular dynamics (EMD), the approach to equilibrium molecular dynamics (AEMD) and the reconstitution of the thermal conductivity through the kinetic theory. The first two are quite popular in the literature, but alternatives exist, such as the Einstein relation based method [Kınac ı *et al.* 2012]. Before starting the description of the methods, it is worth mentioning that because MD is a fully classical simulation, all vibrational modes are accessible at all temperature (no quantization of energy). Thus, the phonon distribution does not follow the Bose Einstein distribution (see equation [1.8]), but rather the Maxwell Boltzmann distribution (see equation [1.9]). As a consequence, the methods that do not correct for the contribution of the different frequencies as a function of the temperature, are valid only above the Debye temperature Θ_D where all mode are populated (see section 1.1.2).

1.6.1 Non Equilibrium Molecular Dynamics

The Non Equilibrium Molecular Dynamics (NEMD) method relies on the creation of a temperature gradient across the system. The (effective) thermal conductivity of the system is then estimated thanks to the Fourier law using the relation:

$$\kappa = \frac{J\Delta x}{S\Delta T} \tag{1.50}$$

where J is the thermal flux going from one thermostat to the other, S the cross-section, $\frac{\Delta T}{\Delta x}$ the thermal gradient. Different thermostat layouts are possible [Schelling *et al.* 2002a], here the focus is on the one described in figure 1.19. In this layout, fixed boundary conditions are used in the direction of the thermal gradient, and the position of the atoms near the extremity are fixed to avoid free surface effects.

The flux is computed directly from the energy exchange rate at each thermostat. The computation of the flux in this way avoids the difficulty of determin-

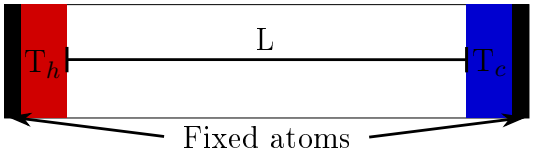

Figure 1.19: Schematic representation of a NEMD simulation, with the hot and cold thermostat represented in red and blue respectively, the region where the atoms are fixed atoms are represented in black.

ing a per atom flux described in section 1.6.2. The temperature gradient is estimated directly from $\frac{\Delta T}{\Delta x} = (T_h - T_c)/L$ with L being the distance between the thermostats (see figure 1.19). Other possibilities for the computation of the flux exists [Jund & Jullien 1999, Müller-Plathe 1997], and other possibilities for the estimation of the thermal gradient are discussed by Li *et al.* [Li *et al.* 2019].

Globally, the NEMD method is a conceptually simple way to compute the effective thermal conductivity of a nanocomposite. This method allows computing the thermal conductivity in a given orientation, with a given flux direction. Thus, with this method, an eventual thermal rectification can be measured (see chapter 3). However, due to ballistic transport, the results may depend on the length [Schelling *et al.* 2002b].

1.6.2 Equilibrium Molecular Dynamics

The EMD relies on the fluctuation dissipation theorem, linking the decay of the fluctuation of an internal variable to its response function. Here, the flux auto-correlation integral is linked to the thermal conductivity using the Green-Kubo formula [Kubo 1957]:

$$\kappa_{\alpha\beta} = \frac{1}{V k_B T^2} \int_0^\infty \langle J_\alpha(0) J_\beta(t) \rangle dt \tag{1.51}$$

with α and β indexing the Cartesian coordinates, V the volume of the system and $J_\beta(t)$ the thermal flux in the direction β at a time t. A discretized version is defined as [Schelling *et al.* 2002b]:

$$\kappa_{\alpha\beta} = \frac{\Delta t}{V k_B T^2} \sum_{m=1}^{M} (m-p)^{-1} \sum_{n=1}^{p} J_\alpha(m+n) J_\beta(m) \tag{1.52}$$

with Δt the time step between two successive flux computations, M the total number of time steps, and p the number of steps over which the auto-correlation function is averaged.

The system has to be equilibrated at a set temperature before the computation of the flux-flux correlation. This equilibration is performed thanks to a Nosé-Hoover thermostat, stabilizing the temperature over a few hundred thousand time steps.

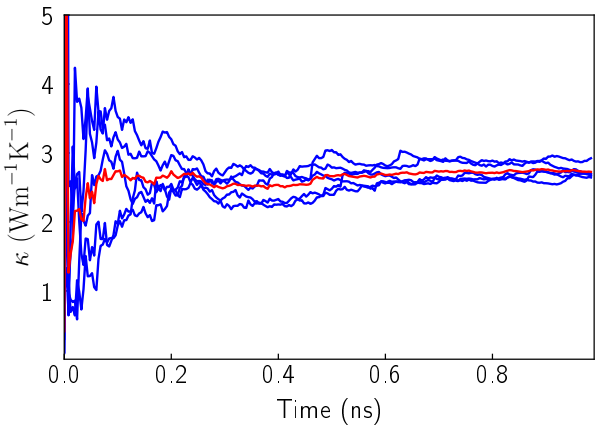

Figure 1.20: Example of convergence of the thermal conductivity computed through equation (1.52), the blue curves represent independent runs and the red curve the average between the runs.

After this equilibration step, the thermostat is removed to ensure that flux auto-correlation is sampled from the NVE ensemble. Then, the flux auto-correlation is computed over a few million times steps.

This equilibration/computation process is repeated a few times using different initial velocities to get better statistics. Equation (1.52) gives access to the thermal conductivity tensor directly without performing a different set of simulations. As it is a statistical measure of the thermal conductivity, it is less sensitive to size effects [Schelling *et al.* 2002a]. However, this method has few shortfalls: long simulations are necessary to converge on a value [Schelling *et al.* 2002a], the computation of the flux is not trivial for manybody potentials [Surblys *et al.* 2019] and it is not possible to compute thermal rectification with this method.

Heat Flux in Molecular Dynamics The computation of the thermal conductivity via the Green Kubo equation (1.52) requires the definition of the heat flux. In MD the heat flux in a volume V can be defined as [Hardy 1963]:

$$\mathbf{j} = \frac{1}{V}(\sum_i E_i \mathbf{v_i} + \bar{\bar{\sigma}}_i \cdot \mathbf{v_i}), \tag{1.53}$$

with E_i the total energy of the atom i, $\mathbf{v_i}$ the velocity of atom i, and $\bar{\bar{\sigma}}_i$ the atomic stress[7] on atom i. This corresponds, to the energy flux due to the movement of atoms (convective term $E_i\mathbf{v_i}$), and part due to the fluctuation of potential energy. This last part can be computed using the virial stresses $\bar{\bar{\sigma}}_i$ that is a sum of the interaction forces between atoms times their distance [Hardy 1963]:

[7] Note that the so-called "atomic stress" components are computed from the interatomic forces. They are homogeneous to a volume times "mechanical stresses". The comparison between the discrete and the continuous expression of the total mechanical energy allows identifying this volume to the volume of the Voronoi cell around each atom [Alexander 1998]

$$\bar{\bar{\sigma}}_i = -\sum_{k \in K_i} \frac{1}{N_k} \sum_{j \in k} \mathbf{r_j^k} \otimes \mathbf{F_j^k}, \tag{1.54}$$

with K_i the number of interaction involving the atom i, N_k is the number of atoms involved in the interaction (two for pair interactions), $\mathbf{r_j^k}$ the position of the atoms j involved in the interaction, $\mathbf{F_j^k}$ the force acting on atom i due to the interaction with atom j for the k body interaction.

However, this method is strictly valid only for pair potentials [Surblys *et al.* 2019]. Fan *et al.*, later Surblys *et al.* and Boone *et al.* proposed another method of computation [Fan *et al.* 2015, Surblys *et al.* 2019, Boone *et al.* 2019]:

$$\bar{\bar{\sigma}}_i = -\sum_{k \in K_i} \frac{1}{N_k} (\mathbf{r_j^k} - \mathbf{r_0^k}) \otimes \mathbf{F_j^k}, \tag{1.55}$$

with $\mathbf{r_0^k}$ the position of the centroid of the atoms involved in the k interaction $\mathbf{r_0^k} = \frac{1}{N_k} \sum_{i \in k} \mathbf{r_i^k}$. This method is appropriate for many body potentials, and starts to be implemented in LAMMPS. However, a large section of the literature (and this work) still uses the implementation of equation (1.54). This approximation is reasonable if the 3 body interactions do not contribute to a large portion of thermal conductivity as for Si and GaN [Fan *et al.* 2015, Zhou 2021, Termentzidis *et al.* 2018a].

1.6.3 Approach to Equilibrium Molecular Dynamics

The approach to equilibrium molecular dynamics is an alternative way to compute the thermal conductivity using MD [Lampin *et al.* 2012]. As its name states, it is based on the monitoring of on the evolution of a system from an out of equilibrium state as it relaxes toward the equilibrium to estimate its thermal properties. Practically, a temperature gradient is set up in a system thanks to a cold and a hot thermostat, after an equilibration period the thermostats are switched off and the system then evolves at constant energy toward equilibrium. The theoretical evolution is displayed in figure 1.21, the blue line represents the temperature profile before switching the thermostats off, the orange and green lines represent the temperature profile as the system evolves toward equilibrium. The temperature profiles displayed use the Fourier series used to fit to the profile obtained in MD. The parameters needed to reproduce the MD distribution are used to estimate the thermal properties of the system. In this aspect, this method is very similar to the laser flash method used to estimate the diffusivity at the macroscale.

This method has the advantage over the EMD and NEMD that only short simulation times are needed (hundreds of ps) and that it does not require the computation of a flux. Moreover, it can be used to study bulk material in general, interfaces [Hahn *et al.* 2015] and nanowires [Lampin *et al.* 2013]. As the NEMD method, the AEMD is sensitive to size effect and for crystals large simulation domain are needed [Zaoui *et al.* 2016].

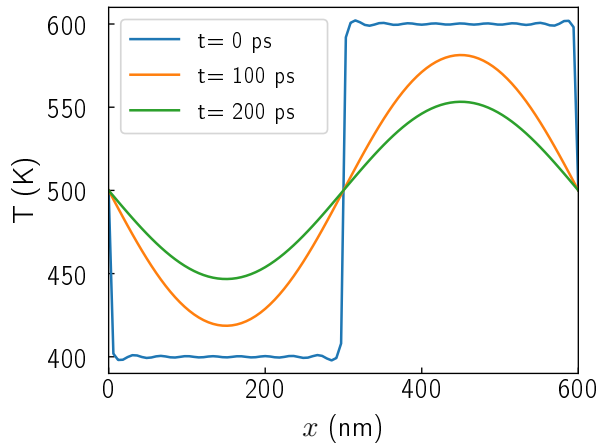

Figure 1.21: Theoretical evolution of the temperature profile during an AEMD procedure, approached via Fourier series.

1.6.4 Thermal Conductivity from the Kinetic Theory

The thermal conductivity of nanocomposites can also be evaluated using their vibrational properties, for this the method developed by Tlili et al. [Tlili *et al.* 2019] can be used. The contribution of the propagative and diffusive modes are separated, as for amorphous material (see section 1.1.5). This method is thus relevant for amorphous/crystalline nanocomposites. The contribution of the propagative modes (modes with a defined wavevector and MFP) (κ_P) is estimated with the following expression:

$$\kappa_P = \sum_{\eta} \int_0^{\nu_{max}} \frac{m_\eta}{3} C(\nu, T) v_\eta^2(\nu) \tau_\eta(\nu) g_\eta(\nu) d\nu, \tag{1.56}$$

with $C(\nu, T)$ the heat capacity[8] at the temperature T and frequency ν, v_η the group velocity, τ_η the phonon lifetime, g_η the density of state, and m_η the degree of freedom associated to the polarization η with $m_l = 1$ for longitudinal an $m_t = 2$ for transverse. ν_{max} is the frequency for which there is no propagation anymore, this corresponds in glasses to the Ioffe-Regel frequency (see section 1.1.5). Equation (1.56) is obtained by substituting the sum of the modes in equation (1.18) by a sum of the integrals over the frequency below Ioffe Regel for each polarization. For the propagating modes, the phonon gas model can be used and thus this equation corresponds to equation (1.16)

The phonon lifetime can be estimated thanks to the MFP computed through wave-packet divided by the group velocity, or alternatively through the fit of the DSF with the damped harmonic oscillators solution (see equation (1.46), below the Ioffe-Regel frequency.

[8] Note that $C(\nu, T)g_\eta$ is equivalent to C_{latt} in equations (1.18) and (1.19)

The diffusive[9] contribution to thermal conductivity (κ_D), of the modes without a defined MFP can be estimated through [Larkin & McGaughey 2013]:

$$\kappa_D = \int_{\nu_{max}}^{\infty} 3C(\nu,T)g(\nu)D(\nu)d\nu, \tag{1.57}$$

with D the diffusivity computed using equation (1.4)[10]. This equation is equivalent to the equation (1.19), the sum being replaced by an integral. The heat capacity, using the Debye model [Ashcroft *et al.* 1976], is given as follows:

$$C(\nu,T) = \frac{Nk_b}{V}(\frac{2\pi\nu\hbar}{k_bT})^2\frac{\exp{(\frac{2\pi\nu\hbar}{k_bT})}}{(\exp{(\frac{2\pi\nu\hbar}{k_bT})}-1)^2}, \tag{1.58}$$

with k_b the Boltzmann constant, $\hbar$ the Planck constant, V the volume, and N the number of atoms. It is worth mentioning that the usual definition of the heat capacity includes the VDOS. Here, the vibrational density of states is separated for the sake of separation of analytically derived terms and terms estimated with MD. Thanks to the weighting of the contributions of each frequency as function of the temperature, this description of the thermal conductivity is valid below the Debye temperature contrary to the methods previously described in this section. The method for the estimation of other components of the equations (1.56) and (1.57) are detailed in the section 1.5.

The total thermal conductivity is simply the sum of the diffusive and propagative contributions.

Lifetime Estimation and Temperature Effect The computation of the thermal conductivity through equation (1.56) relies on the estimation of the phonon lifetime as a function of frequency and polarization. The lifetime is considered to be limited by two phenomena: interfaces or defect scattering, and the phonon-phonon scattering. The former is assumed to depend only on the geometry and is estimated thanks to the MFP computed at 0 K with the wave-packet method and the group velocity:

$$\tau_{geom}^{-1} = \frac{v_\eta(\nu)}{\Lambda_\eta(\nu)}, \tag{1.59}$$

with $\Lambda_\eta(\nu)$ the MFP at frequency ν for the polarization η, and v_η the group velocity.

The wave-packet propagation simulations taking place at 0 K, the reduction of lifetime due to anharmonicity is underestimated. To compensate for this, a lifetime due to phonon-phonon interactions is introduced. This lifetime may be estimated with the empirical relation described in the Callaway model as a function of temperature and frequency [Callaway 1959].

$$\tau_{ph-ph}^{-1} = P(2\pi\nu)^2T\exp(-C_U/T), \tag{1.60}$$

[9] As in for "diffusons", or modes that have a diffusive behavior at the microscale.

[10] The diffusivity is sometimes given as an average over $v_\eta^2(\nu)\tau_\eta(\nu)$, however here it is used to determine the contribution to thermal conductivity of modes for which Λ or τ is not defined

with P and C_U empirical scattering parameters, in this work these parameters are set to the value given by Yang *et al.* [Yang & Dames 2013]. There are alternative expressions for this lifetime reduction due to phonon-phonon processes, such as the one derived analytically by Klemens [Klemens 1958]. However, those do not seem to be effective at room temperature [Asen-Palmer *et al.* 1997].

The global lifetime used in equation (1.56) is then estimated using Matthiessen summation rule:

$$\tau^{-1} = \tau_{geom}^{-1} + \tau_{ph-ph}^{-1}. \tag{1.61}$$

1.7 Other Atomically Resolved Models

Classical MD is not the only atomically resolved method allowing the estimation of thermal conductivity. Many other methods have been developed over the years. In this section, Lattice Dynamics, Atomic Green Function, and *Ab Initio* molecular dynamics are presented shortly.

1.7.1 Lattice Dynamics

One of the earliest methods that considers the atomic structure of materials is Lattice Dynamics. It was developed to address the limitation of the static lattice model [Dove 1993]. It uses the model introduced in section 1.1.2: the atoms are modeled either by mass points or by core-shell structures interacting with each others. To model bulk material, it is considered that the simulated pattern (usually a primitive cell of a crystal lattice) is repeated indefinitely in all directions of space (see figure 1.22) creating an infinite medium. To ease the analysis, the small displacement approximation is made. For most applications, the interaction potentials between atoms are considered harmonic. This amounts to study a network of point masses linked to their nearest neighbors by springs, as introduced in section 1.1.2 and depicted in figure 1.22. This is a reasonably accurate description of perfect crystals at low temperatures. It provides a good description of the dispersion relation of phonons in the different lattice directions and of the VDOS [Dove 1993]. However, the harmonic approximation predicts an infinite thermal conductivity for perfect crystals. To remedy to this problem, higher order estimations of the interaction potential can be used. When higher order terms are added, the method is sometimes called "anharmonic lattice dynamics". The consideration of those terms allows introducing the phonon-phonon interactions described in section 1.1.2 that limit the phonon lifetime and thus the thermal conductivity. The added terms are often limited to the cubic and sometimes quadratic contributions [Ashcroft *et al.* 1976].

Lattice dynamics, although not directly used in this work, is relevant as some concepts derived from it, such as the dynamical matrix (see section 1.5.1), are used. It also provides a useful formalism for the derivation of statistical quantities from the movement of the particles.

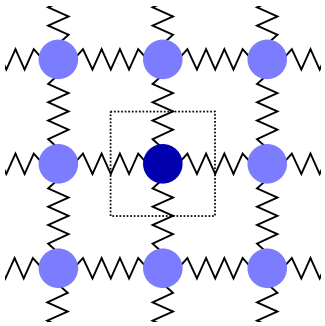

Figure 1.22: Schematic representation of a 2D lattice, with springs representing the interaction between the atoms. The dark blue atoms in the square represent the pattern that is repeated to simulate the bulk.

1.7.2 Atomic Green Function

The Atomic Green Function (AGF) is a formalism very similar to Lattice Dynamics. It models atoms oscillating around an equilibrium position, interacting through a harmonic interatomic potential. However, contrary to Lattice Dynamics it focuses on the properties of a device of limited dimensions with two thermal baths (contacts) and not on the properties of bulk material. A simple representation of an example system is given in figure 1.23. As indicated by its name, the methods relies on a Green function formalism used to determine the interactions of the device with the baths and with itself. This allows computing the transmission rate of phonons through the system and finally the thermal conductivity [Zhang *et al.* 2007, Karamitaheri *et al.* 2015].

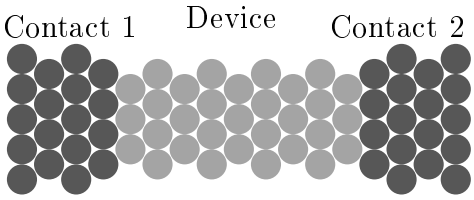

Figure 1.23: Schematic representation of an AGF simulation set up with the device to be studied and the contacts.

This method is particularly useful to model nanoscale devices at low temperature. At low temperatures, the amplitude of the oscillation is limited, and thus the anharmonic effects are negligible in front interface and boundary effects. This approximation is particularly justified for nanoscale devices. It is notably used to model the phonon transmission through interfaces [Yang *et al.* 2018] or the thermal conductivity of superlattices [Tian *et al.* 2012].

1.7.3 *ab initio* Molecular Dynamics

ab initio Molecular Dynamics is a method in which, similarly to classical MD, the trajectories of the atoms are estimated through a stepwise integration of the equation of motion (see section 1.3.1). However, the forces acting on each atom do not depend simply on the position of the atoms through an interaction potential, but are estimated directly from the electronic interactions that are explicitly taken into account. This is done by solving the Schrödinger equation at each time steps using the appropriate approximations, as using the time independent solution and solve using a density functionials [Marx & Hutter 2009]. This allows for a better reproduction of the interactions between the atoms. As the electronic interactions are modeled, the electronic and lattice contributions to the thermal conductivity can be computed [Recoules & Crocombette 2005].

However, *ab initio* simulations are limited to a few hundred, or thousand atoms simulated over a few picoseconds because the resolution of the Schrödinger equation is computationally intensive [Marx & Hutter 2009]. This scale does not allow for the computation of thermal conductivity with the usual MD method EMD and NEMD (see section 1.6), at least not without some modifications [Carbogno *et al.* 2017]. However, AEMD simulation are possible as shown by Martin *et al.* [Martin *et al.* 2018, Duong *et al.* 2020, Duong *et al.* 2019, Duong *et al.* 2021] *ab initio* computations applied to heat transport mainly focuses on the derivation of better interaction potentials for MD [Han & Bester 2011, Zhang *et al.* 2014], the computation of higher order interaction terms for lattice dynamics [Andreoni & Yip 2019] or on the computation of more accurate lifetime and distribution to solve the BTE [Vermeersch *et al.* 2015].

Synthesis of the Chapter

- At the nanoscale the thermal conductivity is not an intrinsic property of the material but depends on the microstructure and on the local dynamics
- The lattice thermal conductivity is linked to the vibrational properties of the system
  - For crystals, it can be modeled by propagating plane waves (phonons) with the phonon gas model
  - In disordered material this phonon gas model breaks down and, diffusive transport has to be considered
- The thermal conductivity at the nanoscale can be evaluated through different models
  - Some of them rely on the Boltzmann Transport Equation, solved thanks to a Monte-Carlo approach or used to derive a continuous equation as the hydrodynamic heat equations
  - Some of them rely on the simulation of the interaction between the atoms, as the Lattice Dynamics, Molecular Dynamics or the Atomic Green Function approaches
- Molecular Dynamics simulations are based on the step by step integration of the classical equation of motion for atoms and can be used to evaluate structural, vibrational or thermal properties
- Four methods allowing the estimation of the thermal conductivity with MD are described:
  - Non Equilibrium Molecular Dynamics relying on the relation between the heat flux and a temperature gradient sustained by thermostats
  - Equilibrium Molecular Dynamics where the thermal conductivity is computed thanks to the decay of the heat flux autocorrelation function
  - Approach to Equilibrium Molecular Dynamics where the evolution of a system toward equilibrium is used to estimate the thermal conductivity
  - Lastly the vibrational properties such as the diffusivity and MFP as a function of the frequency can be used to estimate the thermal conductivity

An overview of the time and length scale that can be studied with each method is visible in figure 1.24. And a more detailed overview is also given in the table 1.1

Table 1.1: Summary of the characteristics of the different simulation methods, SS stands for steady state, κ_l for lattice thermal conductivity, and κ_e for electronic contribution.

	ab initio	**MD**	**AGF**	**MC**	**(A)LD**	**Hydro. Dyn. Eq.**
κ_l	yes	yes	yes	yes	yes	yes
T Range (K)	0-∞	$>\Theta_D$	0-100	0-∞	0-Θ_M	10-400
Size Limit	$\approx$ 1nm	$\approx$100nm	$\approx$1 nm	$\approx$10µm	Bulk	µm
Time Limit	$\approx$ 10ps	$\approx$10ns	SS	ps-SS	SS	ps-SS

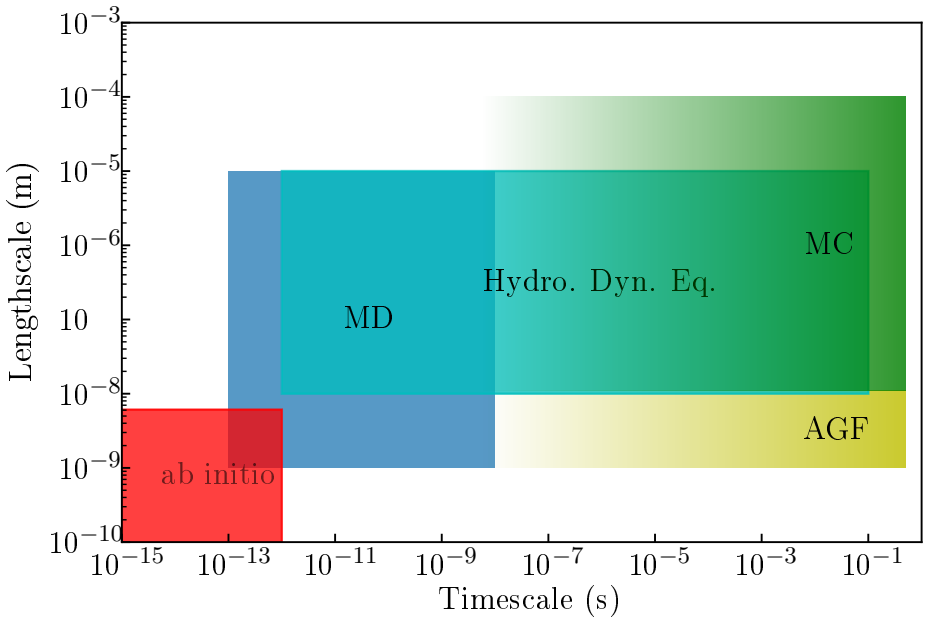

Figure 1.24: Overview of the time and length scales of the application domains of the different methods described in this chapter.

Chapter 2

Nanoclusters and Nanoinclusions

Contents

Many applications in electronics require materials with tailored mechanical, electronic or thermal properties. To this end, the appropriate element, alloy, phase, crystallinity, or a combination of them can be chosen. Nanostructuring allows a further

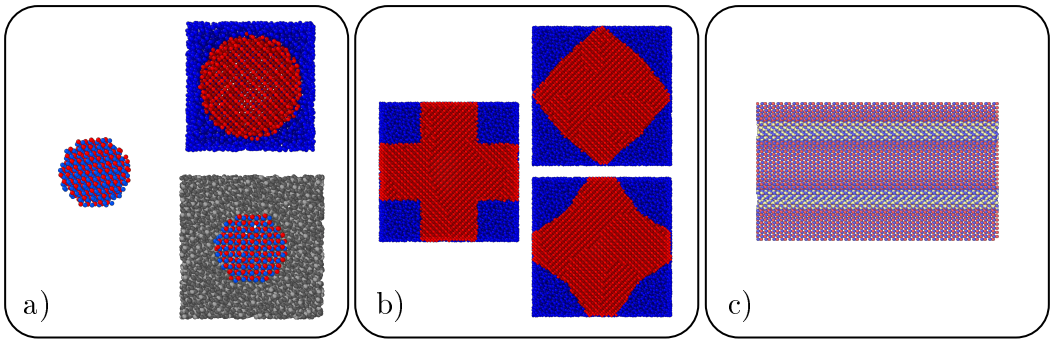

Visual Abstract: Overview of the configurations studied in this section: free and embedded nanospheres (a), shape variation of the nanoinclusion (b), decorated dislocation (c).

improvement of performances. A wide variety of nanocomposites exists, one of the simplest consists of Nanoinclusions (NIs) of a different phase or material embedded in a host matrix. Crystalline NIs in a crystalline matrix are used for many applications, such as thermoelectric generation [Kim *et al.* 2006]. For the same application, crystalline NIs in an amorphous matrix have also been proposed [Zhu *et al.* 2007]. This last possibility takes advantage of the low thermal conductivity of the amorphous matrix, while retaining some electronic transport properties of the added crystal.

However, the NIs and the matrix influence each others [Murray & Saviot 2004, Damart *et al.* 2015], notably their vibrational and thermal properties. A better understanding of the interactions of nanoinclusions and matrix is crucial to further improve the performances of these nanocomposites.

For instance, a particle array can act as a low pass filter, scattering the higher frequencies [Damart *et al.* 2015]. Different parameters have different effects: the rigidity contrast impacts the scattering and eventually pins the energy at the interface [Luo *et al.* 2019]. A higher surface to volume ratio is known to decrease the effective thermal conductivity [Termentzidis *et al.* 2018a]. Less instinctively, it has been shown in the same study that, the relative crystalline orientation between the particles also modifies the thermal conductivity of the material. The size distribution of the nanoinclusion has also been proposed to reduce the thermal conductivity of crystal-crystal nanocomposites [Zhang & Minnich 2015]. Embedded nanosphere of constants diameter can create a Bragg mirror even if they are not constantly spaced [Hu *et al.* 2020]. The resonance effect of single nanoinclusion can also decrease the transmission of energy [Feng *et al.* 2017]. Finally, the presence of NIs can cause an anticipation of the transition from propagative to diffusive regime in amorphous/crystalline nanocomposites [Tlili *et al.* 2019].

In this chapter, different bulk nanocomposites will be studied. It is centered on crystalline NI arrays in an amorphous matrix. It will begin with a study of GaN nanoparticles vibrational properties and their alteration once embedded in a matrix. After this, the effect of the stiffness of the inclusion on the vibrational

properties will be analyzed shortly. Subsequently, the effect of shape and eventual structural percolation on the thermal transport will be explored. Finally, the impact of decorated dislocations over phonon propagation in In doped GaN will be studied.

2.1 Size Effects: Free and Embedded GaN Nanospheres in a-SiO_2

The understanding of nanocomposites vibrational and thermal properties starts with the understanding of the components, here the focus is on Nanoparticles (NPs)[1]. Thanks to the evolution of nanofabrication methods, it is possible to control the sizes, chemical composition and orientation as well as the dispersion characteristics of these nanometric particles. However, they are rarely used alone, they are usually integrated into a liquid solution [Qiu *et al.* 2020] or embedded in a solid matrix [Daudin 2008]. There are several studies in the last two decades which show an increasing interest in the topic, notably on the influence of embedding NPs in a matrix. For instance, in nanofluids, the viscosity, the electrical conductivity and the density have been found to change with NPs concentration [Nabati Shoghl *et al.* 2016]. Metallic NPs have been used to increase the electrical conductivity of polymers [Del Castillo-Castro *et al.* 2007]. NPs have also been proposed for specific applications, for example in nanoplasmonics metallic NPs are used for coupling electromagnetic and mechanical waves [Berweger *et al.* 2011, Girard *et al.* 2016].

The vibrational properties of NPs have been first computed using the continuum mechanics solution for the vibrations of an elastic and isotropic free sphere [Eringen & Suhubi 1975]. This approach was successfully applied to predict resonant modes in NPs down to 1 nm in diameter for crystalline NPs [Juvé *et al.* 2010]. This approximation should theoretically work for amorphous NPs as long as characteristic length scales of the vibrational modes are not smaller than 40 interatomic distances due to specific correlations in the local dynamics of amorphous systems [Wittmer *et al.* 2002]. Transpositions of the original solution exist for anisotropic materials [Saviot & Murray 2009] or embedded NPs [Combe *et al.* 2007, Murray & Saviot 2004]. These models, based on Lamb's model [Lamb 1881] for the vibrational modes of a sphere, predict resonant frequencies depending on material properties, that scale with the diameter. NPs vibrational properties have also been studied using atomistic models, like molecular dynamics (MD) simulations, with a successful comparison with the continuum theory in the case of Ge or Ag [Combe *et al.* 2007, Murray & Saviot 2004]. Some studies have focused on other features of the Vibrational Density of States (VDOS) of NPs, like spectral spreading and surface effects. These effects were observed in the case of monoatomic metal and bimetallic alloys [Sauceda *et al.* 2013, Calvo & Balbuena 2005]. The case of III-V semiconductors has been studied by Han and Bester [Han & Bester 2011, Han & Bester 2012], showing similar size ef-

[1] In this section, the nanometric spheres will be referred to as nanoparticules.

fects on NPs VDOS. Additionally, II-VI semiconductors NPs have been also studied with a focus on the temperature, size and composition impact on the heat capacity and structural properties [Kurban *et al.* 2016, Kurban 2018]. Finally, studies showed that the thermal conductivity of single silicon NP represents only a fraction of the bulk conductivity and increases linearly with the diameter [Li & Zhang 2013, Fang *et al.* 2006].

In this section, the impact of the size of GaN NPs, and whether they are free or embedded in an amorphous SiO_2 matrix, on their VDOS is at hand. It will start with the description of the configurations. After this, the VDOS and participation ratio of free and embedded NPs as well as the thermal conductivity of free NPs will be studied. This is also an occasion to compare the methods for the evaluation of the VDOS described in chapter 1.

2.1.1 Modeling of the Configurations

The GaN nanoincluision studied here are simply nanospheres cut out of a GaN crystal (wurztite crystal). Their radii R range between 1 and 4 nm. Hereafter, the different of different radii NPs will be labelled NP_R. They contain 369 to 23 000 atoms. Once cut out of the crystal, the free NPs (FNPs) are relaxed in an equilibrium position using a conjugated gradient method, then equilibrated at 300 K for 20 ps. Fixed boundary conditions are used for the simulation box to avoid any artifact due to periodic boundary conditions, such as interactions between neighboring NPs.

The embedded NPs (ENPs) are placed in the center of a cubic simulation box containing the a-SiO_2 matrix with a side length corresponding to twice the NP diameter. The a-SiO_2 matrix was cut out of the larger sample obtained using the method described in section 2.4.1, the verification of its structural properties can be found in appendix A.1. The box size was chosen to limit the interactions between neighboring NPs through periodic boundary conditions while limiting the total number of atoms. The NPs are embedded in a spherical pore with a radius larger than the radius of the NPs by 0.1 Å, to prevent any overlapping between matrix and NPs atoms. The system is then relaxed thanks to a conjugated gradient method energy minimization, and an annealing at 300 K for 20 ps. The resulting configurations for a given diameter are depicted in figure 2.1. The Tersoff interaction potential developed by Kioseoglou *et al.* [Kioseoglou *et al.* 2017] is used to describe the interatomic interactions. It combines interatomic potential developed: for SiO_2 [Munetoh *et al.* 2007], for GaN [Nord *et al.* 2003], for oxynitrides [Okeke & Lowther 2009] and for silicon nitride [de Brito Mota *et al.* 1998]. This combined interatomic potential allows the simulations of silica and gallium nitride nanocomposites using the same potential form and it has been used previously with success [Termentzidis *et al.* 2018a].

The Partial Radial Distribution Function (PRDF) of the free NPs was examined. The peaks positions and sharpness do not change relative to the bulk PRDF, even for the smallest diameter NP studied here, which is an indication of minimal surface reconstruction and amorphization of the free surface of the NPs (see appendix A.2 for more details).

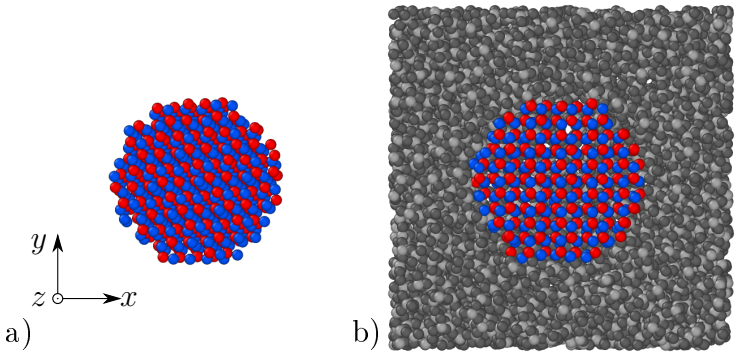

Figure 2.1: Cross-sectional visualization of the free (a) and embedded (b) NPs in silica matrix. The Ga atoms are represented in red, N atoms in blue, Si atoms in light gray and O atoms in dark gray.

2.1.2 Vibrational Density of States of Free Nanoparticles

The vibrational density of states off free nanoparticles (FNPs) of different sizes (colored plain lines) and for bulk GaN (dashed black line) for comparison are depicted in figure 2.2. At first glance, one can notice that bulk and NPs VDOS are quite similar, even for smaller NPs composed of a few hundreds of atoms (see table 2.1). The two acoustic peaks at 5 and 10 THz appear clearly. They can be linked to the Van Hove singularities [Van Hove 1953]. As the diameter of the NPs is reduced, three main effects appear: the first one is the population of the bandgap by 3 main modes at 14, 18 and 20 THz. Their intensities increase as the NPs decrease in size. Their relative importance in the VDOS spectra is confirmed by the difference in Participation Ratio (PR) for different sizes (see left column of figures 2.3). As the radius increases, their PR decreases, indicating that these modes concerns a less and less important fraction of atoms. These modes are related to surface modes, and they have been observed for other III-V semiconductors [Han & Bester 2011]. The increase in PR of those modes with the increase in the surface to volume ratio (see table 2.1) tends to confirm their localization at the surface. It is also worth noticing here that the frequencies of these modes do not depend on the size of the nanoparticles. This means that they cannot be linked to Lamb's modes or other resonant modes. Note also here, that with the VACF method (figure 2.2b) the peak at 14 THz is less sharp.

The second effect is a redshift and/or blurring of the first acoustic peak for radii up to 20 Å. This shift increases with decreasing NPs radius. This phenomenon appears more clearly when the VDOS is estimated through KPM (figure 2.2a) and with the direct method (figure 2.3 left panel). This redshift differs from what was previously observed by Combe *et al.* [Combe *et al.* 2007] for Ge nanodots modeled using Stillinger Weber potential. In the latter work a blue shift was mentioned instead, as it would be expected from the Lamb's theory where the eigenfrequencies of a sphere scale with the inverse of the radius. Nevertheless, there are other

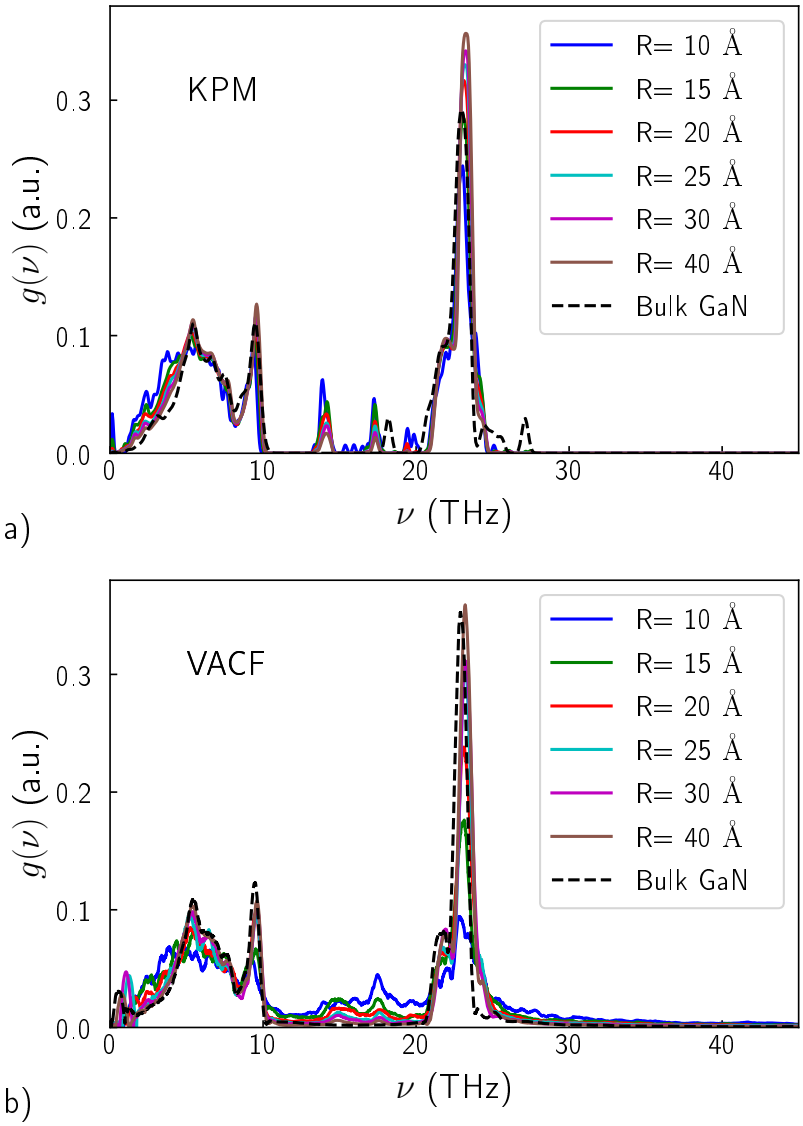

Figure 2.2: VDOS of GaN free nanoparticles computed from the Dynamical Matrix (DM) with Kernel Polynomial Method (KPM) (a) and from the Velocity Auto-Correlation Function (VACF) (b). The colored lines represent the different NPs and the dashed black line the bulk GaN.

studies that confirm these results; a mode softening. This softening was linked to the increased surface-to-volume ratio for metallic NP [Calvo & Balbuena 2005] or GaP NP [Han & Bester 2011]. Now concerning the blurring effect, it can be attributed to the modification of the shape of resonant modes. If the longitudinal and transverse sound velocities given by Polian *et al.* [Polian *et al.* 1996], are used the fundamental Lamb's modes of a free isotropic sphere, corresponding to the NPs sizes of the present study, lies between 1 and 5 THz. Below 3 THz the wavelength of the longitudinal phonons as described by Jiang *et al.* [Jiang *et al.* 2017] exceeds

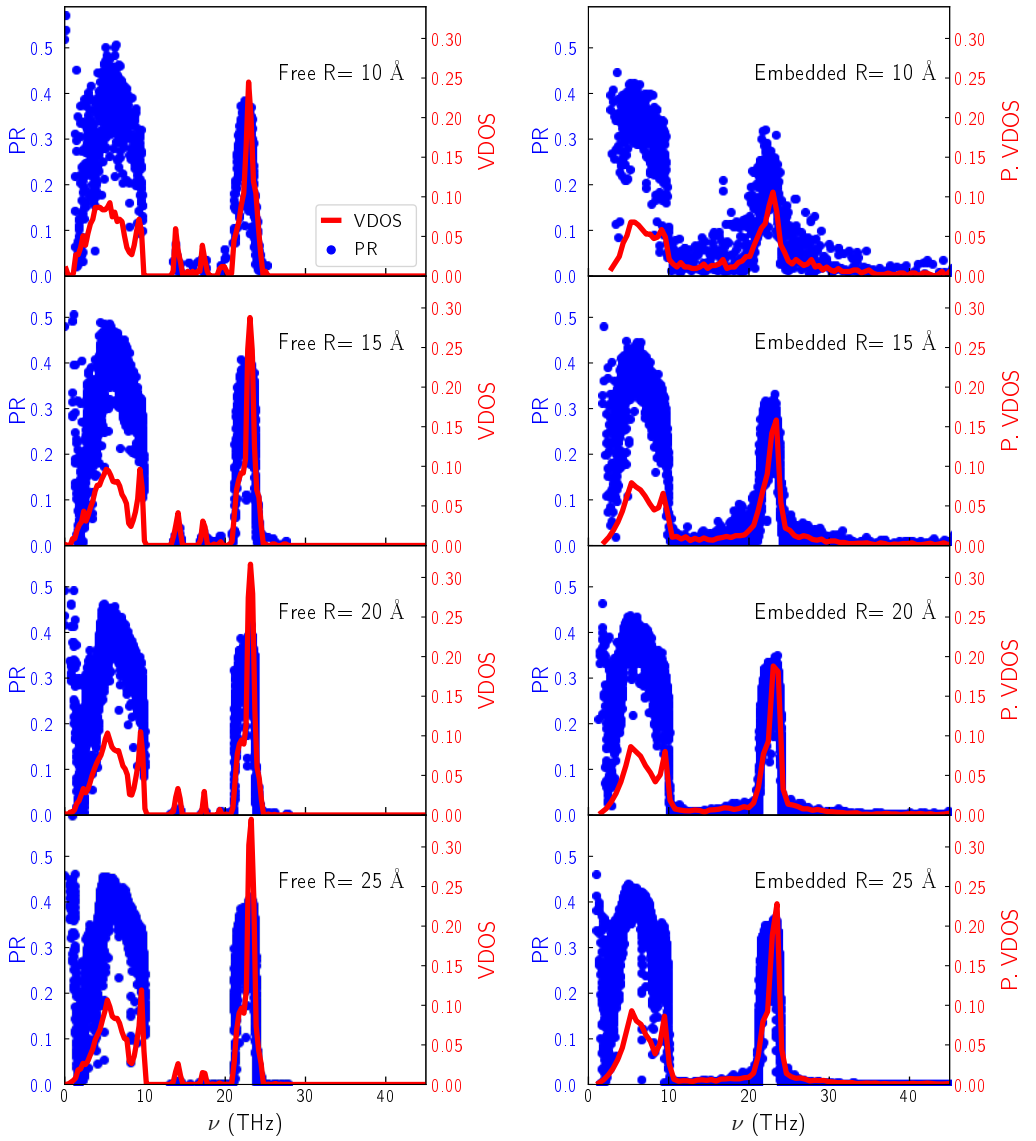

Figure 2.3: VDOS (red lines) and participation ratio (blue dots) derived from the direct diagonalization of the DM for the FNPs (right) and ENPs (left).

largely the smallest NP diameter. But, due to elastic heterogeneities, the effective sound velocity decreases, competing with the decrease in the NPs radius, and thus contributing to enlarge the range of the Lamb's frequencies [Tanguy *et al.* 2002].

The last diameter-dependent feature of VDOS is the intensity decrease of the optical peaks. A broadening of optical peaks was already observed and attributed to changes in the crystalline structure [Han & Bester 2011]. But the crystallinity of the NPs does not seem to change (see A.2). Moreover, the decrease of optical peaks intensities compared to acoustic ones appears also in the direct diagonalization. Thus, this phenomenon is independent of the method used to calculate the VDOS.

The surface effect is the most probable explication of the intensity decrease, as the ratio of Ga to N is constant for all the NPs.

Last but not least, the optic peaks obtained with this interatomic potential is blue shifted when compared to the one obtained from experimental results [Nipko *et al.* 1998] and even more compared to *ab initio* computations [Tang *et al.* 2020, Jiang *et al.* 2017]. The empirical potential used here shows a good agreement for the acoustic modes, but is less accurate for the optic modes (see figure 2.4).

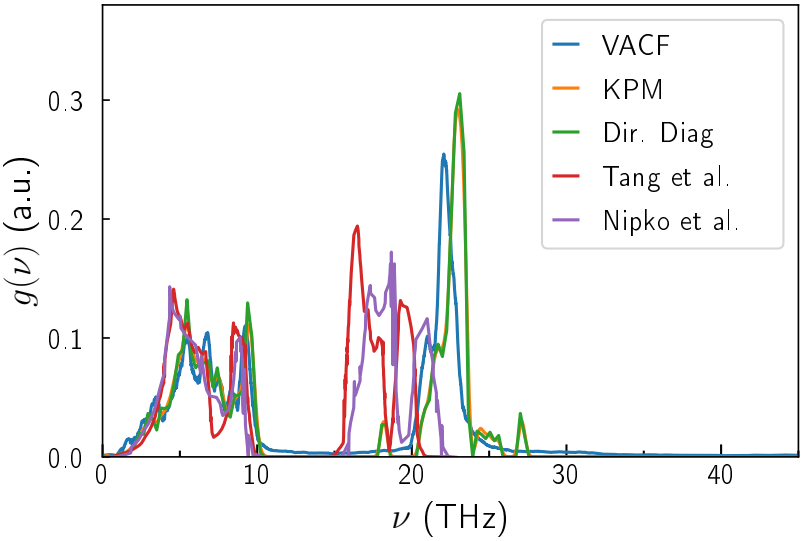

Figure 2.4: Comparison of the VDOS of bulk GaN using KPM, direct diagonalization and VACF along with results from *ab initio* calculation by Tang *et al.* [Tang *et al.* 2020] and experimental results by Nipko *et al.* [Nipko *et al.* 1998].

Briefly, it appears that as the radii of freestanding GaN nanospheres decreases, some acoustic phonons are redshifted, surface modes populate the bandgap and the intensity of the optic peak decreases.

In the next section, the effect of embedding the nanosphere in a silica matrix will be studied.

2.1.3 Vibrational Density of State of Embedded Nanoparticles

The VDOS of GaN nanospheres embedded in SiO_2 (ENPs) are depicted in figure 2.5. It first appears that the frequency shift of acoustic phonons, as well as the defined modes inside the bandgap of bulk GaN at 14, 18 and 20 THz do not appear for the ENP. These modifications can be related to the elimination of the surface modes [Calvo & Balbuena 2005, Han & Bester 2011].

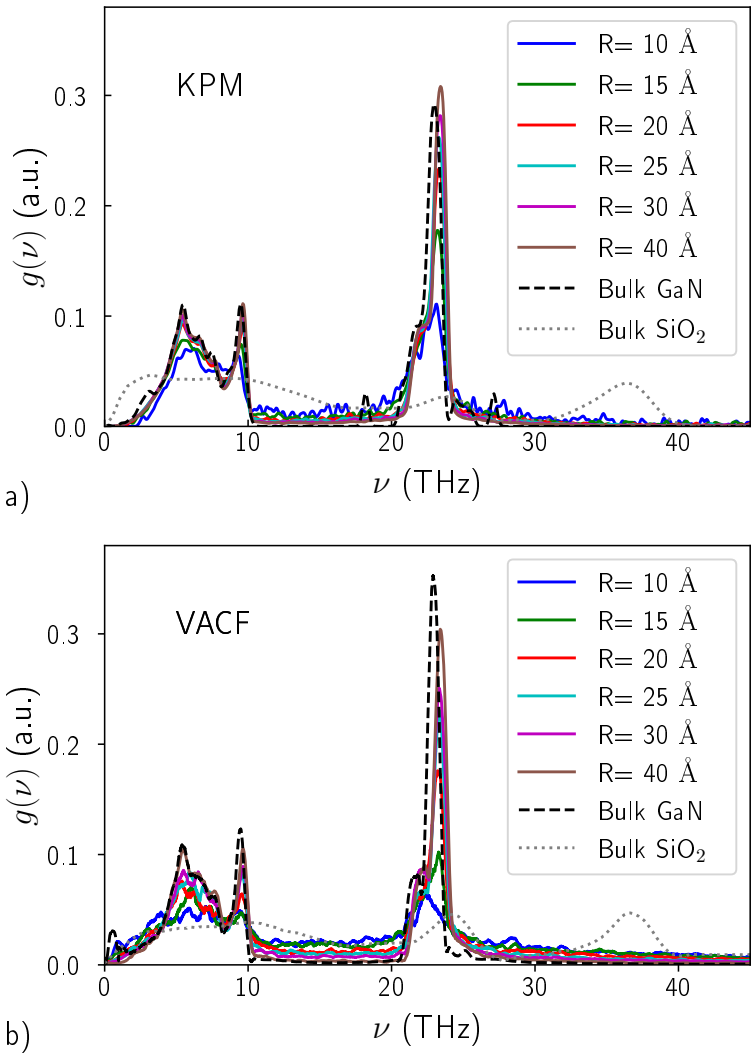

Figure 2.5: VDOS of GaN embedded nanoparticles computed with the DM with KPM (a) and from the VACF (b). The colored lines represent the different NPs, the dashed black line the GaN bulk and the dotted gray line the SiO_2.

The band gap is still populated, but this time in a much more uniform way. This can be understood as the influence of the SiO_2 matrix on the modes. Matrix modes are indeed available at those frequencies, as can be seen in figure 2.5 where the SiO_2 VDOS is represented with a dotted line. Previous works showed that, at the interfaces, modes of the different phases combine together [France-Lanord *et al.* 2014b, Damart *et al.* 2015, Luo *et al.* 2019]. This effect could be used to deduce which mode can be transmitted or reflected on the inclusion. Additionally, new optical branches seem to appear towards high frequencies for all embedded nanoparticle diameters, something that was not observed for free nanoparticles. The most probable explanation for this is the hybridization of the optical modes of the GaN with the

higher frequencies modes of the SiO_2 matrix.

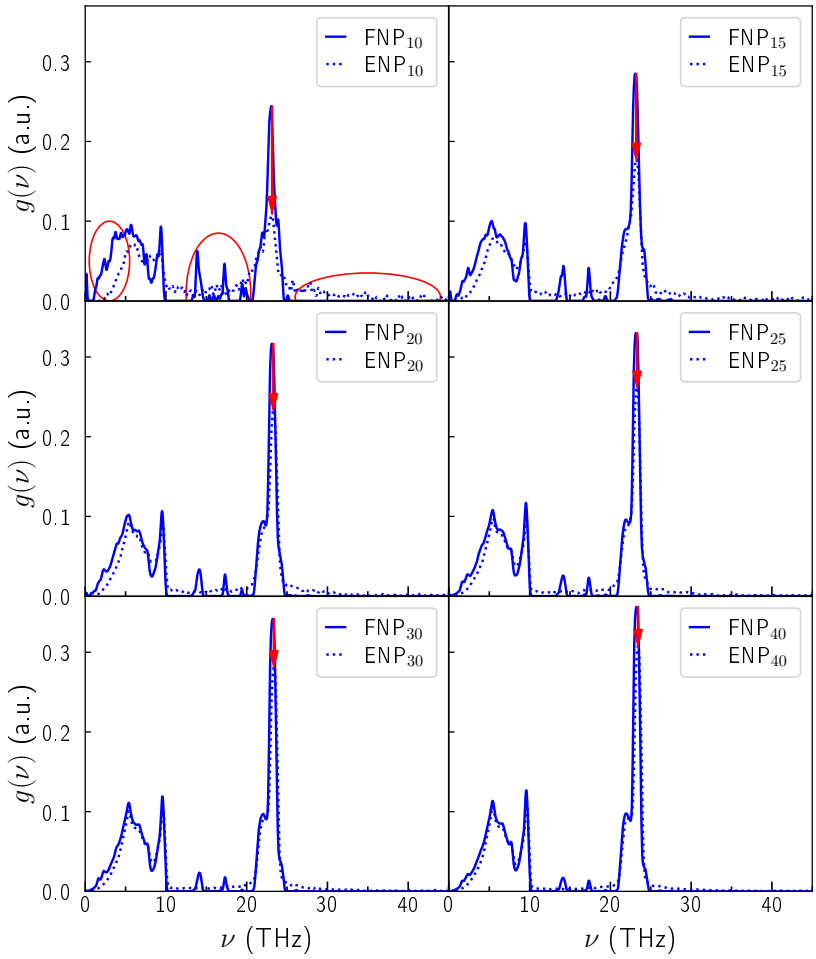

Figure 2.6: VDOS comparison for every NP diameter between free (in continuous line) and embedded (in dotted line), from the DM using KPM.

Finally, the only common tendency between free and embedded nanoparticles is the relative decrease of the optical peaks for small sizes. This effect is even more visible in figure 2.5 compared to figure 2.2. It is partially due to the normalization of the VDOS area (the VDOS is scaled (normalized) so that the integral is one), but the acoustic peaks seem less impacted. As this effect is present for both free and embedded nanoparticles, it cannot be due to free surface effect only. It is most probably related to the amorphization of the surface or interface. Indeed, the embedded nanoparticles seem to show more amorphization than the free ones, as discussed in appendix A.2.

The previous observations on the VDOS of embedded nanoparticles are valid for the two methodologies VACF and KPM. The KPM shows a sharper definition of modes, and it is thus selected to make a more rigorous comparison between the VDOS of free and embedded nanoparticles. The comparison between the two in

figure 2.6 allows underlining the previously cited differences (highlighted in red in the figure). First, the difference in intensity of the optical peaks between the free and embedded nanoparticles can be observed; the peaks for the embedded particles are lower compared to free ones (red arrows). This difference is enhanced when decreasing the size of the NPs. Then the redshift of the transverse acoustic peak for free nanoparticles appears clearly for radii up to 20 Å, while the distinct modes in the bandgap visible for free nanoparticles disappear for the embedded nanoparticles. This confirms the fact, mentioned in the previous paragraph, that these modes are related to free surface effects. Finally, one can observe in the VDOS of embedded nanoparticles background modes, which are related to the matrix.

In a few words, as the NPs are included in an amorphous matrix the redshift and distinct surface modes observed earlier disappear and there is a hybridization with the modes of the matrix.

2.1.4 Discussion of Method of Evaluation of the Vibrational Density of States

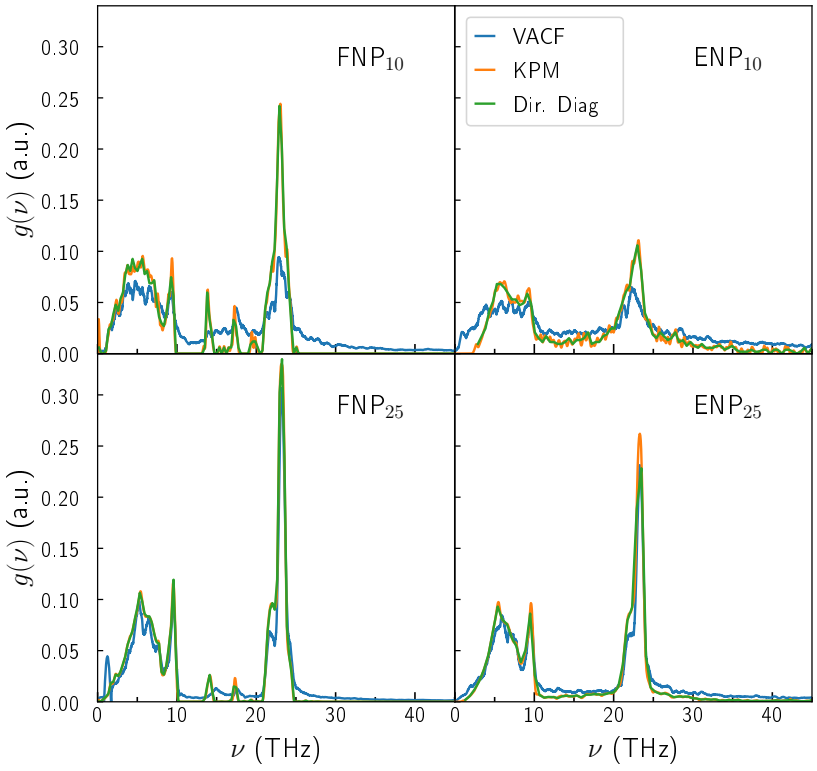

Figure 2.7: VDOS for NP_{10} and NP_{25} free and embedded, using the different method for the evaluation of the VDOS.

Before going on, it is worth comparing the three methods used to estimate the

VDOS of embedded and free NPs namely: direct diagonalization of the dynamical matrix (DM)[2], KPM approximation for DM diagonalization, and VACF. To do so, the VDOS of NPs with two different sizes are depicted in figure 2.7 for each method. The estimations of the VDOS through the DM lead to sharper features in the VDOS, especially for the smallest diameters nanoparticless (top panels of figure 2.7). This can have two origins: the poor statistics of the VACF due to the reduced number of particles, and/or the anharmonicity mainly due to the agitation of surface atoms during simulations. In case of embedded nanoparticles, the vibration of the surrounding matrix is allowed only in the VACF method, and contributes to broaden the VDOS. For bigger diameters, the similarities between the methods using the DM and the VACF validate the fixed interface conditions used when computing the DM. Finally, this shows that the computation of the DM restricted to the NP atoms only is globally adapted to the computation of VDOS of NPs embedded in an amorphous matrix.

In general, the three methods converge for NPs with diameters larger than 5 nm. Nevertheless, for smaller NPs one should be careful about the methodology selection, as the impact of temperature can only be considered directly with the VACF method. On the other hand, the DM approach detects detailed features that the VACF looses due to thermal agitation and poor statistics (small number of atoms). The DM is computable only for small NPs with maximum 1×10^4 atoms because larger number cannot be considered due to CPU limitations related to the direct diagonalization scheme. In contrast, KPM scheme can overpass the direct method limitations, but it is also constrained due to matrix size limitation compared to available RAM.

To complete the study, in the next section will focus on the thermal conductivity as a function of the radii for FNP.

2.1.5 Thermal conductivity of Free Nanoparticles

The thermal conductivity is evaluated using the Equilibrium Molecular Dynamics (EMD) method described in section 1.6. The inclusions are first heated at 300 K, using an initial velocity distribution without overall translational or rotational momentum. The system is then equilibrated at this temperature for 0.5 ns using a Nosé-Hoover thermostat. The flux computed through equation (1.53) is extracted every 10 fs, and the flux autocorrelation computed decay over 40 ps, while the average is done over 5 to 10 ns. To obtain better statistics, the results are averaged over 5 to 10 runs with different seeds for initial velocities. All these simulations were done at 300 K using a Nosé-Hoover thermostat. The NPs were free to move, nevertheless, very few translation or rotational collective movements have been observed. The simulations in which they occurred have been excluded in the statistics for the

[2]LAMMPS evaluates the DM by computing the force modification due to a single atomic displacement. The interactions between the atoms are reduced to their stiffness, as the energy landscape is harmonic. The DM associated with the full system (for FNPs) or only part of it (for ENPs) can be computed. This last one is computed by the motion of every atom belonging to a chosen set. The SiO_2 atoms are fixed, which is equivalent to having a fixed interface around the embedded NPs, allowing the computation of VDOS only for the NPs.

computation of κ. It is assumed that the flux given by equation (1.53) is correct and can be used to compute κ through equation (1.52)

The thermal conductivity (κ) of the FNPs of radii 10, 15, 20, 25, 30 and 40 Å are depicted in figure 2.8 and recorded in table 2.1. In the same table the percentage of surface atoms, belonging to a spherical shell of 2 Å thickness are reported. 2 Å is chosen to encompass every atom appearing visually at the surface.

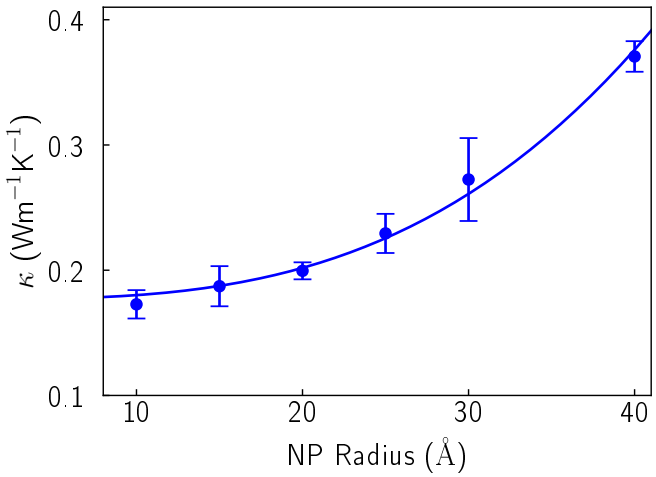

Figure 2.8: Thermal conductivity of free nanoparticles computed with EMD at 300 K, the error bars correspond to the standard deviation between the 5 to 10 independent runs. The blue line is a fit to a cubic scaling law as a guide to the eye.

Table 2.1: Characteristics of the FNP: number of atoms, percentage of surface atom, and thermal conductivity.

	# of atoms	% of surface atom	κ ($W K^{-1} m^{-1}$)
NP_{10}	369	52	0.17 ±.01
NP_{15}	1239	36	0.19±.02
NP_{20}	2952	29	0.20±.01
NP_{25}	5657	24	0.23±.02
NP_{30}	9942	20	0.27±.03
NP_{40}	23580	16	0.37±.02

The κ of FNP, as expected, is only a small fraction of bulk GaN one ($\approx$ 160-220 $W K^{-1} m^{-1}$ [Jezowski *et al.* 2003]). For the smallest NP studied here, it is three orders of magnitude less than the bulk value. When increasing the size of NP, the κ increases non-linearly, in contrast to a previous study for Silicon free NP using the same method (EMD) with diameters 2 to 12 nm in which a linear size dependence was reported [Fang *et al.* 2006].

The previously reported VDOS modifications due to the size effect can impact the κ when considering the separate contribution of each phonon frequency. For in-

stance, modes below 5 THz contribute to 50 % of the thermal conductivity according to Tang *et al.* [Tang *et al.* 2020]. Furthermore, the surface modes in the bandgap gain intensity upon decreasing the radius of NPs. However, these surface modes do not penetrate in the NPs, so they do not contribute much to the overall flux. Size effects are also known to promote phonon mode hybridization that can impact the thermal conductivity [Nomura *et al.* 2018]. The few points in figure 2.8 cannot give the exact tendency nor the whole picture, but a cubic scaling dependence of κ with the diameter seems to appear, which might be related to a volume (r^3) dependence. One could question the meaning of thermal conductivity in such small nanobjects, in the present configuration it quantifies how effective the energy exchange inside the particle is. This is an important effect that one should consider when effective medium approximation (EMA) models are used to estimate the effective κ of a nanocomposite. Moreover, here the particles are big enough to display a VDOS similar to the one of bulk, meaning that energy can be propagated by phonons and flux be computed in a manner similar to bulk .

In brief, the thermal conductivity of GaN free nanoparticles appears to scale with the cube of the diameter rather than linearly as predicted for Si nanoparticles.

2.1.6 Conclusion

To conclude, the vibrational density of states of GaN NPs free or embedded in an SiO_2 matrix was studied. Three different phenomena appear for the free nanoparticles: a redshift of the first acoustic peak, the appearance of surface modes in the bandgap and an intensity decrease of the optical modes. As the particles are embedded in a SiO_2 matrix, only the latter effect persists, and modes induced by the interface with the matrix increase in intensity as the radius of the nanoparticles decreases. No specific peaks for the Lambs modes characterized by a frequency inversely proportional to the radius of the inclusions have been observed: they are indeed hidden in the VDOS spectra, but can be identified easily at low frequencies with the DM. The lowest frequency modes indeed scale with the inverse of the radius (see appendix A.3).

Concerning the thermal conductivity of the FNPs: it does not follow the linear dependence observed for the case of silicon NPs. In III-V semiconducting NPs and more specifically in GaN NPs the thermal conductivity appear to increase in a cubic power low of nanoparticles diameter. The nonlinear size dependence of the thermal conductivity underlines that the mean free path limitation to the NPs size is not the only parameter to consider, otherwise a linear dependence with the size would be observed. This nonlinearity might be due to surface modes and how these modes interact with the heat flux fluctuations in the core of the NP.

Note that collective modes involving the full matrix coupled to the nanoparticle are not taken into account by the DM methods due to the fixed

boundary condition. It was shown in recent articles that the matrix can also play a role [Damart *et al.* 2015], especially from its damping properties [Tlili *et al.* 2019], together with the impedance break between the particle and the matrix [Luo *et al.* 2019]. Collective modes may appear when nanoparticles are embedded in a host matrix.

2.2 Effect of the Orientation of Nanoinclusions

In the introduction of this chapter, it is mentioned that the relative crystalline orientation of the nanoinclusion[3] can influence the thermal conductivity of nanocomposites. This effect has been observed for GaN spherical nanoinclusion in an amorphous silica matrix, where the thermal conductivity is 70 % higher when the inclusion's crystal lattices are aligned than for an arbitrary orientation [Termentzidis *et al.* 2018a].

It is known that the relative crystalline orientation can influence the thermal transfer. For instance, the orientation of neighboring grains will impact the grain boundary resistance of MoS_2 thin films [Sledzinska *et al.* 2017]. The lattice orientation also influences the thermal resistance across graphene sheets [Mohammad Nejad *et al.* 2019]. In these cases, the orientation will select which modes can go through the interface. However, in the case of nanoinclusions, there is a substantial distance between the inclusions, so that the origin of this enhancement is not well understood.

In this section, the effect of the relative orientation of GaN NIs in SiO_2 over the vibrational properties is studied with the goal to understand the origin of the thermal conductivity enhancement. More precisely, the goal is to identify an eventual direct transmission of energy between the inclusions.

2.2.1 Modeling of the Configurations

The configurations used here are similar to the one described in section 2.1. Using the same amorphous SiO_2 sample, two different configurations are created, one with 3 inclusions sharing the same orientation (Iso-oriented NIs or I-NIs) and another where the two external NIs are rotated 60° about the x and then y axis (aniso-oriented NIs A-NIs). The two configurations are represented in figure 2.9.

To reproduce the conditions of the earlier study, the inclusions have a radius of 23 Å and their centers are 107 Å apart. The overall simulation box is a rectangle of 400 by 82 by 85 Å. This geometry allows having a symmetric box to perform WP propagation simulations easily. However, the inter inclusion distance is only respected over the x direction, so that only this direction will be studied. Periodic boundary conditions are used in every direction. The building and relaxation processes are the same as in section 2.1.

[3] From now one, the second phase added in the matrix is referred to as nanoinclusions.

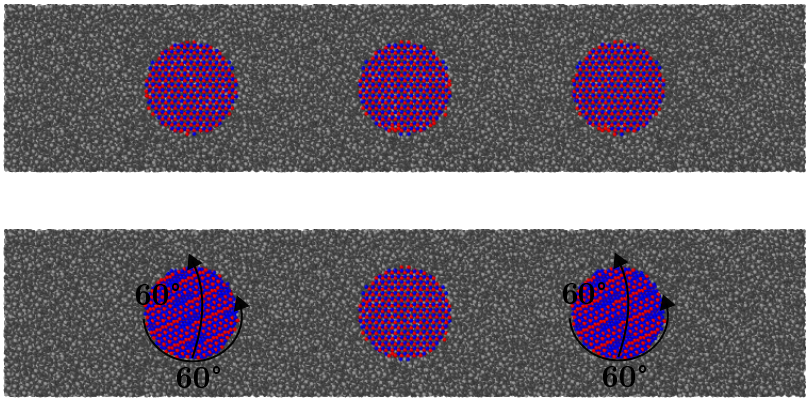

Figure 2.9: Cross-sectional visualization of iso-oriented nanoinclusions (a) and aniso-oriented nanoinclusions (b) configurations. The Ga atoms are represented in red, N atoms in blue, Si atoms in light gray and O atoms in dark gray.

2.2.2 Vibrational Properties

In the original publication [Termentzidis *et al.* 2018a], the increase in thermal conductivity is attributed to phonon tunneling. In this section, phonon tunneling is interpreted as ballistic transport from one inclusion to the next. The possibility of such a transport can be assessed by studying the Mean Free Path (MFP) in amorphous silica. If modes with a MFP of the order of the distance between inclusions exist, there may be a direct energy transmission between the inclusions. This ballistic transmission could be influenced by the orientation of the inclusions, the transport in GaN being anisotropic [Ju *et al.* 2016]. To identify those modes, the MFP in bulk amorphous silica is computed through Wave-Packet (WP) propagation simulations as described in 1.5.3, with a force amplitude of $3.773 \times 10^{-4}\,\mathrm{eV\,\AA^{-1}}$.

In figure 2.10 the MFP computed from the decay rate of the envelope of the wave-packet are displayed for transverse and longitudinal polarizations. It appears that the MFP is quickly reduced to 1.5 nm or below. Only the very low frequencies appear to be able to travel more than a few nanometers. The values of MFP are consistent with the results of Larkin et al. [Larkin & McGaughey 2014]. It is noticeable that, among the frequencies studied, only 0.5 THz appears to be able to carry energy over a distance larger than the distance between two inclusions (82 Å).

Another way to study the transmission of energy between the NIs is to focus on the available modes in the different parts of the nanocomposites. It can be done by comparing the VDOS of the embedded NPs and of the SiO_2 in figure 2.5. Below 1 THz, a frequency for which heat carriers can travel the separating the inclusions ballistically, only a few modes are available in the NPs. This means that it is unlikely that they contribute significantly to the thermal conductivity increase. However, there is a strong overlap of the acoustic phonons peaks between 5 and 10 THz with amorphous silica modes, and a small overlap of optical phonons around 25 THz.

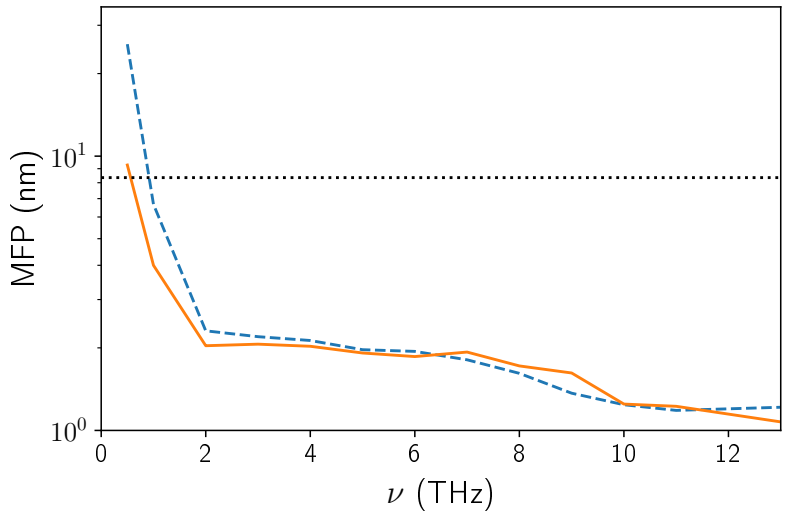

Figure 2.10: MFP in amorphous silica, for the transverse (orange full line), and longitudinal (blue dashed line) polarizations. The horizontal dotted line represents the distance between the inclusions.

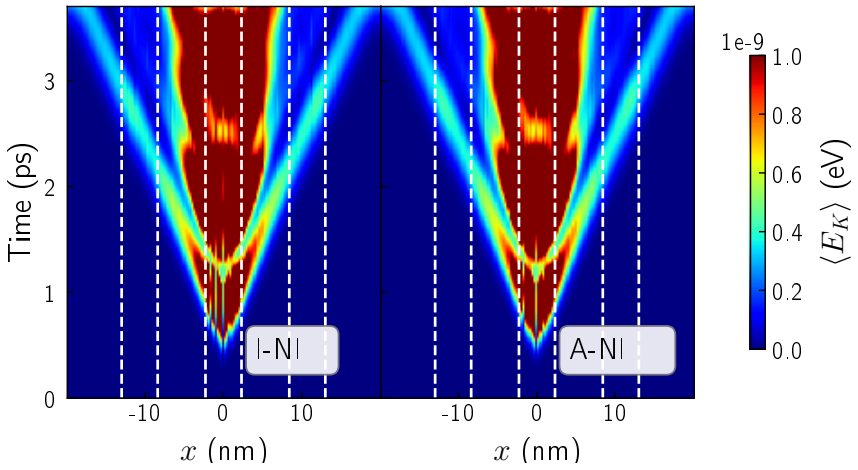

Figure 2.11: Heat maps representing the evolution of average atomic kinetic energy (color) as a function of time (in the vertical axis) and position over x after a 0.5 THz longitudinal excitation for I-NI (left) and A-NI (right). The position of the inclusions are marked by dashed lines.

Nevertheless, one can compare the propagation across the nanocomposites at low frequencies through wave-packet simulations at low frequencies. This could show energy pathways between the inclusions that are influenced by their orientation. To test this, a wave-packet simulation is carried out with an excitation made in a central slice of thickness 2 Å in the central inclusion. The results are displayed in figure 2.11, where the propagation of energy after an excitation at 0.5 THz in

both configurations is represented. A longitudinal excitation is chosen because it appears to be the best case for the ballistic transmission of energy. The color scale gives the average kinetic energy as a function of space (x position) and time. No significant difference between the two spatio-temporal representation can be noted, the transmission through the inclusions is very similar in both cases. There is no apparent reflection or localization of energy at the interface of the external inclusions. This shows that there is no energy transmission that is influenced by the orientation for this mode. The energy in the center corresponds to the part of the wave-packet that is refracted in another direction by the interface of the matrix and the central inclusion and travels in the y and z directions through the periodic boundary conditions.

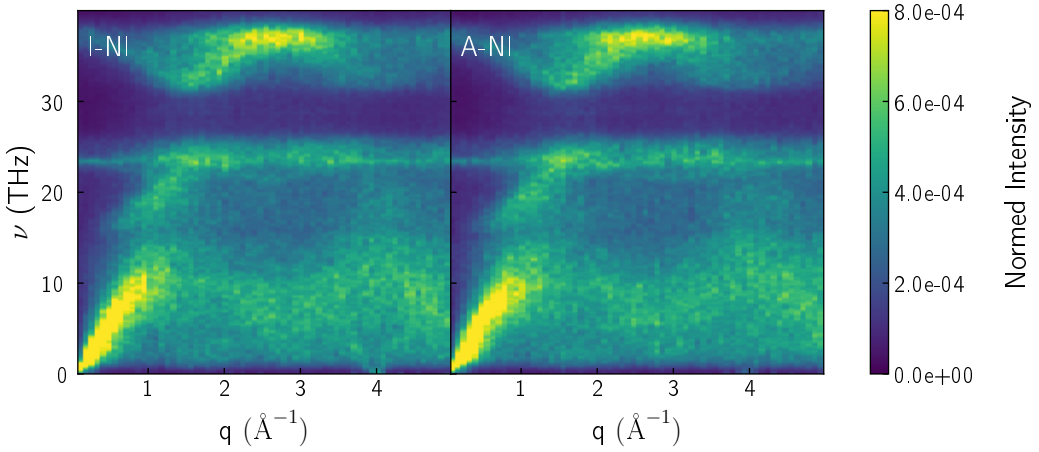

Figure 2.12: Dynamical structure factor in the **x** direction, projected on the longitudinal polarization for I-NI (left) and A-NI (right).

Up to this point, only the longitudinal low frequencies have been investigated. This choice is motivated by the higher MFP across the amorphous silica matrix. However, it does not mean that other modes cannot penetrate through the matrix and tunnel from one inclusion to the other. A broader spectrum is investigated in the Dynamical Structure Factor (DSF) displayed in figure 2.12. In this figure, both for iso and anisoriented nano-inclusions, different features of the VDOS can be identified. First, the propagative modes of silica show up as high intensity modes for wave vectors below 1 Å^{-1} and below 12 THz, this is visible through the thick yellow line starting from the bottom-left corner. Then a small depletion is visible around 12 THz. A horizontal band appears around 23 THz, this corresponds to the optic peak in the GaN NIs. Finally, high frequency modes of silica appear above 30 THz. However, no clear differences appear between the iso or aniso-oriented nanoinclusion. This lack of difference shows that there are little differences in the vibrational properties of the nanocomposites, whether the inclusions are aligned or not. However, the configuration presented here is not same as the one of the original publication [Termentzidis *et al.* 2018a]: the particles are translated in order to have

three aligned particle. As a result, the particles do not present the same crystalline orientation to each others, this might be why no effect of orientation could be seen.

The study of the longitudinal modes in the GaN SiO_2 nanocomposite did not show clear differences between a configuration where the inclusions have an aligned lattice orientation and a configuration with an arbitrary orientation of each inclusions. As the longitudinal inclusions have the highest MFP, they are considered as the most likely to percolate through the structure. This thus indicates that the increase in the thermal conductivity due to the alignment of the inclusions cannot directly be linked to the ballistic transport between the inclusions. The origin of the thermal conductivity variation, is probably more complex and multifactorial. To go further other relative orientation of the inclusions could be studied and NEMD simulation performed to insure that the thermal conductivity enhancement is observable with the structure studied in this work.

2.3 Rigidity Effects: Example of c-Si Inclusions in a-Si Matrix

Having discussed the effects of including crystalline nanospheres in an amorphous matrix in the previous sections, this section will focus on the effect of the stiffness of the nanoinclusions over the nanocomposites vibrational and thermal properties.

As discussed before, the introduction of nanoinclusions modifies the properties of the matrix, a key factor in this modification is the acoustic mismatch between the phases. This acoustic mismatch promotes scattering at the NI/matrix interface and decreases the thermal conductivity [Juangsa *et al.* 2017]. Furthermore, it promotes the pinning of energy (some energy is trapped at the interface), decreasing further the thermal conductivity, as has been shown using continuum models [Luo *et al.* 2019].

To study specifically the effect of the acoustic mismatch, the model system of crystalline Si NIs in an amorphous Si matrix can be used. Indeed, the stiffness of silicon can easily be tuned in MD using the pre-factor of the three body term in the SW interatomic potential (λ in equation [1.33]). This possibility has already been used to study the mechanical [Fusco *et al.* 2010] and vibrational [Beltukov *et al.* 2016] properties of amorphous silicon with different stiffnesses. And the impact of stiffer inclusions has been studied originally in [Tlili *et al.* 2019].

In this section, an extension of the study of Tlili *et al.* is made with a wider variety of systems. Using the wave-packet propagation method, the impact of the stiffness of spherical NIs in an amorphous matrix on the vibrational properties of the nanocomposites will be studied. The qualitative description of the different phenomena will precede the analysis in terms of MFP and diffusivity.

2.3.1 Modeling of the Configurations

The nanocomposites studied in this section are composed of an amorphous matrix elaborated using the melt-quench method described in section 2.4.1. The original sample is a cube of side 17 nm, out of which the cube of side 6 nm used in this study, is cut out. The nanoinclusions are created by hollowing out a sphere of radius 2.5 nm of the cube and then filling it with crystalline Si. The crystal has the $\langle 100 \rangle$ directions aligned with the Cartesian coordinates axis. These dimensions correspond to a nanocomposite with a crystalline volume fraction of 30 %, containing 10.7×10^3 atoms in total. The same cube without inclusion is also studied as a reference. Periodic boundary conditions are used in all the directions to simulate the bulk properties.

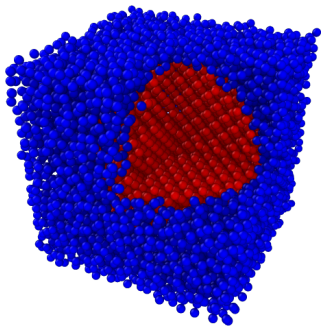

Figure 2.13: Single c-Si nanoinclusion (red) in a-Si matrix (blue).

Before relaxing the structure, the interaction potential is set. The idea is to explore the effect of the rigidity contrast between the matrix and the inclusion. For this, the prefactor of the three body term in the interaction potential λ is modified (see equation [1.34]), by doing so the bending rigidity is tuned and this affects the stiffness. Three possibilities are studied, the usual value ($\lambda = 21$), a stiffer ($\lambda = 100$) and softer silicon with ($\lambda = 5$). To compare the properties of the different phase the elasitic properties of amorphous silicon, and of the different crystalline phases are reported in table 2.2. The different modulii can be computed from the three independent values in the stiffness tensor for cubic isotropic lattices C_{11}, C_{12} and C_{44}, using Voigt indices. For the crystal, they are computed from the stress resulting from small deformation after relaxing the atomic position to minimize the energy of cubic samples (equivalent to quasi-static deformation). They depend on the orientation of the lattice and are here computed with the three axis corresponding to [100], [010], and [001] [Hopcroft *et al.* 2010]. This orientation corresponds to the orientation of the nanoinclusion. The bulk modulus characterizing the compression resistance is given by $K = \frac{1}{3}(C_{11}+2C_{12})$, the shear modulus giving the shear stiffness by $G = C_{44}$, the Poisson ratio characterizing the deformation perpendicular to the loading direction by $\nu = \frac{1}{(1+C_{11}/C_{12})}$ and the Young modulus by $E = 2(1+\nu)K$. The values for the amorphous sample are those of Fusco *et al.* [Fusco *et al.* 2010]. The velocity ratio for transverse v_T and longitudinal v_L waves is computed thanks to the usual formula for sound velocity in isotropic solids, that is $v_T = \sqrt{G}/\sqrt{\rho}$ for the

transverse and $v_L = \sqrt{K + \frac{3}{4}G}/\sqrt{\rho}$ for the longitudinal. So that, here, the values will this corresponds to the speed of sound in the $\langle 100 \rangle$ direction, that is, here, in the propagation direction. As a first approximation, the density is considered constant between the phases so that the ratio of the speed of sound corresponds roughly to the impedance ratio.

Table 2.2: Elastic properties of the amorphous matrix, and bulk pristine crystalline Si for different values of λ, the parameter used to modify the stiffness.

	Am.	λ=100 (Stiff)	λ=5 (Soft)	λ=21 (Standard)
K (GPa)	101	101	101	101,3
G (GPa)	34	139	16	56,4
ν	0,35	-0.06	0.46	0.34
E (GPa)	92	263	47	150
v_T/v_T^{Am}	1,00	2,02	0,70	1,29
v_L/v_L^{Am}	1,00	1,27	0,95	1,07
$\chi = E/E_{Am}$	1,00	2.86	0,51	1,64

In table 2.2 it appears that the bulk modulus is not affected by the variation of λ. However, the Poisson ratio and shear modulus are strongly affected by this change. The Poisson ratio (ν) is reduced when increasing λ, at λ=100 the material is slightly auxetic. The reduction of ν was already documented for amorphous samples [Fusco *et al.* 2010]. The shear modulus increase is consistent with a stiffer angle between the atoms. This results in a strong effect of λ on the group velocity of transverse waves, but less on the longitudinal waves. Choosing, $\lambda = 100$ or $\lambda = 5$ indeed results in an impedance mismatch that is much more sensible on the transverse waves. Moreover, the mismatch is more marked for the stiffer inclusions ($\lambda = 100$). Additionally, the elastic properties with the standard value $\lambda = 21$ are reported in table 2.2, the values obtained correspond to the values reported by [Cowley 1988]. Interestingly, even at constant λ there is an impedance mismatch between a-Si and c-Si.

In the nanocomposite, the modification of the parameter λ concerns only the interaction between the atoms in the nanoinclusion. For the interactions involving atoms in the inclusion and in the matrix, the regular value of $\lambda = 21$ is used.

Once the interaction potentials for the inclusion and for the matrix are set, the resulting configuration is relaxed. For this, a conjugated gradient minimization is performed on the atomic positions to relax the force. After this, the configuration is annealed at 100 K during 10 ps (with a simulation time step of 1 fs). Finally, the system is relaxed again using a CG minimization of the forces to reach local mechanical equilibrium. The resulting nanocomposite is displayed in figure 2.13.

2.3.2 Wave-Packet Propagation

The configurations previously described are studied using the wave-packet propagation method described in section 1.5.3. The medium in which the wave-packet propagates is created by repeating the configuration obtained previously twelve times in the x axis direction. After the assembly, a last conjugated gradient energy minimization is performed to ensure that the system lays in a local energy minimum. To avoid surface effects, the simulations are performed using periodic boundary conditions in all the directions.

The resulting configuration is displayed in the figure 2.14. In this figure, two image structures are depicted for a better representation of the system being studied here, a nanocomposite composed of a 3D array of crystalline nanoinclusions.

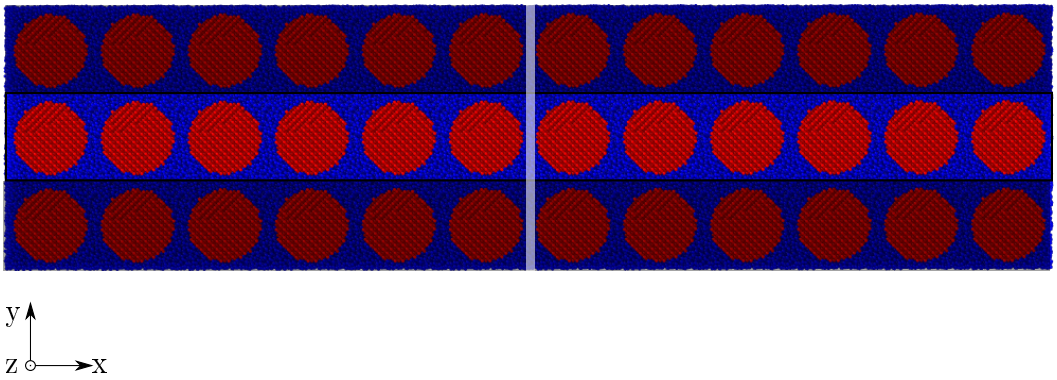

Figure 2.14: Cross-sectional representation of the nanocomposite studied with c-Si nanoinclusions (red) in a-Si matrix (blue). Two image systems are represented slightly shaded out. The excited slice is highlighted in white.

The wave-packet simulations are performed using the method described in section 1.5.3. In this particular implementation, a central slice of 2 Å is excited. As represented in the figure 2.14 the excited slice (in white) lies between two inclusions in the amorphous matrix. The excitation force amplitude is $3.773 \times 10^{-4}\,\mathrm{eV\,\AA^{-1}}$. And the simulations were performed from 1 to 15 THz with a step of 1 THz. These simulation are done at 0 K so that energy is mostly scattered by geometrical defects rather anharmonicity (very low for low temperature and low excitation amplitude).

Propagative, Diffusive and Mixed Regimes Depending on the frequency, different behaviors appear, first at low frequencies the transport is mostly ballistic (propagative without a lot of energy being scattered), at higher frequency the velocity of the wave-packet becomes ill-defined, and the transport is diffusive (that is the energy appears to be spread by diffusons as discussed in 1.1.5). However, the transition from one to another is not sharp, and for frequencies between the two regimes a mixed regime appears. The three different regimes appear more clearly for longitudinal excitations, this polarization will thus be the center of attention.

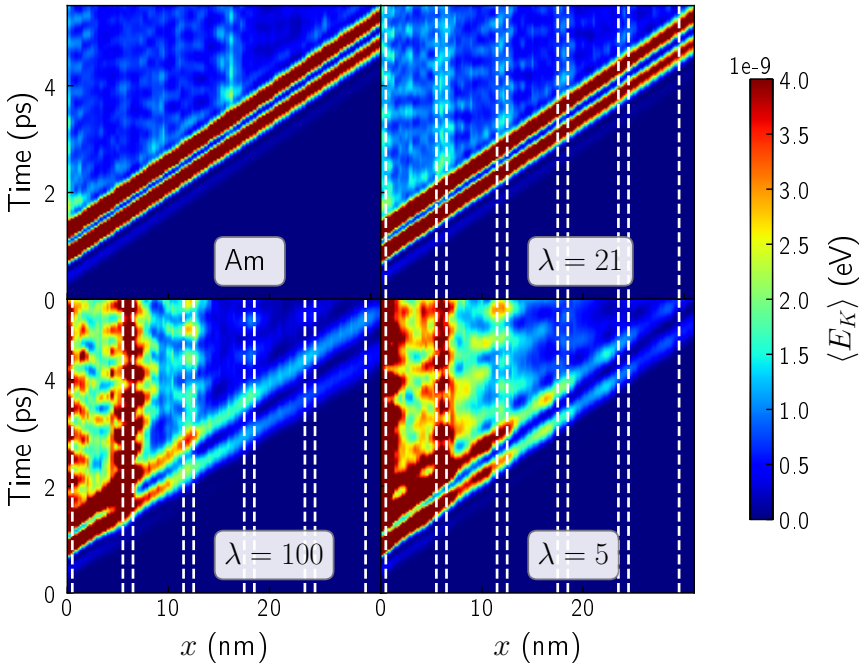

Figure 2.15: Heat maps representing the evolution of average atomic kinetic energy (color) as a function of time (in the vertical axis) and position over x (bottom axis) after a 1 THz longitudinal excitation. Only the right side of the studied configuration is represented, the other being symmetric (see figure 2.14). For the nanocomposites, the positions of the inclusions are marked by dashed lines. The annotations give either the λ (stiffness) of the interatomic potential or distinguish the fully amorphous sample.

The different regimes are represented in figures 2.15 to 2.17. The first one, represents the WP propagation at 1 THz, is the propagative regime. This regime is characterized by a mechanical wave traveling at constant speed through the configuration, with some energy being scattered along the path. This propagative transport is clearly visible in the top left panel of figure 2.15 for the fully amorphous sample, two red stripes corresponding to a wave-packet[4] traveling at constant speed are visible. Some energy is scattered, it is visible in that after the passage of the wave-packet the background energy is higher due to the energy left behind by the wave-packet. For the regular interaction $\lambda = 21$ the behavior is very similar to the one of the fully amorphous configuration. The only notable difference is that the intensity of the WP is decreased at the end (the stripes fade in intensity near the end). This is the sign that more energy is being scattered than for the amorphous sample. For the stiffer and softer inclusions the situation is different, the propagation is much more attenuated and most of the energy seems pinned between the

[4]The two stripes correspond to the two maxima of kinetic energy appearing for a full wavelength.

inclusions. In particular, between the first and second inclusions, the WP appear to be trapped. Especially, for the nanocomposite with the stiffer inclusions ($\lambda = 100$) in the inclusions, the WP seems to be reflected multiple times between the second and third inclusions (around X=6 nm). A similar behavior has been observed in nanoporous Si thin films [de Sousa Oliveira *et al.* 2020]. These reflections could lead to interference. Overall, the dominant transport mechanism seems propagative, with part of the energy reflected at the interfaces, in particular when the impedance mismatch is large.

Finally, it appears in this representation that the WP travels faster in the system with stiffer inclusions than in the one with the softer inclusions. This is consistent with the difference in group velocity reported in table 2.2. This shows that the higher group velocity in the matrix is enough to increase the effective group velocity of the whole structure.

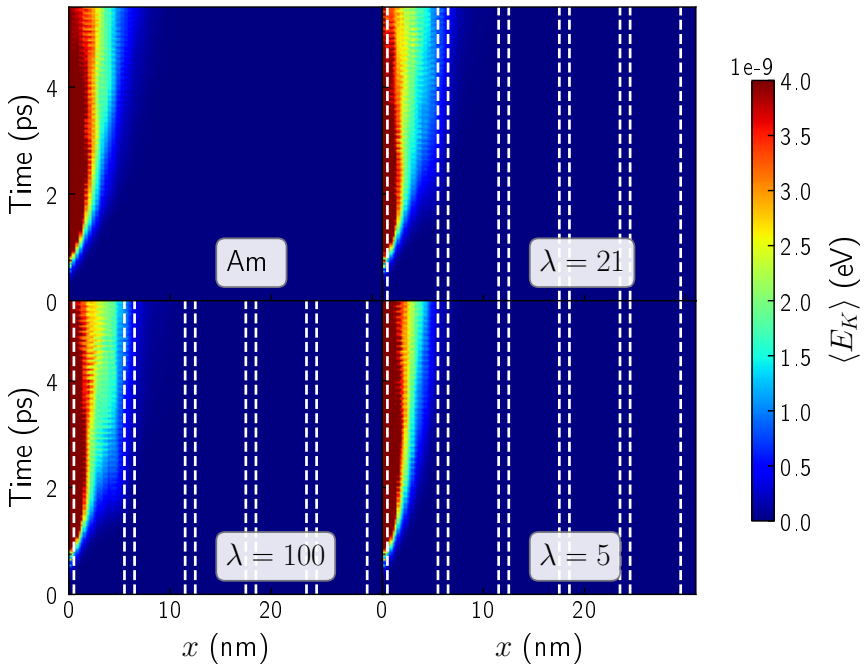

Figure 2.16: Heat maps representing the evolution of average atomic kinetic energy (color) as a function of time (in the vertical axis) and position over x (bottom axis) after a 10 THz longitudinal excitation. Only the right side of the studied configuration is represented, the other being symmetric (see figure 2.14). For the nanocomposites, the positions of the inclusions are marked by dashed lines. The annotations give either the λ (stiffness) of the interatomic potential or distinguish the fully amorphous sample.

The second behavior is diffusive, this happens at high frequency when the energy of the wave-packet does not propagate anymore, but slowly spread through the sample. This behavior is visible in figure 2.16 at 10 THz, in which the red stripes

characterizing the propagative transport have disappeared and the energy slowly diffuse from the center. At this frequency, the attenuation in the amorphous matrix is strong [Beltukov *et al.* 2018], so much that the wave-packet cannot propagate from inclusion to inclusion. If the behaviors are very similar, there is a difference between the amorphous sample and the nanocomposites: for the nanocomposites the spreading seems to be faster for regular and stiffer inclusions (λ=21 and λ=100), probably boosted by the inclusions. This faster spreading is visible mostly in that the central energy peak fades out much more quickly in the presence of these inclusions. For the softer inclusions, on the contrary, the diffusion appears to be slower, which is consistent with the material being softer.

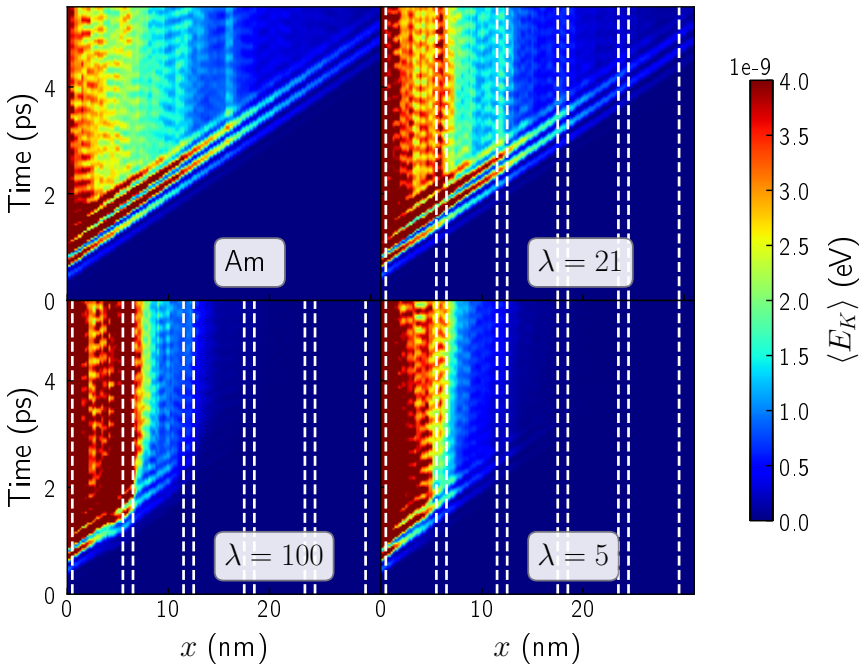

Figure 2.17: Heat map representing the evolution of average atomic kinetic energy (color) as a function of time (in the vertical axis) and position over x (bottom axis) after a 2 THz longitudinal excitation. Only the right side of the studied configuration is represented, the other being symmetric (see figure 2.14). For the nanocomposites, the positions of the inclusions are marked by dashed lines. The annotations give either the λ (stiffness) of the interatomic potential or distinguish the fully amorphous sample.

The last regime represented in the figure 2.17 where $\nu = 2\,\text{THz}$, is the mixed regime, for which both behaviors are visible. For this frequency, both phenomena are visible: there are the stripes characteristic of propagative transport, and a central spot slowly spreading characteristic of diffusive transport. For the propagative part, as in the figure 2.15, the attenuation of the WP is stronger for the nanocomposites and even more in case of large impedance mismatch. At this frequency, some

energy is trapped between the first and second inclusion for both regular and stiffer inclusions (λ=21 and λ=100). However, no successive reflections are visible. For the softer inclusions (λ=5), the energy seems trapped in the first inclusion.

Before going on, it must be addressed that even for the amorphous sample, some energy seems to be trapped after the passage of the WP. This is visible as a vertical strip around 15 nm. This probably corresponds to a small defect inducing the pinning of energy locally.

In brief, the qualitative visualization of the WP allows the distinction between, the propagative regime at very low frequency and the diffusive regimes at higher frequencies. These regimes correspond to the propagons and diffusons whose existence was proposed by Allen and Feldman in amorphous systems [Allen & Feldman 1993]. In between those two regimes, the energy transport regime is mixed: part of the energy travels ballistically and part of it spreads diffusively. The inclusions appear to reduce the intensity of the propagative part of the WP, with a marked effect of the inclusion stiffer than the matrix. The inclusions seem to also affect the diffusion of energy, a softer one slowing down the diffusion while the others accelerate it.

Mean Free Path For the evaluation of the MFP, the decay rate of the envelope of the wave-packet is estimated from 10 nm away from the excitation to 30 nm away from the excitation (see section 1.5.3). This choice allows omitting the eventual diffusive part of the WP that is usually limited to the first inclusion. Both positive and negative x directions are considered (whereas only one is displayed in figures 2.15 to 2.16), and the average between the two directions is considered. The final values of the MFP in figure 2.18 corresponds to the MFP computed through the fit of an exponential decrease up to 12 THz for the longitudinal polarization and up to 6 THz for the transverse polarization, above these frequencies, the penetration length method is used [Beltukov *et al.* 2018].

The longitudinal MFP of the different structures displayed in the left panel confirm what was visible in figures 2.15 to 2.17: the MFP at low frequency is reduced by the presence of inclusions, and this effect is stronger in the case of impedance mismatch between matrix and inclusions. The decrease of MFP is stronger for the softer inclusions. It is also noticeable, that the amorphous sample and the nanocomposites with homogeneous inclusions have a small MFP peak around 8 THz. This peak was already observed for a-Si by Beltukov *et al.* [Beltukov *et al.* 2018]. It has been associated to the decreased number of transverse modes available for coupling at this frequency. This peak is absent in the case of stiffer or softer inclusions. For the MFP of the transverse wave-packet, the situation is very similar. At low frequencies, the stiffer and softer inclusions induce a decrease of MFP. At higher frequencies, only the softer inclusions induce a MFP decrease.

The frequency limit for the transition between the evaluation of the MFP with a fit to a Beer-Lambert law and the use of the penetration length is cho-

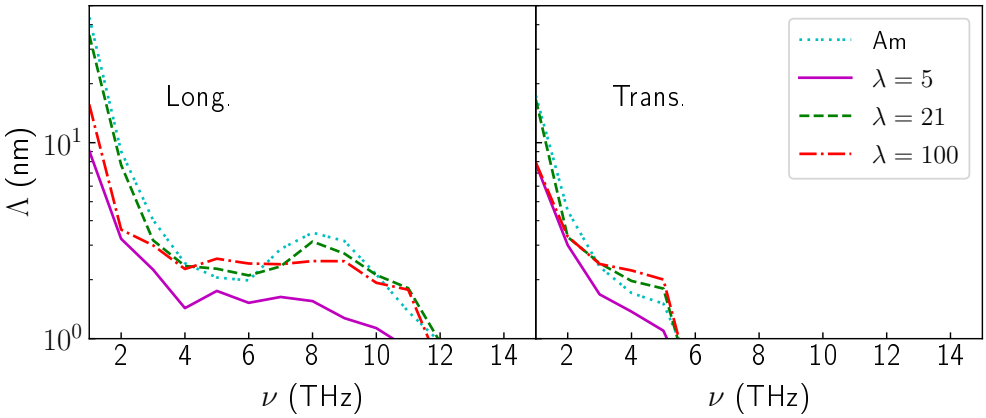

Figure 2.18: MFP as function of the frequency for the different configurations. The left and right panel contain respectively the MFP of the longitudinal and transverse polarization.

sen to be the same for all the configurations. However, as documented in the publication [Tlili *et al.* 2019] and the related work using the finite element method [Luo *et al.* 2019], the inclusions can lower the transition between the propagative and diffusive regime. As a result, the quality of the fit at higher frequencies (above 5 THz for the longitudinal and above 3 THz for the transverse) is questionable. This is particularly marked when there is an impedance mismatch between the matrix and the inclusions.

Moreover, at low frequencies (below 3 THz), the MFP measured for a-Si is lower than the one obtained by Beltukov *et al.* [Beltukov *et al.* 2018]. This difference might be explained by the a-Si sample used, in the previous work the a-Si sample is used as created and here the a-Si sample is cut out of a bigger sample and then repeated in the x direction. It creates an artificial periodicity, and modifies the structure at the junction between two repetitions. This creates "interfaces" that are likely to reduce the MFP at low frequency when it is of the order of the size of the unit box that is repeated, in spite of the annealing. A confirmation of the effect of the size of the repeated simulation box is that for a larger box cut out of the same amorphous sample, the MFP is higher (see figure 2.23 in section 2.4).

Briefly, the inclusions act as scatterers and tend to decrease the mean free path. This effect is stronger for nanocomposites with a marked impedance mismatch between inclusion and matrix (inclusions stiffer or softer than the matrix).

Diffusivity The diffusivity is estimated after an excitation where each atom in the white region in figure 2.14 is excited in a different randomly distributed direction with the method described in section 1.5.3.

The diffusivity as a function of the frequency for the different configurations is

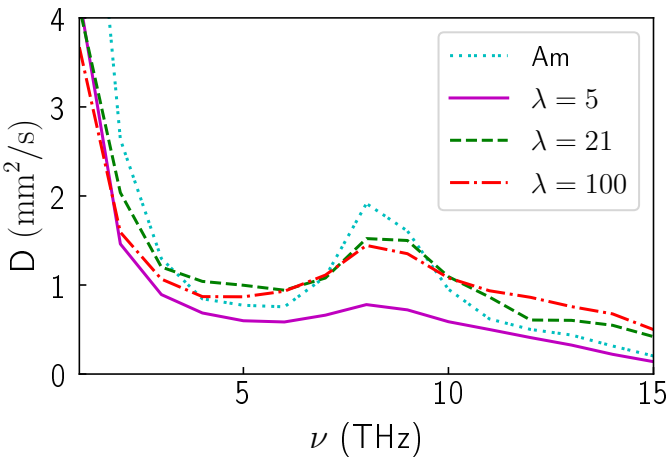

Figure 2.19: Diffusivity as a function of the frequency between 1 and 15 THz in the different configurations.

displayed in figure 2.19. The overall shape of the diffusivity corresponds to one previously described [Beltukov *et al.* 2016]. It starts high at low frequency, has a plateau between 3 and 7 THz, a peak around 8 THz and decreases after that. However, the inclusions modify the profile for λ= 21 or 100 this manifests as a larger diffusivity at high frequencies and a less marked peak, with a stronger effect of the stiffer inclusion (λ= 100). The peak corresponds to the end of the transverse phonon dispersion curve and was already observed by Allen and Feldman [Allen *et al.* 1999]. The softer inclusion, induces a marked decrease in diffusivity at all frequencies, this is consistent with the slower spreading of energy at high frequencies visible in figure 2.16. The high values at low frequency appear because the diffusive behavior of the energy propagation is questionnable, the 1D diffusion law does not any describe the energy propagation. This can lead to divergence in the value of D, that is why the graph is truncated at 4 $mm^2\,s^{-1}$.

Briefly, the addition of inclusions does not suppress the main features of the diffusivity as a function of frequency in a-Si, but makes them slightly fade: increasing the values at high frequency for homogeneous or stiffer inclusions (λ = 21 or 100), or decreasing the overall level for softer inclusions (λ = 5).

2.3.3 Conclusion

In this section, the effect of the stiffness of the inclusions in an a-Si/c-Si nanocomposite was studied. The propagative, diffusive and mixed regimes have been identified through a qualitative analysis of the energy propagation after a longitudinal excitation. When it comes to the analysis of the MFP and diffusivity, it appears that homogenous and stiffer inclusions induce an overall reduction of the propaga-

tive transport and an increase in the diffusive transport at high frequencies. It has been shown, for homogeneous and stiffer inclusions, that overall the thermal conductivity is not affected by the stiffness, the decrease in propagative transport is compensated by the increase in the diffusive transport [Tlili *et al.* 2019]. In the case of the softer inclusions, both the propagative and diffusive transport are reduced, thus a reduction of the thermal conductivity can be expected. The analysis carried here are discussed more in depth in the publication this work contributed to [Tlili *et al.* 2019].

2.4 Shape Effects: c-Si inclusion in a-Si Matrix

Most of the theoretical studies of nanoinclusions impact on the vibrational and thermal properties assume spherical NIs [Damart *et al.* 2015, Termentzidis *et al.* 2018a, Tlili *et al.* 2019, Luo *et al.* 2019, Hu *et al.* 2020]. However, NIs can take multiple shapes [Hofmeister *et al.* 2005]. The shape influences the properties, for instance, NIs with a high surface to volume ratio increase the electrical conductivity in polymers [Vasudevan & Fullerton-Shirey 2019]. This ratio similarly increases the heat transport in nanofluids [Jabbari *et al.* 2017]. Moreover, when their mass fraction is high enough, the NIs can form a percolating network that affects the transport properties [Miura *et al.* 2015]. For Si NIs in a SiO_2 matrix, the percolation can be controlled and modifies the properties of the material [Nakamura *et al.* 2015, Nakamura 2018].

A percolating network of NIs is similar to a nanomesh embedded in an amorphous matrix. Embedded nanowire meshes are already used in polymers to increase their thermal conductivity [Huang *et al.* 2017]. More generally, Car *et al.* showed that it is possible to obtain single crystalline nanowire meshes (NW-M) [Car *et al.* 2014]. These NW-M, in 2D or 3D, are also known to have a low thermal conductivity compared to bulk material [Ma *et al.* 2016, Verdier *et al.* 2018c]. Finally, a crystalline/amorphous nanocomposite is comparable to nanocrystalline materials. For these materials, studies exist about the transmission of phonons, across a single interface [Kimmer *et al.* 2007] or across multiple grain boundaries [Yang & Minnich 2017]. The grain-size and grain-size distribution also impacts the transport [Hori *et al.* 2015].

The purpose of the following section is to explore the effect of the gradual interconnection of crystalline inclusions on the thermal conductivity and ballistic transport. To this end, several structures are studied, using EMD to compute their thermal conductivity and wave-packet propagation method to distinguish the propagative and diffusive contributions. After a description of the configurations, the qualitative impact of the inclusions on energy propagation at different frequencies will be considered, then the vibrational properties of the different configurations will be studied. These properties are used to estimate the thermal conductivity, via the kinetic theory of gases framework, and finally this thermal conductivity will be compared to the results obtained with the EMD methodology. Finally, the impact

of ballistic transport and nanoinclusions interconnection on the effective thermal conductivity are discussed.

2.4.1 Modeling of the Configurations

The nanocomposites studied here are composed of crystalline Si inclusions embedded in an amorphous Si matrix. The nanoinclusion shapes and interconnections are varied to study their impact on the effective thermal conductivity and on the ballistic transport. The incluisions are gradually interconnected, from an array of spheres to a 3D nanowire mesh. The host matrix is an amorphous Si cube of side 11.9 nm containing 84×10^3 atoms cut out of the same sample as in section 2.3. The length of the box is adapted to get an integer number of crystalline primitive cells and thus a monocrystal in case of structural percolation of the crystalline phase. Periodic boundary conditions are used in all directions.

The nanocomposites are formed in the following manner: the NI shape is first hollowed out of the matrix, and then filled by crystalline Si (c-Si). The added crystal has the $\langle 100 \rangle$ direction aligned with the x axis.

For the SC configuration, the central sphere has a radius of 4.6 nm and the added cones have an opening angle of 40°. The apex of the cones are 0.3 nm away from the simulation box edges, and the basis of the cones are prolonged until it intersects with the central sphere. This results in a neck of 0.6 nm between two inclusions. For the STC configuration, the cones have a radius of 1 nm at their junction with the box boundary and are prolonged with an opening angle of 34° until the intersection with the central sphere of radius 3.7 nm. Thus, only the STC and the NW-M have a continuous crystalline path across their simulation box, this continuous crystalline path across the structure will be referred to as crystalline structural percolation. This structural percolation has a minimum diameter of 2 nm for the STC and of 5 nm for the NW-M. Additionally, a porous sample, with spherical pores of the same diameter as the spherical inclusion (see table 2.3 first column), and a fully amorphous sample are also studied for the sake of comparison. The porous configuration contains 58×10^3 atom. In table 2.3, the different NIs are represented in 3D in the first row and in the second row a cross-section at the middle of the corresponding nanocomposite are depicted.

After the geometrical construction, the different configurations are annealed in the following manner. The atomic positions are relaxed using a conjugated gradient (CG) method, then the system is annealed at 100 K for 1 ps and finally a second conjugated gradient force minimization is performed[5].

In this section, a modified Stillinger-Weber potential [Vink *et al.* 2001] was used for its more realistic modeling of the interfaces between c-Si and a-

[5] At this point, it can be mentioned that the relaxation induces small reconfigurations at the surface of the NIs. This interfacial reconfiguration causes a reduction of up to 3 % of the crystalline fraction and can change slightly the surface to volume ratio of the NIs. To take this into account, when computing the surface to volume ratio, only the particles recognized as diamond structure and first and second neighbors by a modified common neighbor analysis [Maras *et al.* 2016] are considered.

Table 2.3: Freestanding nanoparticles (first row) and a cross-section of nanoinclusions embedded in an a-Si matrix (in blue) cross-section (second row).

Pore	Sphere	SC	STC	NW-M
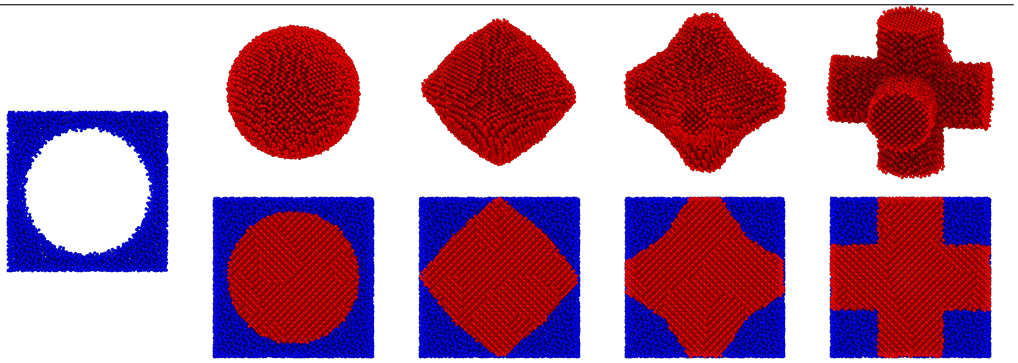				

Si in terms of interfacial energy and of atomic energies inside the two phases [France-Lanord *et al.* 2014b] (see section 3.1.1 for a discussion of the interfacial energy).

2.4.2 Ballisticity through Wave-Packet Simulations

To study the properties of the nanocomposites, wave-packet simulations as described in the section 1.5.3 are performed. The excitation is the one described by the equation (1.47), similarly to section 2.3 in the center of the configuration between the inclusions. The force amplitude chosen is $3.773 \times 10^{-4}\,\mathrm{eV\,\AA^{-1}}$.

A qualitative analysis of the time evolution of the kinetic energy distribution can give physical insights about the impact of nanostructuring on energy propagation. Figure 2.20 shows the atomic kinetic energy on a cross-section for the different configurations after a 2 THz excitation (corresponding to the mixed regime discussed earlier). The excitation is made in the middle of the system and propagates in both the negative and positive x directions. The two directions being symmetric, only one direction (x positive) is represented. This kind of representation is used here as it gives a better visualization of the spatial distribution of energy than the heatmaps of the previous sections. The first half of the table corresponds to the longitudinal polarization. The main observation for most configurations, is that most of the energy travels through the sample as a plane wave. The nanoinclusions do not strongly affect the propagation at this frequency: the wave-packet travels through the nanocomposites and the a-Si similarly. However, there is still some scattering visible through the small spots of high energy concentration after the passage of the wave-packet. These spots are mainly located in a-Si and at the interfaces between inclusions and matrix. This matches closely what was visible for homogeneous stiffness inclusions in section 2.3. For the porous configuration a plane wave is also visible, albeit, its intensity is strongly reduced by the time it reaches the end of the simulation box. But more importantly, most of the energy stays in the center and

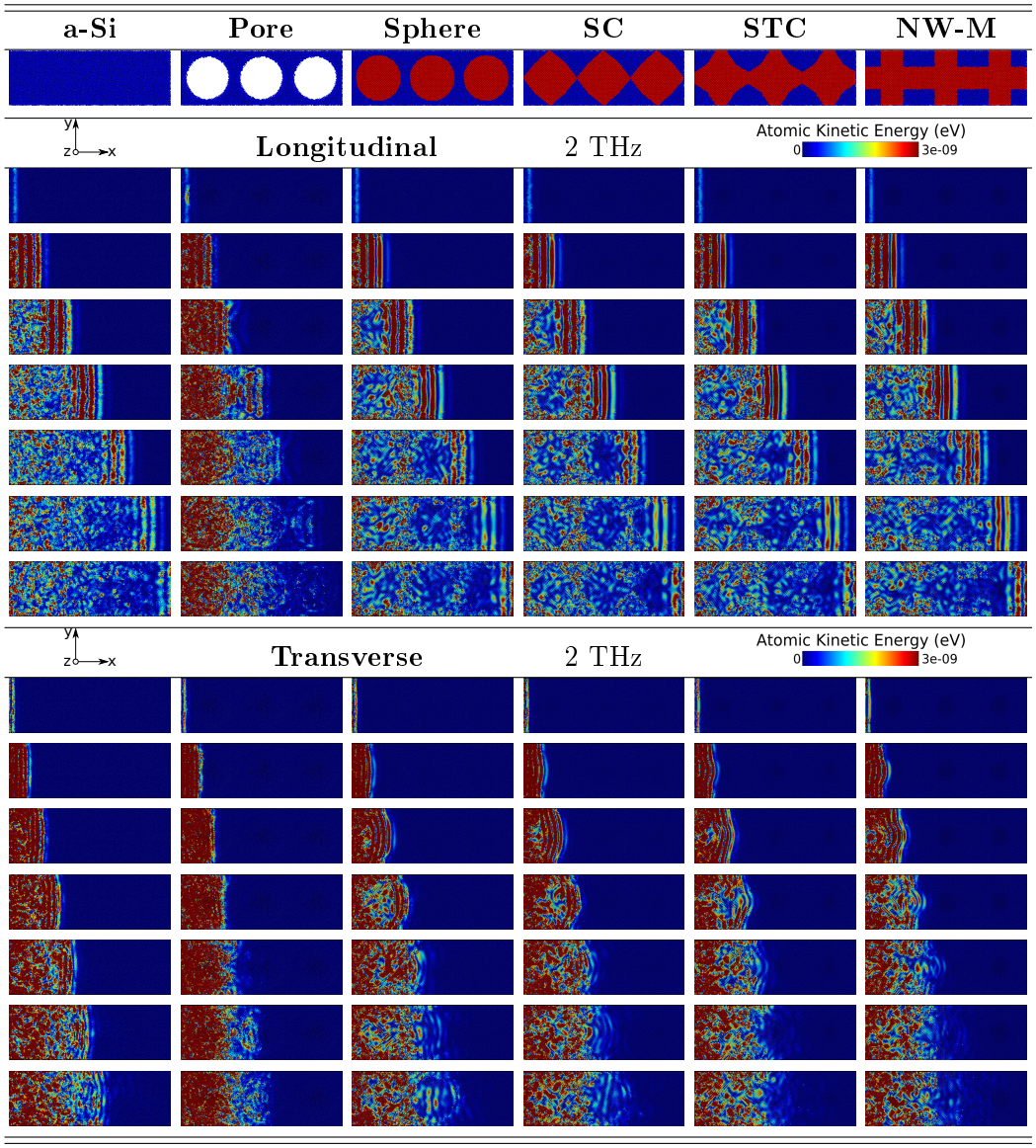

Figure 2.20: Cross-sectional view of a wave-packet going through the different systems after a longitudinal excitation at 2 THz (first part of the table) or a transverse excitation at the same frequency (second part of the table) every .9 ps. The first line represents the geometry of the cross-sections at the middle of the simulation box, with inclusions in red and matrix in blue, note that for the porous configuration a slice is shown, whereas below a cross-section (with the bottom) is used. The color scale going from 0 (blue) to 3×10^{-9} eV (dark red) gives the atomic kinetic energy.

slowly diffuses through the sample. One can note that no reflection is visible for any configuration, thus the wave propagating in the right does not affect the wave on the left and vice versa.

For the transverse waves at the same frequency (displayed in the second half of figure 2.20), the dispersion is more marked. The vertical red lines, characteristic

of plane waves, can be distinguished in the first few images, but disappear before reaching the simulation box boundary. The waves are quickly scattered, and this even for bulk a-Si. In the configurations containing NIs, the vertical lines materializing the plane waves are distorted. This distortion of the wave-front is due to the wave-packet traveling faster in the crystal than in the glass matrix. The porous configuration is, again, the configuration for which the scattering is the strongest.

To sum up about the low frequency wave-packet propagation, one can observe that the shape of the inclusions has no impact on either the longitudinal or transverse waves. The longitudinal plane waves preserve their shape for both interconnected and not interconnected inclusions, and the transverse waves are diffused quickly. The situation is quite different for the nanoporous amorphous silicon, for which the plane waves disappear rapidly for both polarizations. This stresses the fact that an amorphous/crystalline nanocomposite could be "transparent" for low frequency longitudinal waves.

The behavior of the nanocomposites after a high frequency excitation is displayed in figure 2.21. The first part contains the evolution of a longitudinal wave-packet at 10 THz or two thirds of the maximum frequency for which a group velocity can be defined. It appears that there is no propagation in the amorphous matrix. For all configurations, the energy slowly spreads through the amorphous matrix.

However, on top of this diffusion, a propagative behavior[6] limited to the crystal also appears. This is particularly noticeable in case of structural percolation. In this case, the wave-packet takes an oval shape and travels through the structural percolation. In absence of percolation, the propagative part of the wave-packet is scattered at the first crystalline/amorphous interface. Interestingly, no energy appears to be trapped in the perpendicular branches of the percolating configuration, this probably linked to the excitation propagating exactly perpendicular to it.

For the transverse polarization, the selected frequency is 4 THz. As for the longitudinal polarization, this frequency corresponds approximately to two thirds of the frequency for which the group velocity becomes ill-defined (see figure 2.23). The behavior is very similar to the longitudinal polarization: there is ballistic (or propagative) transport limited to the structural percolation region and a diffusive transport acting on a slower timescale. This diffusive behavior is visible close to the left of the images, where the excitation is made. However, in this case, both the crystalline inclusions and the amorphous matrix participate in diffusive energy transport. Diffusive energy transport is not restricted to the amorphous phase, but surprisingly, it spreads as well in the crystalline phase.

[6] That is energy leaves the excited zone rather than slowly spreading.

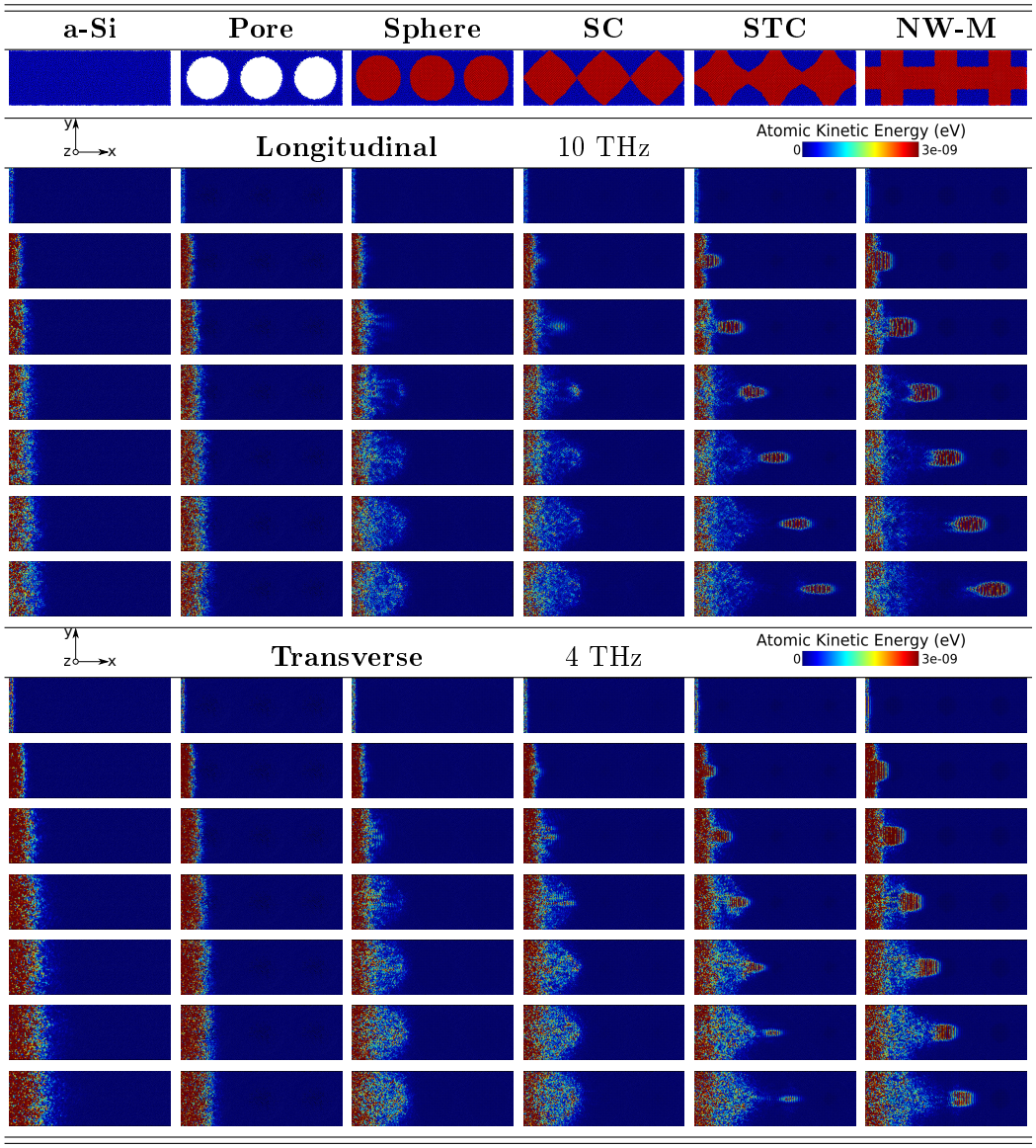

Figure 2.21: Cross-sectional view of a WP going through the different systems after a longitudinal excitation at 10 THz (first part of the table) or a transverse excitation at 4 THz (second part of the table) every .9 ps. The first line represents the geometry of the cross-sections at the middle of the simulation box, with inclusions in red and matrix in blue, note that for the porous configuration a slice is shown, whereas below a cross-section (with the bottom) is used. The color scale going from 0 (blue) to 3×10^{-9} eV (dark red) gives the atomic kinetic energy.

To sum up, concerning the WP propagation at high frequencies, there is a clear differentiation of the crystalline and amorphous phases. There is no ballistic propagation in the amorphous phase. Ballistic transport through the sample

is only possible in the crystalline phase through the structural percolation. We also observe that there is no backscattering nor important deviation of energy in the perpendicular branches of the interconnected inclusions.

2.4.3 Diffusive and Propagative Contributions to the Thermal Conductivity

As described in section 1.6.4, the thermal conductivity can be estimated through the information extracted from the wave-packet propagation simulations. First, the method used for the estimation of the MFPs must be detailed. They are estimated from the decay rate of the envelope of the wave-packet as a function of the distance to the excited slice, as described in section 1.5.3. However, due to the presence of the inclusions, the envelope may contain plateaus and sharp decreases (see figure 2.22), thus to get a meaningful value of the exponential decay fit, the portion on which the least square fit is made has to be chosen appropriately. Moreover, as visible in figure 2.22 in the vicinity of the excited slice a diffusive part is visible, this part is not included in the MFP computation. The propagation taking place in both x positive and x negative directions, the final value of the decay rate is the average between the two. For the configurations without structural percolation, the MFP is estimated through the penetration length for frequencies above 12 THz for the longitudinal excitation. For the transverse excitation, the MFP is substituted above 7 THz by the penetration length for all the configurations in order to avoid artifacts caused by a strong scattering.

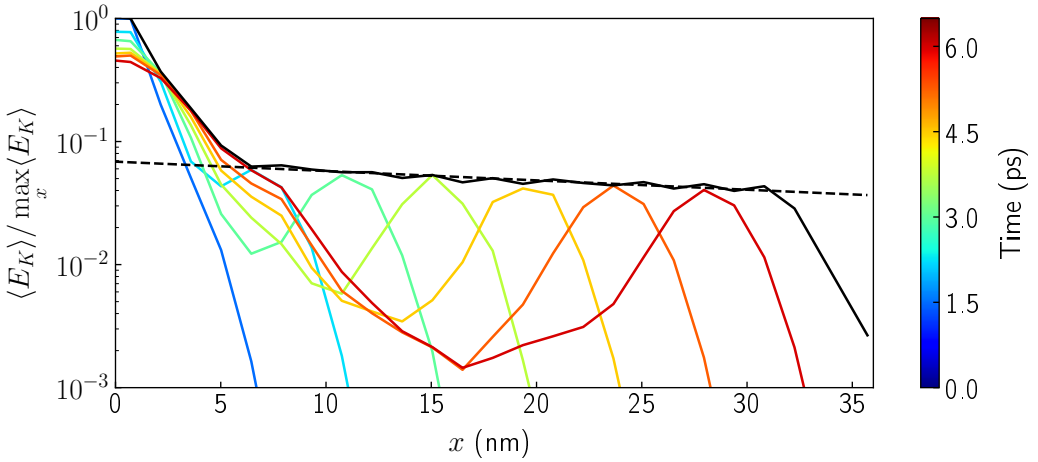

Figure 2.22: Representation of the propagation of an 10 THz longitudinal excitation in the NW-M, with the energy distribution at different time steps (colored lines), the envelope defined as the maximal value of the kinetic energy at a given position (black solid line) and the exponential fit used to compute the MFP (dashed black line).

First, the different components of the propagative contribution to the thermal

conductivity (κ_P), as defined by equation (1.56), are displayed in figure 2.23. In the top left panel, the MFPs of the longitudinal WP for the different configurations are given as a function of the frequency. These curves confirm what was visible in figure 2.20: the MFP is high at low frequencies for all configurations. Below 5 THz, the MFP of the non-porous configuration are very similar. Only the pores decrease the MFP at low frequencies. This confirms the observations of section 2.3: without strong impedance mismatch, the inclusions do not impact the MFP at low frequencies. At higher frequencies, the configurations without structural percolation have a low MFP. This contrasts with the configurations with structural percolation, for which the MFP rises between 5 and 10 THz and decreases strongly after that. The MFP for those configurations, around its maximum between 8 and 12 THz, is almost one order of magnitude higher than without percolation. Moreover, the interconnection degree has an influence. The MFP is higher for the NW-M than for the STC. Moreover, contrary to the results displayed in figure 2.18, for a nanocomposite with a similar volume fraction but a smaller inclusion diameter, the MFP of non-percolating nanocomposite is higher than the amorphous one above 4 THz. However, the difference is small, and may be explained by the larger size of the inclusions of this section. Similarly to what was observed in the previous section 2.3, the porous and fully amorphous configurations have a small MFP peak around 8 THz.

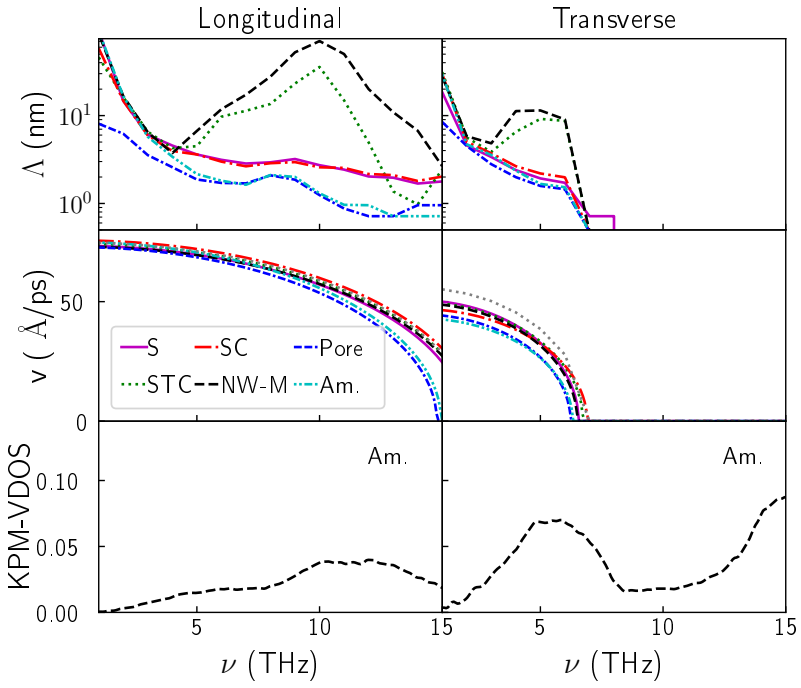

Figure 2.23: From top to bottom: first row longitudinal and transverse mean free path, second longitudinal and transverse group velocity for the studied configurations, third row longitudinal and transverse VDOS of amorphous silicon. Additionally, the group velocity computed for a fully crystal line sample is displayed with a dotted gray line.

For the transverse polarization, in the top right panel of figure 2.23 the behavior is similar. As for the longitudinal polarization, the MFPs of the configurations with a structural percolation have a maximum. In this case, the maximum lays between 5-6 THz. Without a structural percolation, the MFP decreases as the frequency increases. Again, similarly to the longitudinal polarization, most configurations share a very similar MFP at 1 THz, the only exception being the porous configuration, that has a lower MFP.

The group velocities for the longitudinal and transverse polarizations are displayed in the second row of figure 2.23. It is estimated with the method described in section 1.5.2. All the configurations share a very similar group velocity. This is especially true for the longitudinal polarization at low frequencies (below 5 THz). At higher frequencies, the group velocities for the amorphous and porous configurations are lower than the group velocities of the others. The v_g of the configurations containing crystalline inclusions are very similar to the v_g of c-Si. For the transverse polarization, there is also a group velocity difference, although spanning over the whole spectrum. For this polarization, the v_g of the nanocomposites containing inclusions lays in between those of c-Si and a-Si. Finally, the transverse polarization has a null velocity for frequencies higher than 7 THz.

The third row from the top contains the VDOS attributed to the longitudinal and transverse polarizations for the computation of κ_P. For this application, the transverse and longitudinal VDOS used, are the one computed via the KPM method [Beltukov *et al.* 2015] on an a-Si sample. This allows for a good approximation in the 0-12 THz frequency range (see appendix A.4 for more details). On these graphs, it can be noted that the maxima of VDOS at 10 THz for the longitudinal polarization and at 5 THz for the transverse also correspond to MFP maxima. Due to the higher lifetime conjunct with a high VDOS, these modes will contribute significantly to κ_P.

The different terms participating to the diffusive contribution to thermal conductivity κ_D, as defined by equation (1.57), are shown in figure 2.24. The top panel corresponds to the diffusivity computed with equation (1.49). Two main observations can be made: firstly all the configurations containing a crystalline phase share a very similar diffusivity across the whole spectrum, secondly only the porous configuration induces a reduction of diffusivity with respect to the amorphous sample. Here, the addition of crystalline nanoinclusions increases the diffusivity. The VDOS computed through the VACF for the different configurations are displayed in the bottom panel of figure 2.24. All the VDOS are very similar up to 14 THz. At higher frequencies, the configurations containing NIs and the others show differences. The VDOS of a-Si starts to decrease from 14 THz while the others continue to increase. However, this difference has little effect on the κ_D given that the diffusivity is very low at those frequencies.

The different terms displayed in figures 2.23 and 2.24 are used to compute κ_P and κ_D through equation [1.18] and [1.19]. The results for temperatures between 10 and 400 K are shown in figure 2.25. The first column contains the transverse (κ_T) and longitudinal (κ_L) propagative contributions. It confirms that the structural

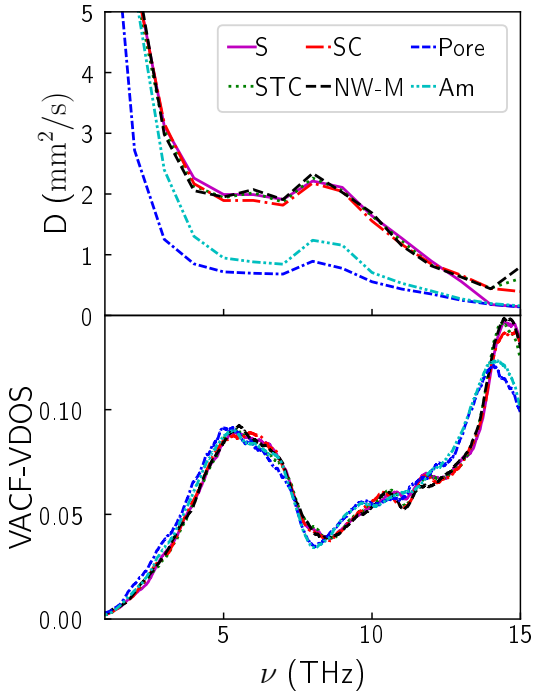

Figure 2.24: Diffusivity and VDOS as a function of frequency for the studied configurations.

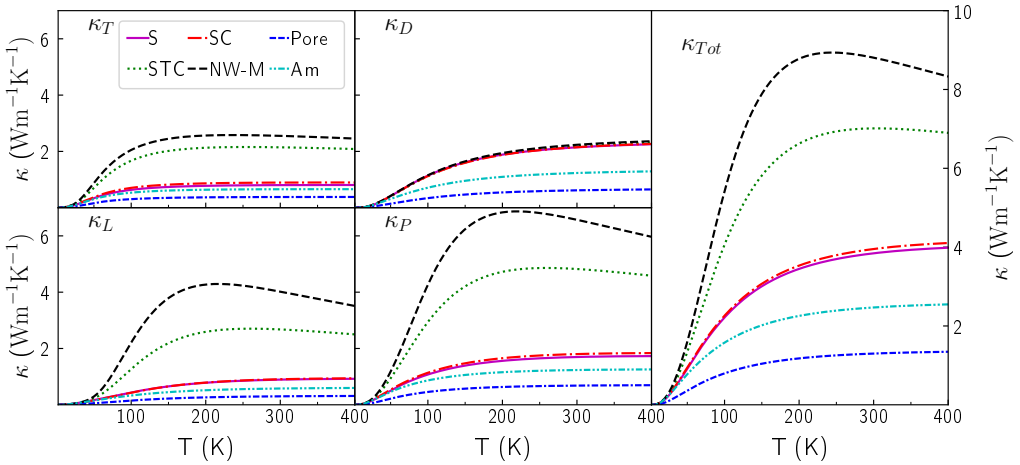

Figure 2.25: Different contributions to the thermal conductivity, the first column contains the contributions of the longitudinal phonons κ_L (bottom) and the transverse phonons κ_T (top), the second column the diffusive contribution κ_D (top) and the overall propagative contribution $\kappa_P = \kappa_L + \kappa_T$ (bottom), the last column contains the sum of the different contribution $\kappa_{Tot} = \kappa_P + \kappa_D$.

percolation induces a marked increase in the propagative contribution: the STC and NW-M have a larger κ_T and κ_L. However, for the diffusive contribution in the top row of the central column, no distinction between the configurations containing

NIs can be made. In this set of configurations, only the pores seem to decrease the diffusive contribution below amorphous values. The propagative contributions, for both polarizations, increase with the degree of interconnection. When looking at the propagative contributions as a function of the temperature, it appears that κ_L increases at higher temperature than κ_T. This is linked to the MFP peak at 10 THz and to $C(T,\omega)$ that limits the impact of high frequencies at low temperature. This important high frequency contribution also results in a maximum of κ_L around 200 K for the NW-M. This is due to the empirically added phonon-phonon term (equation [1.60]) that reduces the contribution of high frequency phonons as the temperature rises. The different contributions (propagative and diffusive) can be compared in the central panel. The diffusive and propagative contributions for the non-percolating configurations have similar values at 300 K.

The sum of the different contributions, κ_{Tot}, is displayed in the last column of figure 2.25. At all temperatures, the same order of κ_{Tot} is preserved. This order is, from the highest to the lowest thermal conductivity, the NW-M, the STC, the SC and the S at very similar values, the amorphous, and finally the porous configuration. The maximum observed for κ_L of the NW-M is still visible on the sum and happens at 244 K. It is due to anharmonic effects (see equation [1.60]).

The different contributions to the thermal conductivity at 300 K are also shown in figure 2.26. With this representation, it appears clearly that: the structural percolation increases κ_P and does not affect κ_D. As a result, the propagative part represents up to 75 % of κ_{Tot} for those nanocomposites. This figure also shows that the addition of non-percolating NIs in an amorphous matrix increases more the diffusive than the propagative transport. For the S and SC configurations, the diffusive transport is dominant. Finally, it appears that despite the overestimation of the thermal conductivity of nanocomposites containing NIs by the kinetic method compared to the results of EMD, the hierarchy in the different structures is preserved. The discrepencies between the methods will be discussed in the following of the chapter (see section 2.4.5)

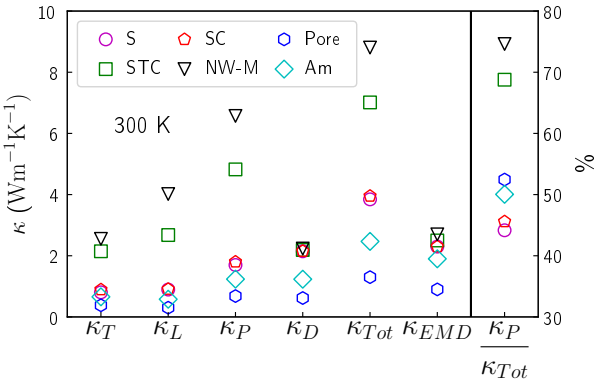

Figure 2.26: Thermal conductivities at 300 K, decomposed through equations (1.56) and (1.57) and computed with EMD. The proportional contribution to the thermal conductivity of the propagative mode is also represented in the right part of the figure (right axis).

To sum up briefly on the results obtained with the kinetic theory, it appears that as predicted previously, the addition of NIs increases κ above bulk a-Si values [Tlili *et al.* 2019]. The crystalline NIs increase the overall thermal conductivity. This is particularly visible in the case of structural percolation, where the MFP peak at high frequencies is concomitant to a VDOS peak, resulting in a large increase of κ_P. This increase occurs mainly at high temperatures (see figure 2.25) due to the temperature dependent frequency weighting of $C(\nu, T)$ (see equation [1.58]). As high frequencies at high temperatures are also more impacted by the phonon-phonon term (equation [1.60]), a maximum of $\kappa_{Tot}(T)$ appears for the NW-M. This maximum contrasts with experimental results for single nanowires of diameter similar to the NW constituting the NW-M. For these single NWs, no maximum of the thermal conductivity has been observed as a function of temperature [Li *et al.* 2003a]. This is a first sign that the propagative contribution, the only which can cause the apparition of a maximum of κ, is overestimated by this implementation of kinetic theory. Moreover, κ_P dominates at these temperatures, contrasting with the predictions of Cahill *et al.* [Cahill & Pohl 1988].

2.4.4 Global Estimation of the Thermal Conductivity

The thermal conductivity can also be estimated from the Green-Kubo relation (equation [1.52]). For this, the following process is performed on one inclusion in the amorphous cube, as represented in the bottom row of table 2.3. They are first heated at 50 K, using a random initial velocity distribution. Subsequently, the temperature is increased from 50 to 600 K at constant pressure in 0.05 ns, that is 1×10^5 time steps. Then the system is annealed at 600 K with a Nosé Hoover thermostat for 0.25 ns (5×10^5 time steps) to ensure better temporal stability. This annealing does not impact the radial distribution function at 300 K, confirming that there is no recrystallization. After this, the temperature is decreased to 300 K at constant pressure in 0.05 ps (1×10^5 time steps) and then equilibrated at 300 K for 1 ns (2×10^7 time steps). The flux auto-correlation function is finally measured during 10 ns (2×10^8 time steps) in a constant energy simulation, using a velocity Verlet integration scheme. For all the simulations, a time step of 0.5 fs is used. For the computation of the auto-correlation, the flux is sampled every 10 fs and the flux auto-correlation decay is computed over 20 ps. These simulations are repeated 5 times, with a different set of initial velocities for each repetition, to get better statistics. The final value is the mean κ across the simulations, and the uncertainty range is defined by the highest and lowest values of the individual runs.

The κ computed for bulk a-Si through EMD is $1.9\,\mathrm{W\,m^{-1}\,K^{-1}}$ which is close to previously reported values [Lv & Henry 2016, Larkin & McGaughey 2014]. The nanoporous a-Si has a sub-amorphous κ due to the additional scattering at the surface of the pores. When the pores are filled with crystalline NIs, the κ is increased

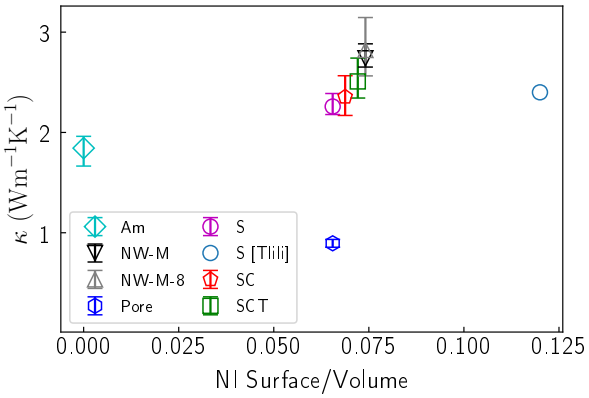

Figure 2.27: Thermal conductivity estimated with EMD for the studied configurations, as a function of their surface to volume ratios. S [Tlili] refers to results of Tlili *et al.* [Tlili *et al.* 2019] with the same crystalline volume fraction and NW-M-8 refers to a cube constituted by a 2x2x2 grid of the configuration NW-M.

by a factor 2.5 to 3 compared to the porous κ and a factor 1.2 to 1.5 compared to a-Si.

The results of the EMD computations are compared to κ_{Tot} obtained in the previous section in table 2.4. As visible in figure 2.26, even if the thermal conductivity predicted by equations (1.56) and (1.57) are higher, both methods predict the same hierarchy of κ. The difference of prediction between the two methods is more pronounced for the configurations containing NIs and even more if there is a structural percolation. The last row of the table shows the results for the estimation via the kinetic theory if $\tau_{phonon-phonon}$ is neglected. It appears that the reduction of thermal conductivity induced by this term is marked only for the configurations with a crystalline continuity.

Table 2.4: Thermal conductivity in $\mathrm{W\,m^{-1}\,K^{-1}}$ at 300 K for the different configurations, computed with EMD, or estimated with equations (1.56) and (1.57).

	Am	**Pore**	**S**	**SC**	**STC**	**NW-M**
EMD	1.9(2)	0.89(4)	2.3(1)	2.3(2)	2.5(2)	2.7(1)
WP w τ_{ph-ph}	2.5	1.3	4.0	4.1	7.2	8.9
WP w/o τ_{ph-ph}	2.6	1.3	4.1	4.2	8.7	14.0

To conclude on the EMD computations, all configurations containing crystalline nano inclusions have a κ between 2.3 and 2.7 $\mathrm{W\,m^{-1}\,K^{-1}}$ (see table 2.4). The nanowire mesh is the only configuration that has a distinctively higher κ than the nanocomposites with non-percolating spherical inclusions. Its thermal conductivity is 20 % higher than the one of the nanocomposite with a spherical inclusion. The values obtained with EMD are notably lower than the values ob-

tained with equations (1.56) and (1.57), but they both give the same hierarchy of thermal conductivity of the different configurations.

Nakamura *et al.* obtained experimentally a thermal conductivity between 1.7 and 1.9 $\mathrm{W\,m^{-1}\,K^{-1}}$ for Si nanocrystallite of similar size in a-SiO_2 [Nakamura *et al.* 2015]. The difference probably comes from the a-SiO_2 having a lower κ than a-Si. Moreover, counter-intuitively, when going from the spherical inclusions to the nanowire mesh, κ seems to increase with the surface to volume ratio. However, usually, an increased density of interfaces leads to a reduction of κ [Minnich & Chen 2007]. The increased surface to volume ratio is here a consequence of the gradual interconnection of the nanoinclusions: as the shape shifts from a sphere to a NW-M the surface to volume ratio indeed increases. In the present case, the interconnection has probably a stronger effect on κ than the surface to volume ratio. In addition, a similar thermal conductivity has been found before for smaller particles having a higher surface to volume ratio but sharing the same volume fraction than the nano-spheres [Tlili *et al.* 2019]. This means that the surface to volume ratio has little effect on crystalline Si nano inclusions in a-Si matrix. This lack of impact of the surface to volume ratio contrasts with the results obtained for GaN NIs in SiO_2 [Termentzidis *et al.* 2018a]. The origin of this difference may be found in the impedance mismatch between GaN and SiO_2.

Furthermore, the κ of a-Si estimated here is consistent with previous results obtained with a similar method [Lv & Henry 2016] and with experimental results [Cahill *et al.* 1994]. Porous a-Si is less studied, nevertheless, the results can be compared with results obtained on porous c-Si amorphized by irradiation [Isaiev *et al.* 2014, Massoud *et al.* 2020]. The experimental results range between 3 and 1.8 $\mathrm{W\,m^{-1}\,K^{-1}}$, thus higher than the 0.89 $\mathrm{W\,m^{-1}\,K^{-1}}$ obtained here. This difference can have multiple origins, two of which are important: the shape of the pores and the presence of gas (humid air) in the pores in the experimental set up. The results for the NW-M can be compared to a similar study of a free standing nanowire meshes [Verdier *et al.* 2018c]. They have found a lower thermal conductivity (0.5 $\mathrm{W\,m^{-1}\,K^{-1}}$) for NWs of similar cross section. However, a direct comparison is harder to make, the geometry (shape of the cross section and distance between crossings) being different. Given that the thermal conductivity of porous a-Si and of the NIs alone are known [Fang *et al.* 2006], it is tempting predicting κ in the corresponding nanocomposite; however, a simple sum of the two thermal conductivities does not predict the correct thermal conductivity. Moreover, even an effective medium approach based on a mixing rule between the NIs and the matrix κ is not able to predict the correct thermal conductivity. A more complex model, such as the one presented by Wang et al. [Wang & Pan 2008], may be able to predict the thermal conductivity. However, as the authors point out, the effective model approach often fails to predict the properties at the nanoscale.

2.4.5 Discussions

Previous analyses of the impact of NIs in amorphous matrices on the vibrational and thermal properties of nanocomposites via MD have focused on the intrinsic properties of spherical NIs and on their role as scatterers [Tlili *et al.* 2019, Termentzidis *et al.* 2018a, Luo *et al.* 2019]. The influence of their shape and eventual interconnection are rarely the center of attention, here their role on the effective thermal conductivity and on the ballistic transport are explored.

Thermal conductivity The gradual interconnection/structural percolation between the NIs increases the effective thermal conductivity of the studied nanocomposites. This enhancement is due to an increase of the propagative part. The diffusive part (κ_D) on the contrary is not affected by the shape of the inclusions nor by the structural percolation. It can, however, be noted that κ_D is increased by the introduction of NIs. The only way to decrease the diffusivity below amorphous values seem to introduce pores as proposed here or softer inclusion as proposed in section 2.3. Finally, it was shown that the two methods used to evaluate κ conserve the same hierarchy between the inclusions.

Having estimated thermal conductivity through two methods (the wave-packet method and the EMD simulation), the respective results can be compared. Firstly, it appears that the two methods give different results. Equations (1.56) and (1.57) of the wave-packet method overestimate the thermal conductivity of all configurations compared to the EMD method, and particularly in case of structural percolation that makes the thermal response very inhomogeneous. It also does not take properly into account the possible thermal sensitivity of the MFP as the wave-packet are performed at low temperature. Secondly, in opposite, the EMD simulations might not capture all the effects induced by the NIs. Additional Non Equilibrium Molecular Dynamics (NEMD) [Schelling *et al.* 2002a] simulations containing multiple NIs could be interesting to perform. In the case of structural percolation, the heat flux will likely concentrate in the crystalline percolation and the effect of this concentration maybe lost in the flux auto-correlation over the whole sample that is used to compute κ with the EMD method.

However, the discrepancies between the values of both models also question the quantitative accurateness of the computation of κ with the kinetic theory. The robustness of the method, in particular for nanocomposites, is not established. To carry out the computations, multiple assumptions are made. These different assumptions will be reviewed later in this section.

Ballistic and Diffusive Transport Concerning ballistic transport, the behavior at high and low frequencies must be distinguished. At low frequencies for the longitudinal polarization, no distinction can be made between the different nanocomposites containing NIs. The WP travels through NIs and matrix alike. At higher frequencies, the waves are strongly attenuated in the amorphous matrix and ballistic transport is possible through the structural percolation only.

At low frequencies, ballistic transport was expected in the amorphous matrix [Beltukov *et al.* 2018]. Moreover, at these frequencies there is no impedance mismatch: the group velocity in a-Si and c-Si are similar (as can be seen when comparing the $v_L(\nu)$ between a-Si and c-Si in the central panel of figure 2.23). The long MFP at low frequencies for a-Si/c-Si nanocomposite is consistent with results obtained with finite elements simulations [Luo *et al.* 2019]. Moreover, the transmission rate through a a-Si/c-Si interface is known to be high[7] for a single interface and for grain boundaries in nanocrystalline Si [Yang *et al.* 2017a, Yang *et al.* 2018]. The combination of a high MFP in the matrix, a lack of an impedance mismatch and a good transmission through the interface results in a reduced impact of the NIs on the MFP at low frequencies for longitudinal polarization. For the transverse polarization, still at low frequencies, the MFP is similar for all the configurations, excepted for the porous one. This similarity happens in spite of the acoustic mismatch between matrix and NI (materialized by the group velocity difference visible in figure 2.23) and the stronger scattering observed in figure 2.20. The latter indicates that ballistic transport at those frequencies is dominated by the matrix and that the inclusions have little effect despite the distortion of the wave front. To conclude on this point, the most effective way to decrease the transmission of low frequency WP relative to bulk a-Si in these nanocomposites is to introduce pores.

While only few differences appear between the configurations at low frequencies, at high frequencies strong disparities between the nanocomposites become clear. At high frequencies the MFP in a-Si is small [Beltukov *et al.* 2018] and there is an impedance mismatch between a-Si and c-Si for both polarizations (see central panel of figure 2.23). As a result, the WP is strongly attenuated in the matrix but travels well through the structural percolation at high frequencies. A similar behavior was observed for NWs with an amorphous shell (see chapter 3). Moreover, differences in MFP between the large inclusions of this section and the smaller inclusions of section 2.3 arise from 4 THz: the MFP is higher when the inclusions are larger. This can be understood as the effect of the high interface density. However, it is also important to note that the MFP is each time of the same order than the inclusions and that the difference in MFP is of 4 nm at most. This difference might thus not be significant.

Interestingly, if the MFP is affected by the shape of the inclusions, the diffusivity is not. All the configurations with crystalline inclusions have a very similar diffusivity. This diffusivity is distinctively higher than the bulk a-Si one (see figure 2.24). The increase in diffusivity induced by the nanospheres is more marked for these 10 nm nanospheres than for the 5 nm nanospheres studied in section 2.3. Larger crystalline inclusions seem to increase the diffusivity, hinting that the diffusivity is decreased by the interface density. Finally, it appears clearly that the only methods to reduce the diffusivity are to introduce pores or softer inclusion.

[7] Above 80 % below 2 THz when computed via Atomic Green Function (AGF)

To sum up on the ballistic transport properties: nanoinclusions were already known to affect the transmission of phonons, for instance, small spherical NIs act as a low pass filter [Damart *et al.* 2015], and here it has been shown that if there is a structural percolation in the nanocomposite it can be used to let high frequency phonons go through the structure. This can happen thanks to the crystalline continuity at the nanoscale.

Discussion of the Hypotheses Equations (1.57) and (1.56) rely on different hypotheses. In the following paragraphs, the validity of these hypotheses along with the possible origins of the discrepancies between κ computed through those equations and through EMD will be reviewed.

First, both the diffusive and the propagative contributions are considered at all frequencies. In previous works the different contributions were separated either based on frequency ranges, or on the periodicity of the modes [DeAngelis *et al.* 2019]. Here, both contributions are included for all the frequencies considered. This is motivated by the fact that both a propagative and a diffusive part appear at all the observed frequencies for those configurations, especially in the mixed regime evidenced here (see figures 2.21 and 2.20). This contributes to the overestimation of the thermal conductivity by the model used here. Indeed, some modes are considered twice, once as diffusive and once as propagative. This is especially true in the low frequency range, where both MFP and diffusivity are high. In such a regime, the relative contributions of expressions (1.56) and (1.57) should be weighted by the relative amount of initial energy in it.

Secondly, the propagative contribution is also very likely overestimated. This overestimation already appears for the bulk a-Si for which the propagons are expected to contribute up to 40 % of κ [Larkin & McGaughey 2014] and the present model gives 50 %. This overestimation can be attributed to the lack of a cut-off frequency for the propagative contribution, as previously discussed. The effect is much more marked for the STC and NW-M nanocomposites, for those, only a small fraction of the system (restricted to the center of the crystalline part) takes part to the ballistic transport at high frequencies (see figure 2.22). The transport only happens in the structural percolation and not in the whole nanocomposite. A manifestation of this phenomenon also appears in figure 2.21, part of the energy is scattered, and a part of it travels ballistically. The diffusive behavior is visible through the gradual flattening of the central peak (0-10 nm). The propagative part appears as a lobe shifting through the sample. This lobe corresponds to the wave-packet travelling in the structural percolation. Yet, in equation (1.56), it is assumed that the whole configuration contributes to κ_P. This leads to an overestimation of κ_P, especially at high frequencies where non-propagating modes are considered in the VDOS but do not contribute to the ballistic transport. The group velocities are extracted from the fitting of the dispersion relations by a sine function, by doing so the eventual confinement effects are neglected. This confinement has been

predicted for free NW [Zou & Balandin 2001] and observed experimentally recently [Kargar *et al.* 2016]. Moreover, in the WP simulations the propagation direction is aligned with the structural percolation. This alignment decreases the interactions of the WP with the interfaces and with the branches perpendicular to the propagation at the crossings for the NW-M and STC. This may artificially increase the MFP measured by WP propagation. The boundary scattering is known to be the main factor limiting the thermal conductivity of NWs, a model has been developed to take it into account by considering a specularity parameter for reflection at the interface [Volz & Chen 1999]. It was even showed recently for argon NW that this specularity parameter has a stronger effect on the thermal conductivity than the confinement effect [Tretiakov & Hyżorek 2021]. Moreover, due to the geometry, boundary scattering impact might be even more important, especially in the case of the NW-M, where back scattering at intersections is expected to play an important role [Verdier *et al.* 2018c], whereas no impact of the intersection of the NW is visible in figure 2.21.

For comparison purposes, the MFP can also be estimated through the Dynamical Structure Factor thanks to the damped harmonic oscillator model (see appendix A.5). Yet, this method is known to give lower lifetimes than the estimation through WP amplitude decay rate [Beltukov *et al.* 2018]. Additionally, the DSF is an averaged quantity computed over the whole unit cells represented in table 2.3. Thus, it cannot take into account the longer MFP due to transport in the structural percolation. As a result, if the MFP computed through the DSF is used to estimate κ_P, the hierarchy of κ between the nanocomposites obtained with EMD is not reproduced. This underlines the necessity to use a spatially resolved method to compute the thermal conductivity in nanocomposite systems.

Finally, the hypothesis made on the effect of temperature are important. Namely, the MFP and the diffusivity are computed at 0 K, then for κ_P a phonon-phonon lifetime term is added to consider the thermal effects. This phonon-phonon scattering parameter is approximated thanks to empirical coefficients derived for bulk c-Si. These coefficients were already successfully used for NWs, albeit NWs with larger characteristic dimensions than the structures studied here [Yang & Dames 2013]. Alternatively, one may consider the expression derived by Klemens [Klemens 1958] for Umklapp processes. Moreover, the phonon-phonon scattering in amorphous materials is negligible. Its effect being small in front of the effect of disorder. Thus, the bulk c-Si scattering coefficients seem to be the best available. Nonetheless, these parameters might be impacted by interface and size effects. The diffusivity can also be influenced by the temperature. To avoid using a temperature correction coefficients, the wave-packet propagation simulations could be performed at higher temperature. However, at higher temperature, the amplitude of the excitation has to be increased to distinguish the wave-packet from the thermal agitation. This larger amplitude may induce other bias, as the overestimation of the effect of anharmonicity.

All those factors lead to an overestimation of the thermal conductivity computed through the kinetic theory and particularly of the propagative part. In future work, the estimation of the thermal conductivity using the kinetic theory could be

improved by including the effect of the reflection at the interface, for instance by introducing a specularity parameter [Volz & Chen 1999].

In brief, the quantitative estimation of the thermal conductivity via the vibrational properties (equations [1.57] and [1.56]) relies on strong assumptions and could be improved. The main possible improvements are: the weighting of the diffusive and propagative contributions depending on the frequency, the consideration of different orientations and a more precise consideration temperature effects.

2.4.6 Conclusion

The vibrational and thermal properties of gradually interconnected c-Si nanoinclusions in an a-Si matrix host matrix have been studied, with the goal of gaining a better understanding of the effects of a crystalline continuity at a constant crystalline volume fraction. WP simulations revealed that the structural percolation has a strong impact on the transmission of energy at high frequencies (8-12 THz), the MFP being increased by an order of magnitude in case of structural percolation. The interconnection also results in a thermal conductivity increase. This enhancement appears for the two methods used for the estimation of κ: WP propagation and EMD computations. However, the kinetic theory predicts a twofold increase of κ between the non-interconnected and the interconnected inclusions, while the EMD simulations predict a more modest increase of 20 %. More generally, the use of equations (1.56) and (1.57) seems to overestimate κ, especially its propagative part κ_P. This difference between the predictions of the two methods has multiple roots: the contribution of all frequencies to both κ_D and κ_P, the overestimation of the MFP due to the alignment of the wave-packet with the percolation and the incomplete consideration of temperature effects. This leads us to conclude that if a very strong increase in ballistic transport can be observed at high frequencies for percolating NIs it does not induce a marked absolute thermal conductivity increase. This kind of configurations could thus be used for applications where a low κ is needed while keeping the coherent transport of phonons at high frequencies. Such properties could be useful for information processing or phonons engineering in a structure.

2.5 From Nanoinclusion to Decorated Dislocation

Sections 2.1, 2.2 and 2.3 focused on the effect of NIs, viewed as volume defects, over the properties of nanocomposites, section 2.4 explored the effect of NI shapes and structural percolation. This section continues with the study of the impact of line defects on the propagation of heat, with the case of In decorated dislocation in GaN.

Dislocations represent a very common defect in crystalline materials, in particular in III-V semiconductors. Their role on elasticity and plasticity has been

widely studied [Hirth *et al.* 1983]. Their effect on the thermal conductivity have been considered since the early kinetic theory implementations [Klemens 1958, Carruthers 1961]. They are introduced as a supplementary scattering source, reducing the phonon lifetime. Their role is also considered in more modern implementations of the kinetic theory [Asen-Palmer *et al.* 1997]. For instance, phonon scattering by dislocations is non-negligible in Si and Ge [Asen-Palmer *et al.* 1997].

GaN nanodevices are used for many applications, such as field-effect transistor [Huang *et al.* 2002] or LASER [Gradečak *et al.* 2005]. These applications necessitate a control of the temperature, and in GaN crystal the high dislocation density strongly decreases the thermal conductivity [Mion *et al.* 2006]. This impact of the dislocation over the heat transport has already been studied, for bulk [Termentzidis *et al.* 2018b] or thin films [Zou *et al.* 2002] for instance.

Dislocations are often considered as line defects, nevertheless, they can also be used to tailor the properties of the material [Ikuhara 2009]. The strain field around them attracts the impurities, this attraction can create the so-called decorated dislocations, which are ultra thin embedded nanowires. Threading edge dislocations have, for example, been used to create conductive Al nanowires in GaN thin films [Amma *et al.* 2010]. The screw dislocations are less common in GaN but are also known to attract In atoms in $In_XGa_{1-X}N$ alloys [Horton *et al.* 2015].

It has been shown that $In_XGa_{1-X}N$ alloys can be used for thermoelectric generation with performances close to SiGe based alloys [Pantha *et al.* 2008]. It is, in particular, useful at high temperatures [Surender *et al.* 2018]. The thermal conductivity of those alloys have been shown to be affected by compositional inhomogenities [Tong *et al.* 2013]. Creating more scattering centers in the form of dislocations could further decrease the thermal conductivity and increase the figure of merit.

This section offers a study of the impact on phonon transport of the presence of decorated screw dislocations in $In_XGa_{1-X}N$. Two compositions, $X = 0.025$ and $X = 0.1$, are considered in four different configurations, to evaluate the anisotropy and compare the decorated dislocation with random alloys.

2.5.1 Modeling of the Configurations

The configurations studied in this section are the one created for publication of Giaremis *et al.* [Giaremis *et al.* 2020], a more detailed description can be found in the paper. Four different GaN wurztite configurations are studied, two with 4 screw dislocations with opposite signs, and two with randomly distributed In atoms. In each case, one configuration contains 1.25 % ($X = 0.025$) of In atoms and the other 5 % ($X = 0.1$) (see figure 2.28 a and b). The simulation boxes containing the dislocations are 5 by 9 by 5 nm rectangular cuboid containing 1.92×10^3 atoms. The dislocations are created using the displacement field described by linear elasticity theory [Hirth *et al.* 1983]:

$$u_x = \frac{b}{2\pi} \arctan \frac{x}{y}, \tag{2.1}$$

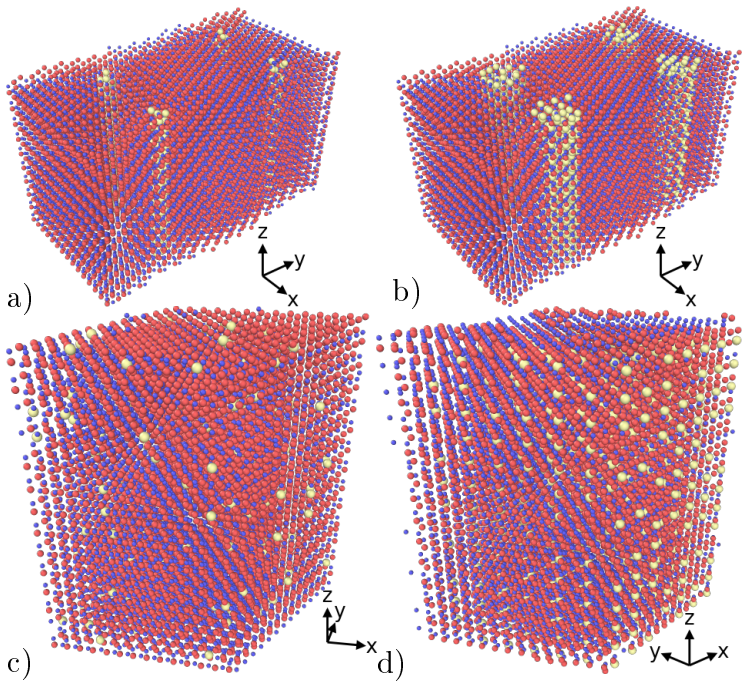

Figure 2.28: Different $In_XGa_{1-X}N$ alloys samples studied: 4 screw dislocations decorated with In atoms for X=0.025 (a) and X=0.1 (b), alloys with randomly distributed In atoms for X=0.025 (c) and X=0.1 (d). The Ga atoms are represented in red, the N atoms in blue and the In atoms in pale yellow.

with b the Burgers vector (displacement magnitude), x and y the cartesian coordinates. b is chosen to correspond to the lattice constant. The Burger vectors of the dislocations cancel each other by pair, so that periodic boundary conditions can be used. The resulting dislocation density is of $1 \times 10^{11}\text{cm}^{-2}$. Once created, the four dislocations are decorated with the heavier In atoms. To do so, the Ga atoms in the core and the neighborhood of the dislocations are substituted by In atoms. A sufficient number of atoms are replaced to reach 1.5 % or 5 % of In atoms.

The random alloys are modeled as right parallelogrammic prisms (4.5 by 3.9 by 8 nm) containing 11×10^3 atoms, in which some Ga atoms are replaced by In atoms in energetically favorable places [Giaremis *et al.* 2020] to reach the desired proportion of In atoms overall (see figure 2.28 c and d).

The configurations described are relaxed to reach mechanical equilibrium. For this, the atomic positions are relaxed using a conjugated gradient method and then a Hessian-free truncated Newton algorithm with a force criterion. The interatomic potential used for this study is a modified Stillinger-Weber (inter-atomic potential) (SW) [Lei *et al.* 2009].

2.5.2 Wave-Packet Propagation

The random alloys and decorated dislocations affect the thermal conductivity differently depending on the In concentration [Giaremis *et al.* 2020]. For instance, the temperature affects differently the configurations depending on the In fraction. The wave-packet propagation simulations provide a microscopic representation of the path and obstacle over energy propagation. This microscopic visualization can help interpret the variation of thermal conductivity in the different cases, by showing which configuration hinders the WP propagation.

The WP simulations are performed for different cases. A propagation parallel to the dislocation line, in which case the simulation box is repeated 15 times in the z direction (see the two first columns of figure 2.29), and for a propagation perpendicular to the dislocation line, in which case the configuration are repeated 18 times in the y direction (see the third and fourth columns of figure 2.29). The random alloys are repeated 15 times in the z direction (see the two last columns of figure 2.29). This creates configurations that are at least 70 nm long to study the decay rate of the envelope of the wave-packet.

The excitation is performed as described by the equation (1.47) in the center of the configuration. The force amplitude chosen is $3.773 \times 10^{-2}\text{eV Å}^{-1}$.

The propagation of the WP in the different configurations are depicted in the figure 2.29, two frequencies are selected, 3 and 6 THz. They correspond either to a frequency at which the MFP and propagation are similar in all the configuration (3 THz), or very different between them (6 THz) (see figure 2.30). For the propagation at 3 THz in the first half of the table, for all configurations, a bundle of plane waves (vertical lines) traveling through the configurations are visible. These lines are slightly distorted by the dislocations. For dislocations parallel to the propagation direction (in the first two columns) the perturbation is continuous: the energy density of the wave front is less intense in and around the dislocation core. However, if the dislocations are perpendicular to the propagation direction, the wave front recovers after crossing them.

It can also be noted that the energy tends to be trapped in the dislocation cores, as it was at interfaces in the previous section of this chapter. This might be enhanced by the impedance mismatch betwenn InN and GaN. This appears clearly for the propagation parallel to the dislocation, where red horizontal lines form after the passage of the WP, showing that energy is trapped in the dislocation. For propagation perpendicular to the dislocation, this is less apparent, and the energy seems to be scattered not only by the dislocations but also by the strain inhomogeneities between them. Indeed, "X" shaped red crosses appear after the passage of the WP, showing that some energy is trapped in these regions.

The only notable difference, induced by the different In content in the random alloys, is that the scattering seems stronger for larger X values. This could be expected due to the increased impurity density, that increases the alloy scattering.

At 6 THz, in the second part of the figure 2.29, the behavior is different. There is no propagation in the In rich region. Indeed, at this frequency there is no

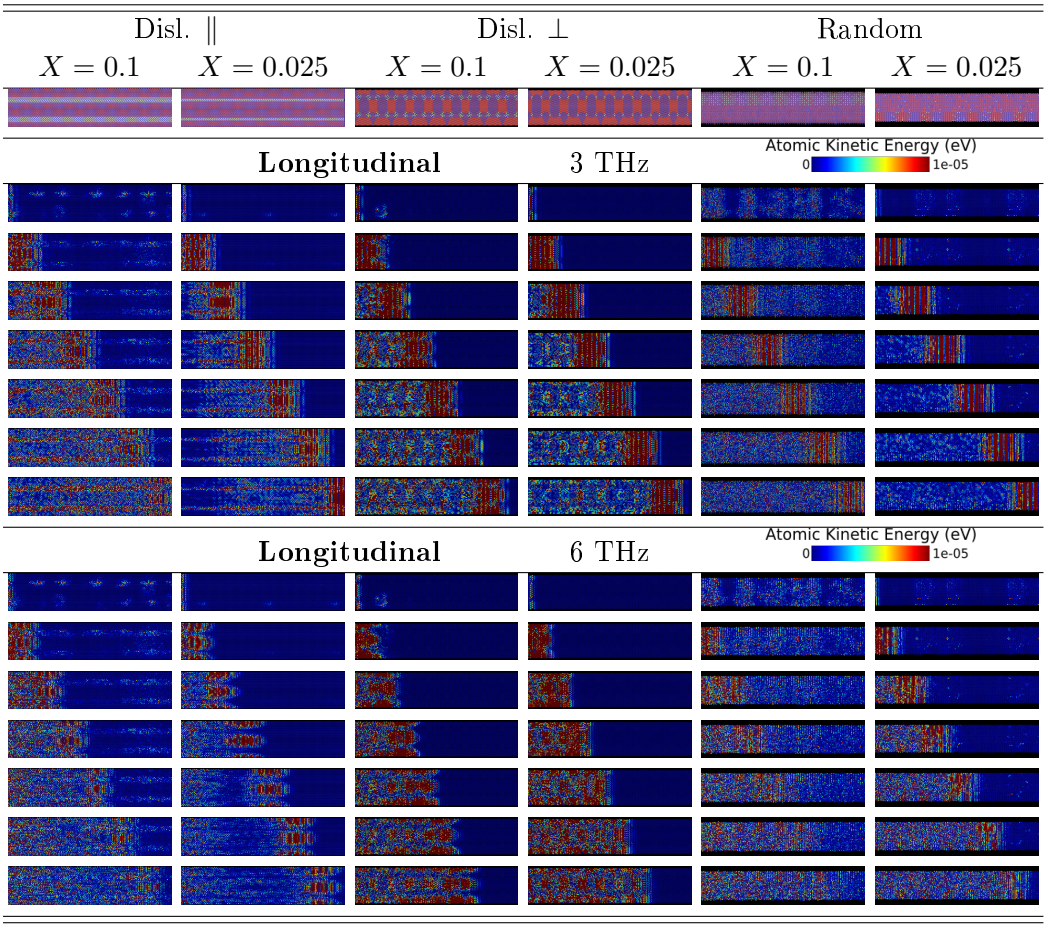

Figure 2.29: Visualization of the WP in the $In_XGa_{1-X}N$ alloys with the different configurations (parallel and perpendicular to the dislocation and in random alloys). In the third row the configurations are displayed, with Ga atoms in red, the N atoms in blue and the In atoms in pale yellow. In each case, the cross-section is chosen to showcase the effect of the dislocation. Only the portion right of the excitation is represented, the other being symmetric. Each row gives the atomic kinetic energy in the cross-section every 9×10^{-4} ns. The first half of the table represents the propagation at 3 THz and the second half of the table at 6 THz.

acoustic phonon branches in InN [Qian *et al.* 2004], and some available in GaN [Jiang *et al.* 2017]. This has a strong effect on the propagation parallel to the dislocation (two first columns of the table), especially for $X = 0.1$. For $X = 0.025$ the propagation outside of the dislocations is not disturbed, and there is no energy propagation in the core of the inclusions (no vibrational modes are available). As a result, the WP propagates without much scattering. The absence of propagation in the In rich region also results in the absence of localization in the dislocation core for propagation perpendicular to the dislocation line. This is especially noticeable for $X = 0.1$. For the other configurations, the behavior is not very different from that at 3 THz, with a stronger attenuation of the WP for larger In content.

Briefly, the WP propagation at 3 and 6 THz show that the scattering is more pronounced for $X = 0.1$. But more importantly, it showed that at 3 THz the WP propagates in the dislocation core and part of it localized in it. Whereas, at 6 THz, the WP does not penetrate in the dislocations.

Mean Free Path The MFPs of the different configurations as a function of the frequency are depicted in the figure 2.30. The six configurations are represented for frequencies from 1 to 10 THz, 10 THz is the maximum frequency of acoustic phonons. To compute the MFP, the decay rate of the WP intensity from 10 to 30 nm away from the excitation is computed. The result is averaged between the two directions. Above 7 THz, the fit to an exponential decay fails, the profile start to be more diffusive, for those frequencies the MFP is substituted by the penetration length 1.5.3. Below 3 THz, the MFP of the longitudinal phonons in the random alloys (circles) are magnitudes orders larger than the size of the system, rendering an accurate estimation difficult.

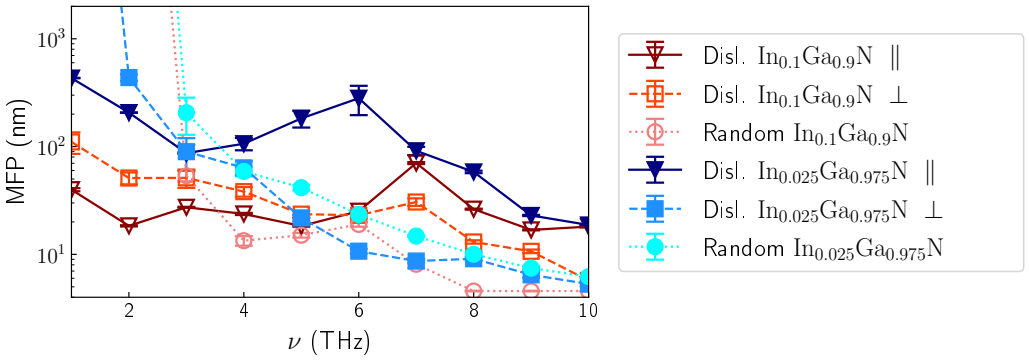

Figure 2.30: MFP in the different configurations, random alloys, perpendicular or parallel to the dislocation line for the $In_XGa_{1-X}N$ with $X = 0.1$ and $X = 0.025$.

The first phenomena that can be noted is that the MFP is higher in similar configurations (parallel, perpendicular or random alloy) for lower In content, this is consistent with the role of alloy scattering. There is an exception: for the propagation perpendicular to the dislocation line above 5 THz the MFP is higher for $X = 0.1$. The smaller core for $X = 0.025$ might impact more the high frequency propagation than the larger core for $X = 0.1$. Comparing the propagation perpendicular or parallel to the dislocation lines, it appears that the MFP is higher when the dislocations are perpendicular up to 3 THz for the $X = 0.025$ and up to 6 THz for the $X = 0.1$. After this, the tendency is reversed, the MFP is higher parallel to the dislocations. This transition seems due to the transition between a regime where energy can locate in the cores to a regime where no modes exist in the dislocation cores, and they interfere less with the propagation. This transition seems to appear at higher frequencies for higher Indium content, probably because of the stronger

scattering reducing the overall MFP.

Interestingly, the MFP for random alloys and for propagation perpendicular to the dislocation line decreases monotonously, and the MFP parallel to the dislocation line have a maximum at higher frequencies. There is an interesting link between the maxima observed here, and the one observed for NW-M in figure 2.23, defects parallel to the propagation affect strongly the propagation when modes are available in both phases and much less if it is not the case.

The MFP showed the anisotropy of propagation, depending on the frequency, the MFP reduction is higher in the parallel or perpendicular direction.

2.5.3 Conclusion

The effect of decorated dislocation in a $In_XGa_{1-X}N$ alloys was studied. A first observation is that at low frequencies, the decorated dislocation affect more the propagation than the random alloys. This is consistent with the long wavelength being less affected by alloying than the shorter wavelength [Upadhyaya & Aksamija 2016]. The dislocations representing either an interface parallel to the flux (see chapter 3), or an array of defects as described in the previous sections tend to affect more the low frequencies. Following the same pattern, the dislocations perpendicular to the propagation direction have a higher effect at low frequency relative to the dislocation perpendicular to it. The dislocation acting as large "point" defects when perpendicular to the propagation.

It is also interesting to compare qualitatively the thermal conductivity reported in the publication [Giaremis *et al.* 2020] and the MFP obtained here. First, κ is higher for lower In content, this is consistent with the higher MFP in most cases. Secondly, κ is higher in the direction parallel to the dislocation, which is consistent with the higher MFP at high frequencies. It appears also that the anisotropy is stronger for the lower In content, this is also consistent with the results in figure 2.30. However, the variation of κ with the temperature cannot be explained using the MFP at 0 K.

To conclude, In decorated dislocations in GaN affect differently the propagation of phonons depending on the orientation and the frequency. At low frequencies the dislocations interact strongly with the propagation, whereas at higher frequencies no modes are available in the In rich dislocation cores. It also appears that the MFP perpendicular to the dislocation line decreases monotonously, the MFP parallel to it tend to increase at high frequency. The variations of MFP seem to be consistent with the variation of thermal conductivity [Giaremis *et al.* 2020].

A deeper analysis of the MFP of the transverse and longitudinal modes as well as an analysis of the phonon dispersion would be necessary for a better understanding of the phenomena at hand. However, this was not done in the frame of this short analysis.

At this point, it is interesting to summarize briefly the observation of this chapter. First, the vibrational properties of nano-objects used as nanoinclusion in nanocomposites are affected by the matrix. This has been shown through the example of GaN in SiO_2. The main effects of the insertion in a matrix are, the suppression of the surface modes and of the redshift of low frequencies, and the apparition of matrix modes.

Secondly, a briefer study of the effect of the impedance mismatch exemplified the diffusive, propagative and mixed propagation modes. Crystalline NI in an amorphous matrix do not seem to impact strongly the propagative regime, unless an impedance mismatch is introduced. In the other hand, the diffusive transport is increased by the addition of inclusions unless these inclusions are softer than the matrix.

Thirdly, the effect of shape of the NI was studied. In particular, it was shown that a structural crystalline percolation can increase the ballistic transport without inducing a large increase of thermal conductivity. For this study, the propagative and diffusive contributions to the thermal conductivity were evaluated. If the model used systematically overestimate the thermal conductivity, it, nevertheless, respects the hierarchy of the nanocomposites, obtained thanks to EMD simulations. At the occasion of this study, it also appeared that the MFP can be non-monotonous with frequency in the case of interface parallel to the propagation. The study of diffusive transport also showed that the diffusivity is increased by the presence of inclusions and is not affected by their shape.

Finally, a brief study of the effect of decorated dislocations on the propagative transport, showed an interesting dependence to the orientation and the frequencies. This dependence can be linked to the thermal conductivity as function of the direction. Interesting links between dislocations perpendicular or parallel to the propagation and percolating or non-percolating NI arrays can be drawn. For instance, for both configuration, there is a MFP maximum at high frequencies.

In the next chapter, the focus will shift from bulk nanocomposites to core shell nanowires.

Synthesis of the Chapter

- The study of free and embedded GaN nanospheres showed that:
  - Free nanospheres vibrational modes are impacted by the diameter reduction
  - The insertion in an amorphous matrix attenuates the acoustic phonon redshift and the importance of surface modes
  - Other effects as the perturbation of acoustic phonon persist and blurring of the acoustic peak
  - The thermal conductivity does not increase linearly with the diameter of free nanospheres
- The stiffness of nanoinclusions affects the propagation of energy
  - When the inclusions are stiffer than the amorphous matrix the MFP decreases and the diffusivity increases
  - When the inclusions are softer, both diffusivity and MFP are decreased
- The shape of the nanoinclusions impacts the energy transfer in amorphous crystalline nanocomposites
  - A structural percolation induces a large enhancement of ballistic transport
  - The MFP enhancement induced by the percolation has a moderate impact on the thermal conductivity computed via EMD
  - The global diffusive transport is not affected by the shape of nanoinclusions but, interestingly, diffusive transport spreads from the matrix to the crystalline inclusions
- Decorated dislocations impact the energy propagation
  - The higher the concentration of impurities is, the lower the MFP is
  - The frequency and direction affected depend on the concentration

Chapter 3

Core Shell Nanowires and Continuous Modeling

Contents

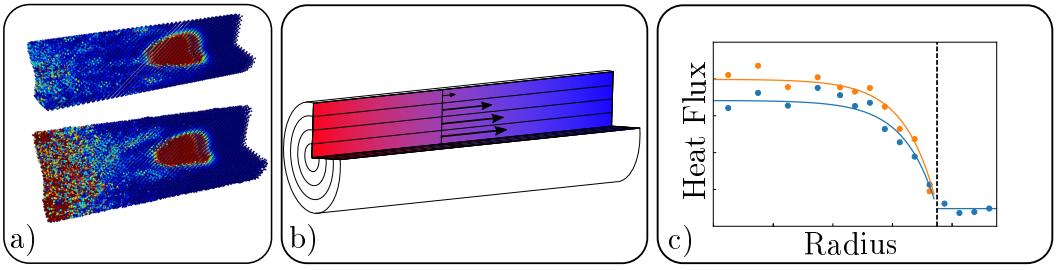

Visual Abstract: shape of the wave-packet (a) illustration of the NEMD set up (b) resulting heat flux radial distribution (c).

This chapter focuses on the vibrational and thermal properties of silicon nanowires. These structures were first discovered in the 60s [Wagner & Ellis 1964], and have been used for a wide range of applications in the last twenty years [Ghosh & Giri 2016]. As a one dimensional object, the smallest dimension allowing transport, NWs are particularly interesting; using them one can take advantage

of confinement [Ponomareva *et al.* 2007], surface [Lim *et al.* 2012, Li & Zhang 2018] and ballistic [Maire *et al.* 2017] effects.

An extensive study of surface effects in Si or Ge NWs has been made by Malhotra *et al.* [Malhotra & Maldovan 2016]. They have shown that in nanowires, compared to the bulk, long wavelength phonons contribute less to the thermal conductivity. A core shell structure adds a supplementary interface, this time parallel to the heat flux, which leads to a further decrease in the thermal conductivity. For this reason, Si-Ge core shell nanowires (CS-NWs) have been the subject of numerous studies showing that the interface between Si and Ge promotes localization of high-frequency phonons [Wang *et al.* 2013]. In these CS-NWs the difference of group velocities between core and shell induces couplings of longitudinal and transverse modes, giving rise to new structure modes with eventually a confinement of the longitudinal components [Chen *et al.* 2011].

The naturally occurring oxidized shells at the surface of Si NWs [Cui *et al.* 2001] can induce similar effects. The amorphous shell, changes the properties of the NW [Guénolé *et al.* 2013], and is known to drastically reduce the thermal conductivity of the NWs [Hu *et al.* 2011, Gao *et al.* 2014]. Early simulations reported a 100-fold decrease of κ attributed to reduced phonon lifetime, in Si NWs with diameters below 4 nm [Donadio & Galli 2009]. More recently, simulations have shown that dispersionless modes at the Si-SiO_2 interface might be responsible for the decrease of κ [Zushi *et al.* 2015]. It has been shown for thin films that the addition of an amorphous layer reduces the thermal conductivity, at constant crystalline content, below what can be modeled with a simple mixing rule [Neogi *et al.* 2015, Verdier *et al.* 2018b]. A periodic modulation of the amorphous shell of a Si CS-NW has also been shown to reduce the thermal conductivity due to nanoconstrictions and phonon blocking [Blandre *et al.* 2015].

In a first section, the impact of the amorphous shell on the vibrational properties of silicon NWs will be studied. After this, a continuum approach, the hydrodynamic heat equations, will be used to describe the heat flux in these NWs, the focus will be on the impact of the amorphous shell on the radial distribution of flux.

3.1 Effect of the Free Surfaces and the Amorphous/Crystalline Interfaces on Heat Transport in Core Shell Nanowires

The main focus of the study of silicon core shell nanowires, here, is to analyze the effect of the oxidation/amorphization on vibrational properties. For this, the properties of a pristine NW are compared to the one of the same NW on which an amorphous shell is added.

3.1.1 Modeling of the Configurations

The pristine NW studied in this section is a 50 nm long cylindrical NW of diameter 5 nm (see figure 3.1a). The cylindrical core-shell NW (CL-CS-NWs) is the same NW to which an amorphous shell of constant thickness is added (see 3.1b). This amorphous shell can be seen as an approximation for the naturally occurring oxide shell [France-Lanord *et al.* 2014b].

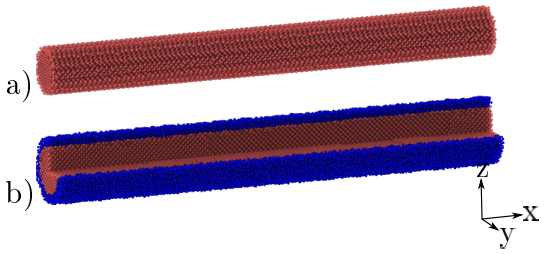

Figure 3.1: Geometries studied in this section: pristine NW (a), cross-sectional view of the CL-CS-NW (b) with crystalline core in red and amorphous shell in blue. A quarter of the atoms are removed to visualize the core/shell structure.

The pristine NW is created by filling a 50 nm long cylinder with a radius of 2.5 nm with c-Si. The growth direction, x, is aligned with the $\langle 100 \rangle$ direction of the crystal lattice. The exact length is adapted to get an integer number of primitive cells, here it is 49.95 nm. This insures that NW is monocrystalline through the periodic boundary condition in x. The cylindrical core shell nanowire is created from the assembly of a hollow cylinder of amorphous silicon (the shell) and a crystalline core, with the method proposed by France-Lannord [France-Lanord *et al.* 2014b] and similar to the one used in chapter 2 to generate nanocomposites. First, the cylindrical shell is cut out of the same a-Si bulk block as in the previous chapter (see 1.4.1). The original sample is a cube with a side length of 17.4 nm repeated 3 times in the x direction to reach the appropriate length before carving out the shell. The empty shells are then filled with the same c-Si cylinder than for the pristine NW. Free boundary conditions are used around the free surface, for this purpose, the nanowire are embedded in a box of far larger dimensions in the perpendicular directions (25 nm).

These structures are then relaxed. For this, a conjugated gradient energy minimization is performed to reach a local mechanical equilibrium. After that, the system is annealed at 100 K during 10 ps. Before this annealing, the box size is increased in the growth direction to prevent thermal stresses leading to buckling. The NW is then quenched using a conjugated gradient energy minimization. A second energy minimization is finally performed, at zero tensile stress inducing a small creep in the periodic direction (that is, strain evolution at a global constant stress). This step insures that there are no remaining thermal stresses after the annealing. To validate that the system is at equilibrium, the fact that the spontaneous evolution of the system over 10 ps does not result in atomic kinetic energy

above 10 feV is checked. This minimization eliminates the thermal noise that could perturb the wave-packet simulations performed at 0 K. A modified SW interatomic potential [Vink *et al.* 2001] allowing a more realistic modeling of the interface between c-Si and a-Si in terms of crystalline/amorphous interfacial energy and regular atomic energies inside the two phases was used [France-Lanord *et al.* 2014b].

Interfacial Potential Energy To assess the quality of the structure obtained, the energy of its different phases and interface are studied. For this, the average potential energy per atom ($\langle E_p \rangle_{at}$) as a function of the radius is plotted in figure 3.2. This quantity is computed for 1 Å concentric hollow cylinders in the pristine NW and CL-CS-NW, by averaging the potential energy of all the atoms in each hollow cylinders.

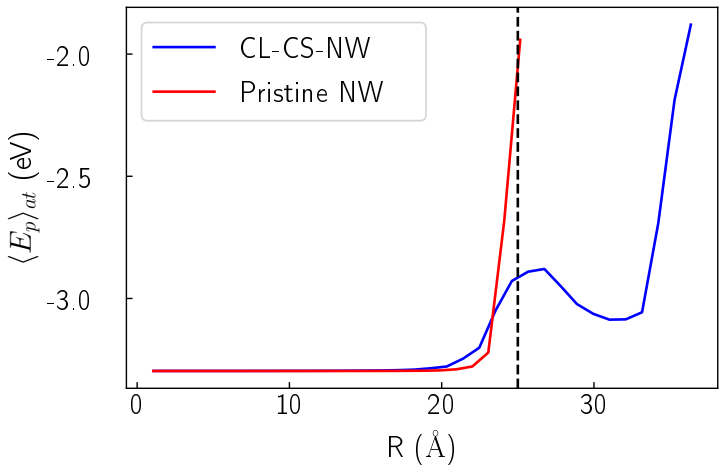

Figure 3.2: Mean potential energy per atom as function of the radius for the pristine NW (red) and the CL-CS-NW (blue). The dashed line represents the position of the surface or crystalline/amorphous interface.

The first observation is that $\langle E_p \rangle_{at}$ is constant in the crystalline core; away from the surface and interface, both structures have a $\langle E_p \rangle_{at}$ of -3.29 eV. This value is set by the potential used and is the same as the one reported in a previous publication [France-Lanord *et al.* 2014b]. This shows that the amorphous shell does not strain the core and that the structure is free of defects that would locally increase the atomic potential energy[1]. Closer to the interface/surface, $\langle E_p \rangle_{at}$ starts to increase. This increase appears for a lower radius for the core shell NW, than for the pristine one. This shows that the crystalline amorphous interface has a more penetrating effect than the free surface. In the case of the pristine NW, during the relaxation process, the atoms at the free surface move to minimize the surface energy, without external influence, whereas, in the case of CL-CS-NW the atoms of the shell interact

[1] The strain/stress values as a function of the radius in a similar structure is studied in the appendix B.4

with the atoms in the core. This induces a local reorganization near the interface and thus a change of potential energy.

The variations of $\langle E_p \rangle_{at}$ in CL-CS-NW corresponds to typical variation observed at interfaces. First, $\langle E_p \rangle_{at}$ increases to reach $-3.29\,\text{eV}$, to then decrease to $-3.08\,\text{eV}$. After the interface, the potential energy re-increases due to the proximity of the free surface. The value reached at the interface, and the plateau in the shell, correspond closely to the values observed for a a-Si/c-Si superlattice and core-shell NW [France-Lanord *et al.* 2014a]. In the aforementioned study, they used these values to compute the interfacial energy and showed that they are reasonably consistent with experimental results. Eventually, it is worth mentioning that the "bulk" value of $\langle E_p \rangle_{at}$ for a-Si is reached in the shell, showing that at least a small layer of the a-Si shell is not affected by the interface nor by the surface.

The pristine and CL-CS-NW created have a potential energy distribution profile compatible with previously reported values. In the following, the effect of the interface and surface and their interactions on the vibrational properties are studied.

3.1.2 Vibrational Density of States

The Vibrational Density of States (VDOS) gives an overview of the frequency distribution of the vibrational modes, and thus allows determining which frequencies are affected by interface and surface effects. The VDOS of the structure were computed using the Velocity Auto-Correlation Function (VACF), as described in section 1.5.1. To showcase the effect of the surface and interface, the system is decomposed in different layers, this starts with a central cylinder of radius 25 Å and continues with 5 Å thick hollow cylinders until the external radius is reached. The resulting decomposition for the pristine and cylindrical core shell NW are shown in the insets of figure 3.3 where the VDOS are depicted. For comparison purposes, the VDOS of bulk a-Si and c-Si are also depicted. These VDOS were obtained using cubes of side 10 nm with periodic boundary conditions in all directions. The a-Si box was obtained by cutting the same a-Si sample used for the shell.

Let's first focus on the effect of surface, for this, one can take a look at the partial VDOS of the external layers (red curve for the pristine NW and brown curve for the CL-CS-NW). When comparing those curves with the VDOS of c-Si Bulk, two phenomena appear: the lowest frequency peak is red shifted and the highest frequencies are depopulated. These phenomena have already been observed for Si Nanoparticle (NP)s of very small dimension, where the surface effects are dominant [Meyer & Comtesse 2011]. In the case of the pristine NW, only the outermost layer (20-25 Å) has a VDOS that differs from the one of bulk c-Si.

If the surface has the strongest effect on the VDOS, the amorphous crystalline interface also affects the VDOS. Let's first focus on the outermost crystalline layer of the core shell nanowire (20-25 Å). The partial VDOS corresponding to this region

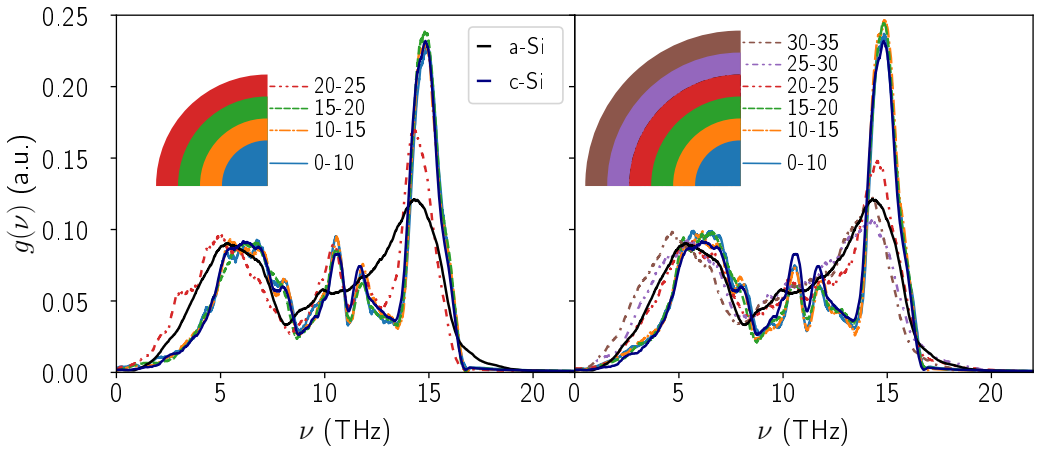

Figure 3.3: Vibrational density of state of the different layers (solid lines) of the pristine NW (left) and the CL-CS-NW (right), the VDOS of bulk c-Si and a-Si are also depicted in, respectively, dark blue and black full lines.

(dashed red line in figure 3.3b), hybridizes both a-Si and c-Si VDOS. In the low frequency region (0-8 THz), it matches the one of a-Si. At larger frequencies, the features of the c-Si VDOS appear. These features are: the variation around 12 THz and the peak at 15 THz. This hybridization between a-Si and c-Si VDOS has already been described in the literature [France-Lanord *et al.* 2014a]. The interface effect is also visible through a redshift of the low frequencies compared to a-Si in the innermost layer of the shell (25-30 Å). In the high frequency region, above 14 THz, there is a depletion of modes compared to the bulk a-Si. The interface appears softer than the bulk a-Si. These observations about the interface were already made for a-Si/c-Si superlattices, indicating that the free surface has no effect on the VDOS of atomes at the amorphous crystalline interface [France-Lanord *et al.* 2014a].

To summarize, the surface and interface mostly impact the low frequencies. A redshift appears at the surface and interface, and in the inner core the VDOS matches the one of c-Si. The impact on higher frequencies is less marked, there is a mode depletion at the surface in both cases, and a hybridization between a-Si and c-Si VDOS at the interface can nevertheless be noted.

3.1.3 Dynamical Structure Factor

To complete the observation made thanks to the VDOS and give a more detailed description of the modes affected by the addition of an amorphous shell, the Dynamical Structure Factor (DSF) is computed using the method described in section 1.5.2. As the interest at hand is the transport properties along the NW, only the DSF corresponding to the wave vector aligned with the growth direction is studied, that

is: $\langle 100 \rangle$ in the direct space, or ΓX in the reciprocal space. The DSF of the pristine NW is displayed in the figure 3.4. In this figure, the longitudinal and transverse acoustic branches and the optic branch appear clearly. The background noise is low and the white lines fitting the dispersion relations seem to match to the DSF. This is particularly true for the longitudinal acoustic branch. The transverse acoustic branch is more blurred. It is to be noted that for the longitudinal polarization, a second branch at low frequencies seems to appear. This branch has already been observed [Zushi *et al.* 2014], and can be linked to surface modes.

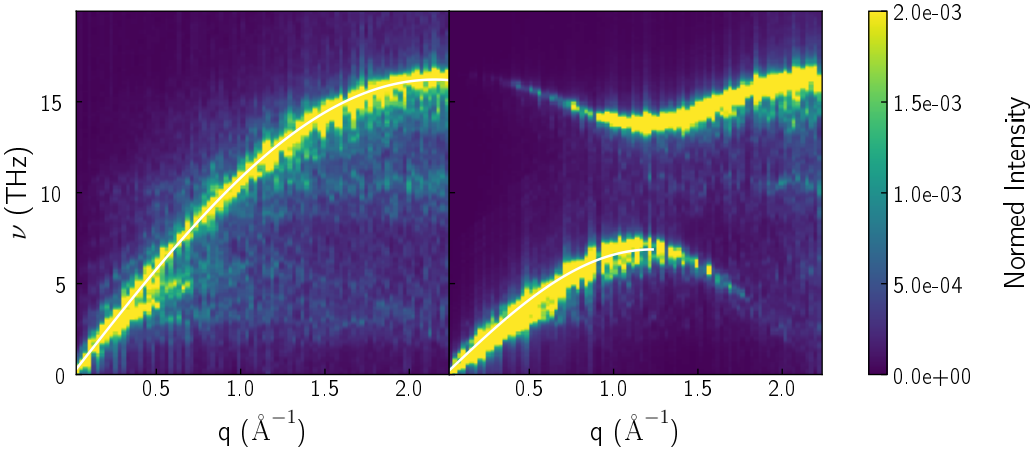

Figure 3.4: Dynamical structure factor for the pristine NW, in the ΓX direction, projected on the longitudinal polarization (left) and transverse polarization (right). The white lines represent the estimated dispersion relations.

This DSF can be compared with the DSF of the core shell nanowire in figure 3.5. At first glance, the two have a very similar aspect, so much so that the dispersion relations are unchanged. The differences lay mainly in the increased linewidth, and background noise. The increase linewidth is associated to a reduced MFP. A decreased MFP was expected in this case. What appears as background noise, corresponds to the DSF of a-Si [Damart *et al.* 2015].

These DSFs would be worth further exploitation, notably to give a better overview of the size effects on the distributions. For this, a thorough comparison with the DSF of bulk Si would be necessary. However, this is not the scope of this study focusing on the comparison between pristine and core shell NW. Nevertheless, it can be the second branch observed at low frequencies for a pristine NW disappears when the amorphous layer is added, confirming that is linked to the surface.

The main observations are that for the cylindrical core shell nanowire a superposition of modes corresponding to the crystal and the amorphous layer is visible. The amorphous layer does not seem to perturb the dispersion relation. Considering the DSF, it appears that two frequency ranges are worth studying,

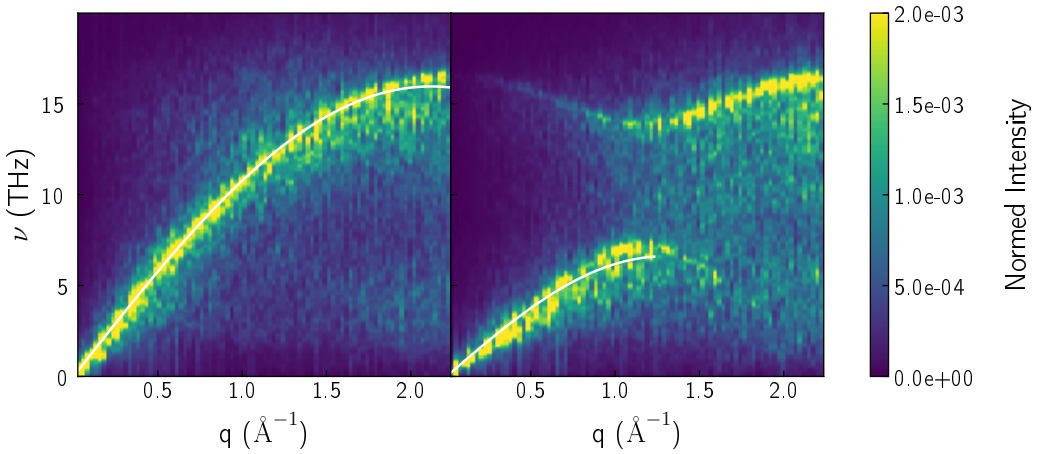

Figure 3.5: Dynamical structure factor for the cylindrical core shell nanowire, in the ΓX direction, projected on the longitudinal polarization (left) and transverse polarization (right). The white lines represent the estimated dispersion relations.

the low frequency range where the surface effect matters and higher frequencies ranges. These higher frequencies are particularly interesting in that no propagation is expected in the amorphous layer (no more propagons: see section 1.1.5).

3.1.4 Wave-Packet Propagation

Wave-packet propagation simulations can give a better understanding of the vibrational properties of the NWs. The wave-packets are induced in the NWs at 0 K by exciting a central 2 Å thick layer with the force excitation described in the section 1.5.3. The force amplitude is of 3.773×10^{-4} eV Å^{-1}. First, a qualitative description of the propagation of wave-packets, through the analysis of the kinetic energy distribution, and of the local displacement at low frequency is given to finish with an analysis of the Mean Free Path (MFP) deduced from these simulations.

Kinetic Energy Propagation Analysis Figure 3.6 gives a cross-sectional view of the atomic kinetic energy in the NWs. For longitudinal and transverse wave-packetss, the behavior at low frequencies is represented by 2 THz excitation, the one at high frequencies by the 12 THz excitation for the longitudinal polarization and 4 THz for the transverse polarization. 12 THz and 4 THz chosen as represents for each polarization the same relative position on the dispersion line: 3/4 of the maximal frequency of the longitudinal branch, it also corresponds to frequencies for which the propagation in a-Si is very limited [Beltukov *et al.* 2018].

In the two columns on the left depicting the propagation at 2 THz, it appears

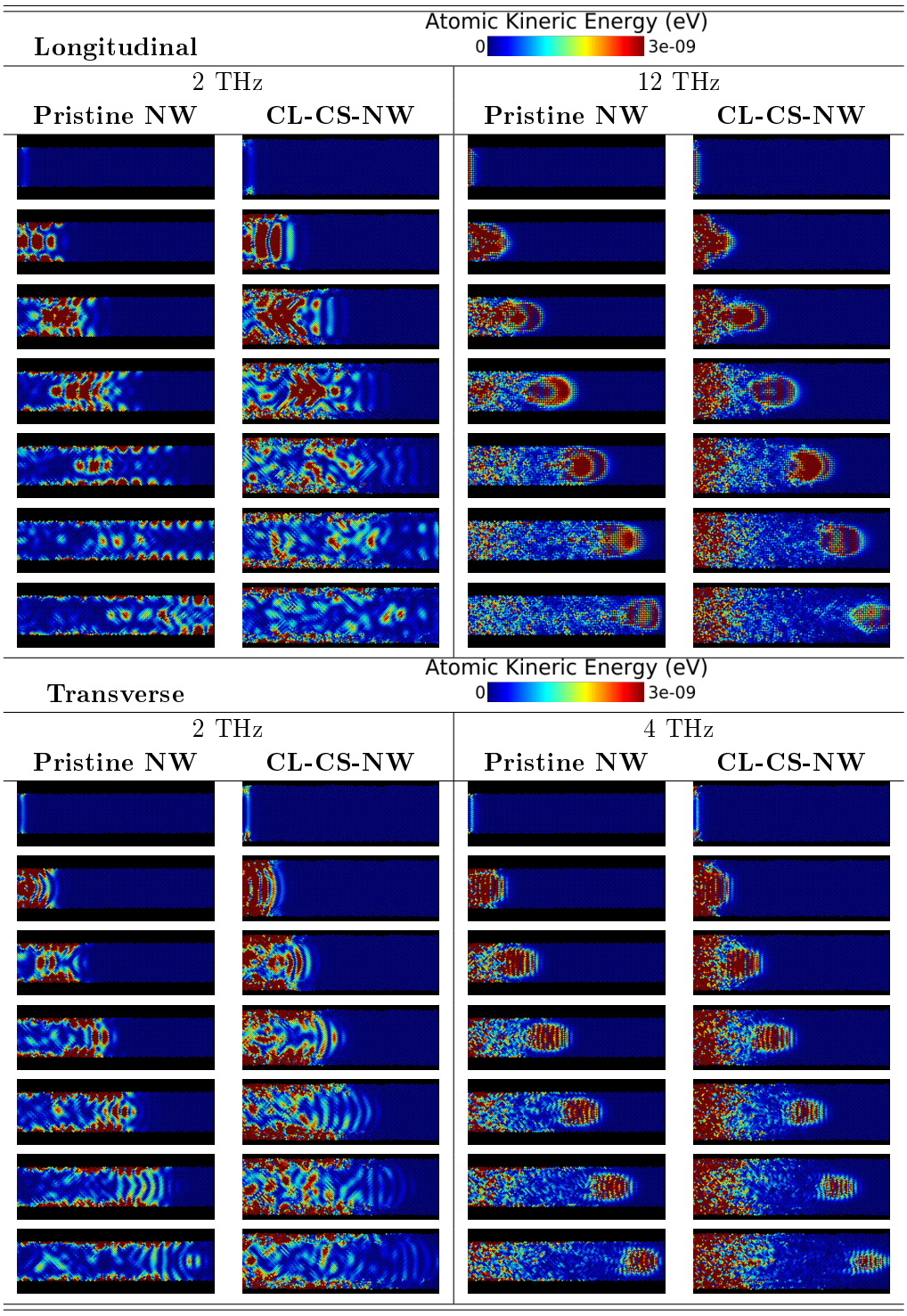

Figure 3.6: Cross-sectional view of a wave-packet going through the pristine NW and the cylindrical core shell NW. The color scale going from 0 (blue) to 3×10^{-9} eV (dark red) gives the atomic kinetic energy. Between each line 0.9 ps has elapsed.

that the free surface has a strong impact on the propagation. This is true for both polarizations and both configuration. For the longitudinal polarization (first part of the table) in the case of the pristine NW, a wave at the surface appears clearly. The propagation in the inner core of the nanowire appears more damped than the wave at the surface. In the cylindrical core shell NW case, the wave-packet can travel in both core and shell and the wave at the surface is less marked than for the pristine NW. The propagation in the core appears less damped. For the transverse polarization, the behavior is very similar. Lastly, after the passage of the wave-packet, some energy appears localized at the free surface and in the amorphous shell.

This strong effect of the free surface at low frequencies, could be expected given that the wavelength of the wave packet and diameter of the NWs are of the same order, in particular for the longitudinal polarization. This explains partially why they are strongly affected by the geometry [Malhotra & Maldovan 2016].

At high frequency, the behavior is more homogeneous, a clear propagation is visible in the center of the NW. Because no propagation is possible in the amorphous layer at this frequency [Beltukov *et al.* 2018], no energy propagates either at the free surface, interface or in the shell. The wave-packet only propagates in the core in the form of an oval shape. This shape results from the combination of the time-limited excitation and interface/surface effects, as seen for the embedded NW mesh in figure 2.21. As the wave-packets goes through the NW, some energy is dispersed in the NW. In the case of CL-CS-NW, a diffusive behavior appears in the vicinity of the excitation location. There, part of the energy does not propagate but slowly spreads in the NW. This behavior, expected for amorphous materials (spreading of heat by diffusons), happens mostly in the amorphous shell but also in the crystalline core. A diffusive peak (spike of energy slowly diffusing from the spot of the excitation rather than a wave-packet exiting the spot of excitation) was expected in the shell, as for most frequencies between 2 and 12 THz the diffusive regimes can be observed after an excitation in a-Si [Beltukov *et al.* 2016]. But its presence in the crystalline core was unexpected.

To summarize on wave-packets propagation, at low frequencies, propagation takes place in the core and shell and is strongly affected by the free surface. The surface participates both in the propagation, and in localization of energy at low frequency. At higher frequencies, the propagation does not seem affected by surface effects and only takes place in the inner part of the crystalline core.

Distribution in the section To complete the analysis of the kinetic energy distribution during wave-packets propagation, a visualization of the mean kinetic energy as a function of the radius is displayed in figure 3.7 for the longitudinal excitation. For this, the energy of atoms in a range of 9 to 16 nm away from where the excitation is made of the NW is averaged for successive coaxial hollow cylinders, this corresponds to the middle of the picture in the representations in figure 3.6. The

decomposition in coaxial hollow cylinders is similar to the one done of the VDOS (see inset of figure 3.3) but this time the shells considered have a thickness of approximately half a lattice length, or 2.71 Å. The energy distributions for these shells are displayed for different time steps with different colors.

With this representation, the effect of the free surface is clearly visible. At 2 THz for the pristine NW, the energy density increases first at the free surface and only then in the center (the blue lines have their maximum values for larger R). This is a manifestation of the waves at the surface shown in figure 3.6. The kinetic energy in the center of the NW at R=0 rises with some delay relative to the surface. After the wave passage, the energy density stays high at the free surface and to a lesser degree in the center. This is the signature of energy localization.

In the case of the cylindrical core shell nanowire, the effect of the free surface is lessened by the presence of the amorphous shell. The wave at the surface is still visible, but is less penetrating. Additionally, the energy peak at R=0 is higher than for the pristine NW and decreases faster after the passage of the wave-packets. This shows that the wave-packets is less dispersed. It also appears that a wave travels through the interface. Finally, as for the pristine NW, energy localization at the free surface is visible.

At high frequency the pristine and cylindrical core shell nanowires have a very similar behavior, there is an energy peak in the middle corresponding to the passage of the wave-packets. Moreover, little to no energy propagates in the outer layer of the crystalline core and even less when there is an amorphous shell. Finally, little energy is localized after the passage of the wave-packet, and the energy dispersed by the wave-packets is evenly distributed.

> The representation of the radial distribution of energy as a function of time showcases what was visible in figure 3.6. Namely, the free surface and interface impact the propagation at low frequency and that the shell seems to attenuate the effect of the surface.

Analysis of the Displacement The effect of free surface and interface on the propagation of wave-packets can be understood more in depth thanks to the visualization of the atomic displacements in the cross-section of the NWs displayed in figure 3.8. The displacements visualization showcases the phase shift appearing in the wave front. To allow a better visualization of the phase shift, a snapshot every 0.3 ps is given, that is 3 times more often than for figure 3.6. With this representation, it appears clearly that the wave at the surface is slower than the wave in the crystal for transverse and longitudinal polarizations, the modes at the surface are slower. This decrease in group velocity of the waves at the surface is consistent with the redshift observed in figure 3.3, the apparition of the second branch in figure 3.5 and was already predicted [Zushi *et al.* 2014].

In the case of the longitudinal polarization, it appears that the displacement in the core is maximum when the shell and core wave are phase shifted by π. The

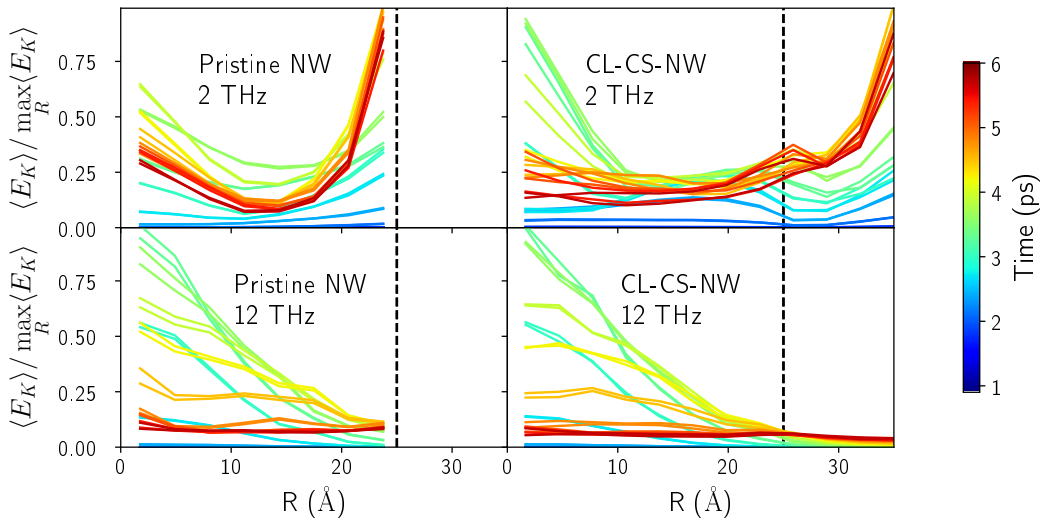

Figure 3.7: Atomic kinetic energy as a function of the radius averaged on a portion of the NWs 9 to 16 nm away from the excitation, for different time steps (colors), for the pristine NW (first column), for the cylindrical core shell nanowire (CL-CS-NW second column) at 2 (first line) and 12 THz (second line). The vertical black dashed line represents the end of the crystalline core.

slower propagation of energy in the core visible in figure 3.7 appears to result from interaction between the wave in the NW and at the free surface. The pattern of displacements suggests a superposition of different modes. The amorphous shell delays the apparition of the phase shift and thus allow a better propagation.

Figure 3.8 allows identifying clearly the phase shift appearing between the inner core of the NW and the free surface. This phase shift appears to induce an interaction between the wave-packets in shell and the wave-packets in core, this interaction seems to perturb the transmission. It also appears that the added layer of a-Si mitigates this phase shift.

Mean Free Path To further analyze the propagation of the wave-packets, the MFP was computed from the decay of the envelope of the wave-packets (see section 1.5.3). This was done for the longitudinal and transverse polarizations for frequencies between 1 and 15 THz. The results are displayed in figure 3.9. For the longitudinal polarization, below 2 THz, the MFP in the pristine NW is larger than in the cylindrical core shell NW. This corresponds to frequencies where a wave at the surface can be observed. Then they both show a minimum at 3 THz. This minimum probably corresponds to the point where surface/interface waves stop interacting with the propagation in the inner part, due to a large velocity difference. After 3 THz the MFP re-increases sharply, until 7 THz, where the MFP of the pristine NW peaks

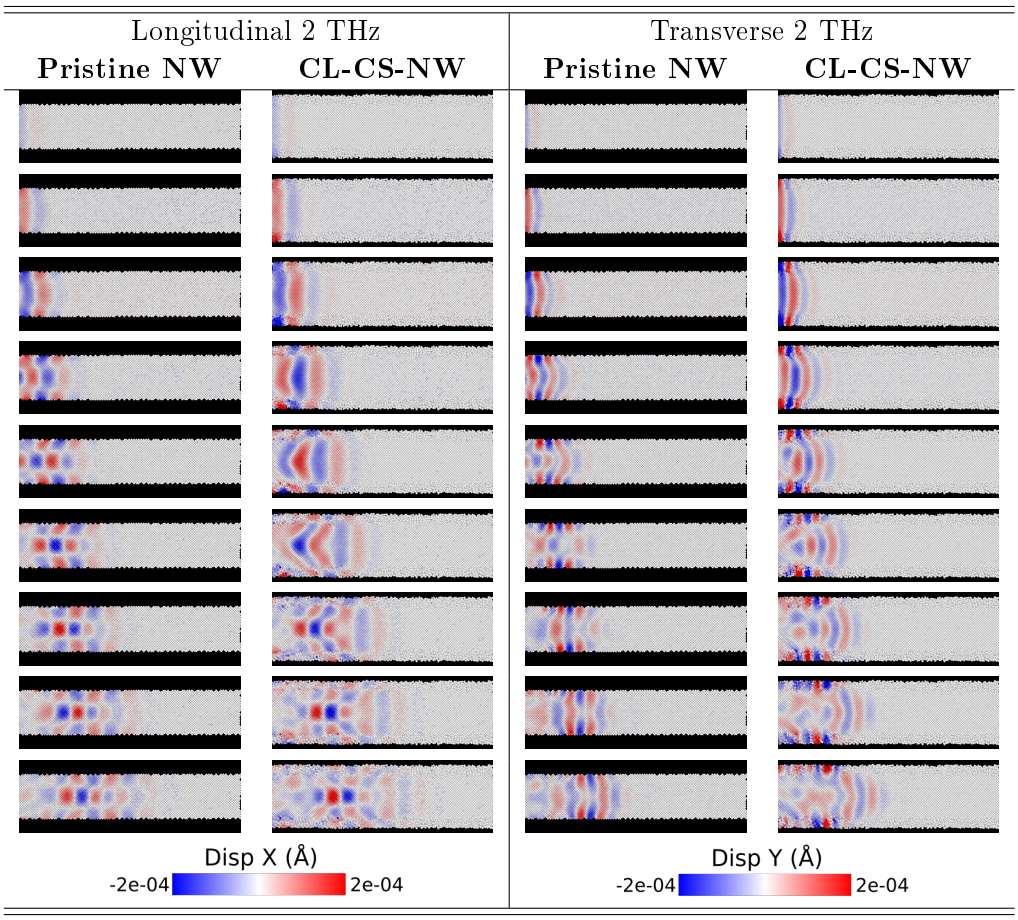

Figure 3.8: Cross-sectional view of a wave-packets going through the pristine NW and the cylindrical core shelle NW (CL-CS-NW) with the representation of atomic displacement in the polarization direction with an excitation at 2 THz. Between each line 0.3 ps has elapsed.

and the one of core shell NW plateaus. Interestingly, 7 THz corresponds roughly to the end of the transverse acoustic branch (see figures 3.5 and 3.4), and thus, at this frequency many modes are available for coupling. This could explain the decrease of MFP. This phenomenon has already been observed for a-Si [Beltukov *et al.* 2018]. After this, another peak appears around 11 THz[2] and then the MFP steadily decreases. In bulk c-Si [Zhou *et al.* 2015] and a-Si [Beltukov *et al.* 2018], or for larger NWs [Xie *et al.* 2014], such variations have not been observed. A rapid decrease of the MFP between 0 and 4 THz followed by a plateau was nevertheless predicted for a NW with square section of similar cross-sectional area [Xiong *et al.* 2016]. The lack of a second maximum in the MFP at high frequencies in the previous study might be due to the temperature effect, as here the MFP is computed without temperature,

[2]One could note that the values obtained here are larger than the nanowire length, however given that it corresponds to an exponential decay fit one can get a value even if the total length is smaller than the MFP. Nevertheless, there are limitations, if the exponential decay is too low to be measured an accurate MFP cannot be extracted, and that is the case at 1 THz.

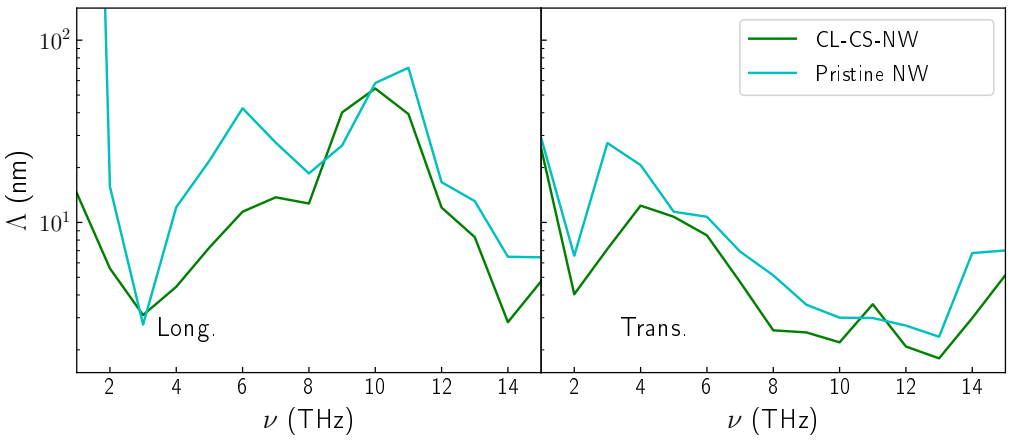

Figure 3.9: Mean free path for the longitudinal (left) and transverse polarization (right) for the pristine NW and the cylindrical core shell NW (CL-CS-NW).

the disorder being the main scattering phenomena. Interstingly the variation of the MFP observed here are similar to the one observed for the nanocomposites with structural percolation of section 2.4 in the direction of the crystalline continuity.

The MFP of transverse wave-packets follows a similar trend, it starts at high values at 1 THz, at 2 THz it decreases to then re-increase until 3-4 THz to then follow a steady decrease.

Due to the way the MFP is computed, small peaks at high frequencies appear but cannot correspond to propagation given that no propagating modes are defined at those frequencies (see figure 3.5). They are artifacts due to the fitting of an exponential fit on very low energy levels. To avoid these artifacts, the MFP can be substituted by the attenuation length, as done in chapter 2. However, at this state of the work this was not done.

Regarding the MFP, the main observations are that two frequency ranges can be distinguished: the low frequencies where the MFP decreases steadily, and the high frequencies where the MFP peaks. The decrease observed at low frequency can be linked to surface/interface effects, while the high frequency peak corresponds to the propagation taking place in the center of the NW unaffected by the free surface or shell.

3.1.5 Conclusion

The free surface has a strong effect on the 5 Å thick layer beneath it, these effects include a redshift of the VDOS, the apparition of a wave at the surface and a localization of energy. They are mainly visible at low frequencies because at higher frequencies the free surface and eventual amorphous shell does not participate in

the energy propagation, the energy propagation happens only through the center of the crystalline core. Additionally, the surface effect appear to be lessened by the addition of an amorphous shell. Finally, the MFP spectra is also interesting, rather than to decrease steadily it has a minimum around 3 THz, and then re-increases. This non-monotonous behavior appears to be a signature of the switch between a surface/interface dominated propagation at low frequency and crystalline core dominated transport at higher frequencies.

In the next section, the study will be extended to NWs of different dimensions. The results of MD simulations will be compared to the results obtained with a continuous model to study the heat flux in these structures.

3.2 Continuous Modeling of Heat Flux

Previously, the focus was laid on the impact of the nanostructuration on thermal transfer. In particular, the Wave-Packet (WP) simulations have been used to study the different energy pathways as a function of the frequency. These analyses showed that the interfaces, whether perpendicular or parallel, affect the transport differently depending on the frequency. In this section, the study of the energy pathways will be taken further with an analysis of the radial distribution of heat flux in Si NWs.

The reduction of thermal conductivity in NWs, is often linked to size effects, and particularly to boundary scattering [Volz & Chen 1999, N. Raja *et al.* 2017]. The main factor limiting the thermal conductivity is thought to be the surface scattering [Martin *et al.* 2009, Malhotra & Maldovan 2016]. More precisely, diffusive scattering at the interfaces is interpreted as the main resistive process [Malhotra & Maldovan 2019]. This interpretation is used to explain the thermal conductivity of ultrathin nanowires, up to a diameter of a few nanometers, for even smaller smaller nanowires a regime change due to the increased role of long wavelength phonons is thought to take place [Zhou *et al.* 2017, Karamitaheri *et al.* 2014]. This boundary scattering leads to a non-uniform flux distribution, that can be observed through MD or Monte-Carlo simulations [Verdier *et al.* 2018a, Melis *et al.* 2019].

As mentioned at the beginning of this chapter, the presence of a native oxide or of an amorphous skin on a NW or a thin film affects the transport in the crystalline part, decreasing the heat flux in the crystal [Verdier *et al.* 2019, Neogi *et al.* 2015, Shao *et al.* 2018]. The main reason for the decrease in thermal conductivity in these amorphous/crystalline nanocomposites is linked to an increased diffusive scattering at the interface. At the free surface, the specular reflections are supposed to be more frequent than at the crystalline amorphous interface [Malhotra & Maldovan 2019]. However, the effect of the addition of an amorphous shell on the heat flux parallel to an interface or a surface has not been extensively studied. Only a study of the temperature profile in pristine and CS-NWs nanowires can be noted [Bejenari *et al.* 2020].

In this section, the radial flux distribution in pristine and core/shell Si NWs are

obtained with MD and then analyzed at the mesoscopic level using the hydrodynamic heat transport equations (see section 1.2). The results using those equations have been provided by A. Beardo and F. X. Alvarez. Such connections between phonon hydrodynamic transport and MD have already been used to study the thermal transport in telescopic Si NW [Melis *et al.* 2019], and to model second sound in germanium [Beardo *et al.* 2021b]. This model might thus overcome the limitation of the Fuchs-Sondheimer model observed by Verdier *et al.* [Verdier *et al.* 2018a]. First, the NWs of interest in this section will be presented. After this, the radial distribution of energy during wave-packets propagation will be studied. Then, the steady-state flux distribution obtained by Non Equilibrium Molecular Dynamics (NEMD) simulations will be analyzed using the hydrodynamic heat transfer equations.

3.2.1 Modeling of the Configurations

To ease the analysis with the continuum model and avoid strong size effects, the nanowires studied heree are slightly larger than in the previous section: the crystalline core has a radius of 37.5 or 50 Å, and the eventual amorphous layer has a thickness of 10 or 20 Å (see figure 3.10). The NWs are 50 nm long. For memory, the different dimensions, along with crystalline ratios and the discretization parameter used, are listed in table 3.1. These structures are constructed and relaxed using the same method as in the see section 3.1.1.

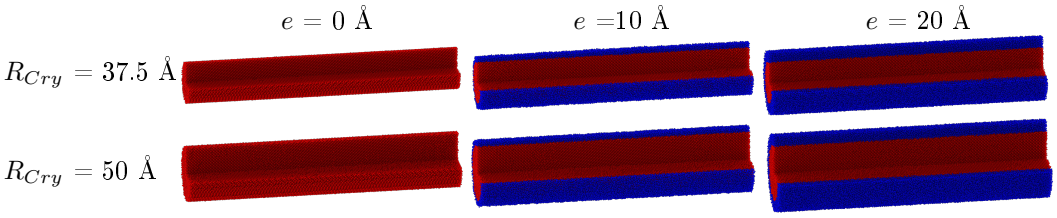

Figure 3.10: Representation of the different configurations, with amorphous atoms in blue and crystalline atoms in red. A quarter of the atoms are removed to visualize the core/shell structure.

Table 3.1: Dimensions of the different configurations with R_{Cry} the crystalline radius, e the amorphous shell thickness, dr the radial resolution of the flux and N_c/N_t the proportion of crystalline atoms .

R_{cry} (Å)	37.5			50		
e (Å)	0	10	20	0	10	20
dr (Å)	2.5	2.5	2.5	2.5	5	5
N_c/N_t (%)	100	62	43	100	69	51

3.2.2 Balisticity as a Function of the Frequency

The first approach, is to repeat the wave-packet propagation simulations performed in the section 3.1 on these new configurations. This allows identifying the different energy pathways as function of the frequency. Here, again, the high and low frequency regimes will be distinguished, with the examples of 12 and 2 THz. The example of the nanowires of R_{Cry}= 37.5 Å and $e = 0$ or 10 Å is taken. This choice is motivated by the economy of data, the largest nanowire producing larger files.

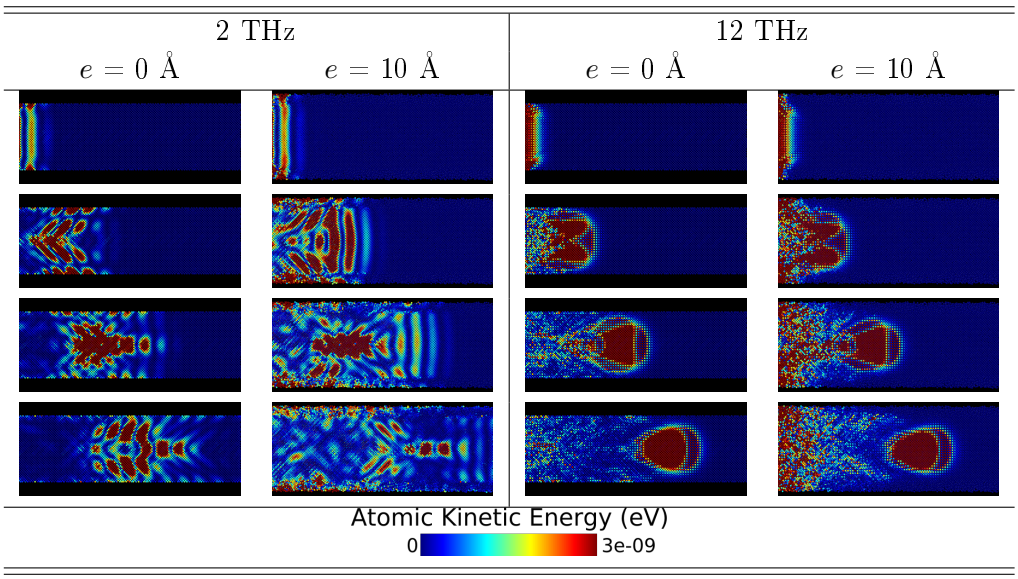

Figure 3.11: Cross-sectional view of a wave-packets going through the nanowires of R_{Cry}= 37.5 Å and $e = 0$ or 10 Å. Only the right side of the NW is represented, the propagation on the left side being symmetric. The color scale in the bottom row going from 0 (blue) to 1×10^{-9} eV (dark red) gives the atomic kinetic energy. Between each line 1.2 ps has elapsed.

In figure 3.11, the distribution of kinetic energy in a cross-section of the NWs after a longitudinal excitation at 2 and 12 THz are represented. At low frequencies, in the first two columns, the wave-packet starts as a plane wave, but is quickly dispersed. At these frequencies, the wave-packets travels at different speeds in the different regions of the NW. This gives rise to interactions between the wave in the shell and the wave in the core, as discussed in section 3.1. Again, the strong perturbation is consistent with the wavelength being of the order of the diameter of the NW. However, it can be noted that more energy is carried by the center of the NW, than for thinner NWs (see figure 3.6).

The radial distribution of the kinetic energy, between 90 to 160 Å away from the excitation, is displayed in figure 3.12. The first line represents the propagation at 2 THz. With this representation, a wave appears clearly at the surface. This wave at the surface has a larger amplitude when there is an amorphous shell. Furthermore, it is visible that the energy first comes in the center and then at R = 20 Å, this lag between the positions is a corresponds to the patterns appearing in the cross-

sections (see figure 3.11), they recall interference patterns and are more marked without amorphous shell.

At 12 THz, the energy propagates differently: most of the energy is carried by the center of the crystalline part, but a scattered diffusive contribution spans the entire cross-section, including the crystalline part, behind the ballistic central part. The profile of the central part of the wave-packets is similar with or without shell, as depicted in the bottom panels of figure 3.12. Little to no energy propagates in the vicinity of the interface/surface, and even less in the amorphous shell. The energy concentration peaks in the center of the NW and decreases when going toward the surface. This shape indicates a strong effect of the free surface/interface that decreases with the distance. The main effect of the amorphous shell is the additional apparition of energy diffusion. This diffusive transport appears as a slowly expending red patch in the rightmost column of figure 3.11. This kind of high-frequency diffusive transport was already observed and discussed in section 3.1.

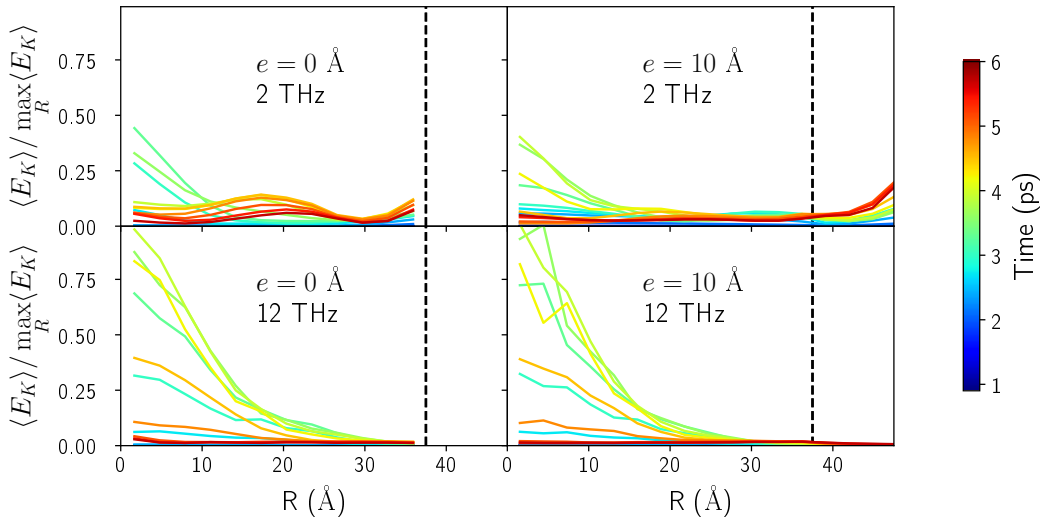

Figure 3.12: Atomic kinetic energy as a function of the radius averaged on a portion of the NWs 90 to 160 Å away from the excited layer, for different time steps (colors). For the nanowires of R_{Cry}= 37.5 Å and $e = 0$ (first column) or 10 Å (second column) at 2 THz (first line) and 12 THz (second line). The values are normed by the maximum reached at 12 THz. The vertical black dashed line represents the end of the crystalline core.

An overview of the behavior at the different frequencies is given in figure 3.13. In this figure, the energy distribution profile is given for the timestep at which the maximal amplitude is reached. This corresponds to the curve of figure 3.12 at the time step where the energy is the highest, for each frequency. All the frequencies share a common tendency, there is little energy transmitted in the vicinity of the free surface/interface. The only exception is at 14 THz where the maximum is near the interface. There are other frequency dependent behaviors, namely, the transport

at the free surface, visible at 2 THz, disappears at 4 THz. This means that surface waves only appear below this frequency[3]. Moreover, the maximal amplitude is not always reached in the center of the NW: for 8 and 10 THz without shell and for 8 THz with a shell, the maximum is around R=20 Å. It is worth noting that the amount of energy injected in the system depends on the frequency used, so that the quantity of energy at the different frequencies are not directly comparable. At higher frequencies, more energy is injected, with, at most, an increase proportional to the frequency.

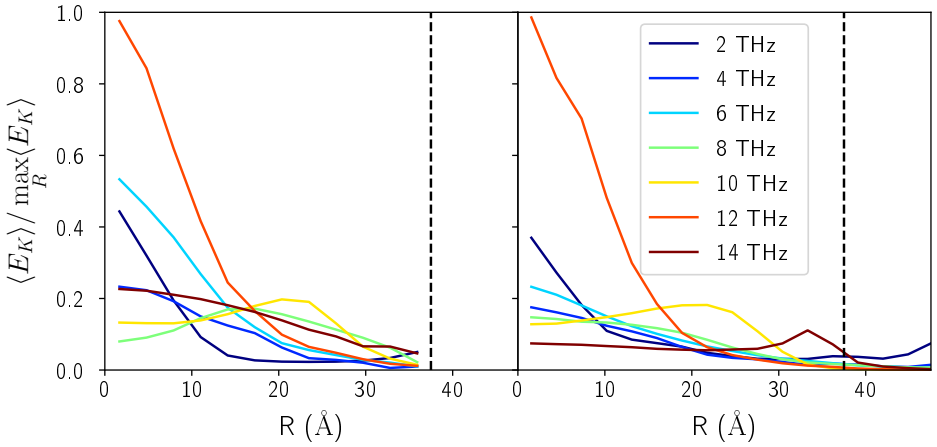

Figure 3.13: Atomic kinetic energy as a function of the radius averaged on a portion of the NWs 90 to 160 Å away from the excited layer, for the time step where the maximal intensity is reached. For the nanowires of R_{Cry}= 37.5 Å and e = 0 (left panel) or 10 Å (right panel). The vertical black dashed line represents the end of the crystalline core.

Overall, apart from complex patterns that appear at 2 THz, the radial distribution of energy during wave-packets propagation is not strongly impacted by the presence of the shell. The main effect appears to be the decrease in the intensity in the center of the nanowire for frequencies below 8 and above 12 THz. This short study of the system through wave-packets propagation, shows that even if the free surface seems to transport energy at low frequencies, most of the energy is carried by the inner parts of the NWs away from the interface or free surface. However, the realistic reconstruction of the radial flux distribution from these simulations is not trivial. To access it more easily, NEMD simulations are performed.

[3]Which is consistent with the interpretation of the minimum of mean free path around this frequency (see figure 3.9)

3.2.3 Radial Distribution of Flux: Effect of the Shell

To study the flux, NEMD simulations are carried out. The procedure used is the one described in section 1.6.1. Before setting up the temperature gradient, the NW are equilibrated at 300 K for 500 ps with an NPT (isothermal-isobaric) thermostats, to prevent buckling. After this thermalization, the boundary conditions in the growth direction are switched from periodic to fixed to avoid a direct interaction between the heat baths. The atoms within 10 Å of the extremities are fixed to avoid free surface effects, and the atoms from 20 to 10 Å away from those extremities are thermostated at 320 K on one side and at 280 K on the other. In these thermostats, a simple velocity rescaling method is used[4]. The flux is averaged over the last 1000 ps of a 2000 ps simulation, when the steady state is reached. The steady state is considered reached when both the temperature profile is stabilized and the energy exchanged at the thermostats increases linearly with time. For better statistics, these simulations are repeated 5 times for each configuration, with each time a different initial velocity distribution. This can give an idea of the uncertainty, an example is given in appendix B.

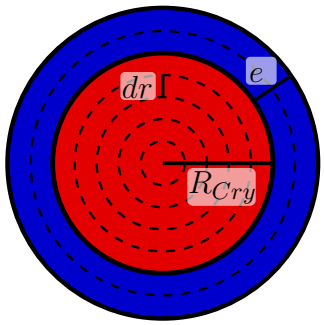

Figure 3.14: Schematic representation of the cross-section with R_{Cry} the radius of the crystalline core (in red) and e the thickness of the amorphous layer (in blue). The dotted lines represent the discretization for the computation of the flux as a function of the radius.

The flux is computed in concentric shells of thickness $\delta r = 2.5$ or 5 Å (see figure 3.14) from 10 Å away of the thermostated regions. Each studied configuration is listed in table 3.1. For the largest configurations, a smaller shell thickness is used to decrease computing time. The flux is computed through the equation (1.53), sampled every 0.5 ps and averaged over the steady state. Equation (1.53) involves a sum over the atoms, so that in the center of the NW there are fewer atoms per shell. This decreased number of atoms increases the variability of the computed flux, in particular, when the concentric shell have a thickness of 2.5 Å. For this reason, the average over two shells is used for radii inferior to 20 Å.

The results for the nanowires of R_{Cry}= 37.5 Å are reported in figure 3.15. First, it appears that with or without shell the flux is maximum in the center of the NW, stays high until R = 20 Å and decreases as it comes closer to the free surface/interface.

[4]Using a NH does not affect the results (see appendix B)

This is very similar to what was observed by Verdier et al. [Verdier *et al.* 2018a]. The overall shape recalls a Poiseuille flow. Whereas, in the amorphous shell, the flux does not depend on R. There, the reduced MFP, renders the non-local effects negligible and diffusive transport is recovered.

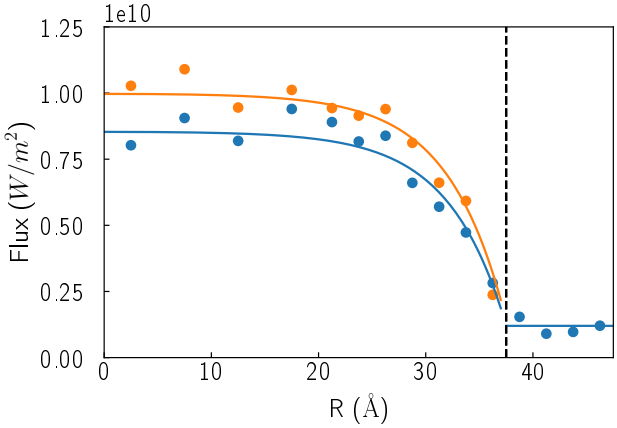

Figure 3.15: Flux in the NW as a function of the radius for R_{Cry}= 37.5 Å and $e = 0$ (blue) or 10 Å (orange). The dots report the value obtained with equation (1.53) in the different layers, and the full lines the flux obtained with the hydrodynamic heat transport equations ([1.23] and [1.27]). The vertical black dashed line represents surface/interface position.

The heat flux profile of the pristine and core shell NWs are very similar, the only notable difference is the decrease of the flux in the center of the crystalline core. An overall reduction of the flux/thermal conductivity in the crystal due to the addition of an amorphous layer has already been observed for thin films [Verdier *et al.* 2019]. A first explanation for the flux decrease observed near the surface/interface, can be looked for in modifications of the available vibrational modes in the crystalline core. For instance, high frequency localized modes could appear in the region where the flux is decreased. Alternatively, a softening could be observed, explaining a thermal conductivity decrease. To test this hypothesis, the partial VDOS in the different layers of the NWs with or without shell are represented in the figure 3.16. The same procedure as in section 3.1.2 is used. As for the nanowires of smaller radius of section 3.1, only the crystalline layer within 5 Å of the surface/interface (red dashed line) is affected. This corresponds to the layer where the structure of the crystal differs the most from bulk c-Si due to the surface re-structuration or influence of the crystalline shell as discussed in section 3.1.1, a more in-depth analysis is given in appendix B.4. On the contrary, in the inner core, the partial VDOS is very close to the one of c-Si, and in the shell very close to the one of a-Si. In the end, the perturbations of the partial VDOS does not extend to the whole region where the flux is reduced. As a result, the local flux variations cannot be explained simply by modifications of the available modes in the NW core.

The heat flux profile obtained can be modeled with the hydrodynamic heat transport equations. As explained in the section 1.2.3, the hydrodynamic heat transport

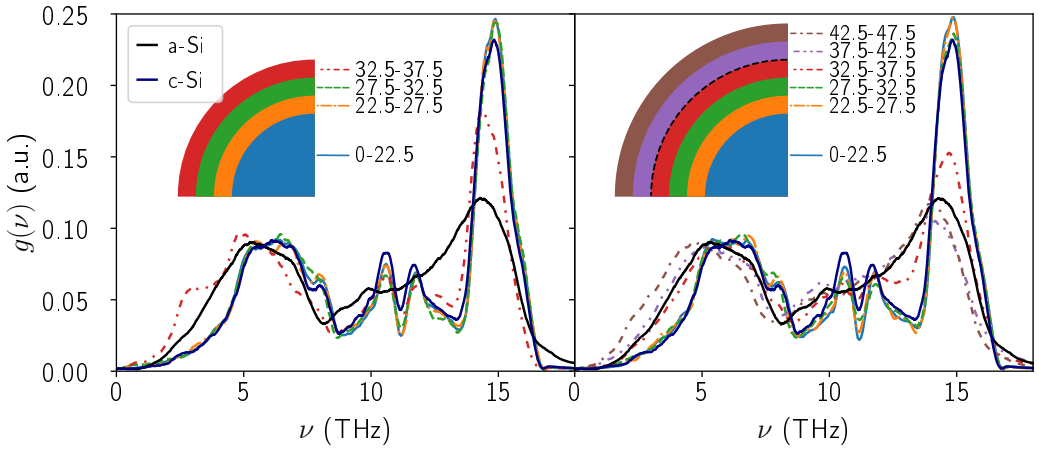

Figure 3.16: Partial VDOS of the different layers in the nanowires of R_{Cry}= 37.5 Å and e = 0 (left panel) or 10 Å (right panel), the VDOS of bulk c-Si and a-Si are also depicted in, respectively, dark blue and black full lines. The insets give the different colors associated with the different layers of the NW. In the inset, the black dashed line represents the interface.

equations are continuous equations derived from the Boltzmann transport equations. They take into account the usual thermal conductivity, but also a relaxation time and non local effects [Sendra *et al.* 2021]. Here, to reproduce the heat flux profile, the same temperature gradient is imposed across the NW, and the different parameters of the equations (1.23) and (1.27) are fitted to reproduce the results obtained with NEMD simulations. This is done using the finite element method, with the software *COMSOL Multiphysics* [Beardo *et al.* 2019]. Note that, as the steady state is considered reached, equation (1.23) is simplified, and the memory term vanishes. Consequently, the only non-Fourier term that survives is the Laplacian term associated to shear viscosity effects ($l^2[\nabla^2\mathbf{j}]$). To obtain the fits, each parameter is adjusted one after the other, κ is set first to fit with the central plateau obtained with MD, then the decrease is adjusted by modifying ℓ and finally C is fitted to correspond to the flux at the interface. Each fitting is performed using a least square minimization on the concerned region. The solid lines in figure 3.15, are obtained using this method, for the flux in the crystalline core. In the amorphous shell, the flux does not depend on the radius and is modeled by a Fourier law with $\kappa = 1.5\,\mathrm{W\,m^{-1}\,K^{-1}}$, which is consistent with the value reported for a-Si in chapter 2.

The parameters used to obtain the profiles in the crystalline part are reported in the table 3.2. The easiest parameter to interpret is C, it defines the flux at the interface/free surface. It depends on the specularity of phonon scattering at the interface [Beardo *et al.* 2019]. It appears clearly in the figure 3.15 that the flux within the last 2.5 Å crystalline layer before the interface is the same whether there is an amorphous shell or not. This explains why the value of C does not depend on the presence of the shell. In the other hand, the non local length ℓ characterizes

the distance over which the flux is affected by the boundary, it can be understood as a length over which the flux is self correlated. This depends on the dispersion relation in the crystal and the relaxation time [Sendra *et al.* 2021]. In the present situation, ℓ characterizes how deeply the heat flux in the core is impacted by the free surface or interface. Again, in figure 3.15 the flux starts high in the center and plateaus until R = 20 Å, with or without shell. Thus, neither ℓ nor C can explain the heat flux profile modifications appearing with the addition of an amorphous shell. Therefore, the influence of the amorphous shell can not be directly related with a significant modification of boundary scattering within this model. The decrease of the saturation value is best modeled as a decrease of the effective intrinsic thermal conductivity κ in equation (1.23). Indeed, the values obtained are very low compared to the one of c-Si (≈150 $\mathrm{W\,m^{-1}\,K^{-1}}$), and of the order of the thermal conductivity of nanowires of larger diameter. In the following of this section the origin of this thermal conductivity decrease will be studied.

Table 3.2: Values of the parameters of equation (1.23) used to obtain the flux profile of the different NWs.

R_{cry} (Å)	e (Å)	κ ($\mathrm{W\,m^{-1}\,K^{-1}}$)	ℓ (Å)	C
37.5	0	12.5	5	0.3
	10	10.7	5	0.3
	20	10.7	5	0.3
50	0	14	8	0.3
	10	12.3	8	0.3
	20	12.3	8	0.3

Impact over the Dispersion Relation A first approach to understand the decrease of κ is to monitor the dispersion relations with or without shell. The influence of the shell on the parameters of the hydrodynamic heat transport equation could be explained by a modification of this relation. Indeed, both κ and ℓ depend on the group velocity and the relaxation time [Sendra *et al.* 2021]. The Dynamical Structure Factor and dispersion relations are displayed respectively in figure 3.17 and 3.18.

Even before the extraction of the dispersion relations, it appears that the main features of the DSF, with or without amorphous shell, are very similar. In both cases, the acoustic branch appears clearly between 0 and 17 THz. The main difference between the two is the background noise, appearing in the DSF when there is an amorphous shell. This corresponds to a-Si modes as discussed in section 3.1[5].

The dispersion relations extracted from the DSF, are displayed in figure 3.15. For a more meaningful comparison, the dispersion given by the maximal intensity is filtered with a polynomial filter rather than fitted to a sine function as suggested

[5]Note that the small branch at low frequencies associated to surface modes discussed in section3.1 appears here also.

in section 1.5.2. It appears clearly that the two curves superimpose nicely. So that the shell does not impact the dispersion relation in the NW for the propagation in the principal direction, and thus does not impact the group velocity either.

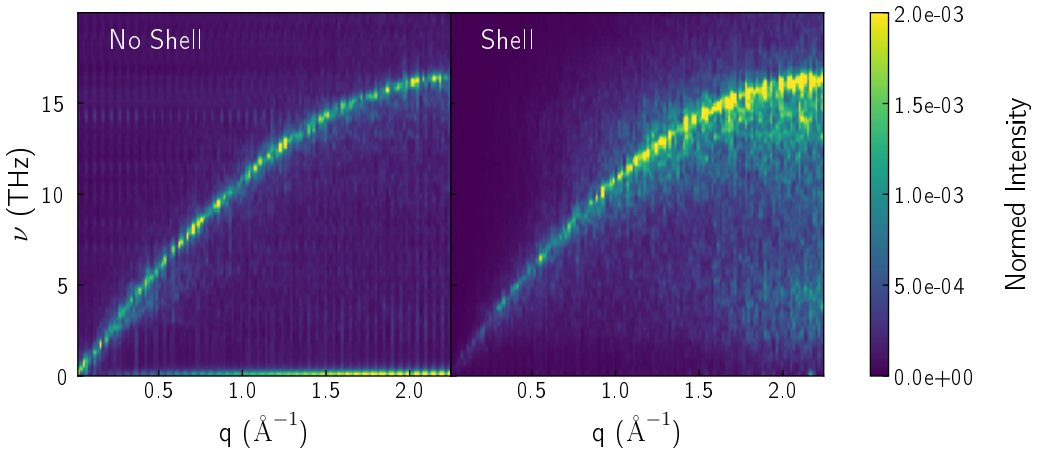

Figure 3.17: Dynamical structure factor in the ΓX direction, projected on the longitudinal polarization for the nanowires of R_{Cry}= 37.5 Å and e = 0 (left) or 10 Å (right).

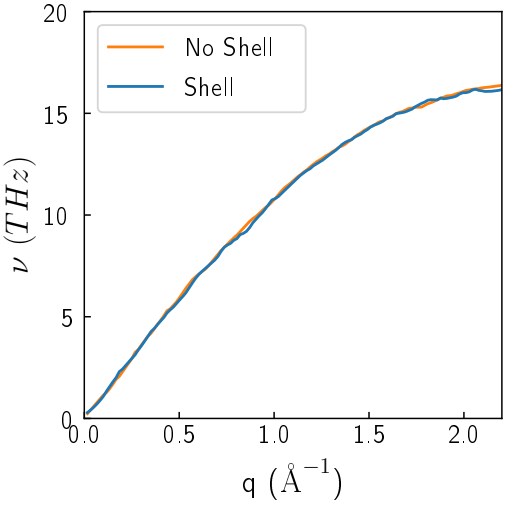

Figure 3.18: Dispersion extracted from the DSF for the nanowires of R_{Cry}= 37.5 Å and e = 0 or 10 Å.

Impact over the Mean Free Path The remaining microscopic quantity that can be linked to the mesoscopic transport parameters is the MFP, or phonon life time. The phonon lifetime can be extracted from the DSF using the Damped Harmonic Oscillator (DHO) (see section 1.5.2) and is given by the enlargment of the DSF around the line of maximum intensity (linewidth). To obtain the MFP, the life time is simply multiplied by the group velocity. The results are displayed in figure 3.19.

The MFP without shell is, overall, larger, in particular above 6 THz. This increase can be linked to the linewidth increase (and thus MFP decrease) due to the amorphous modes visible in figure 3.17 for the NW with an amorphous shell. Two small peaks are also visible in the MFP of the pristine NW, around 6 and 10 THz. The MFPs obtained with this method are notably small compared to the results obtained for similar NWs using the time domain normal-mode analysis [Zhou & Hu 2016] but of the same order as the results obtained with wave-packet propagation in figure 3.9.

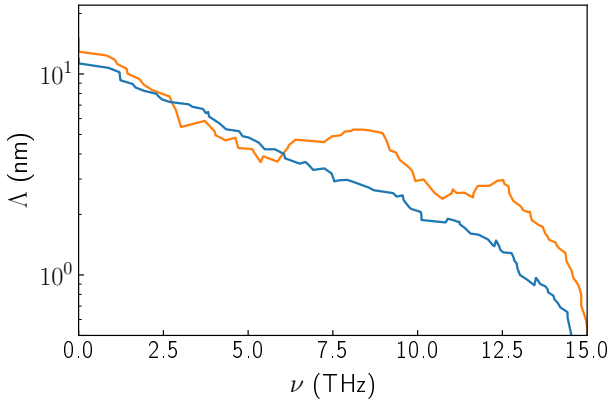

Figure 3.19: MFP as extracted using the DHO from the DSF for the nanowires of R_{Cry}= 37.5 Å and $e = 0$ (orange) or 10 Å (blue).

This MFP decrease due to the addition of the amorphous shell could partially explain the decrease in thermal conductivity. If the relaxation time appears in both the definitions of ℓ and κ (see equations [1.24] and [1.26]) it is not weighted equivalently in both expressions. And the MFP/relaxation time variations may affect mostly one over the other. Low frequencies are less impacted by the addition of the shell, probably because the interface is transparent for these frequencies [Shao *et al.* 2018, Yang *et al.* 2018]. As ℓ is less sensitive to the variation of the relaxation time at high frequencies than κ, the variation of the MFP as a function of frequency may explain why κ is affected by the shell and not ℓ. However, as the MFP is measured on the whole NW including the amorphous shell the decrease might be overestimated.

In this section, it is shown that the heat flux in a crystalline NW is comparable to a Poiseuille flow. Its maximum is in the center of the NW and decreases as it comes closer to the free surface or interface. The flux at the interface is similar whether there is an amorphous shell or not. The main effect of the shell is to reduce the saturation value in the center of the NW. Such a flux profile can be reproduced with the hydrodynamic heat transport equations, the variation due to the addition of the shell being reproduced by a decrease of the effective κ in the crystalline core. In the amorphous shell, the flux does not depend on the radius and can be modeled by a Fourier law. Before pushing the analysis

further, it is interesting to study the effect of the variation of the shell thickness and crystalline core radius.

3.2.4 Modulation of Diameter and Shell Thickness

In this section, size effects are explored with a study of the impact of the R_{cry} and e. To this end, the larger NW and the two shell thicknesses are considered.

In the figure 3.20 the flux for the different R_{cry} are represented, without shell (left panel) or with a 10 or 20 Å shell (right panel). In both cases, the profiles are very similar for the two crystalline radii. The only difference is the saturation level that increases with the crystalline radius. As in figure 3.15, the flux decreases in the vicinity of the interface and has the same value in the amorphous shell for the two radii.

The flux distributions for shells of 10 and 20 Å are displayed in the right panel of figure 3.20 (red and olive dots for R =50 Å, blue and gray dots for R = 37.5 Å). The reported values are very similar for both thicknesses. This shows that the shell thickness does not affect the flux in the crystalline core. The two first values, for radii below 15 Å, for the smaller NW with the thick shell (R_{cry} = 37.5 Å and e = 20 Å) do not fit this analysis. However, as in the first concentric shells, the average in equation (1.53) is performed over less atoms and thus more statistical variations can be expected, this difference is not considered relevant.

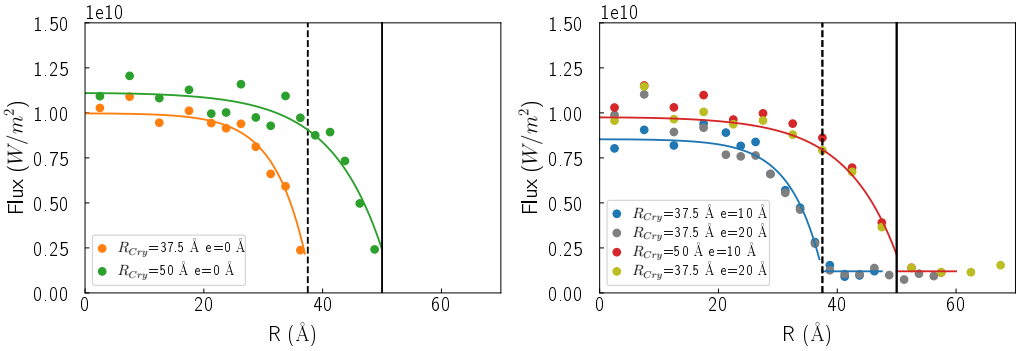

Figure 3.20: Radial flux distribution for R_{cry}=37.5 and 50 Å, without shell (left), and with a shell (right). The orange, blue, and gray represent respectively the value without shell and with a 10 or 20 Å thick shell for R_{cry}=37.5 Å. Likewise, the green, red, and olive represent respectively the value without a shell and with a 10 or 20 Å thick shell for R_{cry}=50 Å. The dots report the values in the different layers computed with equation (1.53), and the full lines the distribution modeled by the hydrodynamic heat transport equations (1.23) and (1.27). The vertical black full and dashed line represent, respectively, surface/interface position for R_{cry}=37.5 and 50 Å.

The parameters used to reproduce the distributions using the hydrodynamic heat transport equations are reported in table 3.2. It first appears that the same value is used for the slip coefficient C in each case. This could be predicted from

the similarity of the flux at the interface in the different cases. Then as the radius increases, κ is increased to reach the higher saturation level in the center of the NW. Again, this value is slightly reduced upon the addition of a shell. The non local length ℓ is also increased when switching from R_{cry}=37.5 to 50 Å. A similar effect has already been found for telescopic NWs [Melis *et al.* 2019]. Again, it is worth noting that both κ and ℓ in equation (1.53) are linked to the MFP. The MFP increases as the radius increases (see figure B.4), this can thus explain the variations of κ and ℓ. It is worth noting that the thickness of the shell does not impact these values, only the presence or absence of the shell impacts the flux distribution.

In this section, it appeared that increasing the amorphous shell thickness does not affect the flux in the crystalline core. In the other end, increasing the radius of the core increases the flux in the center of the NW, but does not change the shape of the radial flux distribution profile.

3.2.5 Discussions

The radial energy distribution of the wave-packet in figure 3.13 can be compared with the NEMD results. For instance, little energy is transported ballistically in the amorphous shell. This is consistent with diffusive transport in amorphous Si [Tlili *et al.* 2019]. This diffusive transport explains that the heat flux in the amorphous shell can be approximated by a Fourier law.

Secondly, as one gets closer to the interface/surface, there is less energy transmitted. For most of the explored frequencies, the energy maximum is reached in the center of the NW. This energy distribution can be seen as a qualitative measure of the flux at different frequencies. The energy density reported, multiplied by the group velocity, would give an approximate flux at each frequency. However, this approach is too crude for a direct heat flux estimation, as the frequencies need to be weighted according to the Bose Einstein distribution and the other propagation direction/polarization considered. Nevertheless, the radial distribution of energy in the wave-packets indicate that the individual heat carriers may already favor a Poiseuille like flux radial distribution.

The results from the NEMD simulations, confirms that the intensity of the heat flux is low at the interface/surface and in the amorphous shell. Moreover, the overall flux is flat beginning from the center of the NW and decreases as it comes closer to the interface. This decrease appears at a distance of 20 Å from free surface or crystalline/amorphous interface. This is similar to what was found through MD and Monte-Carlo simulations [Verdier *et al.* 2018a, Liu *et al.* 2019b], and with MD and hydrodynamic heat transport equation [Melis *et al.* 2019] without shell.

Impact of the Amorphous Shell The lack of impact of the shell thickness over the flux profile apparently contradicts the results of Shao et al. [Shao *et al.* 2018] who reported that the specularity decreased when the thickness increases. However,

in their definition of specularity they included the diffusion in the shell, whereas here only the interface matters. This also contradicts the interpretation of the decrease in thermal conductivity in the CS NW as an effect of the crystalline amorphous interface, decreasing the specularity of boundary scattering compared to the free surface [Malhotra & Maldovan 2019]. It is also to be noted, that the crystalline/amorphous interfaces are not visually rougher than the free surface of the crystal.

The only parameter of equation (1.23) that is affected by the addition of the amorphous shell is κ. The increase of R_{cry} increases both ℓ and κ. As in the NWs studied, the dispersion relations are not affected, neither by R_{cry} nor by the shell presence or thickness (see appendix B.3), the variations of those parameters are probably due to variation of the MFP/relaxation time, as discussed in 3.2.3. However, a decrease of MFP is not the only hypothesis that could explain a decrease of κ. By definition, the thermal conductivity in equation (1.23) considers that the behavior is ballistic at the microscale (it is based on the phonon gas picture). However, figure 3.11 shows that at high frequency, part of the transport is diffusive in the core and in the shell. A partially diffusive transport usually corresponds to an amorphous like thermal conductivity, for which the phonon gas model breaks down [Allen & Feldman 1993, Larkin & McGaughey 2013, Beltukov *et al.* 2018]. This transition contributes to a decrease of κ, since the diffusive part becomes more important at the expense of the dominant ballistic part, and manifests itself as a decay of the effective κ in equation (1.23).

Since the specularity at the interface does not appear to be modified by the addition of the shell, the hydrodynamic heat transport equations suggest that the reduction of thermal conductivity due to the addition of shell cannot be solely explained by a reduced specularity at a c-Si/a-Si interface than at a free surface.

Limitations and Perspectives The simulations carried out can be compared to the continuous models within the limit of their validity. As stated in section 1.2.3, in the original implementation of hydrodynamic heat transport equation, ℓ and κ are estimated from *ab initio* simulations on the bulk properties of silicon [Sendra *et al.* 2021]. This estimation gives a value of a few hundred of nanometers for ℓ. However, in the present case, the diameter of the NW (7.5 nm) is below half this value, so that the *ab initio* derived parameters are no longer valid [Sendra *et al.* 2021]. They are replaced by empirical values, to fit the results obtained with the NEMD method. The resulting curves correspond well to the NEMD results, not only in the present study, but also in a previous work [Melis *et al.* 2019]. Even though the *ab initio* calculated parameters can not be used, it is shown here that the phenomena observed in the NEMD simulations can be captured with equation (1.23). Nevertheless, as the diameter is further decreased, this analysis appears to reach its limit. For instance, for a radius of 25 Å, to fit the MD profiles with equation (1.23) both κ and ℓ have to be increased (see appendix B.5). Moreover, around this diameter, other authors suspect a change of regime

inducing an increase in thermal conductivity due to the selection of the modes by the geometry [Zhou *et al.* 2017]. Also, it is important to note that, here the surface are very smooth, so that the results might differ if roughness is introduced.

One of the observation of the study is that when recreating the profiles with equation (1.23) and boundary condition (1.27) the addition of the shell induces a decrease of the "global" parameter κ and does not affect ℓ and C, that influence the flux near the interface. This relies on the hypothesis the specularity of the interface affects the flux locally. However, at the scale considered, it might affect the whole structure. Indeed, the MFP is of the order of the diameter, and the wavelength is not negligible in front of the diameter so that boundary effects might affect the flux in the whole NW and not just at the interface.

The determination of thermal conductivity with NEMD shows strong size effects [Schelling *et al.* 2002b] so that the radial distribution obtained may depend on the length of the NW. This may affect more the pristine NWs than the CS NWs [Gao *et al.* 2014]. However, the point of this study is to compare the distribution of energy upon the addition of an amorphous shell at constant length. However, an impact is expected as even in NWs of the diameter considered here, phonon with a large MFP are expected to play an important role on thermal conductivity [Zaoui *et al.* 2016]. This importance of long MFP phonons can induce size effects.

There is a small discrepancy between the flux computed with equation (1.53) and the flux computed from the energy exchange rate at the thermostat (see appendix B.2). This discrepancy is lower than the uncertainty due to the statistical distribution of the results over the repetitions. However, a trend can be noted, without shell the discrepancy is higher, and it increases for thicker NWs.

3.2.6 Conclusion

In this section, the radial flux distribution obtained by a NEMD simulation of nanowires of diameter of 37.5 and 50 Å, pristine or with an amorphous shell, are computed. For all NWs, the distribution in the crystalline part is similar: it resembles a Poiseuille fluid flow. The addition of an amorphous shell decreases the heat flux in the center of the NW, but the flow at the boundary of the crystalline part is not affected by the presence of a shell. To go further, this profile can be reproduced with the hydrodynamic heat transport equations (equations [1.23] and [1.27]), for this the parameters need to be adapted. Doing so, it appears that the addition of the shell can be reproduced by a decrease in the thermal conductivity used to model the transport in the crystalline core, such a behavior has already been predicted for other geometries [Verdier *et al.* 2019, Shao *et al.* 2018]. The non Fourier parameters of the equation do not appear to be impacted for the geometries considered. As a result, within this model, the effect of shell is global, rather than localized at the interface. It is interpreted as a lack of impact of the shell on the specularity at the interface (as it is taken into account inside the model). The effective thermal conductivity decrease may be linked to a partially diffusive heat transport, and

to a modification of the MFP spectra. A clearer picture may be obtained with a frequency dependent analysis of the thermal conductivity [Sääskilahti *et al.* 2015].

In this chapter, the study of vibrational properties of silicon nanowires with a crystalline diameter of 5 nm showed that the addition of an amorphous shell modifies the transport of phonons. The amorphous shell not only impacts the properties of the free surface, but also the transport in the crystalline core. This impact is noticeable on the MFP spectrum. If low frequencies seem to be the most impacted by the addition of an amorphous shell, the whole spectrum is affected. Following on these results, the heat flux in these NWs can be modeled using a mesoscopic approach. The model used shows that the addition of the shell does not correspond to a modified boundary condition but to a reduced effective thermal conductivity.

Synthesis of the Chapter

- The amorphous shell forming at the surface of NWs affects the vibrational properties
  - The low frequencies are more impacted due to a strong interaction with the waves at the surface
  - At high frequencies the propagation takes place in the center of the NW and is less affected by surface or interface
- The radial heat flux distribution in Si NWs resembles a Poiseuille flow
- Core/Shell NWs and pristine NW share a similar flux profile in the crystalline core
  - Only the maximal flux is decreased
  - The flux at the free surface and interface are similar
  - The shell thickness does not affect the profile
  - In the shell, the flux is independent of the radius
- The radial distribution of flux can be reproduced using the hydrodynamics heat transport equation with fitted parameters
  - The addition of shell corresponds in this model to a decrease of κ while the non Fourier parameter are constant
  - The heat flux in the shell can be fitted with a Fourier law
  - An increase of the diameter corresponds with this model to:
    - a slight increase of the non local length
    - an increase of the thermal conductivity
- These results indicate that it is necessary to go beyond simple usual descriptions of the specularity to take properly into account boundary effects induced by the shell in core shell NWs

Chapter 4

Thermal Rectification in Nanowires with a Conical Amorphous Shell

Contents

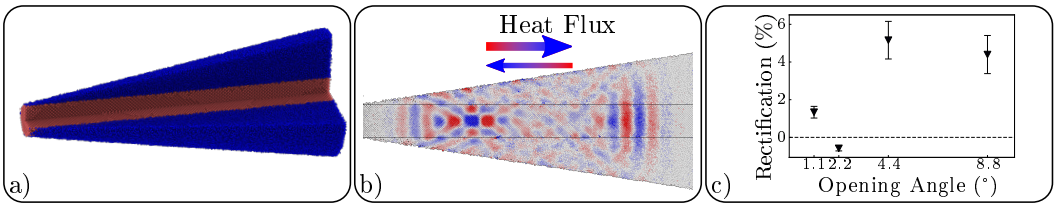

Visual Abstract: Overview of the configurations studied in this section: asymmetrical core shell nanowire (a), asymmetrical transport (b), reported thermal rectification.

Thermal rectification describes the dependencies of the heat transport not only on the temperature difference, but also on the direction of the thermal gradient. In reference to the electronic diode, devices having such a property are called thermal diodes. A schematic representation of a thermal diode is given in figure 4.1.

A large panel of methods can be used to induce thermal rectification, any it is possible with kind of heat transport: conductive [Kobayashi *et al.* 2009], radiative [Ben-Abdallah & Biehs 2013], convective [Wong *et al.* 2019]. Thermal diodes can be designed from the nano to the macroscale [Roberts & Walker 2011a]. If the main

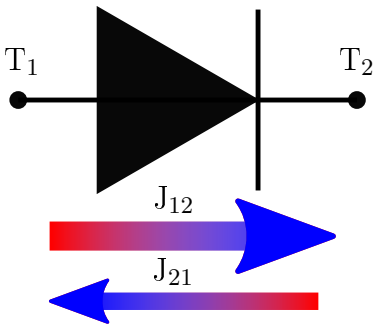

Figure 4.1: Schematic representation of a thermal diode with J_{12} as the preferential flux direction.

application for thermal rectification is thermal management, the control of the heat flux direction has other applications, such as thermal computing [Wang & Li 2007, Sklan 2015, Wehmeyer *et al.* 2017]. Here the focus is on thermal rectification using heat conduction through the lattice at the nanoscale.

Considering conduction only, thermal rectification appears when the effective thermal conductivity depends on the sign of the thermal gradient. Thus, it relies both on the space and temperature dependence of κ. Terraneo *et al.* [Terraneo *et al.* 2002] have shown that such a dependence was possible using a monoatomic chain with an anharmonic interaction potential. This model has then been adjusted for different temperatures [Li *et al.* 2004]. Peyrard has proposed a simple model to estimate rectification using a spatial and temperature dependence of κ, and to optimize the rectification as a function of the temperature gradient [Peyrard 2006]. The different strategies used to get thermal rectification are regrouped in recent review articles [Roberts & Walker 2011a, Liu *et al.* 2019a, Wong *et al.* 2021]. The two main approaches are either to join two materials with different thermal properties or to take advantage of geometrical effects.

Thermal rectification can be induced through the junction of two materials. For this, several configurations have been proposed: in metal/insulator junctions, the rectification is due to the direction dependent electron-phonon scattering rate at the interface [Roberts & Walker 2011a]. An insulator/insulator junction can induce rectification as well, if the thermal conductivity has a different temperature dependence on each side [Kobayashi *et al.* 2009]. The interface properties themselves can even induce rectification in bulk systems [López-Suárez *et al.* 2018, Hahn *et al.* 2015]. Interface induced rectification has also been predicted between graphene nanoribbons with different carbon isotopes [Pei *et al.* 2012], or at the interface between a nanotube and a silicon substrate [Zhang *et al.* 2013]. Finally, a crystalline Si/amorphous polymer interface has been predicted to cause rectification due to the strong temperature dependence of the vibrational modes of the polymer, causing the interfacial conductance to depend on the direction of the thermal gradient [Hu *et al.* 2008].

At the nanoscale, the geometry of the samples can induce rectification as well. At this scale, size effects impact the thermal conductivity and its dependence on the temperature [Li *et al.* 2003b] and promotes the localization of phonons [Hu *et al.* 2018]. These effects have been used to induce rectification in asymmetric nanostructure using suspended graphene and diamond cones [Wang *et al.* 2014, Lee & Hwang 2012], silicon thin films [Ju & Liang 2012b] and carbon nanotubes [Wu & Li 2007]. Experimental studies have shown rectification induced by asymmetrically mass loaded nanotubes [Chang *et al.* 2006], asymmetric nanoribbons [Wang *et al.* 2017], and very recently, for silicon thin films with a gradual hole concentration [Kasprzak *et al.* 2020]. Rectification using Si NW is an already documented subject, telescopic shaped NW [Cartoixà *et al.* 2015] or sawtooth roughness [Roberts & Walker 2011b] have been proposed. Finally, it is worth mentioning that rectification has been predicted for silicon nanocones, a geometry very close to NWs [Zhang *et al.* 2016].

In asymmetric geometries, where more mass or mass density is present on one side, the majority of the existing literature reports an increased heat flux toward the direction of decreasing mass or mass density. This mass gradient is created either by using an asymmetrical shape or by mass loading one side. This bias direction has been linked to the increased scattering rate in the lighter (smaller) part [Wang *et al.* 2017], the dependence of κ on space and temperature [Dettori *et al.* 2016], or the Vibrational Density of States (VDOS) mismatch between the smaller (lighter) and larger (heavier) sides [Yang *et al.* 2009]. However, Ju *et al.* [Ju & Liang 2012a] have predicted a higher heat flux from the smaller to the larger cross-section of a Si trapezoid thin film, showing that the heat conduction is not always higher from the heavier regions to the lighter ones. Similarly, Wang *et al.* [Wang *et al.* 2017] have obtained a better flux from a defected graphene region to a pristine one than in the opposite direction, and, more recently, Kasprzak *et al.* [Kasprzak *et al.* 2020] have also shown a better heat flux from the high-porosity region toward the low-porosity region in a silicon thin film.

In this section, the structuration of the amorphous shell of crystalline NWs is used to induce an asymmetric transport and thus thermal rectification.

4.1 Vibrational Properties of Asymmetrical Core Shell Nanowires

In the previous chapter, the effect of the addition of an amorphous shell on a pristine NW was studied. Here, a similar analysis is made on CS-NWs with a varying shell thickness, creating an asymmetric structure. This structure is created to induce direction dependent transport properties, that are not possible in fully symmetric structures. First, the new geometries are described and their global vibrational properties described, before analyzing the results of wave-packet propagation to finally estimate the different contribution to the thermal conductivity.

4.1.1 Modeling of the Configurations

The asymmetrical core shell NWs are created by increasing the thickness of the amorphous shell linearly to form conical-shaped NWs. They will be referred to as conical core shell NWs or CO-CS-NWs (see figure 4.3). The added amorphous starts with a null thickness at one extremity to reach 0.9, 1.9, 3.8, or 7.6 nm at the opposite extremity. This results in an opening angle $\phi = \arctan(\frac{R_{Shell}-R_{Core}}{L})$ of 1.1°, 2.2°, 4.4° or 8.8° respectively, with R_{Shell} the maximal shell radius, R_{Core} the core radius, and L the NW length (see figure 4.2). These NWs are obtained and relaxed with the same procedure as the CL-CS-NW (see section 3.1.1).

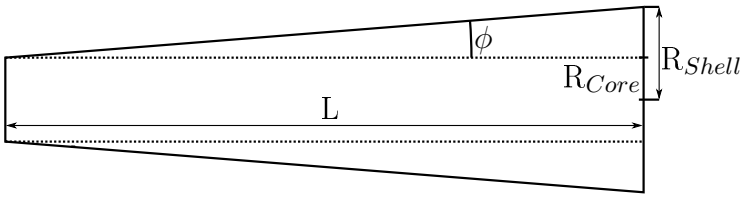

Figure 4.2: Geometry of the CO-CS-NW, with the length L, opening angle ϕ, and core and shell radius. The dashed line represents the crystalline amorphous junction.

Before going on with the study, it must be noted that constant diameter crystalline NWs embedded in a conical amorphous shell are not common. Nanowires can take a conical shape, as the result of the competition between catalyzed axial growth and uncatalyzed radial growth. In this case, the resulting NW is fully crystalline. Alternatively, the oxidation could result in the formation of an oxide shell of uniform thickness. Nevertheless, cylindrical core/conical shell structures have already been obtained experimentally by Lin *et al.* in 2004 with a silicon carbide core and an amorphous silica shell [Lin *et al.* 2004] and by Huo *et al.* with TiO_2 nanowire cores and carbon conical shells [Huo *et al.* 2008]. These elaboration examples show the possibility of realization of such asymmetric NWs, via chemical vapor deposition.

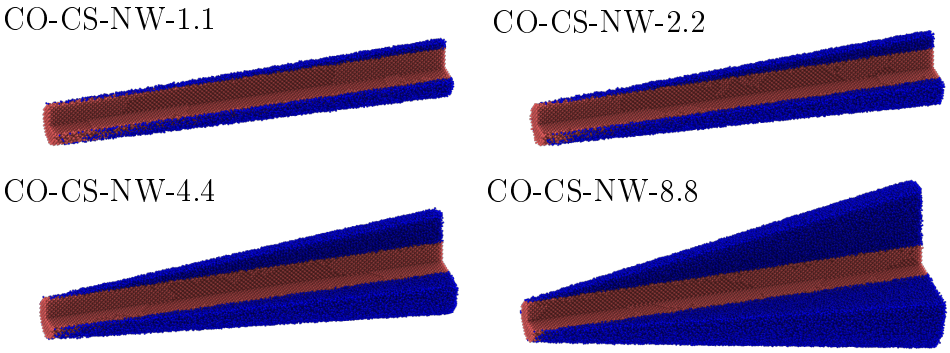

Figure 4.3: Visualization of the conical core shell nanowires (CO-CS-NW) with different opening angles. The crystalline core is colored in red in red and amorphous shell in blue.

4.1.2 Vibrational Density of States

As for the cylindrical core shell nanowire (CL-CS-NW), let's first study the VDOS, to see the eventual impact of the shell geometry on the frequency distribution of the modes. For this, the VDOS of the different coaxial hollow cylinder of the crystalline core of the NW are plotted for different longitudinal sections of the NW (see figure 4.4). It appears that, the VDOS of the core of the conical core shell nanowire with $\phi = 4.4°$ is not affected by the position along the growth direction (here represented by the colors) but only by the proximity to the crystalline/amorphous interface (see figure 4.4). The VDOS in the crystalline core is not affected by the thickness of the amorphous layer above it, but only by the proximity to the crystalline/amorphous interface.

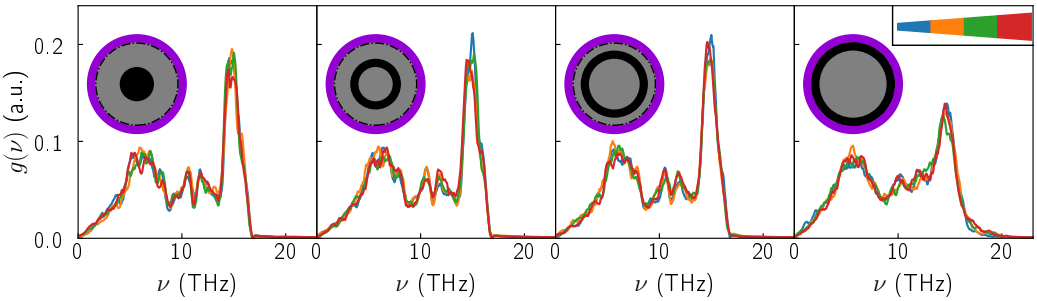

Figure 4.4: Vibrational density of state for different coaxial hollow cylinder of the crystalline core (four columns) and for different section along the CO-CS-NW-4.4 (colored lines). The insets left of each figure link the column and the considered hollow cylinders. The black circle in the insets represents the part of the nanowire core considered, the gray the whole crystalline core, and the amorphous shell is represented by the purple outer circle and is not to scale. The mixed line represents the crystalline amorphous interface. The inset in the upper right links the section and the colors of the lines.

The analysis of the VDOS at the different length portion does not indicate any strong dependence to the thickness of the shell. The VDOS of the different layers are very similar to the VDOS of the constant shell thickness CS-NW. As a result, asymmetric behavior can be noted by a simple study of the VDOS.

4.1.3 Wave-Packet Propagation

The VDOS does not indicate a change of vibrational properties of the core as a function of the position. To showcase eventual direction dependent properties, wave-packet propagation simulations can be used. For this, the same method as for the CL-CS-NW is used. A force excitation at particular frequency is made in the center of the NW at $L/2$. This allows distinguishing the propagation in the small to large direction (SL) and in the large to small direction (LS).

Qualitative Visualization of the WP As for the constant thickness core shell NW, let's start with a qualitative description of the displacements and kinetic energy distribution in the conical core shell nanowire with the largest opening angle. The largest opening angle has been chosen as it amplifies the difference between the directions. The same frequencies as in chapter 3 are selected for the qualitative analysis.

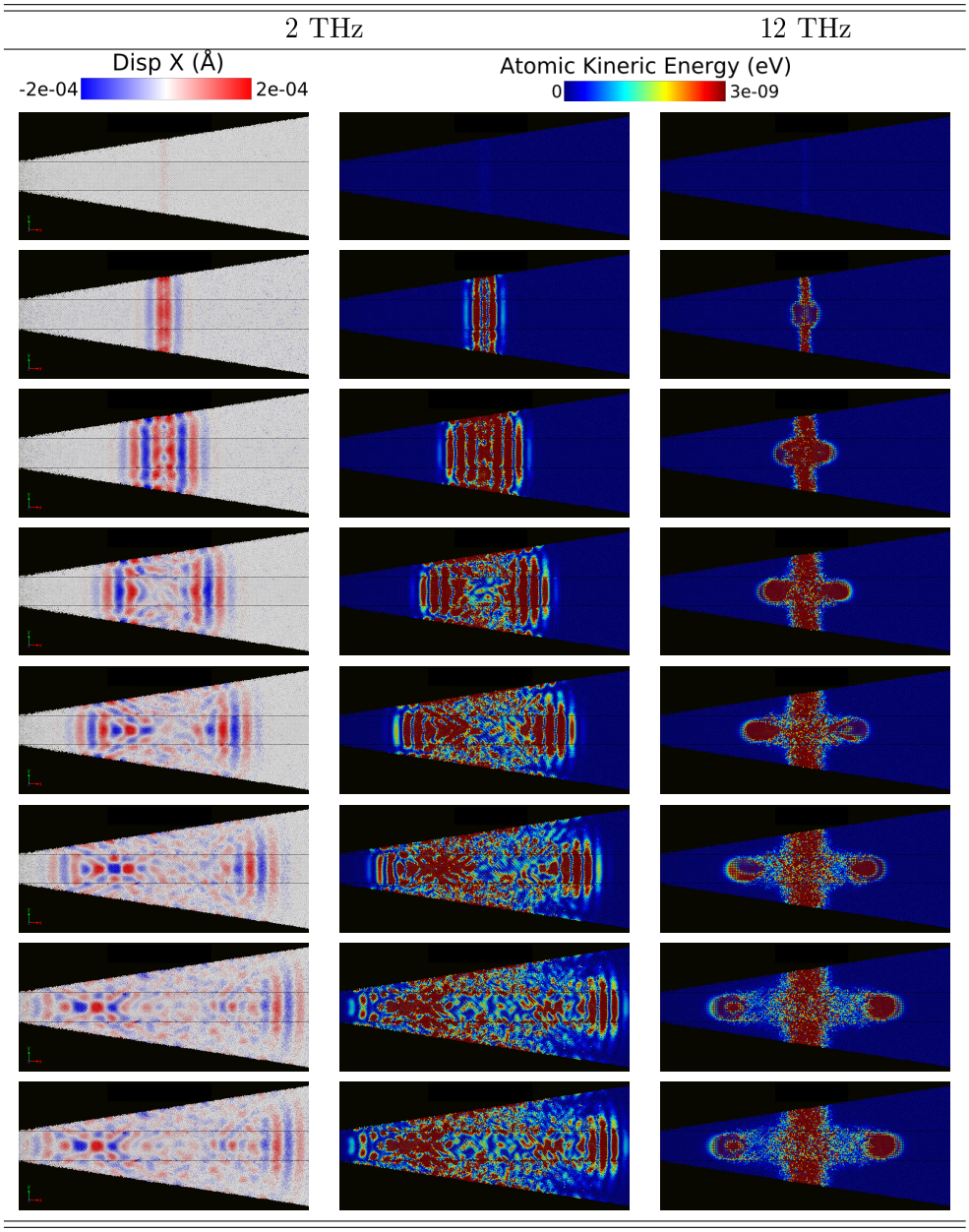

Figure 4.5: Cross-sectional view of wave-packet evolution after a longitudinal excitation in the CO-CS-NW-8.8. Left column: Atomic displacement in the polarization direction with an excitation at 2 THz. Middle column: The atomic kinetic energy at 2 THz. Right column: The atomic kinetic energy at 4 THz.

For this nanowire, the propagation is asymmetric at low frequencies. This asymmetry appears in the energy distribution in the central column of figure 4.5. Contrary to what was observed for cylindrical core shell thickness nanowire (CL-CS-NW), the wave-packet travels without coherence losses in the Small to Large cross section direction (SL) (the maxima and minima of kinetic energy are visible during the whole propagation). In the Large to Small cross section (LS) direction the WP is more dispersed/attenuated, the behavior is similar to what was observed for a constant shell thickness (see figure 3.6). The shape and reduced thickness of the shell induces strong interactions between the waves supported by the shell and by the core in the converging LS direction, but keep them apart in the diverging SL direction. This coupling is confirmed by the analysis of the displacements in the left column of figure 4.5: in the SL direction, the wave front travels through the NW without coherence loss, through core and shell alike. But in the LS direction, the wave in the shell is phase shifted, with different displacement directions for a given x. As observed for the CL-CS-NW, this phase shifted surface wave seem to interact with the wave in the core. This phenomenon is affected by the shell thickness: for a thicker shell, the wave in the core is less affected by the free surface (see right column of figure 4.5), whereas for thinner shells, either for the CO-CS-NW-8.8 in the LS direction or for the CL-CS-NW, a clear phase shift occurs at the interface (see figure 3.8). A sufficiently thick shell seems to shield the transport in the core from the effect of the free surface.

For the transverse polarization (figure 4.6), still at low frequency, the effect of the shell thickness is less clear. The phase shift at the interface does not disappear in the SL direction. However, shell and core seem to interact more in the LS direction than in the SL direction, with larger displacements at the interface.

At higher frequencies, here represented by 12 THz for the longitudinal polarization and by 4 THz for the transverse polarization, the behaviors in the SL and in the LS directions are much more similar. In figures 4.5 and 4.6 (rightmost columns), the propagative part[1], exiting the excitation zone, takes an ellipsoidal shape limited to the inner core as was visible in figure 3.6 for symmetric geometries. The energy left behind by those propagating waves is dispersed evenly in the core section. The absence of irregularities on the WP path could explain why the MFP is higher than at lower frequencies, where the interfaces continuously hinder the propagation.

In the CO-CS-NW-8.8, the WP propagation is direction dependent at low frequencies. When the amorphous shell is thick enough, the wave at the surface and the wave in the core stop deforming each other and WP travels without coherence loss creating a direction dependent transmission[2].

[1] Akin to a regular phonon or a propagon

[2] Note that direction dependent propagation is different from region dependent that cannot lead to rectification without an additional temperature dependence [Chakraborty *et al.* 2019]

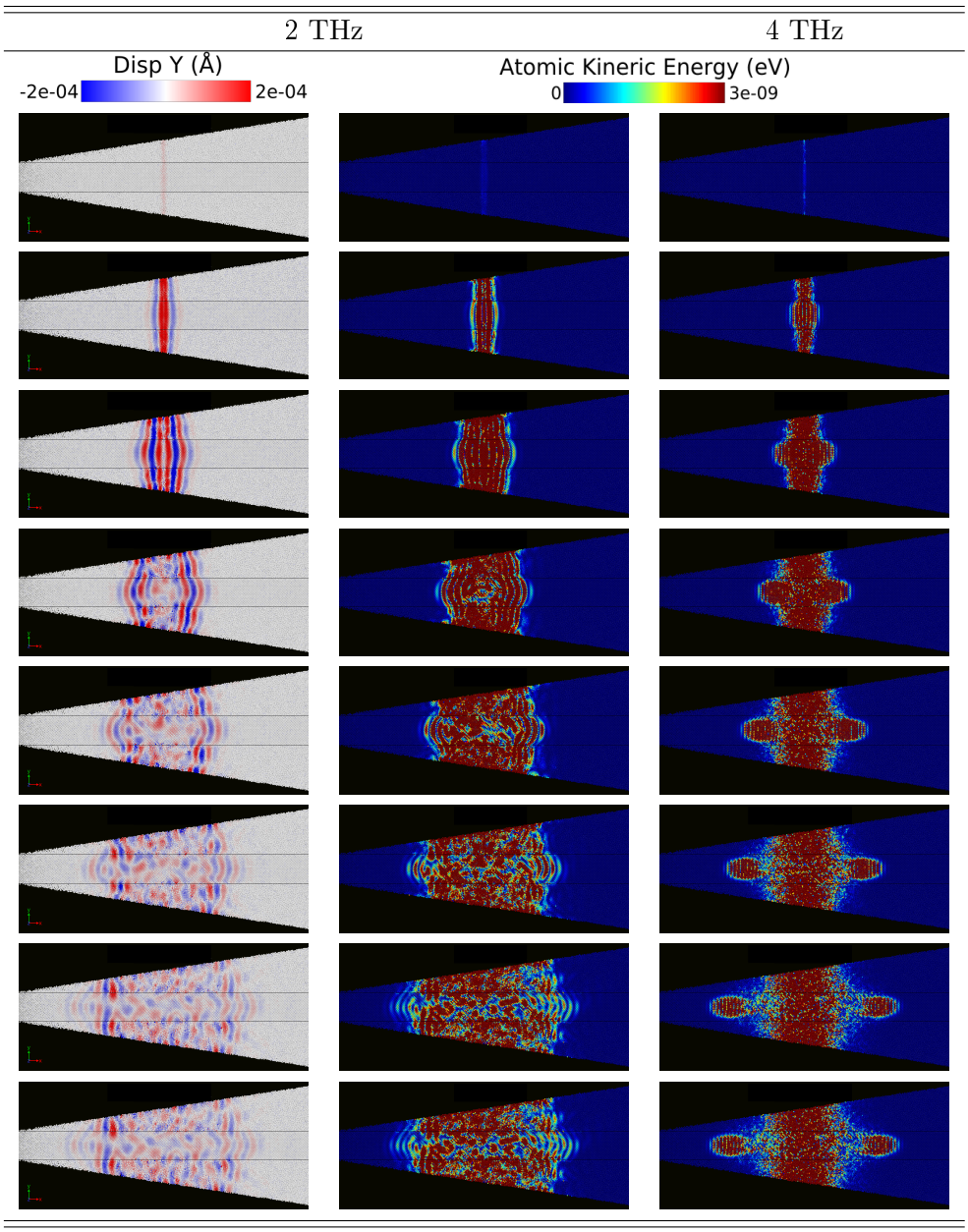

Figure 4.6: Cross-sectional view of wave-packet evolution after a transverse excitation in the CO-CS-NW-8.8. Left column: Atomic displacement in the polarization direction with an excitation at 4 THz. Middle column: The atomic kinetic energy at 2 THz. Right column: The atomic kinetic energy at 4 THz.

Distribution of Kinetic Energy The asymmetry of propagation is first studied through the representation of the kinetic energy distribution as function of the position along the principal axis for the core and shell in figure 4.7. After the initial nonrandom excitation, two parts are visible at all frequencies: a propagative wave traveling along the NW mainly inside the core of the NW and a slowly broadening

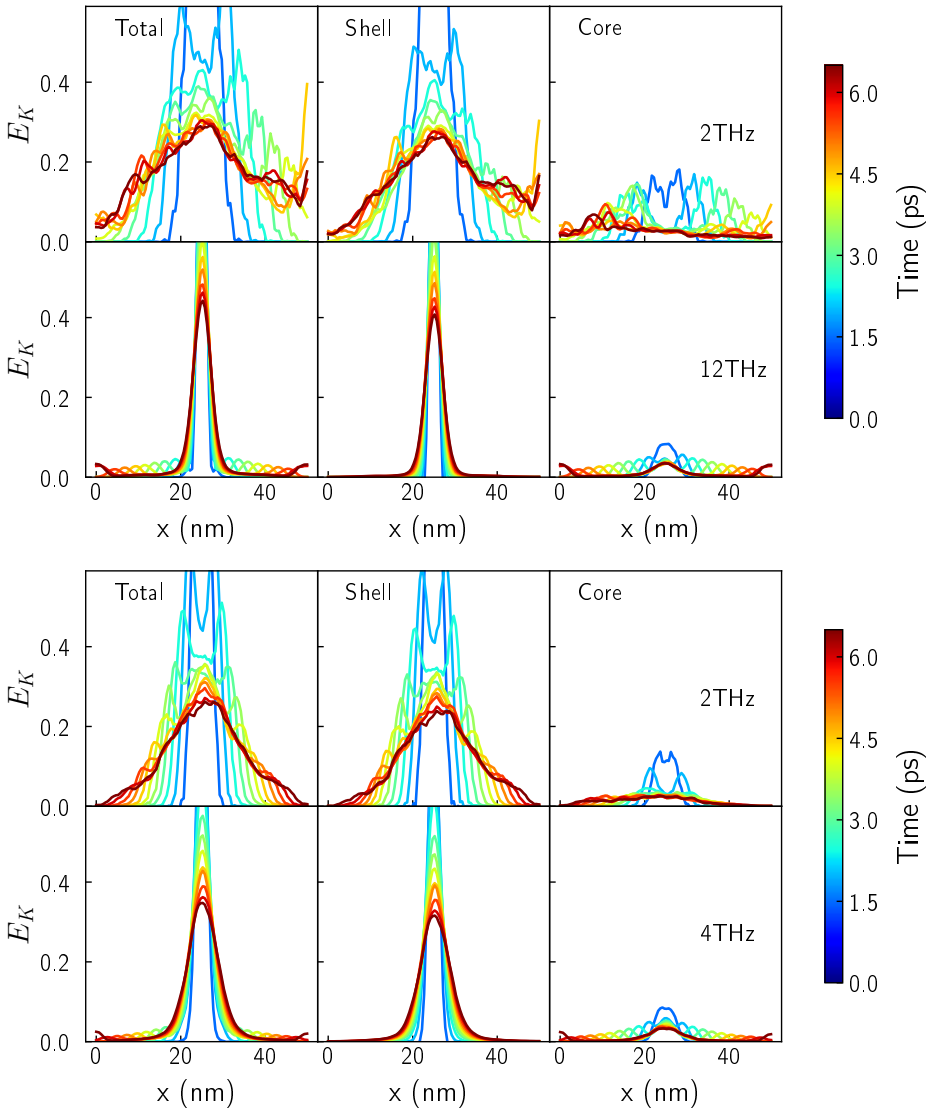

Figure 4.7: Evolution of the kinetic energy distribution along the wire (sum of atomic kinetic energy in each of the individual slices filtered with a polynomial filter) after a longitudinal (upper figure) or transverse (lower figure) excitation for the CO-CS-NW-8.8. The total energy is separated in the core and the shell at 2 THz (first row of each panel) and 12 THz for the longitudinal excitation (second row of the upper figure) and 4 THz for the transverse one (second row of the lower figure). The energy is normalized by the maximum value for the whole NW.

diffusive peak. In figure 4.7 the propagative part manifests as distinct lobes that are shifted in the propagation direction at every time step. These features are particularly visible for the CO-CS-NW-8.8 at 12 THz (figure 4.7 first figure bottom row) but are present to some extent in all CO-CS-NW at all frequencies below 15 THz. The diffusive peak is present in both shell and core, as for the CL-CS-NW. This central peak is mostly visible at 12 THz for the longitudinal excitation,

and at 4 THz for the transverse excitation, but is nevertheless already present at 2 THz for both polarizations. This diffusive behavior of thin core shell Si NWs was already observed by Donadio *et al.* [Donadio & Galli 2009], although this behavior was thought to be limited to the amorphous layer. As a purely propagative behavior is expected in c-Si, a diffusive part indicates either an energy transfer from the shell to the core or an influence of the interface on the propagation. The influence of the amorphous shell on the crystalline core vibrational properties has already been assessed in figure 3.3. Atoms in the core, within 0.5 nm from the interface have a very similar VDOS to the one of a-Si, but this limited effect is not sufficient to explain the diffusive transfer inside the whole crystalline core. This must be due to a strong dynamical effect induced by the long-range influence of the amorphous/crystalline interface.

Additionally, there is no important propagation of high-frequency phonons in the shell and the propagation in the core is not affected by the shell thickness at those frequencies. However, for the diffusive transport, a slight asymmetry is visible in the diffusive peak in the shell after a transverse excitation at 5 THz (figure 4.7).

Another mark of the interactions between the shell and the core can be seen in figure 4.7: the energy distribution in the core for the CO-CS-NW-8.8 in the Large to Small (LS) direction after a transverse excitation does not follow a monotonous decrease from the excitation origin to the end of the NW. On the contrary, it increases, confirming that there is an energy transfer from the shell into the core.

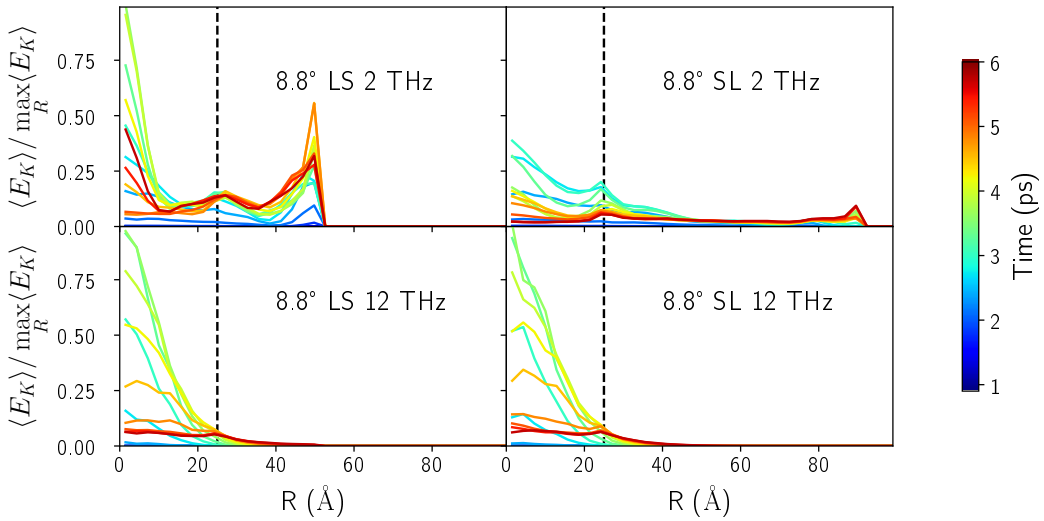

Figure 4.8: Atomic kinetic energy as a function of the radius in 7-nm-thick slice, 9 nm away from the excitation source after a longitudinal excitation, for different time steps, for the CO-CS-NW-8.8 at 2 Thz (upper row) and 12 THz (lower row). The energy values are normalized by the maximum value for each given frequency. The vertical dashed line represents the amorphous/crystalline interface.

The visualizations of the atomic kinetic energy can be completed by the visualization of E_K as a function of the radius (see figure 4.8) with this time a distinction

between the SL and LS directions. For the 2 THz excitation, there is a clear wave propagation at the free surface, as observed for the pristine and CL-CS-NW in figure 3.7. However, in this case the wave at the surface is asymmetric, it has a high amplitude in the LS direction and a low amplitude in the SL direction. This is most probably due to the convergent and divergent geometries. The asymmetry is also visible in the core, where the amplitude is higher in the LS direction, this higher amplitude can be linked to the redirection of energy from the shell to the core. Likewise, it is noticeable that the energy remains high for a longer while in the LS direction, indicating a stronger dispersion of the WP. Finally, the radial kinetic energy distribution of the CL-CS-NW in figure 3.7 is very similar to the one of the CO-CS-NW-8.8 in the LS direction. This similarity hints that the proximity of the surface has a strong influence on low-frequency phonons. At 12 THz the differences between the SL and the LS directions disappear; the energy mainly flows in the core for both directions.

Moreover, for low frequencies, there is a net energy exchange between the core and the shell. This is visible through the unbalanced energy ratio between the two sides of the excitation in figure 4.9. There is more energy in the shell and less in the core for the SL part of the NW for all CO-CS-NWs. As the energy is overall evenly distributed between the SL and LS parts when considering the whole NWs (see upper panels of figure 4.9), this distribution is only possible through an energy transfer between the core and the shell. The shell transfers energy back to the core in the LS direction, especially in the low-frequency range, confirming that the wave in the shell interacts with the wave in the core. The energy distribution for the shell of the conical core shell nanowire with $\phi = 1.1°$ seems different from the others opening angles. This can be explained by the reduced number of atoms in the shell (see figure 4.3b) making the energy ratio more sensitive to small variations.

To conclude on the qualitative analysis of the WP propagation in asymmetric NWs: in the large to small direction the constriction tends to redirect energy from the shell to the core at low frequency, the strong interaction between the wave at the surface and propagation in the core is disturbed in the large to small direction.

Quantitative Analysis of the WP The effects of the geometry on the heat transport can be estimated through the evaluation of the contribution of different frequencies, as done in section 2.4. The mean free path is a way to quantify the effect of the geometry on the propagation at different frequencies. For example, a higher MFP in a specific direction could result in thermal rectification. This is assessed in figure 4.10 where the MFP of longitudinal and transverse phonons with frequencies between 1 and 15 THz in both directions of propagation in the NW (LS and SL) are depicted for the CO-CS-NWs and the CL-CS-NW for comparison, along with the VDOS of the configurations.

Firstly, it is noticeable that the unusual frequency dependence of the MFPs

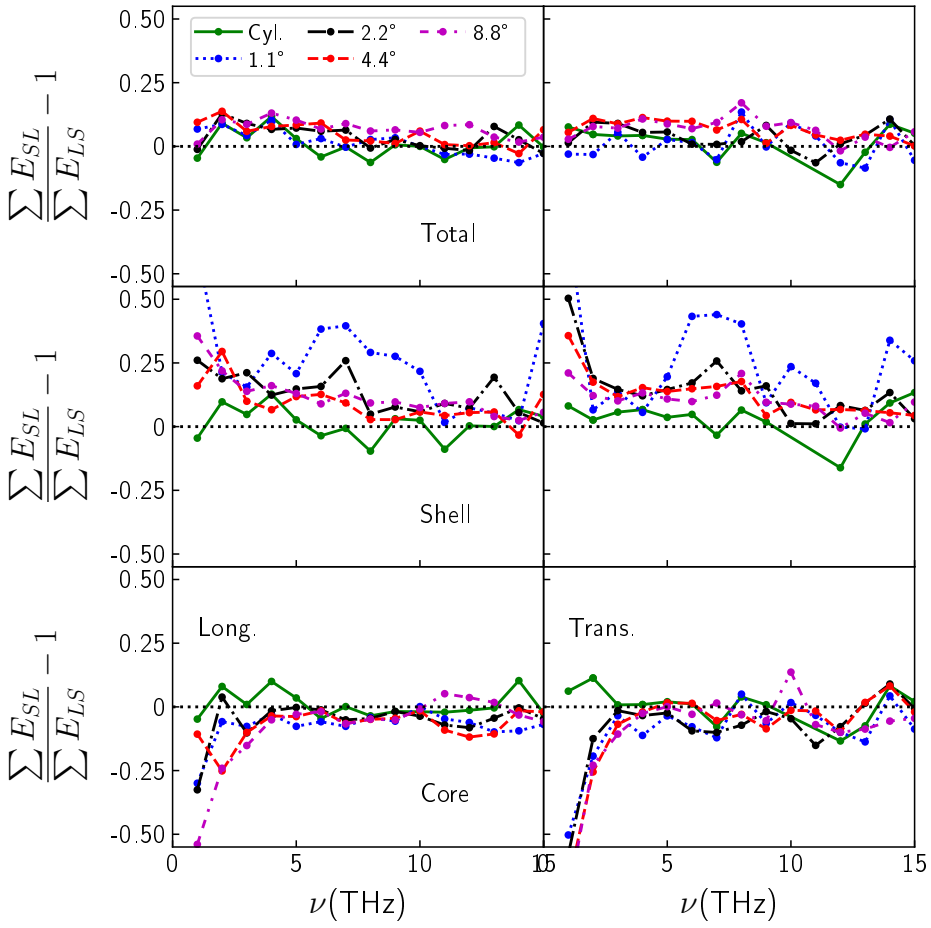

Figure 4.9: Kinetic energy ratio: Sum of atomic kinetic energy in the SL direction (e_{SL}, right of the excitation) divided by the sum of atomic kinetic energy in the LS direction (e_{LS}, left of the excitation), and the mean from the end of the excitation of propagation until the wave front reaches the boundaries. For the longitudinal (left column) and transverse (right column) excitation.

observed for the CL-CS-NW in section 3.1 appears for all the CO-CS-NW. In particular, the MFP peak at high frequencies (11 THz) is visible for all configurations.

Then, the transport in the small to large (full lines) and in the large to small (dashed lines) direction can be compared. For longitudinal phonons, the MFP is higher in SL than in LS direction at low frequencies (1-3 THz) for conical core shell nanowires of opening angle 4.4° and 8.8°. The transverse phonons at 1-2 THz have, similarly, a higher MFP in the SL direction. This characterizes an asymmetric transport favoring the SL direction. However, this is not the case for all frequency ranges and all configurations. For example, the MFP in the LS direction is higher in the 3-5 THz frequency range for longitudinal phonons and in the 1-6 THz frequency range for transverse phonons for CO-CS-NW-1.1. While comparing the directions, it also appears that the shoulder at 8 THz in the longitudinal MFP tends to fade

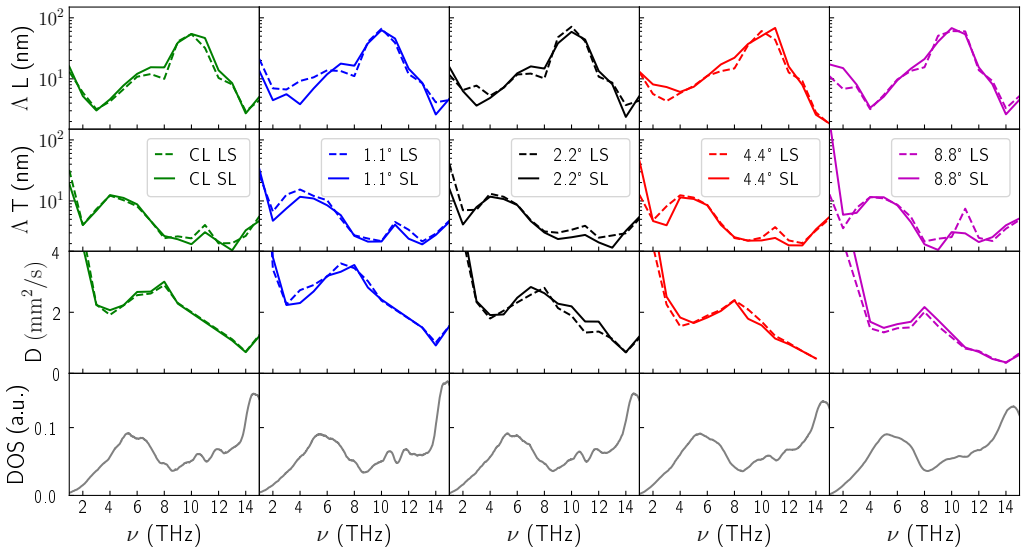

Figure 4.10: Longitudinal (first row) and transverse (second row) MFP, diffusivity (third row), and VDOS (last row) for all studied configurations. The solid colored lines represent the SL direction and the dashed ones the LS direction. The different configurations are identified by their opening angles for the CO-CS-NW and by CL for the constant thickness CS-NW.

as the opening angle increases. This fading is more pronounced in the SL direction, confirming that this plateau is correlated with the amorphous layer thickness, as was already visible for the pristine and CL-CS-NW in figure 3.9. If some asymmetry appears in the MFP, it is not possible to conclude on a global asymmetry in heat transport from those representations.

As the studied systems are composed of a large amorphous part, it is important to consider the influence of the non-propagative modes to complete the study. These non-propagating modes are visible in the kinetic energy distribution after a non-random excitation, but the diffusivity of the different frequencies can be evaluated in the SL and LS directions with the method described in 1.5.3. The results are shown in the figure 4.10 (third row). First, one can observe that the diffusivity in our systems is comparable to the bulk amorphous silicon diffusivity (see figure 2.24). This similarity appears even for the CO-CS-NW-1.1 where the amorphous shell is very thin, especially in the LS direction. In increasing the overall amorphous fraction (1.1° to 8.8° opening angles) of the systems, the diffusivity decreases. Nevertheless, when comparing the directions for the larger opening angles 4.4° and 8.8°, it appears that the diffusivity is higher in the SL direction where the amorphous shell becomes thicker. This higher diffusivity suggests a better diffusive heat transport in the small to large direction.

Finally, the global VDOS in the last row is worth taking a look at. As the opening angle increases, the peaks linked to c-Si are smoothed out. This shows the gradual importance of the amorphous shell as its thickness increases.

The analysis of the MFP and diffusivity has shown that the MFP of the different configurations are very similar to the MFP of the CL-CS-NW. However, for the asymmetric structures, differences appear between the SL and LS directions, in particular at low frequency. The diffusivity, keeps a very similar profile for all the configurations and decreases with the crystalline fraction. Yet, these variations with direction are not systematic nor strong enough to conclude on a strong asymmetry in the overall heat transfer.

4.1.4 Thermal Conductivity Estimation

The analysis of the WP showed the heat transfer in the CS-NW contains a ballistic and a diffusive component. Using the method described in 1.6.4, the frequency dependence of the thermal conductivity together with the ratio of ballistic to diffusive contributions to the thermal conductivity can be estimated. In this section, the computation for the CO-CS-NW-4.4 is detailed.

The diffusivity and MFP of the NW being already computed, the only missing quantities are the group velocity and the density of state associated to the different polarizations. These missing quantities are estimated thanks to the Dynamical Structure Factor (DSF).

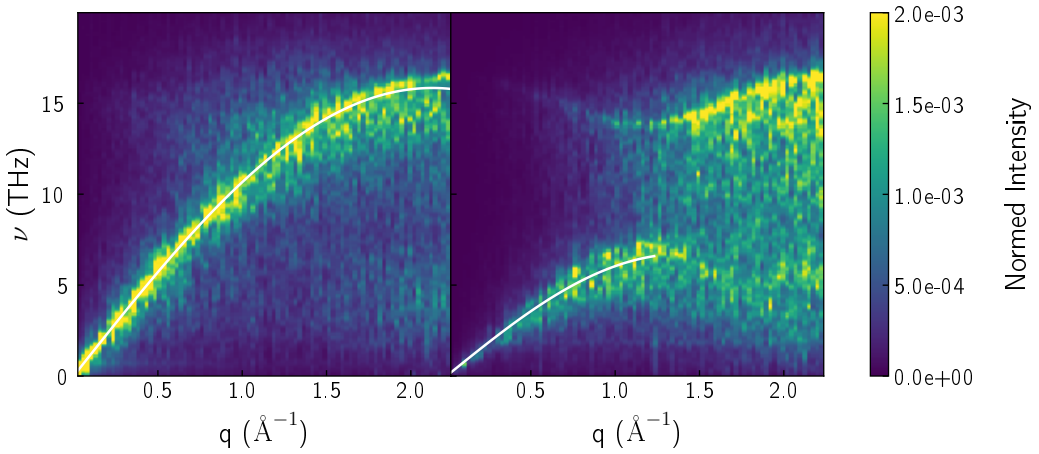

Figure 4.11: Dynamical structure factor for the CO-CS-NW-4.4, in the ΓX direction, projected on the longitudinal polarization (left) and transverse polarization (right). The white lines represent the estimated dispersion relations.

The DSF of the CO-CS-NW-4.4 is displayed in figure 4.11, along with the dispersion estimation. It was obtained using the method described in 1.5.2 (that is via the diffusive and propagative contribution to thermal conductivity estimated via equations [1.56] and [1.57]). As for the CL-CS-NW (see figure 3.5) the DSF corresponds to the superposition of the DSF of c-Si and a-Si. However, lines corresponding to the dispersion of relation are less marked, the amorphous fraction being higher in

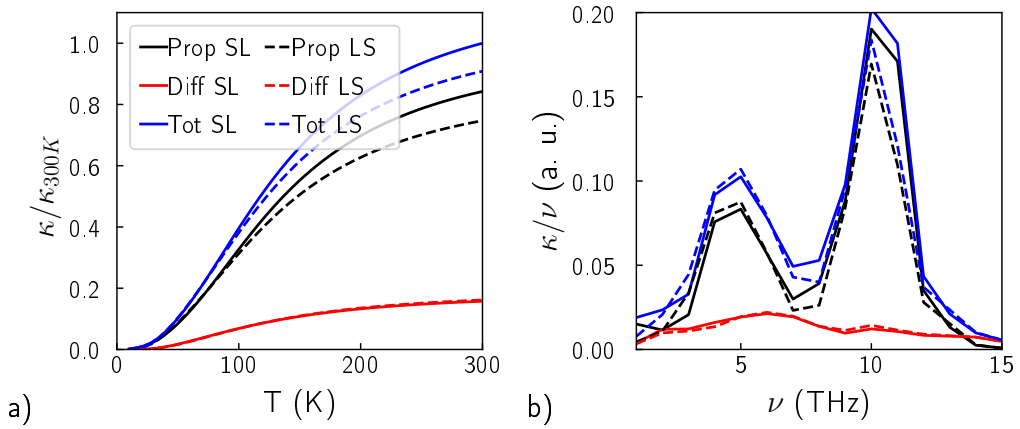

Figure 4.12: Thermal conductivity of propagative modes κ_P (in black), and thermal conductivity of the diffusive modes κ_D (in red) and total thermal conductivity $\kappa_P + \kappa_D$ (in blue) for the CS-NW-CO-4.4: as a function of temperature (a) and contribution of the different frequencies (b) at 300 K in the right panel. The dashed and plain lines represents respectively the LS and SL directions.

the case of the CO-CS-NW-4.4. The polarization dependent VDOS is estimated, from the average of the DSF in the different directions of the Brillouin zone.

The different contributions to the thermal conductivity as a function of temperature are represented in figure 4.12 (left). It appears clearly that the propagative contribution dominates the heat transport. The diffusive modes account for less than 20 % of the total thermal conductivity.

The relative contributions to κ as a function of the frequency at 300 K in the left panel of figure 4.12, shows that κ_P is higher than κ_D for all frequencies. It also appears that the peak in MFP around 10 THz has a strong effect on the thermal conductivity. However, as seen in section 2.4, this contribution might be overestimated due to the orientation of WP, selecting for the less perturbed direction. Note that here the correction for temperature is not included.

With the example of the CO-CS-NW-4.4, it has been shown, that the diffusive contribution to the thermal conductivity is 5 times smaller than the propagative one, and that both contributions appear to favor the small to large direction.

4.1.5 Conclusion

In this section, thanks to WP propagation simulations, it appeared that: the larger wavelengths seem to be more influenced by the geometry of the shell and the proximity of the interface/surface than smaller wavelengths. This can explain why the WPs are more strongly dispersed in the SL direction than in the LS direction (see

central column of figures 4.5 and 4.6). The similarity between the pattern of displacements (left column) for the CO-CS-NW-8.8 in SL direction where the section is smaller and the one of the CL-CS-NW indicates that the free surface proximity impacts the propagation in the core through the shell. Moreover, at low frequencies (around 2 THz) a wave appears at the surface and part of the energy seems to be confined at the free surface during the WP propagation. The perturbation of long wavelength modes, localization at the free surface and their effect on the thermal conductivity in thin NWs is already well documented [Rurali 2010]. For the WP at 2 THz, a phase shift appears between the center of the core and the core-shell interface, as the wave propagates in the CL-CS-NW and CO-CS-NW-8.8 (see figures 3.6 and 4.5). However, this phase shift disappears in the SL direction for the CO-CS-NW-8.8. In the larger section, the wave-packet has an ellipsoidal shape with a section larger than the core, meaning that the amorphous/crystalline interface does not perturb the propagation at this frequency in this direction. This implies that the free surface plays a more important role on the propagation than the interface in this direction at those frequencies. Whereas at higher frequencies, for instance at 12 THz (see figures 3.6 and 4.5 right column), ballistic transport happens only in the inner parts of the core where the interfaces do not affect the propagation anymore.

The diffusive transport is also influenced by the presence of amorphous/crystalline interfaces. Indeed, a diffusivity comparable to the values found in the purely amorphous samples is measured even when the amount of amorphous shell is negligible (see figure 4.10). The presence of the amorphous/crystalline interfaces aligned with the direction of propagation is thus sufficient to induce a diffusive transport in the crystalline core as well. This strong influence of the shell on the diffusive transport has been already suggested here by the presence of a diffusive part in the core after a nonrandom excitation (see figure 4.7). However, the diffusive modes are not dominant on the heat transport. It appears clearly in figure 4.12 that the propagative mode's contribution dominates the heat transport in the CO-CS-NW-4.4.

In summary, a variable thickness of amorphous shell modifies the behavior of WP imposed in the center of the NW. At low frequencies, a direction dependency appears in the large to small direction, part of the energy is transferred from the shell to the core. The conical shell seems to modify the interaction between the core and the shell, in the small to large direction, the phase shift observed for CL-CS-NW disappears. However, at higher frequencies, little difference appear. Finally, the quantitative analysis of the transport properties obtained from WP appears to indicate a direction dependent transport, without allowing a definitive conclusion. For a more definitive conclusion studies including explicitly the temperature effects are needed.

4.2 Thermal Rectification in Asymmetrical Core Shell Nanowires

In the previous section, it has been shown that the thickness variation of the amorphous shell in core shell NWs caused a direction dependent propagation of WPs. However, using those results alone, it is not possible to conclude quantitatively on an eventual thermal diode effect. In this section, the results from Non Equilibrium Molecular Dynamics (NEMD) simulations are used to study the directional dependence of thermal transport in asymmetric core shell nanowires.

Supplementary geometries In this section, two supplementary geometries are introduced to complete the study. The first one is a telescopic-shaped NW with a 3.5 nm amorphous thick shell covering half of its length, referred to as TE-CS-NW (left of figure 4.13). It is introduced to investigate the effect of an asymmetric distribution of amorphous shell without the gradual asymmetry. The shell thickness is chosen to have the same amorphous fraction as the CO-CS-NW-4.4 for the chosen NW length (50 nm). The second geometry is simply a CO-CS-NW-4.4 that has been prolonged to reach 100 nm. This geometry was introduced to investigate eventual size effects (right of figure 4.13). These configurations are created using the same method as the other geometries of the chapter. The different configurations investigated in this section are listed in table 4.1.

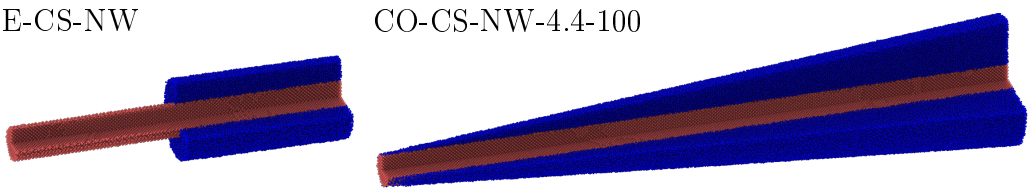

Figure 4.13: Telescopic core shell nanowire (TE-CS-NW) and conical core shell nanowire with an opening angle of 4.4° and a length of 100 nm CO-CS-NW-4.4-100 crystalline core in red and amorphous shell in blue.

Table 4.1: Effective radius, shell radius, length, total number of atoms and fraction of atoms belonging to crystalline phase for the 3 groups (in total 7 configurations) of NWs.

	CL-CS	CO-CS					TE-CS
		1.1°	2.2°	4.4°		8.8°	
R_{Effect} (nm)	3.5	2.6	2.6	2.8	3.1	3.5	2.5
R_{Shell} (nm)	3.5	3.46	4.42	6.3	10.1	10.1	6.0
L (nm)	50	50	50	50	100	50	50
N_t	95029	69617	95342	161353	689023	345766	161340
N_c/N_t	51%	70%	51%	30%	14%	14%	30%

4.2.1 Estimation of the Rectification

The effective thermal conductivity of all the samples are evaluated using the NEMD method. For this, a temperature gradient is imposed across the NW and the thermal conductivity is then derived from $\kappa = \frac{J\Delta x}{S_{Effect}\Delta T}$ with J the kinetic energy transfer rate between the thermostats, S_{Effect} the effective section (that is the smallest section that the flux crosses), and $\frac{\Delta T}{\Delta x}$ the temperature gradient. As in chapter 3, the position of the atoms within 1 nm of the simulation box edges are fixed ("f" regions in figure 4.14). Finally, the two thermostats are added next to the fixed atoms (T_1 and T_2 in figure 4.14). The number of atoms in the thermostats

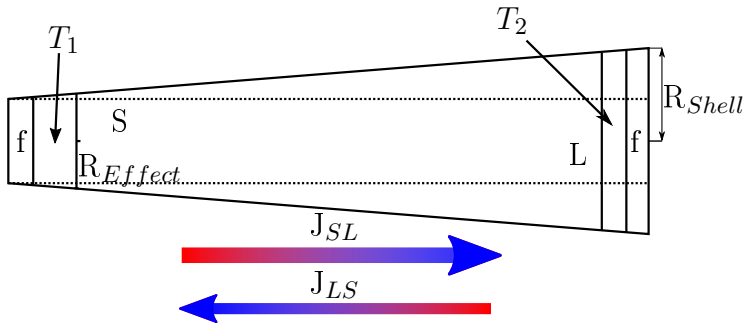

Figure 4.14: Schematic representation of the NWs, with the thermostats (T_1, T_2) and fixed atomic positions (f) on the conical CS configurations. Several characteristic elements, such as the effective, core, and shell radii, and the angle of the amorphous shell opening and large (L) and small (S) extremities of the NW are noted along with the flux direction J_{SL} and J_{LS}. R_{Effect} is the effective radius for the computation of the flux, it is here also the smallest radius that the flux crosses.

on the large side and the small side are kept similar within 1 % by varying their thicknesses between 0.5 and 5 nm. A simple velocity rescaling is used to maintain the cold side at 280 K and the hot side at 320 K for a ΔT of 40 K, or 260 K and 340 K respectively, for simulations with a ΔT of 80 K. The time step used is 0.5 fs. For the 50 np-long-NWs, the stability of the temperature profile obtained after the first 1000 ps indicates that a steady state is reached, the flux is then computed over the next 1000 ps. For the 100 nm-long-NW these times are doubled. The flux is averaged over five independent simulations with different initial velocity to decrease the statistical error (see section C.2 for details on the flux computation). The heat flux is computed twice, switching the hot and cold thermostats to obtain the heat flux in both directions. The effective section S_{Effect} considered for the computation of κ, if not otherwise specified, is the limiting cross-section for heat transport, that is, the smallest section that the flux crosses, at the end of the thermostat T_1 in figure 4.14 (the corresponding effective radius R_{Effect} is reported in table 4.1). The temperature gradient is defined as the temperature difference between the thermostats divided by the distance separating the two thermostats $\Delta x = L - L_{T_1} - L_{T_2} - 2L_f$ [Li *et al.* 2019].

The thermal rectification is computed as:

$$\eta = \frac{\langle \kappa_{SL} \rangle - \langle \kappa_{LS} \rangle}{\langle \kappa_{SL} \rangle}, \tag{4.1}$$

with $\langle \kappa \rangle$ the mean thermal conductivity over five repetitions. κ can be replaced by J in the previous equation as the thermal gradient is the same excepted for the sign, provided that the effective section is the same. The uncertainty is derived from the standard deviation σ of the thermal conductivity value:

$$\Delta\eta = \eta \left(\frac{\sigma(\kappa_{SL})}{\langle \kappa_{SL} \rangle} + \frac{\sigma(\kappa_{LS})}{\langle \kappa_{LS} \rangle} \right) \tag{4.2}$$

4.2.2 Thermal Transport and Rectification in Core Shell Nanowires

This section reports and discuss the effect of the asymmetry of amorphous shells on the overall thermal transports. In figure 4.15 both the heat flux or the thermal conductivity and the rectification (green right axis) for different directions, as a function of the opening angles of the samples, or as a function of the amorphous fraction. It appears first that the flux and the thermal conductivity in the small to large direction (red empty circle) is superior to the heat flux or thermal conductivity in the large to small direction (blue star). This observation is consistent with the less disturbed propagation of phonons in the small to large direction. There are two ways to define rectification; using the heat flux or the thermal conductivity. For a constant cross-section, the two quantities will give the same rectification. Here, as the studied configurations are asymmetric, the heat flux was chosen because it is independent of the choice of the cross-section (in figures 4.15 a and b). Nevertheless, the results in terms of the effective thermal conductivity with two different cross-sections are also depicted in figure 4.15c using the smallest cross-section (S_{Effect}), related to the vision of the nanoconstriction which usually drives the phenomena at the nanoscale, and in figure 4.15d using the cross-section next to the hot thermostat related to the vision of the energy dissipation area for a given system. The pertinence of the choice between the two cross-sections is discussed later.

In figures 4.15 a and c, it appears that the asymmetric amorphous shell induces a thermal rectification for the conical core shell nanowires with the two largest opening angles (4.4° and 8.8°) and for the telescopic core shell nanowire. The rectification, measured on the heat flux (η= 5%), is of the order of the rectification obtained experimentally for a similar system [Chang *et al.* 2006]. However, the rectification is lower for an opening angle of 8.8° than for an opening angle of 8.8°, showing that the relation between the opening angle/amorphous fraction and the rectification is not monotonic. Moreover, these simulations indicate that there is a threshold effect for rectification in either opening angle between 2.2° and 4.4° or in amorphous fraction, between 50 % and 70 % for the length L = 50 nm (figure 4.15b). The rectification measured for the conical core shell nanowires with the two smallest opening angle are not significant. Thus, an important thickness of amorphous shell is necessary to induce rectification. Moreover, as the telescopic geometry induces less rectification

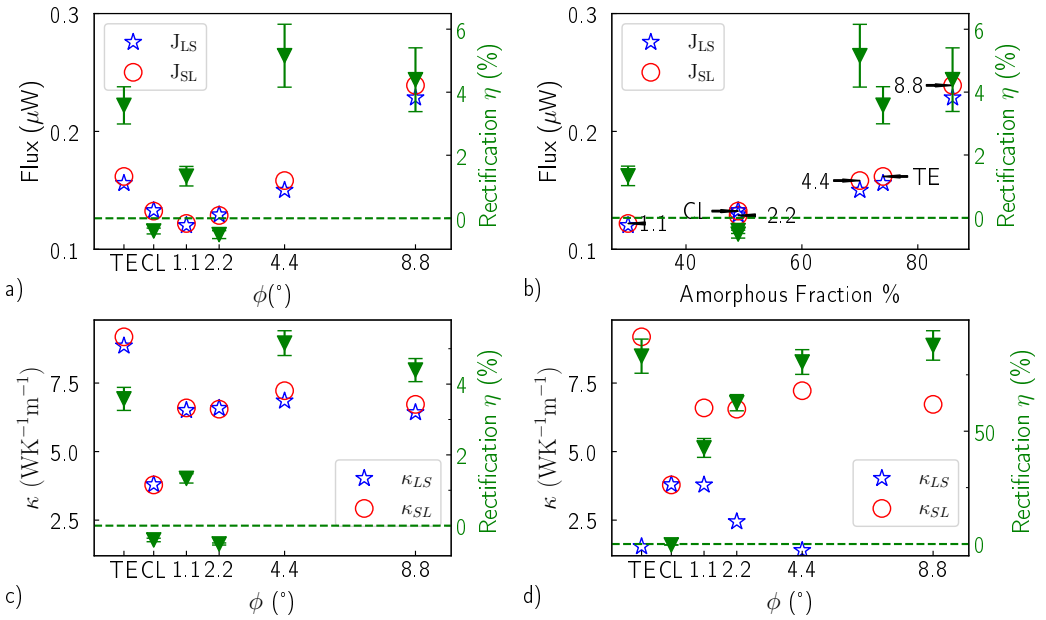

Figure 4.15: Power exchanged (flux) and rectification for all the 50-nm-long NWs as a function of the opening angle of the amorphous shell (a), of the amorphous fraction (b) or thermal conductivity and rectification as a function of the opening angle computed with the effective section defined in table 4.1 (c) or with the section next to the hot thermostat (d). The different configurations are identified by their opening angles for the (Conical Core Shell nanowire) CO-CS-NW and by TE for "telescopic" or CL (cylindrical). On the left y axis, κ_{LS} or J_{LS} are represented by blue stars and κ_{SL} or J_{SL} by red circles. The rectification values on the right y axis are represented by green triangles, with error bars determined from equation (4.2) and the green dashed line gives the zero rectification.

than the conical shell with $\phi = 4.4°$ with similar amorphous fraction, it follows that the asymmetry of the amorphous shell plays an important role, but is not the only factor responsible for the observed rectification. Finally, it is interesting to note here that the preferred direction for the flux, from small to large cross section, is not the same as the one obtained for homogeneous samples with conical shape, as shown by Wang *et al.* [Wang *et al.* 2014].

Interestingly, the total heat flux increases monotonously with the amorphous fraction (figure 4.15b). As the crystalline part has a constant diameter, an increasing amorphous fraction means that the section through which the heat flux can go through increases. The core diameter being constant, a significant part of the heat flux has to go through the amorphous shell. However, the thermal conductivity of a-Si being roughly two orders of magnitude below the c-Si one, a smaller enhancement was expected. This important difference in the total flux between the conical core shell nanowires with different opening angles indicates a considerable energy exchange at the interface between the core and shell.

All the conical core shell nanowires share similar thermal conductivity values. Once normalized by S_{Effect} (see table 4.1), the disparities in flux disappear (see

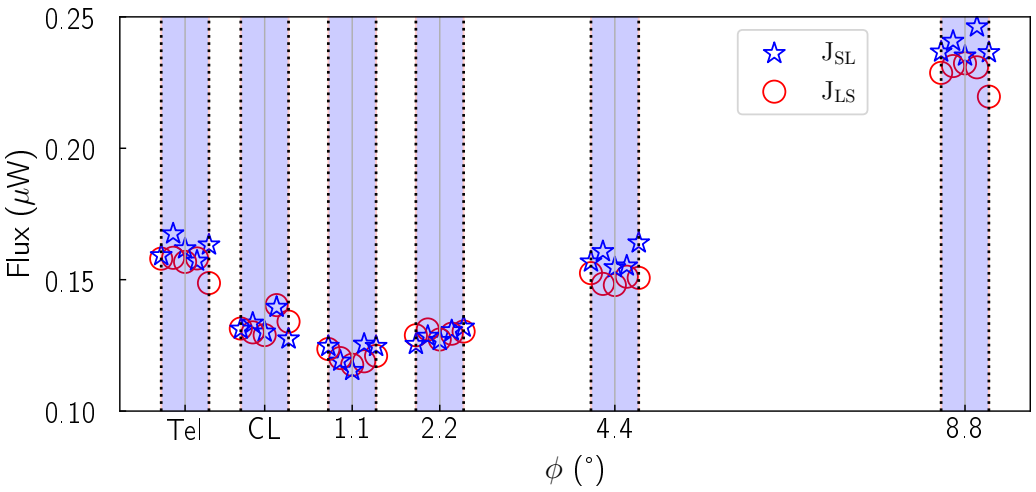

Figure 4.16: Power exchanged between the thermostat for all the 50-nm-long NWs as a function of the opening angle of the amorphous shell for every individual runs, the values within the blue shaded regions are individual runs for the same configuration. LS marks the large to small direction, while SL marks the small to large direction.

figure 4.15c). It is noteworthy that the TE-CS-NW has a much larger thermal conductivity due to the fully crystalline reduced effective section; similarly, the thermal conductivity of CL-CS-NW, having a large effective cross-section, is lower. With this effective section definition, neither the effective cross-section nor the distance between the thermostats varies. Thus, the rectification is independent of the choice of J or κ. However, as already mentioned before, the thermal rectification can change with another choice for the effective cross-section. For instance, in figure 4.15d, the estimation of the thermal conductivity using each time the section corresponding to the hot thermostat (that is the section of the incoming flux) is chosen. This choice of effective cross-section results in very high η values (90 %). However, this variation is mainly due to the change of the effective section depending on the direction of the thermal gradient. To compare the direction of propagation, a comparison of the flux or of the effective thermal conductivity using always the same cross-section is more meaningful. In all cases, the thermal conductivity estimations are of the same order as in the previous simulation of Verdier *et al.* [Verdier *et al.* 2019].

Figure 4.16 features the heat flux computed for the individual runs in both SL and LS directions. This representation of the dispersion of the measures shows that the heat flux is systematically higher in the SL direction for the conical core shell nanowires with the two largest opening angle and more dispersed in the case of the telescopic core shell nanowire. Moreover, this visualization highlights the disparity of the measure for the cylindrical core shell nanowire and the two lowest opening angle: depending on the simulation considered, the rectification is either positive or negative. This confirms that the rectification for these small opening angles is not significant.

Summarizing on the interpretation of figures 4.15 and 4.16, it was shown that the core shell nanowires with opening angles of 4.4° and 8.8° induce a flux rectification of about 5 %. This rectification favors the flux in the small to large direction over the flux in the large to small direction. This direction corresponds to the direction in which the propagation of WP was less impeded. The next paragraphs focus on the parameters influencing the measure of this rectification.

Size Effects At the nanoscale, size effect matters, to get an idea of the influence of the size on the rectification coefficient, a core shell nanowire with $\phi = 4.4°$ with a doubled length (100 nm) was studied. The results are displayed in table 4.2. For the long NW two temperature differences between the thermostats are tested: one with the usual ΔT of 40 K and one with a ΔT of 80 K to keep the same temperature gradient, $\Delta T/L$, as for the 50 nm NWs. Due to the computational cost for the 100 nm NW only two independent runs were performed. First, one can notice that the rectification still appears when the length is doubled and that it can even increase for the ΔT of 40 K. However, in increasing the ΔT to 80 K, the rectification decreases.

Table 4.2: Size and temperature impact on thermal rectification: length of NW, imposed ΔT between the two thermostats, temperature gradient, mean flux in the two directions, rectification, and number of independent runs for the CO-CS-NW-4.4.

L (nm)	ΔT (K)	$\Delta T/L$ (K nm^{-1})	J_{SL} (µW)	J_{LS} (µW)	η (%)	$\#_{run}$
50	40	0.8	0.158	0.150	5.2	5
100	40	0.4	0.126	0.115	8.4	2
	80	0.8	0.246	0.238	3.2	2

These simulations confirm that the rectification observed is not strongly dependent on the length. But also that the temperature difference has an effect on the rectification coefficient. In the following, the temperature effect is investigated more in depth.

Temperature effect The effect of temperature over the rectification was investigated by performing two different sets of simulations for the CO-CS-NW-4.4 one at 200 K of mean temperature and one with a ΔT of 120 K to test the influence of the temperature gradient. The results reported in this section are given for three independent simulations for each thermostat set up.

The thermal transport in the NW is mostly propagative, and geometry based rectification relies on the ballisticity of phonons [Wang *et al.* 2014]. Thus, by decreasing the average temperature the rectification is expected to increase, due to the decreased importance of phonon-phonon processes relative to boundary scattering

[Yang *et al.* 2008]. To validate this hypothesis, simulations at 200 K are performed. For them, the equilibration temperature is 200 K and set the hot thermostat at 180 K and the cold one at 220 K. The resulting flux and rectification are displayed in table 4.3. It appears that the temperature decrease does not increase the thermal rectification, on the contrary, it seems to decrease it. The average flux does not seem to be affected, meaning that the overall heat transfer is not strongly affected by the temperature decrease. This dependence on temperature seems to indicate that the rectification observed does not simply rely on ballistic effect but on more complex processes, sensitive to temperature.

Table 4.3: Average temperature impact on thermal rectification: average temperature, imposed ΔT between the two thermostats, mean flux in the two directions, rectification, and number of independent runs for the conical core shell nanowire with an opening angle of 4.4°.

T	ΔT (K)	J_{SL} (µW)	J_{LS} (µW)	η (%)	$\#_{run}$
200	40	0.155	0.153	1.1	3
300	40	0.158	0.150	5.1	5

The temperature difference between the thermostats is also a factor in the rectification [Wong *et al.* 2021]. The rectification coefficient usually increases for large temperature difference. Thus, the rectification effect was measured for a ΔT of 120 K with a cold thermostat at 240 K and a hot one at 360 K. The results are displayed in table 4.4, it appears that the rectification is smaller with a ΔT of 120 K than with a ΔT of 40 K. This result confirms the tendency observed in table 4.2, a larger temperature difference does not increase the rectification observed here. Before going further, simulations were attempted using a smaller ΔT with 10 K, but the simulation did not converge properly, the individual measures are too dispersed to be interpreted.

Table 4.4: Impact of the temperature difference on thermal rectification: imposed ΔT between the two thermostats, average temperature, mean flux in the two directions, rectification, and number of independent runs for the CO-CS-NW-4.4.

ΔT (K)	T	J_{SL} (µW)	J_{LS} (µW)	η (%)	$\#_{run}$
40	300	0.158	0.150	5.1	5
120	300	0.47	0.46	1.1	3

In this paragraph it was shown that the thermal rectification is decreased for lower average temperature down to 200 K and also that it does not increase for a larger temperature difference. More points would be needed to draw definitive tendencies. A more in depth discussion of the effect of the thermostats is given in appendix C.

4.2.3 Discussion on the Rectification Observed

A new strategy of thermal rectification is examined here, with an asymmetric core/shell nanowire and, as driving phenomenon, the interaction between the amorphous shell and crystalline core. The rectification estimated is of the order of 5 %, indicating a better heat flux from the smaller part to the larger one. This finding contrasts with some of the previous systems studied in the literature where the reverse bias is observed, as shown experimentally in nanoribbons [Wang *et al.* 2017] or for mass loaded graphene nanotube [Chang *et al.* 2006], and predicted for nanohorns [Yang *et al.* 2008] as well as for nanocones [Zhang *et al.* 2016], but in agreement with others [Ju & Liang 2012a]. Different explanations could be proposed for this discrepancy; it may be due, for example, to the fact that for devices involving graphene the MFP is much larger than the studied samples. Phonons generated on the larger side reach ballistically the other side, while modes generated on the smaller side tend to be scattered before reaching the other side due to edge effects [Wang *et al.* 2012, Wang *et al.* 2017]. For the Si NWs studied here, most of the modes have a MFP lower than or comparable to the NWs length (see figure 4.10).

For the geometries of this chapter, the effect of the shell shape and the interface parallel to the heat flux on the propagation of the low-frequency phonons and on the diffusive transport appears to be the main causes of rectification. This is confirmed by the fact that effective medium models fails to predict the observed rectification. An example is the interesting model proposed by Peyrard [Peyrard 2006] based on the Fourier law, where the flux is estimated thanks to an iterative method that uses κ as a function of the temperature and the position from the imposed temperature gradient. This flux is then used to update the temperature profile. This new temperature profile allows updating $\kappa(x,T)$ for the next iteration. Here, the thermal conductivity κ along the nanowire, assuming a common temperature gradient, and by simple summation of the thermal fluxes, could be approximated as:

$$\kappa(x,T) = \kappa_{a-Si}(T)\frac{V_{a-Si}(x)}{V_{a-Si}(x)+V_{c-Si}(x)} + \kappa_{c-Si}(T)\frac{V_{c-Si}(x)}{V_{a-Si}(x)+V_{c-Si}(x)}, \quad (4.3)$$

with $V_{a-Si}(x)$ and $V_{c-Si}(x)$ the respective volumes of the amorphous and crystalline phases as a function of the position and $\kappa_{a-Si}(T)$ and $\kappa_{c-Si}(T)$ the thermal conductivities of the different phases as a function of the temperature [Allen *et al.* 1999, Glassbrenner & Slack 1964]. This model, however, fails to predict the rectification observed for the CO-CS-NW-4.4 and 8.8, since it does not induce a sensible directional dependence at 300 K. However, rectification could be expected, but in the opposite direction, since around above 60 K and thus at 300 K the thermal conductivity of a-Si increases with temperature while the κ of c-Si decreases with temperature. This model would, indeed, induce a smaller flux in the SL direction, when the small section (composed mainly of c-Si) is at high temperature and the larger part (where the a-Si dominates) is at lower temperature.

However, with the NEMD simulations, the opposite bias is reported. The same remark holds for the diffusivity, that should decrease, based on a simple summation

rule, in the direction where the amorphous fraction increases (SL). This is clearly not the case here. These two points indicate that existing models, not considering interfaces, can not explain the thermal rectification in the geometries studied. Heat transport directionality, here, results from the impact of the variable shell thickness on the behavior of phonon scattering at the crystalline/amorphous interface; thinner shell increases phonon scattering at these interfaces. Thus, the propagation of phonons depends on the direction (see figure 4.5).

The thermal rectification increases in increasing the distance between the two thermostats for a constant ΔT of 40 K. This enhancement is surprising and contrasts with existing studies in which the rectification either decreases [Yang *et al.* 2009] or is constant when the length is increased [Ju & Liang 2012a]. In the case of rectification due to interfacial effect, when the interface between the two materials is perpendicular to the heat flux, the rectification fades away as the length increases [Yang *et al.* 2009]. In the CO-CS-NW case, the interface is parallel to the heat flux and this induces an opposite impact of the length on the rectification. The larger interfacial area seems to induce a higher rectification for the longer asymmetric nanowire.

Increasing the temperature difference decreases the rectification observed. This contrasts with the previous systems where rectification was based only on geometrical effects [Yang *et al.* 2009, Wu & Li 2008, Wang *et al.* 2014, Cartoixà *et al.* 2015]. In the later studies, the rectification increases on increasing the temperature difference. This opposite behavior could be explained by the enhancement of the phonon-phonon scattering processes compared to the boundary/interface scattering [Pei *et al.* 2012, Yang *et al.* 2008].

The rectification does not increase for a lower mean temperature. This is in agreement with Ju *et al.* [Ju & Liang 2012a] who have shown that the rectification tends to decrease when the temperature decreases below 500 K for Si nanoribbons. The effect of length and temperature is thus not so trivial, since it may result from complex processes and there is no quantitative predictive explanation until now. Further studies and simulations are needed to understand more in depth the results obtained. In particular, the precise role of the energy drift and the signs of dependence to the annealing temperature discussed in appendix C could not be explained.

Finally, it is worth mentioning that the flux rectification obtained here is lower compared to the results obtained for nanoribbons [Wang *et al.* 2017] or nanohorns [Wu & Li 2008], for example. Moreover, the present configuration could be improved by texturing the amorphous/crystalline interface with a sawtooth pattern, which is known to promote rectification [Roberts & Walker 2011b], or by using a cascade of nanowires in pyramidal shape, as proposed by Yang *et al.* [Yang *et al.* 2017b]. As the interfaces and free surfaces are the driving forces for the rectification, their asymmetric roughness and atomic structure could enhance the observed thermal rectification.

In this chapter, it is shown that an asymmetric shell, with a varying thickness amorphous layer, can create a direction dependent phonon propagation. In particular, the ballistic transport at low frequencies is affected differently by the interfaces in the two directions, with a stronger scattering in the large to small cross-section direction. The transport in the amorphous shell, at the core/shell interface, and at the surface of the shell are also impacted by the geometry of the shell.

This direction dependence of WP propagation appears to result in a thermal rectification favoring the small to large cross-section direction, in contrast to the majority of the existing literature results. The heat transport in the amorphous shell seems to be an important factor of the rectification, as only the configurations with a large amorphous fraction showed a significant rectification. The opening angle of the asymmetric amorphous shell does not seem to have a linear impact on the rectification; for small opening angles there is almost no rectification, while for angles 4.4° and 8.8° the heat flux rectification is constant and around 5 %. Finally, the shape of the shell is also an important factor; the telescopic NWs have a lower rectification than the conical CS-NWs. The conical shape increases the rectification, probably by favoring coupling between the core and the shell.

Synthesis of the Chapter

- An asymmetric shell induces a direction dependent phonon transmission
  - A larger shell thickness seems to protect the propagation in the core
  - The asymmetric geometries induces energy transfer between the core and shell
- This direction dependent transmission seems to results in thermal rectification of 5% (90% if referred to the cross-section at the incoming flux). This kind of rectification is decreased at lower temperatures and is sensitive to the temperature gradient between the thermostats.

General Conclusion

Along the different chapters, the thermal and vibrational properties of several nanocomposites and nanostructures have been explored. The focus has been laid on amorphous crystalline nanocomposites, either 3D or 1D. The effect of structuration and interfaces over the thermal properties have been studied using molecular dynamics both in a traditional way (equilibrium and non-equilibrium molecular dynamics), and by using the vibrational properties via the wave-packet method. Thanks to this last method, both the ballistic and diffusive transport have been studied, using the analysis frame of amorphous material. This distinction allows for a better understanding of the origin of the variation of the thermal conductivity due to the structuration. This approach is finally completed by a comparison to a continuous model: the hydrodynamic heat equations.

In the first chapter, it is shown that the simple models developed to describe the thermal conductivity at the microscale tend to fail when the periodicity is broken. More complex models, such as Monte Carlo (MC), Atomic Green Function (AGF), classical and *ab initio* molecular dynamics (MD), have been developed for different applications, depending on the time and length scale as well as the geometry studied. Among these models, two kinds have been separated, the continuous models using mesoscopic parameters and the discrete models relying on an atomic level description of the matter. As this work uses mostly an atomistic approach, a more in-depth description of MD, used to create and study the nanocomposites, was given. This includes the methods used for the estimation of the thermal conductivity, but also for the analysis of structural and vibrational properties.

These methods have first been used to study different bulk nanocomposites, mainly amorphous/crystalline ones, but also, fully crystalline. In a first time, GaN nanoparticles have been studied, in particular the effect of the size. The size reduction induces the emergence of modes in the acoustic/optic bandgap and an overall spectral broadening, as already predicted [Han & Bester 2011]. When included in an amorphous silica matrix, the properties of nanopaticles are modified, only the broadening persists and the surface modes disappear. At the same time, it as also been observed that the thermal conductivity of GaN nanoinclusions does not increase linearly with the diameter, contrary to Si nanoparticles [Fang *et al.* 2006]. Such findings may inform the parameters used in effective medium models. This study was also the occasion to build on the original publication [Termentzidis *et al.* 2018a], and to investigate the effect of the alignment of the crystal lattice of the inclusions on the ballistic transmission of energy across them. No indication of direct transmission of energy between the inclusions, nor variations of energy transport due to the orientation, have been observed. Then, the effect of inclusion stiffness over energy transmission was studied via wave-packet propagation. Inclusions in an amorphous matrix reduce the ballistic transmission of energy. However, they also increase the diffusivity, so that the overall thermal conductivity is increased, confirming earlier

results [Tlili *et al.* 2019]. The only way to reduce the propagative and diffusive contributions is to use inclusions that are softer than the matrix. After this, the effect of the shape of the inclusions over the transmission of energy is explored. Shapes ranging from sparse nanospheres to a percolating network of nanowiress have been studied. This has shown that even though a crystalline structural percolation increases greatly the ballistic transmission in a given direction, its impact on the overall thermal conductivity is comparatively small. In the system studied, with a crystalline fraction of 30 % most of the heat transfer appears to be diffusive, and the shape of the nanoinclusions does not impact the diffusivity. These findings could be useful for phonon engineering, or to help to predict the thermal conductivity of nanocomposites with fractal shaped inclusions [Xu *et al.* 2018, Luo *et al.* 2021]. A last study, focused on the effect of decorated dislocations, has shown that the alloying level affects differently the propagation as a function of the frequency, depending on their size and orientation with respect to the heat flux.

In a third part, similar methods have been used for the analysis of propagation of energy in core shell NWs, with the goal of understanding the effect of the amorphous shells on thermal transport. This was done first through a comparison of the vibrational properties of a pristine nanowire and a core/shell nanowire sharing the same crystalline diameter. It revealed that at low frequencies, propagation at the surface/in the shell is possible, as predicted by Zushi *et al.* for pristine nanowire [Zushi *et al.* 2014]. Whereas at high frequencies, the propagation is only possible in the inner core of the nanowire. Then, an effort is made to understand the effect of a crystalline amorphous interface more in depth, with the analysis of the radial flux distribution. The flux profile obtained by with molecular dynamics simulations is similar to a Poiseuille flow, as has already been shown by previous studies [Verdier *et al.* 2018a, Melis *et al.* 2019]. This has motivated the comparison with a modelisation based on the hydrodynamic heat transport equations. Through these simulations, it is shown that the addition of the shell does not disturb the flow close to the interface, but rather decreases the maximal intensity in the center. This effect is interpreted in the framework of the continuous modelling, as a decay of the effective thermal conductivity (confirmed by a global mean-free path analysis at the microscopic level), but does not involve any modification of the non-local length and/or of the slip coefficient at the boundaries. This analysis points out that the change of the specularity of phonon reflection at the interfaces due to the presence of the amorphous shell may not the leading phenomenon in the reduction of the global heat flux due to the addition of the shell. This appears to contradict earlier results [Malhotra & Maldovan 2019] but indicates simply, that the reduction is rather due to a global effect of the shell on the mean free path of heat carriers.

In the final section, the study of the effect of the shell is continued by the exploration of the impact of conical shells of different dimensions. In those conical core shell nanowires, wave-packet propagation studies showed that at low frequencies a large shell thickness prevents the wave in the shell to deform the wave in the core in the small to large direction while promoting it in the other direction. Non equilibrium molecular dynamics simulations then showed that the conical nanowires

induced a flux rectification of 5 % favoring the small to large direction. This result shows, that the structuration of the oxide layer can influence the transport in the nanowire, as already suggested [Blandre *et al.* 2015, Malhotra & Maldovan 2019]. These kinds of structure might be useful, for example, in phononic computing [Wehmeyer *et al.* 2017].

This thesis is centered on the impact of the nanostructuration over the thermal properties of nanocomposites (here amorphous/crystalline). It showed that inclusions and interfaces have an impact that depends on their shape, rigidity, interconnection orientation compared to the heat flux. The effect over the propagative and diffusive contribution to the thermal conductivity has been studied frequency wise. This work can thus inform the design of material with precise vibrational properties, for phonon engineering. Given the right structure, it is possible to tailor energy pathways, create band-pass filters or even induce thermal rectification. As suggested before, the thermal transport inhomogeneities could be useful for thermal management, by creating "heat pipes" at the nanometer level.

One of the main theoretical take out of this thesis is that for nanocomposites, it is useful to go beyond the study of thermal resistance of interfaces that is already well documented [Landry & McGaughey 2009, Giri *et al.* 2016, Hu *et al.* 2008, Merabia & Termentzidis 2014]. At the nanoscale, the whole structure has to be considered for an accurate estimation of the thermal properties, the shape and size impacting the thermal transfer through different forms of collective dynamics. Here it has been shown that important characteristics of the thermal transfer can be estimated through wave-packet simulations but also through a comparison with a continuous approach. These characteristics, such has the propagative to diffusive ratio for the first one, or non local parameters given by the latter, might be used to develop a more detailed approach in effective medium models [Wang & Pan 2008].

The wave-packet propagation analysis is one of the central approaches of this thesis. As it is implemented here, it is a rather simplified way to study the heat transport in a nanocomposite. But it allows both for an estimation of global properties such as mean free path or diffusivity, and a more local qualitative vision of the energy pathways and potential hot spots where the energy localizes. Overall, the information extracted from the wave-packet do not allow a precise estimation of the thermal conductivity, but it can predict the global trends and could be used to inform the design of nanocomposites at a low computational cost. The approach used, exciting a plane and monitoring the propagation, is quite simple compared to other implementations, where single modes are excited [de Sousa Oliveira *et al.* 2020]. However, such an approach, is justified in amorphous materials and large complex structures where the exact modes are harder to identify or less relevant for the estimation of the thermal conductivity. Moreover, the results presented in this chapter are potentially closer to the results of thermoreflectance experiments and allow the sampling over broad bands. For the estimation of thermal conductivity of fully amorphous material, the main difficulty is to weight correctly the diffusive and propagative contributions. For nanocomposites, the issue of anisotropy, and the averaging over

multiple inclusions quickly arises, preventing an accurate description of thermal conductivity but, again, interestingly, the global trends are recovered. Overall, WP is a useful tool that can complement the more quantitative estimation of the thermal conductivity with (non) equilibrium molecular dynamics. With it one can quickly, not only estimate the spacial and frequency dependent heat transport but also separate the diffusive and propagative contributions.

A wide spectrum of nanocomposites has been studied, with each a particular approach and properties to evaluate. However, before generalizing the results to a broad application field, further study using different approaches, theoretical or experimental could be useful. In particular, a point that might be missing to complete the analysis, is a frequency resolved thermal conductivity computation. This would complete nicely most of the studies. Such a method exists [Sääskilahti *et al.* 2015], however, implementing them for the large simulation proposed in this work is quite challenging.

As a more general prospective, some other points are worth studying further. For instance, the study of the energy pathways in nanocomposites could be improved by considering the propagation in other directions and considering an eventual anisotropy of transport. On another point, the same flux distribution analysis carried out for nanowires could be extended to more complex shapes. An analysis of high symmetry, simpler structures such as super lattices, with similar methods would also be interesting and might complete the understanding of their thermal properties. Finally, the wave-packet method could be used to study the effect of phonon coherence on thermal transport, in thin films or in nanowires.

Appendices

Appendix A

Additional Structural and Vibrational Properties of Bulk Nanocomposites

In this section, multiple structural and vibrationnal analysis of some of the nanocomposites studied in the chapter 2 are given. They are not essential for the demonstration, but nevertheless worth mentioning.

A.1 Silica Glass Properties

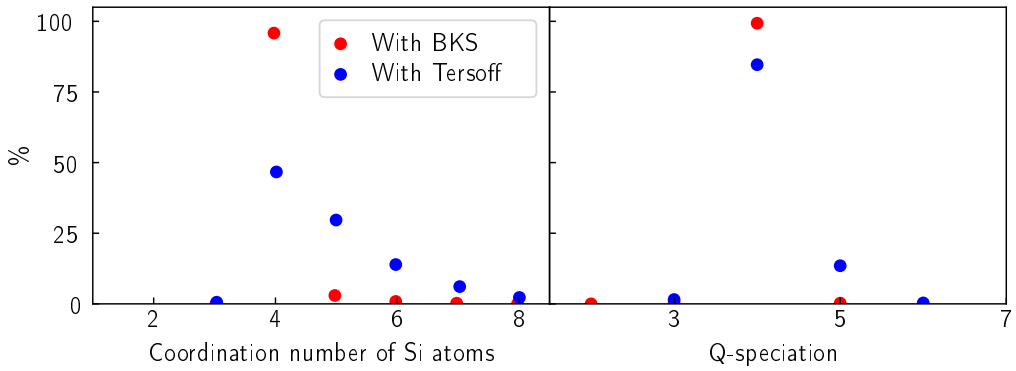

Figure A.1: Percentage of Si atoms for each coordination number (left panel) or for each Q speciation (right panel), for the amorphous silica samples obtained with (blue) or without (red) using the BKS interatomic potential for the melt quench procedure.

The silica glass sample is obtained through the method described in section 2.4.1. It involves switching between a BKS interatomic potential [van Beest *et al.* 1990] and a Tersoff potential [Tersoff 1988]. The use of a Tersoff potential for the melt quench procedures leads to an amorphous silica micro-structure with 50 % of coordination defects (Si atoms with a coordination different from 4 see figure A.1). Whereas, at the normal pressure range, almost no coordination defects are expected [Liang *et al.* 2007], which is what is obtained by using the BKS potential at high temperature. The structure of can also be checked through the Q speciation (see 1.4.3), for pure SiO_2 the overwhelming speciation should be Q_4 [Sen & Youngman 2003] and on the figure A.1 one can check that it is indeed the

case for the procedure using the BKS potential, but not the case when the Tersoff is used all along the procedure.

A.2 Partial Radial Distribution Function of GaN

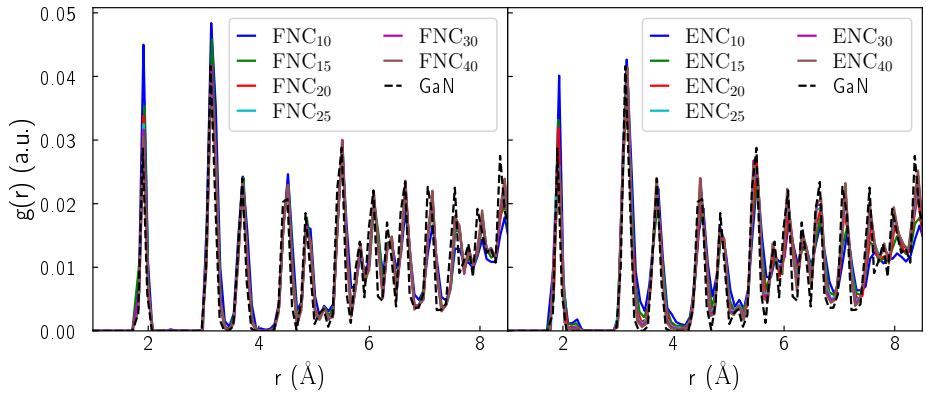

Figure A.2: RDF for GaN atoms at 300 Kfor FNP (a) and partial RDF of GaN in ENP (b) compared with the RDF of bulk GaN.

In this section, the Radial Distribution Function (RDF) of the Nanoparticle (NP)s studied in section 2.1 are analyzed. The RDF of free and embedded[1] nanoparticles are represented in figure A.2. The RDF allows comparing the crystalline structure of the NPs with decreasing radius and the differences with the bulk. The first peak represents the distance to the nearest neighbor, the second one the distance to the second nearest neighbor and so on. Here, little to no changes to the PRDF going from bulk to free NPs are visible. A similar analysis made on Si NPs with a Tersoff potential showed reorganization at the surface [Li & Zhang 2013], this discrepancy may come from the higher temperature (1600K) annealing of their NPs. For the embedded NPs on the opposite, a peak broadening can be observed. It is visible from the second nearest neighbor on. This broadening increases with decreasing diameter, which is symptomatic of amorphization at the interface due to the contact with a-SiO_2. These observations confirm that for the configurations of this thesis, the GaN-SiO_2 interface has more impact on the vibrational properties than the free surface of FNPs.

A.3 Nanoinclusion Low Frequency Scaling

In this section, the evolution of the frequency of the first vibrational modes of the NPs studied in section 2.1 is explored. To showcase that modes whose frequency depends on the diameter exists, the frequencies of the first few modes are plotted as a function of the inverse of the diameter in figure A.3. It appears clearly that for both

[1] Here, partial radial distribution function since the matrix is ignored.

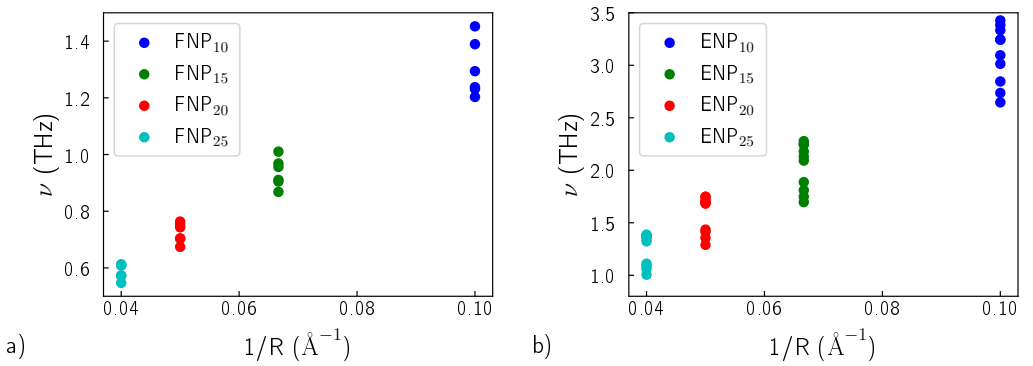

Figure A.3: Frequencies of the first modes computed via direct diagonalization of the Dynamical Matrix (DM) for free NPs (a) and embedded NPs (b) as a function of the inverse of the radius.

the free and embedded nanoparticles the frequencies of the first modes scales with the inverse of the radius as expected for Lamb's modes [Eringen & Suhubi 1974]. These modes collective modes do not appear directly in the VDOS in figures (2.6 and 2.7), being probably drowned in other modes.

A.4 Estimation of the Vibrational Density of States of Silicon Nanocomposites

In this section, the method of estimation of the longitudinal and transverse VDOS used in the section 2.4 is discussed.

The VDOS can be estimated thanks to the integral of the DSF over the wave vectors. This allows a distinction between the different wave vector directions and polarizations. To consider the anisotropy of c-Si the sum for the different vector direction of the Brillouin zone (BZ) are considered. The VDOS obtained are then filtered using Savitzky-Golay polynomial filter.

However, a choice has to be made regarding the range of wave vector considered for the integration. The different possibilities tested are displayed in figure A.4. They are compared with the results of the VACF, which will serve as a reference point. The first possibility is to consider the whole DSF computed, that is from 0 up to $2.25\,\text{Å}^{-1}$ ("Full DSF" in figure A.4). Another possibility is to consider the point at which the estimated group velocity of the phonons is nil ("Nil Vel. DSF" in the figure A.4), relying on the fact that near the BZ limit, the velocity is nil. The last possibility is to consider the theoretical end of the BZ computed for the lattice parameter used ("Brill. Edge DSF" in figure A.4). Another comparison point for the study is the separation of transverse and longitudinal VDOS by the KPM method [Beltukov *et al.* 2015] on a fully amorphous sample, given that the configurations are mostly amorphous (70% of a-Si and 30 % of c-Si).

When comparing the different VDOS it appears that the total VDOS computed

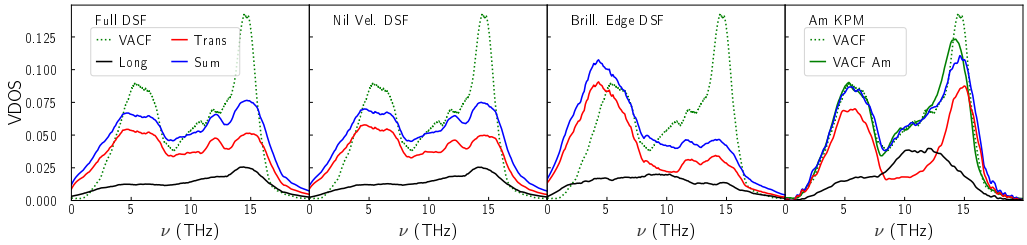

Figure A.4: VDOS computed using different methods, the red and blue lines correspond respectively to the transverse and longitudinal polarizations, the solid blue and green dashed lines correspond to the total VDOS computed respectively via the DSF or the VACF. The first panel starting from the left uses the full DSF, the second the DSF limited to the theoretical wave vector limit of the BZ of c-Si, the third the DSF limited to the wave vector giving a 0 velocity and the last displays the results using the KPM method for an amorphous sample.

using DSF does not match with the VACF results, whatever the wave vector limit used. If all the peaks seem to be present, their relative size does not match, and they are flattened. This is even more marked when considering the theoretical end of the BZ (third panel in Figure A.4). The failure to reproduce the VDOS using the DSF can partially be attributed to the fact that the BZ is not defined for the amorphous Si.

In the other hand, the VDOS of a-Si of computed via the KPM method matches comparatively well the VDOS of the NW-M configuration computed via VACF. Still, in this case some differences arise after 12 THz, but given the reduced MFP at those frequencies, its impact on the computation of κ_P is negligible.

A.5 Estimation of the Mean Free Path through the Dynamical Structure Factor

In this section, the choice of the method of estimation of MFP in the section 2.4 is discussed.

The DSF can be used to determine both the dispersion relation and the MFP using the method described in section 1.5.2. The result of the fitting to a Damped Harmonic Oscillator (DHO) model for a longitudinal polarization for the NW-M is displayed in the left panel of Figure 1.15 for a few wave vectors. The expression (1.46) seems to fit to the DSF computed via quation (1.44) reasonably well at low frequencies. However, as the frequency increases the DSF is increasingly noisy, degrading the fit quality. The MFP can also be extracted (left panel of figure 1.15). It then appears that the MFP peak at 10 THz observed with the WP disappears. The MFP computed with this method steadily decreases. This discrepancy can be attributed to the low frequency limit of validity of this fit discussed in [Beltukov *et al.* 2016] or to the fact that this MFP is computed using a quantity averaged over the whole sample. This spatial average cannot capture the effect of

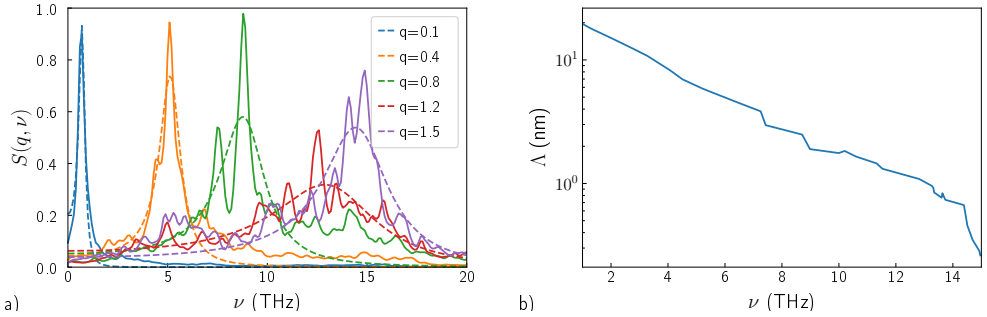

Figure A.5: Dynamical structure factor as fitted from equation (1.46) (left panel) and resulting MFP (right panel) for the NW-M configuration for the longitudinal polarization.

the structural percolation, showcased with the WP method.

The successive fits of different wave vectors enable the computation of the dispersion relations $\omega_\eta(q)$. Dispersion relations from which the group velocity can be computed. However, the method includes more parameter to fit than the method described in section 1.5.2 and is thus a less robust approach.

Appendix B

Hydrodynamic Transport in Nanowires: supplementary material

This chapter contains the various analysis mentioned in chapter 3.

B.1 Effect of the Thermostat Used

In this section, the individual results for the radial distribution of flux using either a velocity rescaling thermostat or a Nosé-Hoover thermostat are compared for a NW with R_{Cry}= 37.5 Å (see figure B.1). No notable differences can be seen, neither of the two Nosé-Hoover individual runs differs notably from the distribution established by the velocity rescaling examples.

This figure can also give an idea of the dispersion of the measures.

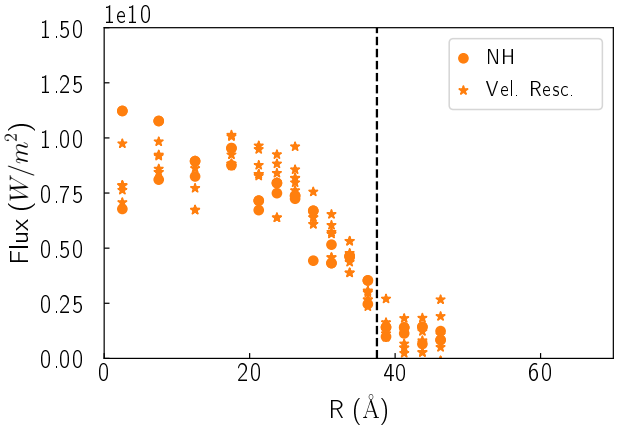

Figure B.1: Flux in the NW as a function of the radius of the nanowires with R_{Cry} = 37.5 Å and e = 10 Å, using a velocity rescaling (stars) or a Nosé-Hoover thermostat (dots). The vertical black dashed line represents surface/interface position.

B.2 Comparison of Flux Computation Method

The comparison of the thermal conductivity obtained with the equation (1.53) and the method described in chapter 3 is represented in table B.1. It appears that the

values are comparable in most cases. A small discrepency is nevertheless to be noted for the pristine NW, equation (1.53) underestimates the thermal conductivity.

Table B.1: Comparison of the thermal conductivity obtained with the equation (1.53 and the average of the energy exchanged at the thermostats during steady state (see chapter 3).

R_{Cry} (Å)	e (Å)	$\frac{J_x L}{\Delta T}$ ($\mathrm{W\,K^{-1}\,m^{-1}}$)	$\frac{dE/dt L}{S_{Effect}\Delta T}$ ($\mathrm{W\,K^{-1}\,m^{-1}}$)
	0	8.9	10.7
37.5	10	5.7	5.8
	20	4.5	4.3
	0	9.9	11.7
50	10	6.9	7.5
	20	5.3	5.6

B.3 Dynamical Structure Factor and Mean Free Path for Larger Nanowires

In this section the DSF, MFP and dispersion relations for the nanowires with R_{Cry}= 50 Å are compared with the results of the R_{Cry}= 37.5 Å.

First, the DSF is displayed for the pristine NW and the one with a 10 Å thick shell in figure B.2. The same features as for the smaller NW appear. The background noise due to the amorphous shell and the second branch appearing for the pristine NW (see discussion in section 3.1).

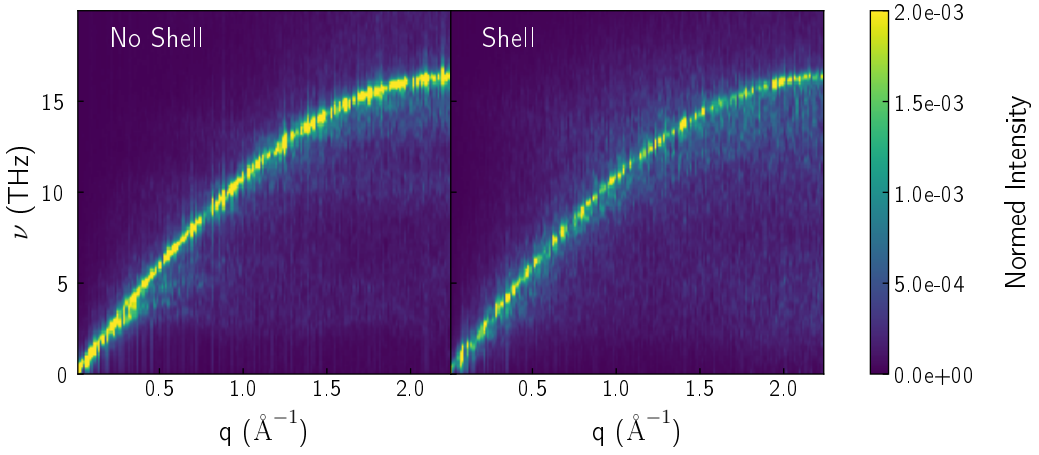

Figure B.2: Dynamical structure factor in the ΓX direct 50 Å and e = 0 (left) or 10 Å (right).

Secondly, in figure B.3 the dispersion relations for the different NWs are given. It appears that all the NWs share the same dispersion relation for the longitudinal

phonon in growing direction of the NWs. This confirms that neither the size nor the presence of an amorphous shell influences phase or group velocity in the NWs studied.

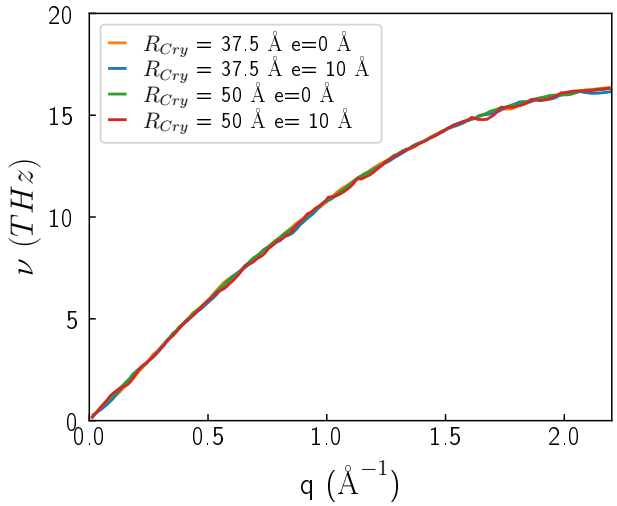

Figure B.3: Dispersion extracted from the DSF for the nanowires of R_{Cry}= 37.5-50 Å and e = 0 or 10 Å.

Finally, in figure B.4 the MFP estimated from the DSF for the different NWs are given. The decrease of the MFP at high frequencies induced by the shell appears clearly for the two radii. However, from this picture, it is not possible to conclude that the increase in thermal conductivity induced by the increase of the crystalline core radius is linked to a variation of the MFP in this direction.

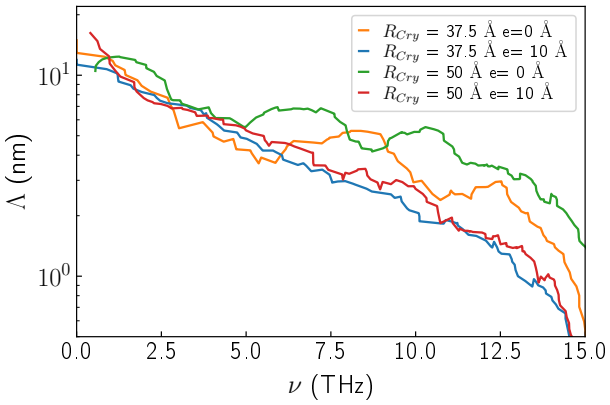

Figure B.4: MFP as extracted using the DHO from the DSF for the nanowires of R_{Cry}= 37.5-50 Å and e = 0 (blue-red) or 10 Å (orange-green).

B.4 Strain and Stresses

This section contains a short analysis of the strain/stress state of the NW studied in the chapter 4. This stress analysis is another way to analyze the eventual modification of the properties of the NW upon the addition of a shell.

The computation of strain in MD is possible by computing the displacement vectors between a reference configuration and the present configuration and using it to compute the strain tensor. This is what is done in OVITO [Stukowski 2009]. Here, to have an estimation of the strain state, the reference configuration will be the configuration before the annealing and relaxation of the construction stresses. This allows to compare the structure with the equivalent bulk structure (crystalline or amorphous) and thus to consider the deformation due to interface or surface effect. However, this also means that the thermal strains are also considered.

To understand the decrease of κ upon the addition of shell, it is interesting to analyze the strain state of the NWs. Equation (1.54) is used to represent the stress profile in the NW in figure B.5 (left panel). For the pristine NW, the stress increases slightly, from 0 to 20 MPa between the center and 5 Å from the free surface and increases up to 170 MPa in the last layer. Such free surface stresses have already been reported for Si NWs [Nasr Esfahani & Jabbari 2020]. These surface stresses are consistent with the variation of potential energy observed for thinner NWs in figure 3.2. For the core shell NWs, the profile starts slightly in expansion (positive stress) and decrease to 0 MPa 5 nm away from the interface. After this, it increases to 50 MPa at the interface. In the amorphous shell, the stress level decreases before re-increasing at the interface. Again, the profile is consistent with the potential energy profile observed in figure 3.2. This means that the addition of the amorphous shell does not induce large stresses at the interface, on the contrary, the stress level at the interface is lower than at the free surface. In the same figure, it also appears that the addition of the shell makes the stress state in the NW switch from a relaxed state to an expended state (positive stress). Positive stresses, or more explicitly positive strains, are linked to a thermal conductivity decrease [Li *et al.* 2010].

To confirm that these stresses are linked with an expansion, the volume variations with respect to the configuration as constructed before the relaxation are represented in the right panel of the figure B.5. For the pristine NW, there is very little volume variations. There is only a small expansion, uniform over R. However, in the case of the core shell NW there are more variations, with a marked volume increase near the boundary. This strain profile can explain the stress profile: in the core/shell NWs there are relaxations at the amorphous/crystalline interface, these relaxations decrease the stresses and increase the strains. It is important to note that with the reference chosen (before construction stress relaxation) the strains are certainly overestimated, in particular at the interface where there is a substantial reconfiguration of the position of the atoms. The difference between the pristine and core/shell NW are very small, below 0.25 %, and cannot justify alone the decrease in thermal conductivity (20 %) [Li *et al.* 2012].

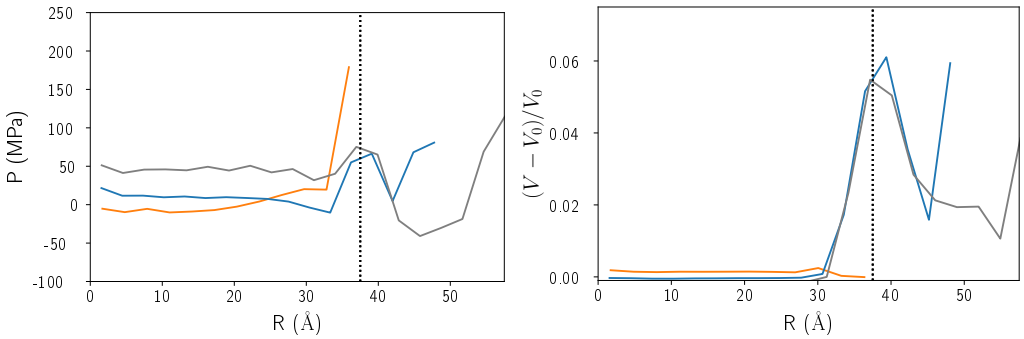

Figure B.5: Trace of the stress tensor obtained with equation (1.54) (left panel) local variation of the volume estimated from the strain tensor (right panel) as a function of the radius for the R_{Cry} =37.5 Å NW, the blue, green and red line represent respectively the case of $e = 0$, 1 and 2 nm. The vertical dotted line represents the interface.

B.5 Complementary Results for $R_{Cry} = 25$ Å

In this section, the results for a small diameter, corresponding to the configuration studied in section 3.1 are displayed. These results have been excluded of the analysis, as discussed in section 3.2.5.

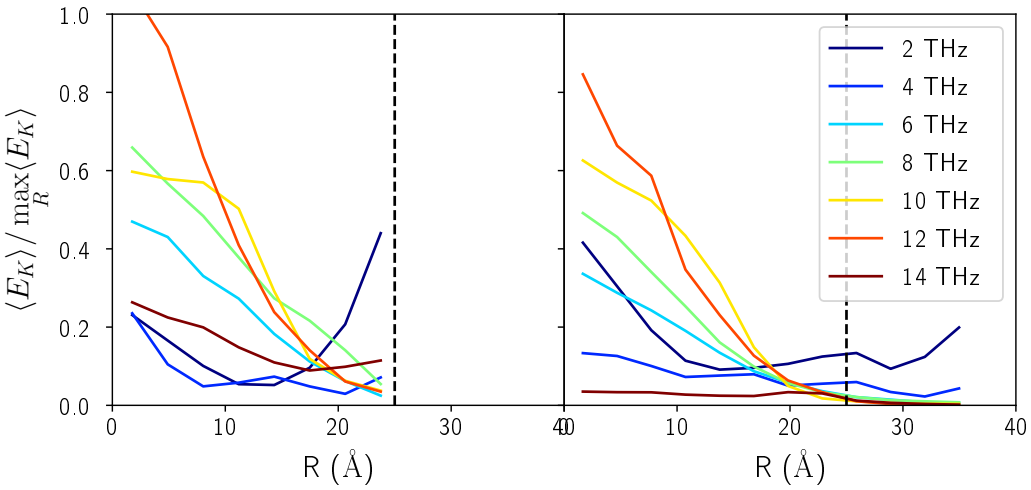

Figure B.6: Atomic kinetic energy as a function of the radius averaged on a portion of the NWs 90 to 160 Å away from the excited layer, for the time step where the maximal intensity is reached. For the nanowires of R_{Cry}= 50 Å and $e = 0$ (left panel) and 10 Å (right panel). The vertical black dashed line represents the end of the crystalline core.

The first figure represents the energy distribution at different frequencies during WP propagation. The results are very similar than for larger diameters (see figure 3.13). Two differences are notable: the energy level at the surface at 2 THz is much higher in this case, and for higher frequencies the energy level is maximal in

the center and decreases monotonously. There is no second maxima as for larger diameters.

The flux radial distribution is displayed in figure B.7. For this case, the flux does not appear to plateau in the center, even though the value reached in the center is similar. Notice that the absence of a plateau is consistent with the monotonous decrease observed for all frequencies in figure B.6. However, the other observations made for the larger diameter still hold, the addition of a shell decreases the value of the flux, the thickness of the shell has no influence, and the flux in the shell is constant.

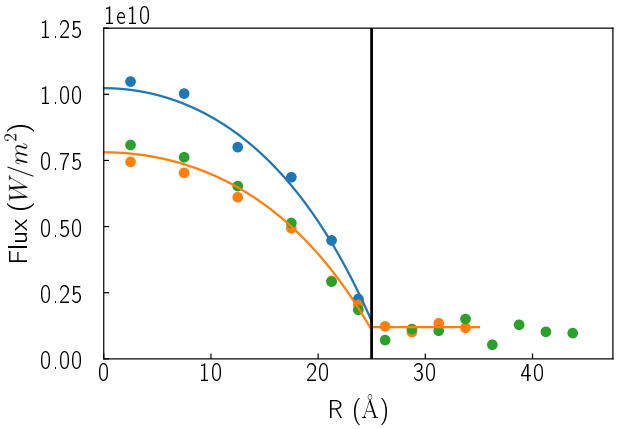

Figure B.7: Flux in the NW as a function of the radius for the nanowires with R_{Cry}= 25 Å and e = 0 (blue), 10 (orange) and 20 Å (green). The dots report the value obtained with equation (1.53) in the different layers, and the full lines the flux obtained with the hydrodynamic heat transport equation. The vertical black line represents surface/interface position.

The parameters of equation (1.23) needed to fit the flux are displayed in table B.2. As discussed in section 3.2.5, it can be hard to make sense of the values obtained: κ is larger than for R_{Cry}= 37.5 Å, ℓ and C decreases. However, the results might be interpreted as a regime change for ultra-thin NWs as suggested by [Zhou *et al.* 2017]. In this interpretation, the increase of κ upon the change of diameter can be linked to reduction of the scattering due to the selection of phonons. The decrease non-local length is also compatible with a decreased scattering. However, more studies would be needed to confirm those observations.

Table B.2: Parameters of equation (1.23) used to model the NW in the different conditions.

R_{cry} (nm)	e (nm)	κ (W m^{-1} K^{-1})	ℓ (nm)	C
25	0	19.0	1.1	0.14
	1	14.5	1.1	0.14

Appendix C

Effect of Thermostats and Flux Computation

In this appendix, the effects of thermostats shape and flux computation methods during the NEMD simulation performed to measure the rectification in section 4.2 are explored.

C.1 Thermostat Shape

To ensure that the shape of the thermostated regions does not impact the measure, supplementary simulations were performed with thermostats placed outside of the device. For this, the extremities of the CO-CS-NW-4.4 are elongated: the small extremity is prolonged by a pristine crystalline NW and the large extremity with a CS-NW of constant shell thickness. The prolongations are 11 nm long, with 1 nm for the frozen atoms and 10 nm for the thermostated regions. With this geometry, the thermostats are external and not internal to the device. The resulting configuration is represented in figure C.1. This thermostat placement can be considered more realistic, in that it is closer to a hypothetical experimental case where the two ends would be glued to a heater and a heat sink [Chang *et al.* 2006].

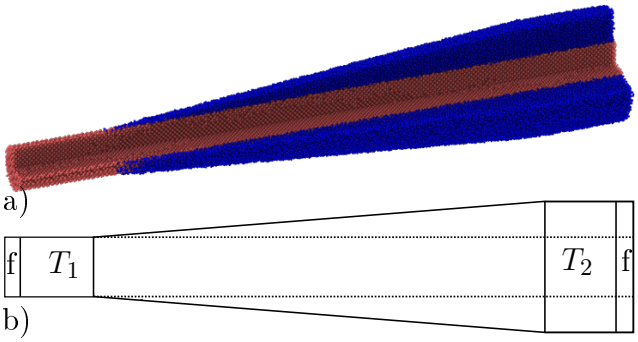

Figure C.1: CO-CS-NW-4.4 with prolonged extremities, atomic representation (a), and position of the thermostats and fixed atoms regions (b).

Two independent simulations in each flux direction are performed for this configuration, the results in therms of exchanged energy and rectification are reported in table C.1. It appears that the rectification is not suppressed and seems increased. The two simulations performed does not allow a meaningful quantitative comparison

of the rectification values. The increase would be consistent with the rectification increase upon the length increase in section 4.2. This increased distance between the thermostats also explains the flux decrease.

Table C.1: Impact on thermal rectification of the shape of the thermostats: mean flux in the two directions, rectification, and number of independent runs for the CO-CS-NW-4.4.

Thermostat	J_{SL} (µW)	J_{LS} (µW)	η (%)	$\#_{run}$
Internal	0.158	0.150	5.2	5
External	0.140	0.128	9.4	2

C.2 Power Exchanged at each Thermostat

To compute the thermal flux in each direction, the cumulative energy exchanged by the thermostats is used, as displayed in the first row of figures C.2a and C.2b. First, in order to compute a reliable flux, the transient behavior due to the setting up of the thermal gradient must be avoided. To this end, the exchange rate is computed from 1 ns after the setting up of the thermostats, when the temperature profile is stabilized, during the next 1 ns. The slope of the cumulative exchanged energy by the thermostat during steady state gives the flux imposed by this thermostat. This slope is computed thanks to a least-squares fit to a linear function. This power exchanged is displayed in the second row of figures C.2 a and b, the symbols (circles and triangles) representing the average slope over five runs, with the error bars corresponding to the dispersion. For the computation of the rectification, the flux (or power exchange) in the SL case (solid lines) is compared to the LS case (dashed lines). For this, the power exchanged at each thermostat is computed (see second row of figure C.2). However, in spite of a stable temperature profile, the power exchanged at the cold thermostat (in blue) is higher than at the hot thermostat (in red), for both the SL and LS cases, represented respectively by circles and triangles in figure C.2. This means that more energy is retrieved than added, in spite of the stable temperature profile. This is true for the CL-CS-NW in figure C.2a and the CO-CS-NW-4.4 in figure C.2b. Thus, this difference is not directly caused by the asymmetric shape of the sample. The average between the power exchanged at the cold and hot thermostats is used to have a single representative value for both thermostats set up SL and LS (see the third row of figure C.2). Finally, as in equation 4.1, this value is compared between the SL and LS direction to compute the thermal rectification. The power exchanged in the SL case is systematically higher than in the LS case, for the geometries inducing rectification like the CO-CS-NW-4.4 in figure C.2, indicating that the rectification direction is not sensitive to the choice of the (cold or hot) thermostat where the measurement is made.

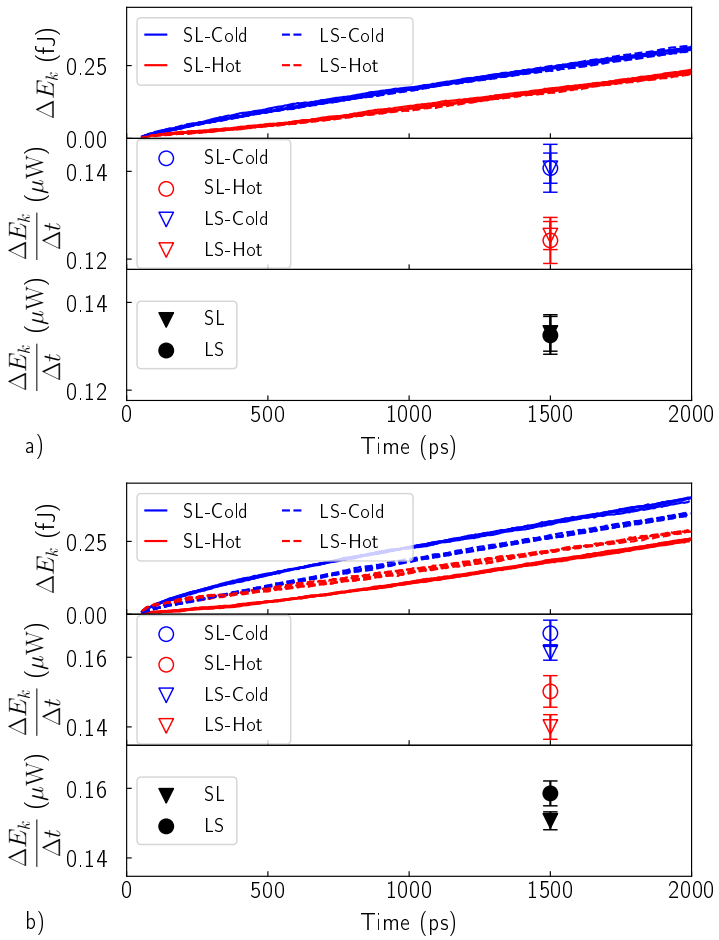

Figure C.2: Energy exchanged by the thermostats, for the CL-CS-NW and the CO-CS-NW-4.4: The first row represents the energy exchanged at each thermostat for five runs, the blue lines represent the energy retrieved by the cold thermostats, and the red lines the energy injected by the hot thermostats. The dashed lines distinguish the SL from the LS thermostats set up represented by the continuous line. The second rows represent the estimation of the energy flux, computed from 1 to 2 ns, the red symbols represent the hot thermostats, the blue symbols represent the cold thermostats. In the third row, the black symbols represent flux taken as the average between hot and cold thermostat. The inverted triangles represent the LS case and the circles the SL.

C.3 Temperature Profile

This section features the temperature profile during a NEMD in the small to large and large to small directions for a conical core-shell nanowire of opening angle 8.8° (figure C.3). First it appears that the temperature profile is very stable during the simulation. Secondly it is also visible that the profile is not linear, showing that the thermal conductivity is not constant along the nanowire, it varies with X. Moreover, the fact that both curves are not symmetric (one is concave and the other

convex) shows that the thermal conductivity is not the same as a function of the temperature.

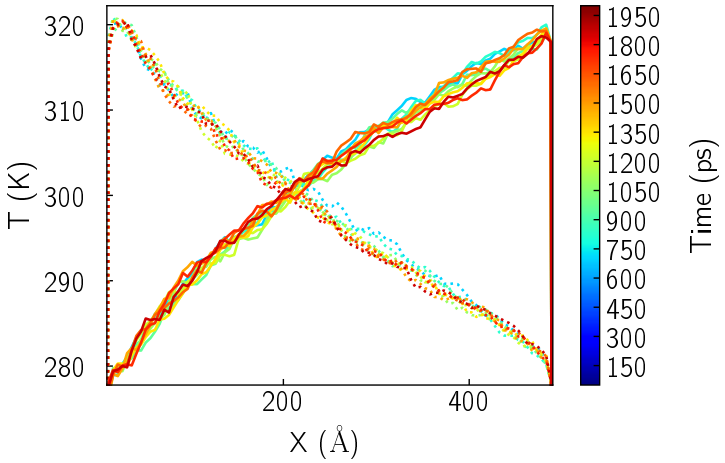

Figure C.3: Temperature profile of the CO-CS-NW-4.4 in the large to small (full lines) and small to large direction (dotted lines). For different time-steps (different colors)

C.3.1 Energy Drift

The visualization of the energy variations can help to understand the difference of power exchanged between the hot and cold thermostats, this is the goal of figure C.4 a and b. In these figures, the difference of energy exchanged between the hot and cold thermostat is displayed along the variation of kinetic, potential and total energy from the beginning of the simulation (upper panel) or from 1 ns are represented (lower panel). In the upper part of these figures, it appears that in both cases (SL and LS) the difference of energy between the thermostats corresponds to the sum of the potential and kinetic energy variations since the beginning of the simulation. This means that no energy is lost in the system other than through the thermostats. The lower part of the figures, with 1 ns as a reference point for the computation of the differences, showcases the energy variations during the time span over which the flux is computed. Doing so, it appears that the kinetic energy is almost constant, there are still some variations but no global tendency, which is consistent with the stable temperature profile. The energy drift is, after 1 ns, mostly due to potential energy variations. Additionally, this drift is similar for the SL and LS configurations, meaning that it is not strongly dependent on the heat flux direction and thus should not impact the rectification measured.

Figures C.4 c and d depict the variation of the kinetic and potential energy as a function of time in the amorphous shell and in the crystalline core. In these figures, it appears that the variations of energy are stronger in the amorphous part, and even more so after 1 ns. This offers an explanation for the energy drift: there are small structural relaxations happening in the amorphous part, these relaxations release energy, creating an energy drift.

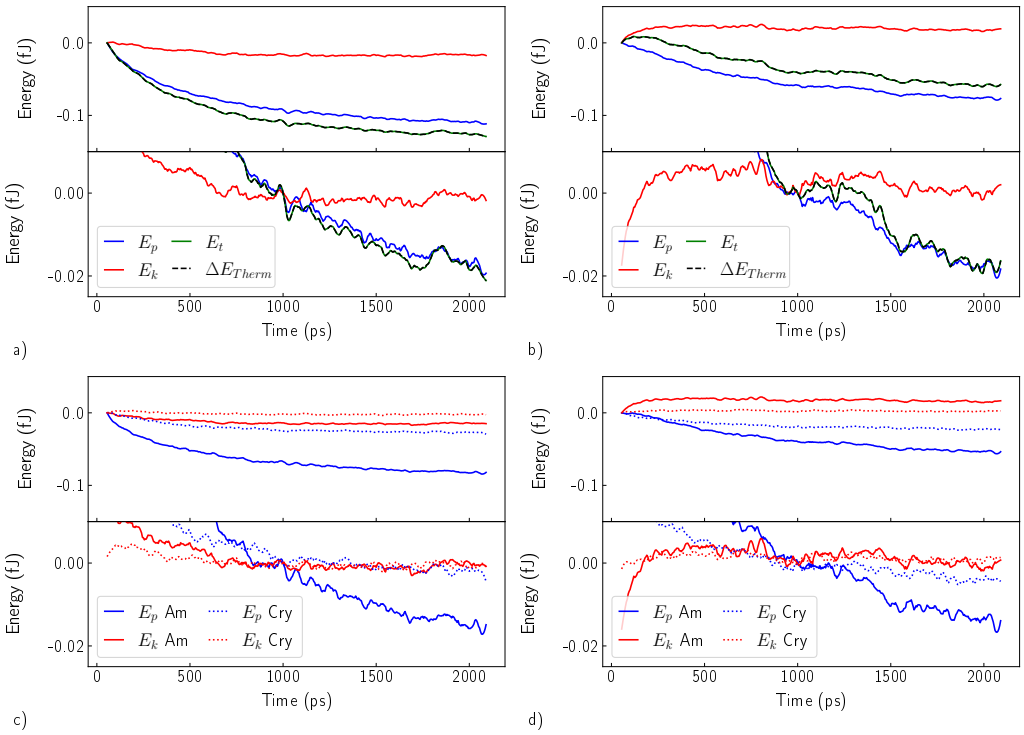

Figure C.4: Energy variations in the CO-CS-NW-4.4 configuration during a NEMD simulation for the global configuration for the SL (a) and LS (b) flux direction. The lower figures show the variation in the amorphous and crystalline parts for the SL (a) and LS (b) flux direction. The kinetic and potential energy are displayed in red and blue respectively, while the total energy is displayed in green, the difference of the energy removed by the cold thermostat and added by the hot is displayed with a black dashed line. The energies are set to zero as the hot and cold thermostat are set up (upper graph) or when energy exchange begin to be considered to compute the flux (lower graph).

In an attempt to reduce the energy drift, the procedure was slightly modified to include a short annealing at 400 K. The idea being that the higher temperature annealing should relax more the structure and reduce the energy drift. However, not only did this not sensibly reduce the thermal drift, but it reverted the thermal rectification observed. Indicating that the thermal rectification is dependent on the annealing of the system. Due to the lack of repetition, this result is not robust but is worth mentioning for eventual future exploration of this system.

In this section, it is shown that the energy exchange rate at the cold thermostat does not match exactly with the energy exchange rate at the hot thermostat. The difference corresponds to a decrease of potential energy in the amorphous shell. As this difference in flux appears for both CL and CO-CS-NW, and similarly for the two flux directions after the equilibration time, it is safe to assume that this energy drift is not the origin of the rectification, but can affect it.

Publications List

Published Articles

- *Ballistic Heat Transport in Nanocomposite: The Role of the Shape and Interconnection of Nanoinclusions*, Paul Desmarchelier, Alice Carré, Konstantinos Termentzidis, and Anne Tanguy. Nanomaterials, vol. 11, no. 8. 2021

- *Thermal rectification in asymmetric two-phase nanowires*, Paul Desmarchelier, Anne Tanguy, and Konstantinos Termentzidis. Phys. Rev. B, vol. 103, p. 014202.2021.

- *Vibrational density of states of free and embedded semiconducting GaN nanoparticles*, Paul Desmarchelier, Konstantinos Termentzidis, and Anne Tanguy. Semiconductor Science and Technology 35.9, p. 094001. 2020

- *Decorated Dislocations against Phonon Propagation for Thermal Management*, Stefanos Giaremis, Joseph Kioseoglou, Paul Desmarchelier, Anne Tanguy, Mykola Isaiev, Imad Belabbas, Philomela Komninou and Konstantinos Termentzidis. ACS Applied Energy Materials, vol. 3, no. 3 2020 pages 2682-2694, 2020

- *Enhancement and anticipation of the Ioffe-Regel crossover in amorphous/-nanocrystalline composites*, Amani Tlili, Valentina Giordano, Yaroslav Beltukov, Paul Desmarchelier, Samy Merabia and Anne Tanguy. Nanoscale, vol. 11, pages 21502-21512, 2019.

Article in Preparation

- *Heat Flux Radial Distribution in Core/Shell Nanowires: Atomistic and Hydrodynamic Heat Transport Approach*, Paul Desmarchelier, Albert Beardo, Konstantinos Termentzidis, Anne Tanguy, Xavier Alvarez.

Oral Contributions

- *Thermal Rectification in Asymmetric Core/Shell Nanowires*, Paul Desmarchelier, Konstantinos Termentzidis and Anne Tanguy. Virtual MRS Spring Meeting. April 2021. Online

- *Influence of the shape and interconnection of nanoparticles on the lattice thermal conductivity in a c-Si/a-Si nanocomposite*, Paul Desmarchelier, Anne Tanguy, Konstantinos Termentzidis. Journée Virtuelle de la Thermoélectricité, November 2020. Online

- *Tuning ballisticity/diffusivity in asymmetric nanowire*, Paul Desmarchelier, Anne Tanguy, Konstantinos Termentzidis. Virtual Conference on Thermoelectrics, July 2020. Online
- *Ballisticity and Rectification in Conical Nanowires*, Paul Desmarchelier, Konstantinos Termentzidis and Anne Tanguy. Nanoscale Heat Transport Days, Jan. 2020, Paris
- Paul Desmarchelier, Valentina Giordano, Yaroslav Beltukov, Anne Tanguy, Konstantinos Termentzidis. *Propagation and Diffusion of Excitation in Amorphous/Nano-Crystalline Composites*. International Congress on Glass, June 2019, Boston

Posters

- *Study of anomalous effects in thermal conductivity in c-GaN/a-SiO2 nanocomposites*, Paul Desmarchelier, Konstantinos Termentzidis and Anne Tanguy. E-MRS Fall Meeting 2019. Warsaw
- *Wave-Packet Propagation in Silicon Nano-Composite*, Paul Desmarchelier, Konstantinos Termentzidis and Anne Tanguy. DGG-USTV. 2019. Nuremberg

Project Funded

- Preparation of an application for access to the French national super computer
  - 850×10^3 obtained in 2019
  - Renewed for 1000×10^3 obtained in 2020

Bibliography

[Alajlouni *et al.* 2021] Sami Alajlouni, Albert Beardo, Lluc Sendra, Amirkoushyar Ziabari, Javier Bafaluy, Juan Camacho, Yi Xuan, F Xavier Alvarez and Ali Shakouri. *Geometrical quasi-ballistic effects on thermal transport in nanostructured devices.* Nano Research, vol. 14, no. 4, pages 945–952, 2021. (Cited on page 19.)

[Alder & Wainwright 1959] B. J. Alder and T. E. Wainwright. *Studies in Molecular Dynamics. I. General Method.* jcp, vol. 31, no. 2, pages 459–466, August 1959. (Cited on page 19.)

[Alexander 1998] Shlomo Alexander. *Amorphous solids: their structure, lattice dynamics and elasticity.* Physics Reports, vol. 296, no. 2, pages 65–236, 1998. (Cited on page 39.)

[Allen & Feldman 1993] Philip B. Allen and Joseph L. Feldman. *Thermal conductivity of disordered harmonic solids.* Phys. Rev. B, vol. 48, pages 12581–12588, Nov 1993. (Cited on pages 3, 14, 74 and 132.)

[Allen & Tildesley 2017] Michael P Allen and Dominic J Tildesley. Computer simulation of liquids. Oxford university press, 2017. (Cited on pages 24 and 25.)

[Allen *et al.* 1999] Philip B. Allen, Joseph L. Feldman, Jaroslav Fabian and Frederick Wooten. *Diffusons, locons and propagons: Character of atomie yibrations in amorphous Si.* Philosophical Magazine B, vol. 79, no. 11-12, pages 1715–1731, 1999. (Cited on pages 14, 76 and 160.)

[Allen 1991] David H. Allen. *Thermomechanical Coupling in Inelastic Solids.* Applied Mechanics Reviews, vol. 44, no. 8, pages 361–373, 08 1991. (Cited on page 1.)

[Amma *et al.* 2010] Shin-ichi Amma, Yuki Tokumoto, Keiichi Edagawa, Naoya Shibata, Teruyasu Mizoguchi, Takahisa Yamamoto and Yuichi Ikuhara. *Electrical current flow at conductive nanowires formed in GaN thin films by a dislocation template technique.* Applied Physics Letters, vol. 96, no. 19, page 193109, 2010. (Cited on page 96.)

[Anderson 1958] P. W. Anderson. *Absence of Diffusion in Certain Random Lattices.* Phys. Rev., vol. 109, pages 1492–1505, Mar 1958. (Cited on page 14.)

[Andreoni & Yip 2019] Wanda Andreoni and Sidney Yip. Handbook of materials modeling: Methods: Theory and modeling. Springer, 2019. (Cited on page 45.)

[Asen-Palmer *et al.* 1997] M. Asen-Palmer, K. Bartkowski, E. Gmelin, M. Cardona, A. P. Zhernov, A. V. Inyushkin, A. Taldenkov, V. I. Ozhogin, K. M. Itoh and E. E. Haller. *Thermal conductivity of germanium crystals with different isotopic compositions.* Phys. Rev. B, vol. 56, pages 9431–9447, Oct 1997. (Cited on pages 43 and 96.)

[Ashcroft *et al.* 1976] Neil W Ashcroft, N David Mermin*et al.* Solid state physics, volume 2005. holt, rinehart and winston, new york London, 1976. (Cited on pages 2, 8, 9, 13, 21, 42 and 43.)

[Bartels *et al.* 2006] A. Bartels, F. Hudert, C. Janke, T. Dekorsy and K. Köhler. *Femtosecond time-resolved optical pump-probe spectroscopy at kilohertz-scan-rates over nanosecond-time-delays without mechanical delay line.* Applied Physics Letters, vol. 88, no. 4, page 041117, 2006. (Cited on page 35.)

[Beardo *et al.* 2019] A. Beardo, M. Calvo-Schwarzwälder, J. Camacho, T.G. Myers, P. Torres, L. Sendra, F.X. Alvarez and J. Bafaluy. *Hydrodynamic Heat Transport in Compact and Holey Silicon Thin Films.* Phys. Rev. Applied, vol. 11, page 034003, Mar 2019. (Cited on pages 19 and 126.)

[Beardo *et al.* 2020] A. Beardo, M. G. Hennessy, L. Sendra, J. Camacho, T. G. Myers, J. Bafaluy and F. X. Alvarez. *Phonon hydrodynamics in frequency-domain thermoreflectance experiments.* Phys. Rev. B, vol. 101, page 075303, Feb 2020. (Cited on page 19.)

[Beardo *et al.* 2021a] Albert Beardo, Joshua L. Knobloch, Lluc Sendra, Javier Bafaluy, Travis D. Frazer, Weilun Chao, Jorge N. Hernandez-Charpak, Henry C. Kapteyn, Begoña Abad, Margaret M. Murnane, F. Xavier Alvarez and Juan Camacho. *A General and Predictive Understanding of Thermal Transport from 1D- and 2D-Confined Nanostructures: Theory and Experiment.* ACS Nano, vol. 0, no. 0, page null, 2021. PMID: 34328719. (Cited on page 19.)

[Beardo *et al.* 2021b] Albert Beardo, Miquel López-Suárez, Luis Alberto Pérez, Lluc Sendra, Maria Isabel Alonso, Claudio Melis, Javier Bafaluy, Juan Camacho, Luciano Colombo, Riccardo Rurali, Francesc Xavier Alvarez and Juan Sebastián Reparaz. *Observation of second sound in a rapidly varying temperature field in Ge.* Science Advances, vol. 7, no. 27, 2021. (Cited on page 120.)

[Bejenari *et al.* 2020] Igor Bejenari, Alexander Burenkov, Peter Pichler, Ioannis Deretzis and Antonino La Magna. *Molecular Dynamics Modeling of the Radial Heat Transfer from Silicon Nanowires.* In 2020 International Conference on Simulation of Semiconductor Processes and Devices (SISPAD), pages 67–70, 2020. (Cited on page 119.)

[Beltukov *et al.* 2013] Y. M. Beltukov, V. I. Kozub and D. A. Parshin. *Ioffe-Regel criterion and diffusion of vibrations in random lattices.* Phys. Rev. B, vol. 87, page 134203, Apr 2013. (Cited on pages 15, 32, 35 and 36.)

[Beltukov *et al.* 2015] Y M Beltukov, C Fusco, A Tanguy and D A Parshin. *Transverse and longitudinal vibrations in amorphous silicon.* Journal of Physics: Conference Series, vol. 661, page 012056, dec 2015. (Cited on pages 32, 85 and 171.)

[Beltukov *et al.* 2016] Y. M. Beltukov, C. Fusco, D. A. Parshin and A. Tanguy. *Boson peak and Ioffe-Regel criterion in amorphous siliconlike materials: The effect of bond directionality.* Phys. Rev. E, vol. 93, page 023006, Feb 2016. (Cited on pages 14, 15, 32, 33, 34, 67, 76, 114 and 172.)

[Beltukov *et al.* 2018] Y. M. Beltukov, D. A. Parshin, V. M. Giordano and A. Tanguy. *Propagative and diffusive regimes of acoustic damping in bulk amorphous material.* Phys. Rev. E, vol. 98, page 023005, Aug 2018. (Cited on pages 14, 16, 35, 73, 74, 75, 92, 94, 112, 114, 117 and 132.)

[Ben-Abdallah & Biehs 2013] Philippe Ben-Abdallah and Svend-Age Biehs. *Phase-change radiative thermal diode.* Applied Physics Letters, vol. 103, no. 19, page 191907, 2013. (Cited on page 137.)

[Berweger *et al.* 2011] Samuel Berweger, Joanna M. Atkin, Xiaoji G. Xu, Robert L. Olmon and Markus B. Raschke. *Femtosecond nanofocusing with full optical waveform control.* Nano Letters, vol. 11, no. 10, pages 4309–4313, 2011. (Cited on page 51.)

[Blandre *et al.* 2015] Etienne Blandre, Laurent Chaput, Samy Merabia, David Lacroix and Konstantinos Termentzidis. *Modeling the reduction of thermal conductivity in core/shell and diameter-modulated silicon nanowires.* Phys. Rev. B, vol. 91, page 115404, Mar 2015. (Cited on pages 106 and 165.)

[Boltzmann 1903] J. Boltzmann L.and Nabl. Kinetische theorie der materie, pages 493–557. Vieweg+Teubner Verlag, Wiesbaden, 1903. (Cited on page 1.)

[Boon & Yip 1991] Jean Pierre Boon and Sidney Yip. Molecular hydrodynamics. Courier Corporation, 1991. (Cited on page 32.)

[Boone *et al.* 2019] Paul Boone, Hasan Babaei and Christopher E. Wilmer. *Heat Flux for Many-Body Interactions: Corrections to LAMMPS.* Journal of Chemical Theory and Computation, vol. 15, no. 10, pages 5579–5587, 2019. PMID: 31369260. (Cited on page 40.)

[Cahill & Pohl 1988] D G Cahill and R O Pohl. *Lattice Vibrations and Heat Transport in Crystals and Glasses.* Annual Review of Physical Chemistry, vol. 39, no. 1, pages 93–121, 1988. (Cited on page 88.)

[Cahill *et al.* 1994] David G. Cahill, M. Katiyar and J. R. Abelson. *Thermal conductivity of a-Si:H thin films.* Phys. Rev. B, vol. 50, pages 6077–6081, Sep 1994. (Cited on page 90.)

[Callaway 1959] Joseph Callaway. *Model for Lattice Thermal Conductivity at Low Temperatures.* Phys. Rev., vol. 113, pages 1046–1051, Feb 1959. (Cited on pages 16 and 42.)

[Calvo & Balbuena 2005] Sergio R. Calvo and Perla B. Balbuena. *Molecular dynamics studies of phonon spectra in mono- and bimetallic nanoclusters.* Surface Science, vol. 581, no. 2-3, pages 213–224, 2005. (Cited on pages 51, 54 and 56.)

[Car *et al.* 2014] Diana Car, Jia Wang, Marcel A. Verheijen, Erik P. A. M. Bakkers and Sébastien R. Plissard. *Rationally Designed Single-Crystalline Nanowire Networks.* Advanced Materials, vol. 26, no. 28, pages 4875–4879, 2014. (Cited on page 77.)

[Carbogno *et al.* 2017] Christian Carbogno, Rampi Ramprasad and Matthias Scheffler. *Ab Initio Green-Kubo Approach for the Thermal Conductivity of Solids.* Phys. Rev. Lett., vol. 118, page 175901, Apr 2017. (Cited on page 45.)

[Carruthers 1961] Peter Carruthers. *Theory of Thermal Conductivity of Solids at Low Temperatures.* Rev. Mod. Phys., vol. 33, pages 92–138, Jan 1961. (Cited on page 96.)

[Carré *et al.* 2007] Antoine Carré, Ludovic Berthier, Jürgen Horbach, Simona Ispas and Walter Kob. *Amorphous silica modeled with truncated and screened Coulomb interactions: A molecular dynamics simulation study.* The Journal of Chemical Physics, vol. 127, no. 11, page 114512, 2007. (Cited on page 22.)

[Cartoixà *et al.* 2015] Xavier Cartoixà, Luciano Colombo and Riccardo Rurali. *Thermal rectification by design in telescopic Si nanowires.* Nano letters, vol. 15, no. 12, pages 8255–8259, 2015. (Cited on pages 139 and 161.)

[Cepellotti *et al.* 2015] Andrea Cepellotti, Giorgia Fugallo, Lorenzo Paulatto, Michele Lazzeri, Francesco Mauri and Nicola Marzari. *Phonon hydrodynamics in two-dimensional materials.* Nature communications, vol. 6, no. 1, pages 1–7, 2015. (Cited on page 19.)

[Chakraborty *et al.* 2019] Dhritiman Chakraborty, Joshua Brooke, Nicholas C S Hulse and Neophytos Neophytou. *Thermal rectification optimization in nanoporous Si using Monte Carlo simulations.* Journal of Applied Physics, vol. 126, no. 18, page 184303, 2019. (Cited on page 143.)

[Chang *et al.* 2006] C. W. Chang, D. Okawa, A. Majumdar and A. Zettl. *Solid-State Thermal Rectifier.* Science, vol. 314, no. 5802, pages 1121–1124, 2006. (Cited on pages 139, 155, 160 and 181.)

[Chen *et al.* 2011] Jie Chen, Gang Zhang and Baowen Li. *Phonon coherent resonance and its effect on thermal transport in core-shell nanowires.* The Journal of Chemical Physics, vol. 135, no. 10, page 104508, 2011. (Cited on page 106.)

[Chrysochoos & Peyroux 1997] André Chrysochoos and Robert Peyroux. *Modélisation numérique des couplages en thermomécanique des solides.* Revue Européenne des Éléments Finis, vol. 6, no. 5-6, pages 673–724, 1997. (Cited on page 1.)

[Combe *et al.* 2007] Nicolas Combe, Jean Roch Huntzinger and Adnen Mlayah. *Vibrations of quantum dots and light scattering properties: Atomistic versus continuous models.* Phys. Rev. B, vol. 76, no. 20, pages 1–12, 2007. (Cited on pages 51 and 53.)

[Cowley 1988] E. Roger Cowley. *Lattice Dynamics of Silicon with Empirical Many-Body Potentials.* Phys. Rev. Lett., vol. 60, pages 2379–2381, Jun 1988. (Cited on page 69.)

[Cui *et al.* 2001] Yi Cui, Lincoln J. Lauhon, Mark S. Gudiksen, Jianfang Wang and Charles M. Lieber. *Diameter-controlled synthesis of single-crystal silicon nanowires.* Applied Physics Letters, vol. 78, no. 15, pages 2214–2216, 2001. (Cited on page 106.)

[Damart *et al.* 2015] T. Damart, V. M. Giordano and A. Tanguy. *Nanocrystalline inclusions as a low-pass filter for thermal transport in a -Si.* Physical Review B, vol. 92, no. 9, pages 1–11, 2015. (Cited on pages 33, 50, 57, 63, 77, 93 and 111.)

[Daudin 2008] Bruno Daudin. *Polar and nonpolar GaN quantum dots.* Journal of Physics Condensed Matter, vol. 20, no. 47, page 473201, 2008. (Cited on page 51.)

[de Brito Mota *et al.* 1998] F. de Brito Mota, J. Justo and A. Fazzio. *Structural properties of amorphous silicon nitride.* Phys. Rev. B, vol. 58, no. 13, pages 8323–8328, 1998. (Cited on page 52.)

[de Sousa Oliveira *et al.* 2020] Laura de Sousa Oliveira, S. Aria Hosseini, Alex Greaney and Neophytos Neophytou. *Heat current anticorrelation effects leading to thermal conductivity reduction in nanoporous Si.* Phys. Rev. B, vol. 102, page 205405, Nov 2020. (Cited on pages 72 and 165.)

[DeAngelis *et al.* 2019] Freddy DeAngelis, Murali Gopal Muraleedharan, Jaeyun Moon, Hamid Reza Seyf, Austin J. Minnich, Alan J. H. McGaughey and Asegun Henry. *Thermal Transport in Disordered Materials.* Nanoscale and Microscale Thermophysical Engineering, vol. 23, no. 2, pages 81–116, 2019. (Cited on page 93.)

[Del Castillo-Castro *et al.* 2007] T. Del Castillo-Castro, E. Larios-Rodriguez, Z. Molina-Arenas, M. M. Castillo-Ortega and J. Tanori. *Synthesis and characterization of metallic nanoparticles and their incorporation into electroconductive polymer composites.* Composites Part A: Applied Science and Manufacturing, vol. 38, no. 1, pages 107–113, 2007. (Cited on page 51.)

[Dettori *et al.* 2016] Riccardo Dettori, Claudio Melis, Riccardo Rurali and Luciano Colombo. *Thermal rectification in silicon by a graded distribution of defects.* Journal of Applied Physics, vol. 119, no. 21, page 215102, 2016. (Cited on page 139.)

[Dilhaire *et al.* 2011] S. Dilhaire, G. Pernot, G. Calbris, J. M. Rampnoux and S. Grauby. *Heterodyne picosecond thermoreflectance applied to nanoscale thermal metrology.* Journal of Applied Physics, vol. 110, no. 11, page 114314, 2011. (Cited on page 35.)

[Diu & Guthmann 1989] Bernard Diu and Claudine Guthmann. Eléments de physique statistique, volume 37. Editions Hermann, 1989. (Cited on pages 6, 12, 19 and 25.)

[Donadio & Galli 2009] Davide Donadio and Giulia Galli. *Atomistic Simulations of Heat Transport in Silicon Nanowires.* Phys. Rev. Lett., vol. 102, page 195901, May 2009. (Cited on pages 106 and 146.)

[Dove 1993] Martin T. Dove. Time correlation functions, page 229–232. Cambridge Topics in Mineral Physics and Chemistry. Cambridge University Press, 1993. (Cited on pages 9, 10, 30 and 43.)

[Duong *et al.* 2019] Thuy-Quynh Duong, Carlo Massobrio, Guido Ori, Mauro Boero and Evelyne Martin. *Thermal conductivity and transport modes in glassy* $GeTe_4$ *by first-principles molecular dynamics.* Phys. Rev. Materials, vol. 3, page 105401, Oct 2019. (Cited on page 45.)

[Duong *et al.* 2020] Thuy-Quynh Duong, Carlo Massobrio, Guido Ori, Mauro Boero and Evelyne Martin. *Thermal resistance of an interfacial molecular layer by first-principles molecular dynamics.* The Journal of Chemical Physics, vol. 153, no. 7, page 074704, 2020. (Cited on page 45.)

[Duong *et al.* 2021] Thuy-Quynh Duong, Assil Bouzid, Carlo Massobrio, Guido Ori, Mauro Boero and Evelyne Martin. *First-principles thermal transport in amorphous Ge2Sb2Te5 at the nanoscale.* RSC Adv., vol. 11, pages 10747–10752, 2021. (Cited on page 45.)

[Eringen & Suhubi 1974] AC Eringen and ES Suhubi. *Elastodynamics. Finite Motions, vol. 1*, 1974. (Cited on page 171.)

[Eringen & Suhubi 1975] A Cemal Eringen and Erdogan Suhubi. Elastodynamics, volume II. Academic Press, New York, academic édition, 1975. (Cited on page 51.)

[Faez *et al.* 2009] Sanli Faez, Anatoliy Strybulevych, John H. Page, Ad Lagendijk and Bart A. van Tiggelen. *Observation of Multifractality in Anderson Localization of Ultrasound.* Phys. Rev. Lett., vol. 103, page 155703, Oct 2009. (Cited on page 14.)

[Fan *et al.* 2015] Zheyong Fan, Luiz Felipe C. Pereira, Hui-Qiong Wang, Jin-Cheng Zheng, Davide Donadio and Ari Harju. *Force and heat current formulas for many-body potentials in molecular dynamics simulations with applications to thermal conductivity calculations.* Phys. Rev. B, vol. 92, page 094301, Sep 2015. (Cited on page 40.)

[Fang *et al.* 2006] Kuan-Chuan Fang, Cheng-I Weng and Shin-Pon Ju. *An investigation into the structural features and thermal conductivity of silicon nanoparticles using molecular dynamics simulations.* Nanotechnology, vol. 17, no. 15, pages 3909–3914, jul 2006. (Cited on pages 52, 61, 90 and 163.)

[Feldman *et al.* 1993] Joseph L. Feldman, Mark D. Kluge, Philip B. Allen and Frederick Wooten. *Thermal conductivity and localization in glasses: Numerical study of a model of amorphous silicon.* Phys. Rev. B, vol. 48, pages 12589–12602, Nov 1993. (Cited on pages 14 and 15.)

[Feldman *et al.* 1999] Joseph L. Feldman, Philip B. Allen and Scott R. Bickham. *Numerical study of low-frequency vibrations in amorphous silicon.* Phys. Rev. B, vol. 59, pages 3551–3559, Feb 1999. (Cited on page 14.)

[Feng *et al.* 2017] Lei Feng, Takuma Shiga, Haoxue Han, Shenghong Ju, Yuriy A. Kosevich and Junichiro Shiomi. *Phonon-interference resonance effects by nanoparticles embedded in a matrix.* Phys. Rev. B, vol. 96, page 220301, Dec 2017. (Cited on page 50.)

[Forman *et al.* 2016] Clemens Forman, Ibrahim Kolawole Muritala, Robert Pardemann and Bernd Meyer. *Estimating the global waste heat potential.* Renewable and Sustainable Energy Reviews, vol. 57, pages 1568–1579, 2016. (Cited on page 1.)

[Fortner & Lannin 1989] J. Fortner and J. S. Lannin. *Radial distribution functions of amorphous silicon.* Phys. Rev. B, vol. 39, pages 5527–5530, Mar 1989. (Cited on page 28.)

[Fourier 1822] Jean Baptiste Joseph Fourier. Théorie analytique de la chaleur. Chez Firmin Didot, père et fils, 1822. (Cited on page 1.)

[France-Lanord *et al.* 2014a] Arthur France-Lanord, Etienne Blandre, Tristan Albaret, Samy Merabia, David Lacroix and Konstantinos Termentzidis.

Atomistic amorphous/crystalline interface modelling for superlattices and core/shell nanowires. Journal of Physics Condensed Matter, vol. 26, no. 5, page 055011, 2014. (Cited on pages 22, 27, 109 and 110.)

[France-Lanord *et al.* 2014b] Arthur France-Lanord, Samy Merabia, Tristan Albaret, David Lacroix and Konstantinos Termentzidis. *Thermal properties of amorphous/crystalline silicon superlattices.* Journal of Physics: Condensed Matter, vol. 26, no. 35, page 355801, aug 2014. (Cited on pages 57, 79, 107 and 108.)

[Frenkel & Smit 2001] Daan Frenkel and Berend Smit. Understanding molecular simulation: from algorithms to applications, volume 1. Elsevier, 2001. (Cited on pages 20, 25 and 28.)

[Fusco *et al.* 2010] C. Fusco, T. Albaret and A. Tanguy. *Role of local order in the small-scale plasticity of model amorphous materials.* Phys. Rev. E, vol. 82, page 066116, Dec 2010. (Cited on pages 26, 29, 67, 68 and 69.)

[Gao *et al.* 2014] Yufei Gao, Wenbo Bao, Qingyuan Meng, Yuhang Jing and Xiaoxu Song. *The thermal transport properties of single-crystalline nanowires covered with amorphous shell: A molecular dynamics study.* Journal of Non-Crystalline Solids, vol. 387, pages 132–138, 2014. (Cited on pages 106 and 133.)

[Ghosh & Giri 2016] Ramesh Ghosh and P K Giri. *Silicon nanowire heterostructures for advanced energy and environmental applications: a review.* Nanotechnology, vol. 28, no. 1, page 012001, nov 2016. (Cited on page 105.)

[Giaremis *et al.* 2020] Stefanos Giaremis, Joseph Kioseoglou, Paul Desmarchelier, Anne Tanguy, Mykola Isaiev, Imad Belabbas, Philomela Komninou and Konstantinos Termentzidis. *Decorated Dislocations against Phonon Propagation for Thermal Management.* ACS Applied Energy Materials, vol. 3, no. 3, pages 2682–2694, 2020. (Cited on pages 96, 97, 98 and 101.)

[Girard *et al.* 2016] A. Girard, H. Gehan, A. Crut, A. Mermet, L. Saviot and J. Margueritat. *Mechanical coupling in gold nanoparticles supermolecules revealed by plasmon-enhanced ultralow frequency raman spectroscopy.* Nano Letters, vol. 16, no. 6, pages 3843–3849, 2016. (Cited on page 51.)

[Giri *et al.* 2016] Ashutosh Giri, Jeffrey L. Braun and Patrick E. Hopkins. *Effect of crystalline/amorphous interfaces on thermal transport across confined thin films and superlattices.* Journal of Applied Physics, vol. 119, no. 23, page 235305, 2016. (Cited on page 165.)

[Glassbrenner & Slack 1964] C. J. Glassbrenner and Glen A. Slack. *Thermal Conductivity of Silicon and Germanium from 3 K to the Melting Point.* Phys. Rev., vol. 134, pages A1058–A1069, May 1964. (Cited on page 160.)

[Gradečak *et al.* 2005] Silvija Gradečak, Fang Qian, Yat Li, Hong-Gyu Park and Charles M. Lieber. *GaN nanowire lasers with low lasing thresholds.* Applied Physics Letters, vol. 87, no. 17, page 173111, 2005. (Cited on page 96.)

[Guénolé *et al.* 2013] Julien Guénolé, Julien Godet and Sandrine Brochard. *Plasticity in crystalline-amorphous core-shell Si nanowires controlled by native interface defects.* Phys. Rev. B, vol. 87, page 045201, Jan 2013. (Cited on pages 26 and 106.)

[Guo *et al.* 2018] Yangyu Guo, David Jou and Moran Wang. *Nonequilibrium thermodynamics of phonon hydrodynamic model for nanoscale heat transport.* Phys. Rev. B, vol. 98, page 104304, Sep 2018. (Cited on page 19.)

[Guyer & Krumhansl 1966a] R. A. Guyer and J. A. Krumhansl. *Solution of the Linearized Phonon Boltzmann Equation.* Phys. Rev., vol. 148, pages 766–778, Aug 1966. (Cited on page 18.)

[Guyer & Krumhansl 1966b] R. A. Guyer and J. A. Krumhansl. *Thermal Conductivity, Second Sound, and Phonon Hydrodynamic Phenomena in Nonmetallic Crystals.* Phys. Rev., vol. 148, pages 778–788, Aug 1966. (Cited on pages 18 and 19.)

[Hahn *et al.* 2015] Konstanze R. Hahn, Marcello Puligheddu and Luciano Colombo. *Thermal boundary resistance at Si/Ge interfaces determined by approach-to-equilibrium molecular dynamics simulations.* Phys. Rev. B, vol. 91, page 195313, May 2015. (Cited on pages 40 and 138.)

[Han & Bester 2011] Peng Han and Gabriel Bester. *Interatomic potentials for the vibrational properties of III-V semiconductor nanostructures.* Phys. Rev. B, vol. 83, no. 17, pages 1–8, 2011. (Cited on pages 45, 51, 53, 54, 55, 56 and 163.)

[Han & Bester 2012] Peng Han and Gabriel Bester. *Confinement effects on the vibrational properties of III-V and II-VI nanoclusters.* Phys. Rev. B, vol. 85, no. 4, pages 1–4, 2012. (Cited on page 51.)

[Haras & Skotnicki 2018] Maciej Haras and Thomas Skotnicki. *Thermoelectricity for IoT – A review.* Nano Energy, vol. 54, pages 461–476, 2018. (Cited on page 2.)

[Hardy 1963] Robert J. Hardy. *Energy-Flux Operator for a Lattice.* Phys. Rev., vol. 132, pages 168–177, Oct 1963. (Cited on page 39.)

[Hirth *et al.* 1983] John Price Hirth, Jens Lothe and T Mura. *Theory of dislocations.* Journal of Applied Mechanics, vol. 50, no. 2, page 476, 1983. (Cited on page 96.)

[Hofmeister *et al.* 2005] H Hofmeister, GL Tan and M Dubiel. *Shape and internal structure of silver nanoparticles embedded in glass.* Journal of materials research, vol. 20, no. 6, pages 1551–1562, 2005. (Cited on page 77.)

[Hopcroft *et al.* 2010] Matthew A. Hopcroft, William D. Nix and Thomas W. Kenny. *What is the Young's Modulus of Silicon?* Journal of Microelectromechanical Systems, vol. 19, no. 2, pages 229–238, 2010. (Cited on page 68.)

[Hori *et al.* 2015] Takuma Hori, Junichiro Shiomi and Chris Dames. *Effective phonon mean free path in polycrystalline nanostructures.* Applied Physics Letters, vol. 106, no. 17, page 171901, 2015. (Cited on page 77.)

[Horton *et al.* 2015] Matthew K. Horton, Sneha Rhode, Suman-Lata Sahonta, Menno J. Kappers, Sarah J. Haigh, Timothy J. Pennycook, Colin J. Humphreys, Rajiv O. Dusane and Michelle A. Moram. *Segregation of In to Dislocations in InGaN.* Nano Letters, vol. 15, no. 2, pages 923–930, 2015. PMID: 25594363. (Cited on page 96.)

[Hu *et al.* 2008] Ming Hu, Pawel Keblinski and Baowen Li. *Thermal rectification at silicon-amorphous polyethylene interface.* Applied Physics Letters, vol. 92, no. 21, page 211908, 2008. (Cited on pages 138 and 165.)

[Hu *et al.* 2011] Ming Hu, Xiaoliang Zhang, Konstantinos P. Giapis and Dimos Poulikakos. *Thermal conductivity reduction in core-shell nanowires.* Phys. Rev. B, vol. 84, page 085442, Aug 2011. (Cited on page 106.)

[Hu *et al.* 2018] Shiqian Hu, Zhongwei Zhang, Pengfei Jiang, Jie Chen, Sebastian Volz, Masahiro Nomura and Baowen Li. *Randomness-induced phonon localization in graphene heat conduction.* The journal of physical chemistry letters, vol. 9, no. 14, pages 3959–3968, 2018. (Cited on page 139.)

[Hu *et al.* 2020] Shiqian Hu, Lei Feng, Cheng Shao, Ivan A. Strelnikov, Yuriy A. Kosevich and Junichiro Shiomi. *Two-path phonon interference resonance induces a stop band in a silicon crystal matrix with a multilayer array of embedded nanoparticles.* Phys. Rev. B, vol. 102, page 024301, Jul 2020. (Cited on pages 50 and 77.)

[Huang *et al.* 2002] Yu Huang, Xiangfeng Duan, Yi Cui and Charles M. Lieber. *Gallium Nitride Nanowire Nanodevices.* Nano Letters, vol. 2, no. 2, pages 101–104, 2002. (Cited on page 96.)

[Huang *et al.* 2017] Yun Huang, Jiantao Hu, Yimin Yao, Xiaoliang Zeng, Jiajia Sun, Guiran Pan, Rong Sun, Jian-Bin Xu and Ching-Ping Wong. *Manipulating Orientation of Silicon Carbide Nanowire in Polymer Composites to Achieve High Thermal Conductivity.* Advanced Materials Interfaces, vol. 4, no. 17, page 1700446, 2017. (Cited on page 77.)

[Huo *et al.* 2008] Kaifu Huo, Xuming Zhang, Liangsheng Hu, Xianjiao Sun, Jijiang Fu and Paul K. Chu. *One-step growth and field emission properties of quasialigned TiO2 nanowire/carbon nanocone core-shell nanostructure arrays on Ti substrates.* Applied Physics Letters, vol. 93, no. 1, page 013105, 2008. (Cited on page 140.)

[Ikuhara 2009] Yuichi Ikuhara. *Nanowire design by dislocation technology.* Progress in Materials Science, vol. 54, no. 6, pages 770–791, 2009. "THE NABARRO LEGACY – PERSPECTIVES FOR ADVANCED MATERIALS IN THE 21ST CENTURY" A collection of invited lectures at the MRS Spring Meeting 2008. (Cited on page 96.)

[Isaiev *et al.* 2014] Mykola Isaiev, Pascal J. Newby, Bruno Canut, Alona Tytarenko, Pavlo Lishchuk, Dmytro Andrusenko, Séverine Gomès, Jean-Marie Bluet, Luc G. Fréchette, Vladimir Lysenko and Roman Burbelo. *Thermal conductivity of partially amorphous porous silicon by photoacoustic technique.* Materials Letters, vol. 128, pages 71–74, 2014. (Cited on page 90.)

[Ishimaru *et al.* 1997] Manabu Ishimaru, Shinji Munetoh and Teruaki Motooka. *Generation of amorphous silicon structures by rapid quenching: A molecular-dynamics study.* Phys. Rev. B, vol. 56, pages 15133–15138, Dec 1997. (Cited on page 26.)

[Jabbari *et al.* 2017] Fatemeh Jabbari, Ali Rajabpour and Seifollah Saedodin. *Thermal conductivity and viscosity of nanofluids: A review of recent molecular dynamics studies.* Chemical Engineering Science, vol. 174, pages 67–81, 2017. (Cited on pages 3 and 77.)

[Jezowski *et al.* 2003] A. Jezowski, B. A. Danilchenko, M. Boćkowski, I. Grzegory, S. Krukowski, T. Suski and T. Paszkiewicz. *Thermal conductivity of GaN crystals in 4.2-300 K range.* Solid State Communications, vol. 128, no. 2-3, pages 69–73, 2003. (Cited on page 61.)

[Jiang *et al.* 2017] Yongqiang Jiang, Shuang Cai, Yi Tao, Zhiyong Wei, Kedong Bi and Yunfei Chen. *Phonon transport properties of bulk and monolayer GaN from first-principles calculations.* Computational Materials Science, vol. 138, pages 419–425, 2017. (Cited on pages 54, 56 and 99.)

[Joule 1851] James Prescott Joule. *On the mechanical equivalent of heat.* In Abstracts of the Papers Communicated to the Royal Society of London, number 5, pages 839–839. The Royal Society London, 1851. (Cited on page 6.)

[Ju & Liang 2012a] Shenghong Ju and Xingang Liang. *Thermal rectification and phonon scattering in asymmetric silicon nanoribbons.* Journal of Applied Physics, vol. 112, no. 2, page 024307, 2012. (Cited on pages 139, 160 and 161.)

[Ju & Liang 2012b] Shenghong Ju and Xingang Liang. *Thermal rectification and phonon scattering in silicon nanofilm with cone cavity.* Journal of Applied Physics, vol. 112, no. 5, page 054312, 2012. (Cited on page 139.)

[Ju *et al.* 2016] Wenjing Ju, Zhongyuan Zhou and Zhiyong Wei. *Anisotropic thermal transport property of defect-free GaN.* AIP Advances, vol. 6, no. 6, page 065328, 2016. (Cited on page 64.)

[Juangsa *et al.* 2017] Firman Bagja Juangsa, Yoshiki Muroya, Meguya Ryu, Junko Morikawa and Tomohiro Nozaki. *Comparative study of thermal conductivity in crystalline and amorphous nanocomposite.* Applied Physics Letters, vol. 110, no. 25, page 253105, 2017. (Cited on page 67.)

[Jund & Jullien 1999] Philippe Jund and Rémi Jullien. *Molecular-dynamics calculation of the thermal conductivity of vitreous silica.* Phys. Rev. B, vol. 59, pages 13707–13711, Jun 1999. (Cited on page 38.)

[Juvé *et al.* 2010] Vincent Juvé, Aurélien Crut, Paolo Maioli, Michel Pellarin, Michel Broyer, Natalia Del Fatti and Fabrice Vallée. *Probing elasticity at the nanoscale: Terahertz acoustic vibration of small metal nanoparticles.* Nano Letters, vol. 10, no. 5, pages 1853–1858, 2010. (Cited on page 51.)

[Karamitaheri *et al.* 2014] Hossein Karamitaheri, Neophytos Neophytou and Hans Kosina. *Anomalous diameter dependence of thermal transport in ultra-narrow Si nanowires.* Journal of Applied Physics, vol. 115, no. 2, page 024302, 2014. (Cited on page 119.)

[Karamitaheri *et al.* 2015] Hossein Karamitaheri, Mahdi Pourfath, Hans Kosina and Neophytos Neophytou. *Low-dimensional phonon transport effects in ultranarrow disordered graphene nanoribbons.* Phys. Rev. B, vol. 91, page 165410, Apr 2015. (Cited on page 44.)

[Kargar *et al.* 2016] Fariborz Kargar, Bishwajit Debnath, Joona-Pekko Kakko, Antti Säynätjoki, Harri Lipsanen, Denis L Nika, Roger K Lake and Alexander A Balandin. *Direct observation of confined acoustic phonon polarization branches in free-standing semiconductor nanowires.* Nature communications, vol. 7, no. 1, pages 1–7, 2016. (Cited on page 94.)

[Kasprzak *et al.* 2020] Maciej Kasprzak, Marianna Sledzinska, Karol Zaleski, Igor Iatsunskyi, Francesc Alzina, Sebastian Volz, Clivia M. Sotomayor Torres and Bartlomiej Graczykowski. *High-temperature silicon thermal diode and switch.* Nano Energy, vol. 78, page 105261, 2020. (Cited on pages 2 and 139.)

[Kınac ı *et al.* 2012] Alper Kınac ı, Justin B. Haskins, Cem Sevik and Tahir Çağ ın. *Thermal conductivity of BN-C nanostructures.* Phys. Rev. B, vol. 86, page 115410, Sep 2012. (Cited on page 37.)

[Kim *et al.* 2006] Woochul Kim, Joshua Zide, Arthur Gossard, Dmitri Klenov, Susanne Stemmer, Ali Shakouri and Arun Majumdar. *Thermal Conductivity Reduction and Thermoelectric Figure of Merit Increase by Embedding Nanoparticles in Crystalline Semiconductors.* Phys. Rev. Lett., vol. 96, page 045901, Feb 2006. (Cited on page 50.)

[Kimmer *et al.* 2007] Chris Kimmer, Sylvie Aubry, Ashton Skye and Patrick K. Schelling. *Scattering of phonons from a high-energy grain boundary in silicon: Dependence on angle of incidence.* Phys. Rev. B, vol. 75, page 144105, Apr 2007. (Cited on page 77.)

[Kioseoglou *et al.* 2017] J. Kioseoglou, M. Katsikini, K. Termentzidis, I. Karakostas and E. C. Paloura. *Mechanism and crucial parameters on GaN nanocluster formation in a silica matrix.* Journal of Applied Physics, vol. 121, no. 5, page 054301, 2017. (Cited on page 52.)

[Kishore & Priya 2018] Ravi Anant Kishore and Shashank Priya. *A Review on Low-Grade Thermal Energy Harvesting: Materials, Methods and Devices.* Materials, vol. 11, no. 8, 2018. (Cited on page 1.)

[Kishore *et al.* 2021] S.E. Kishore, R. Sujithra and B. Dhatreyi. *A review on latest acoustic noise mitigation materials.* Materials Today: Proceedings, 2021. (Cited on page 3.)

[Kittel 1976] C Kittel. *Introduction to solid state physics. Fifth edition*, Jan 1976. (Cited on pages 2, 7, 8, 10, 11 and 12.)

[Klemens 1955] P G Klemens. *The Scattering of Low-Frequency Lattice Waves by Static Imperfections.* Proceedings of the Physical Society. Section A, vol. 68, no. 12, pages 1113–1128, dec 1955. (Cited on page 16.)

[Klemens 1958] P.G. Klemens. Thermal conductivity and lattice vibrational modes, volume 7 of *Solid State Physics.* Academic Press, 1958. (Cited on pages 16, 43, 94 and 96.)

[Kobayashi *et al.* 2009] W. Kobayashi, Y. Teraoka and I. Terasaki. *An oxide thermal rectifier.* Applied Physics Letters, vol. 95, no. 17, page 171905, 2009. (Cited on pages 137 and 138.)

[Kreuzer 1981] H. J. Kreuzer. Nonequilibrium thermodynamics and its statistical foundations. Oxford university press, 1981. (Cited on page 12.)

[Kubo 1957] Ryogo Kubo. *Statistical-mechanical theory of irreversible processes. I. General theory and simple applications to magnetic and conduction problems.* Journal of the Physical Society of Japan, vol. 12, no. 6, pages 570–586, 1957. (Cited on page 38.)

[Kurban *et al.* 2016] Mustafa Kurban, O Barış Malcıoğlu and Şakir Erkoç. *Structural and thermal properties of Cd-Zn-Te ternary nanoparticles: Molecular-dynamics simulations.* Chemical Physics, vol. 464, pages 40–45, 2016. (Cited on page 52.)

[Kurban 2018] Mustafa Kurban. *Size and composition-dependent structure of ternary Cd-Te-Se nanoparticles.* Turkish Journal of Physics, vol. 42, no. 4, pages 443–454, 2018. (Cited on page 52.)

[Lacroix *et al.* 2006] David Lacroix, Karl Joulain, Damian Terris and Denis Lemonnier. *Monte Carlo simulation of phonon confinement in silicon nanostructures: Application to the determination of the thermal conductivity of silicon nanowires.* Applied Physics Letters, vol. 89, no. 10, page 103104, 2006. (Cited on page 16.)

[Lamb 1881] Horace Lamb. *On the vibrations of an elastic sphere.* Proceedings of the London Mathematical Society, vol. 1, no. 1, pages 189–212, 1881. (Cited on page 51.)

[Lampin *et al.* 2012] E. Lampin, Q.-H. Nguyen, P. A. Francioso and F. Cleri. *Thermal boundary resistance at silicon-silica interfaces by molecular dynamics simulations.* Applied Physics Letters, vol. 100, no. 13, page 131906, 2012. (Cited on page 40.)

[Lampin *et al.* 2013] E. Lampin, P. L. Palla, P.-A. Francioso and F. Cleri. *Thermal conductivity from approach-to-equilibrium molecular dynamics.* Journal of Applied Physics, vol. 114, no. 3, page 033525, 2013. (Cited on page 40.)

[Landry & McGaughey 2009] E. S. Landry and A. J. H. McGaughey. *Effect of interfacial species mixing on phonon transport in semiconductor superlattices.* Phys. Rev. B, vol. 79, page 075316, Feb 2009. (Cited on page 165.)

[Larkin & McGaughey 2013] Jason M. Larkin and Alan J. H. McGaughey. *Predicting alloy vibrational mode properties using lattice dynamics calculations, molecular dynamics simulations, and the virtual crystal approximation.* Journal of Applied Physics, vol. 114, no. 2, page 023507, 2013. (Cited on pages 42 and 132.)

[Larkin & McGaughey 2014] Jason M. Larkin and Alan J. H. McGaughey. *Thermal conductivity accumulation in amorphous silica and amorphous silicon.* Phys. Rev. B, vol. 89, page 144303, Apr 2014. (Cited on pages 15, 64, 88 and 93.)

[Larsen *et al.* 2017] Ask Hjorth Larsen, Jens Jørgen Mortensen, Jakob Blomqvist, Ivano E Castelli, Rune Christensen, Marcin Dułak, Jesper Friis, Michael N Groves, Bjørk Hammer, Cory Hargus, Eric D Hermes, Paul C Jennings, Peter Bjerre Jensen, James Kermode, John R Kitchin, Esben Leonhard Kolsbjerg, Joseph Kubal, Kristen Kaasbjerg, Steen Lysgaard, Jón Bergmann

Maronsson, Tristan Maxson, Thomas Olsen, Lars Pastewka, Andrew Peterson, Carsten Rostgaard, Jakob Schiøtz, Ole Schütt, Mikkel Strange, Kristian S Thygesen, Tejs Vegge, Lasse Vilhelmsen, Michael Walter, Zhenhua Zeng and Karsten W Jacobsen. *The atomic simulation environment—a Python library for working with atoms.* Journal of Physics: Condensed Matter, vol. 29, no. 27, page 273002, jun 2017. (Cited on page 27.)

[Lee & Hwang 2012] Yongjin Lee and Gyeong S. Hwang. *Force-matching-based parameterization of the Stillinger-Weber potential for thermal conduction in silicon.* Phys. Rev. B, vol. 85, page 125204, Mar 2012. (Cited on page 139.)

[Lee *et al.* 2006] Byoung Min Lee, Hong Koo Baik, Baek Seok Seong, Shinji Munetoh and Teruaki Motooka. *Generation of glass SiO2 structures by various cooling rates: A molecular-dynamics study.* Computational Materials Science, vol. 37, no. 3, pages 203–208, 2006. (Cited on page 26.)

[Lee *et al.* 2015] Sangyeop Lee, David Broido, Keivan Esfarjani and Gang Chen. *Hydrodynamic phonon transport in suspended graphene.* Nature communications, vol. 6, no. 1, pages 1–10, 2015. (Cited on page 19.)

[Lehoucq *et al.* 1998] Richard B Lehoucq, Danny C Sorensen and Chao Yang. Arpack users' guide: solution of large-scale eigenvalue problems with implicitly restarted arnoldi methods, volume 6. Siam, 1998. (Cited on page 31.)

[Lei *et al.* 2009] Huaping Lei, Jun Chen, Xunya Jiang and Gérard Nouet. *Microstructure analysis in strained-InGaN/GaN multiple quantum wells.* Microelectronics Journal, vol. 40, no. 2, pages 342–345, 2009. Wide Band Gap Semiconductor Nanostructures for Optoelectronic Applications. (Cited on page 97.)

[Lester *et al.* 2015] Brian T Lester, Theocharis Baxevanis, Yves Chemisky and Dimitris C Lagoudas. *Review and perspectives: shape memory alloy composite systems.* Acta Mechanica, vol. 226, no. 12, pages 3907–3960, 2015. (Cited on page 1.)

[Li & Zhang 2013] Hai Peng Li and Rui Qin Zhang. *Size-dependent structural characteristics and phonon thermal transport in silicon nanoclusters.* AIP Advances, vol. 3, page 082114, 2013. (Cited on pages 52 and 170.)

[Li & Zhang 2018] Hai-Peng Li and Rui-Qin Zhang. *Surface effects on the thermal conductivity of silicon nanowires.* Chinese Physics B, vol. 27, no. 3, page 036801, mar 2018. (Cited on page 106.)

[Li *et al.* 2003a] Deyu Li, Yiying Wu, Philip Kim, Li Shi, Peidong Yang and Arun Majumdar. *Thermal conductivity of individual silicon nanowires.* Applied Physics Letters, vol. 83, no. 14, pages 2934–2936, 2003. (Cited on page 88.)

[Li *et al.* 2003b] Deyu Li, Yiying Wu, Philip Kim, Li Shi, Peidong Yang and Arun Majumdar. *Thermal conductivity of individual silicon nanowires.* Applied Physics Letters, vol. 83, no. 14, pages 2934–2936, 2003. (Cited on page 139.)

[Li *et al.* 2004] Baowen Li, Lei Wang and Giulio Casati. *Thermal Diode: Rectification of Heat Flux.* Phys. Rev. Lett., vol. 93, page 184301, Oct 2004. (Cited on page 138.)

[Li *et al.* 2010] Xiaobo Li, Kurt Maute, Martin L. Dunn and Ronggui Yang. *Strain effects on the thermal conductivity of nanostructures.* Phys. Rev. B, vol. 81, page 245318, Jun 2010. (Cited on page 178.)

[Li *et al.* 2012] Nianbei Li, Jie Ren, Lei Wang, Gang Zhang, Peter Hänggi and Baowen Li. *Colloquium: Phononics: Manipulating heat flow with electronic analogs and beyond.* Rev. Mod. Phys., vol. 84, pages 1045–1066, Jul 2012. (Cited on page 178.)

[Li *et al.* 2019] Zhen Li, Shiyun Xiong, Charles Sievers, Yue Hu, Zheyong Fan, Ning Wei, Hua Bao, Shunda Chen, Davide Donadio and Tapio Ala-Nissila. *Influence of thermostatting on nonequilibrium molecular dynamics simulations of heat conduction in solids.* The Journal of Chemical Physics, vol. 151, no. 23, page 234105, 2019. (Cited on pages 38 and 154.)

[Liang *et al.* 2007] Yunfeng Liang, Caetano R Miranda and Sandro Scandolo. *Mechanical strength and coordination defects in compressed silica glass : Molecular dynamics simulations.* Physical Review B, vol. 75, no. 2, pages 1–5, 2007. (Cited on page 169.)

[Lily 2021] Paul Lily. *TSMC 3nm Chip Production On Track For Late 2022 With Huge Power Efficiency Gains.* hot hard ware, 2021. (Cited on page 1.)

[Lim *et al.* 2012] Jongwoo Lim, Kedar Hippalgaonkar, Sean C. Andrews, Arun Majumdar and Peidong Yang. *Quantifying Surface Roughness Effects on Phonon Transport in Silicon Nanowires.* Nano Letters, vol. 12, no. 5, pages 2475–2482, 2012. PMID: 22524211. (Cited on page 106.)

[Lin *et al.* 2004] Ming Lin, Kian Ping Loh, Chris Boothroyd and Anyan Du. *Nanocantilevers made of bent silicon carbide nanowire-in-silicon oxide nanocones.* Applied Physics Letters, vol. 85, no. 22, pages 5388–5390, 2004. (Cited on page 140.)

[Liu *et al.* 2019a] Hexin Liu, Haidong Wang and Xing Zhang. *A Brief Review on the Recent Experimental Advances in Thermal Rectification at the Nanoscale.* Applied Sciences, vol. 9, no. 2, page 344, 2019. (Cited on page 138.)

[Liu *et al.* 2019b] Xiangjun Liu, Hangbo Zhou, Gang Zhang and Yong-Wei Zhang. *The effects of curvature on the thermal conduction of bent silicon nanowire.*

Journal of Applied Physics, vol. 125, no. 8, page 082505, 2019. (Cited on page 131.)

[López-Suárez *et al.* 2018] Miquel López-Suárez, Miquel Royo and Riccardo Rurali. *Interface-driven thermal rectification in nanoscale systems.* Phys. Rev. Materials, vol. 2, page 113001, Nov 2018. (Cited on page 138.)

[Luo *et al.* 2019] Haoming Luo, Anthony Gravouil, Valentina Giordano and Anne Tanguy. *Thermal Transport in a 2D Nanophononic Solid: Role of bi-Phasic Materials Properties on Acoustic Attenuation and Thermal Diffusivity.* Nanomaterials, vol. 9, no. 10, 2019. (Cited on pages 50, 57, 63, 67, 75, 77, 91 and 92.)

[Luo *et al.* 2021] H. Luo, Y. Ren, A. Gravouil, V. M. Giordano, Q. Zhou, H. Wang and A. Tanguy. *Role of a fractal shape of the inclusions on acoustic attenuation in a nanocomposite.* APL Materials, vol. 9, no. 8, page 081109, 2021. (Cited on page 164.)

[Lv & Henry 2016] Wei Lv and Asegun Henry. *Direct calculation of modal contributions to thermal conductivity via Green–Kubo modal analysis.* New Journal of Physics, vol. 18, no. 1, page 013028, jan 2016. (Cited on pages 88 and 90.)

[Ma *et al.* 2016] Dengke Ma, Hongru Ding, Han Meng, Lei Feng, Yue Wu, Junichiro Shiomi and Nuo Yang. *Nano-cross-junction effect on phonon transport in silicon nanowire cages.* Phys. Rev. B, vol. 94, page 165434, Oct 2016. (Cited on page 77.)

[Maire *et al.* 2017] Jeremie Maire, Roman Anufriev and Masahiro Nomura. *Ballistic thermal transport in silicon nanowires.* Scientific reports, vol. 7, no. 1, pages 1–8, 2017. (Cited on page 106.)

[Maldovan 2013] Martin Maldovan. *Sound and heat revolutions in phononics.* Nature, vol. 503, no. 7475, pages 209–217, 2013. (Cited on page 3.)

[Malhotra & Maldovan 2016] Abhinav Malhotra and Martin Maldovan. *Impact of phonon surface scattering on thermal energy distribution of Si and SiGe nanowires.* Scientific reports, vol. 6, no. 1, pages 1–13, 2016. (Cited on pages 106, 114 and 119.)

[Malhotra & Maldovan 2019] Abhinav Malhotra and Martin Maldovan. *Phononic pathways towards rational design of nanowire heat conduction.* Nanotechnology, vol. 30, no. 37, page 372002, jul 2019. (Cited on pages 119, 132, 164 and 165.)

[Mantisi *et al.* 2012] B Mantisi, Arnaud Tanguy, G Kermouche and E Barthel. *Atomistic response of a model silica glass under shear and pressure.* The European Physical Journal B, vol. 85, no. 9, pages 1–13, 2012. (Cited on page 26.)

[Maras *et al.* 2016] E. Maras, O. Trushin, A. Stukowski, T. Ala-Nissila and H. Jónsson. *Global transition path search for dislocation formation in Ge on Si(001).* Computer Physics Communications, vol. 205, pages 13–21, 2016. (Cited on page 78.)

[Martin *et al.* 2009] Pierre Martin, Zlatan Aksamija, Eric Pop and Umberto Ravaioli. *Impact of Phonon-Surface Roughness Scattering on Thermal Conductivity of Thin Si Nanowires.* Phys. Rev. Lett., vol. 102, page 125503, Mar 2009. (Cited on page 119.)

[Martin *et al.* 2018] Evelyne Martin, Pier Luca Palla, Fabrizio Cleri, Assil Bouzid, Guido Ori, Sébastien Le Roux, Mauro Boero and Carlo Massobrio. *On the occurrence of size effects in the calculation of thermal conductivity by first-principles molecular dynamics: The case of glassy GeTe4.* Journal of Non-Crystalline Solids, vol. 498, pages 190–193, 2018. (Cited on page 45.)

[Martyna *et al.* 1994] Glenn J. Martyna, Douglas J. Tobias and Michael L. Klein. *Constant pressure molecular dynamics algorithms.* The Journal of Chemical Physics, vol. 101, no. 5, pages 4177–4189, 1994. (Cited on page 25.)

[Marx & Hutter 2009] Dominik Marx and Jürg Hutter. Ab initio molecular dynamics: basic theory and advanced methods. Cambridge University Press, 2009. (Cited on page 45.)

[Massoud *et al.* 2020] A. M. Massoud, P.-O. Chapuis, B. Canut and J.-M. Bluet. *Thermal conductivity of irradiated porous silicon down to the oxide limit investigated by Raman thermometry and scanning thermal microscopy.* Journal of Applied Physics, vol. 128, no. 17, page 175109, 2020. (Cited on page 90.)

[Melis *et al.* 2019] Claudio Melis, Riccardo Rurali, Xavier Cartoixà and F. Xavier Alvarez. *Indications of Phonon Hydrodynamics in Telescopic Silicon Nanowires.* Phys. Rev. Applied, vol. 11, page 054059, May 2019. (Cited on pages 19, 119, 120, 131, 132 and 164.)

[Merabia & Termentzidis 2014] Samy Merabia and Konstantinos Termentzidis. *Thermal boundary conductance across rough interfaces probed by molecular dynamics.* Phys. Rev. B, vol. 89, page 054309, Feb 2014. (Cited on page 165.)

[Meyer & Comtesse 2011] R. Meyer and D. Comtesse. *Vibrational density of states of silicon nanoparticles.* Phys. Rev. B, vol. 83, page 014301, Jan 2011. (Cited on page 109.)

[Minnich & Chen 2007] Austin Minnich and Gang Chen. *Modified effective medium formulation for the thermal conductivity of nanocomposites.* Applied Physics Letters, vol. 91, no. 7, page 073105, 2007. (Cited on page 90.)

[Mion *et al.* 2006] C. Mion, J. F. Muth, E. A. Preble and D. Hanser. *Accurate dependence of gallium nitride thermal conductivity on dislocation density.* Applied Physics Letters, vol. 89, no. 9, page 092123, 2006. (Cited on page 96.)

[Miura *et al.* 2015] Asuka Miura, Shu Zhou, Tomohiro Nozaki and Junichiro Shiomi. *Crystalline–Amorphous Silicon Nanocomposites with Reduced Thermal Conductivity for Bulk Thermoelectrics.* ACS Applied Materials & Interfaces, vol. 7, no. 24, pages 13484–13489, 2015. PMID: 26046688. (Cited on page 77.)

[Mohammad Nejad *et al.* 2019] Shahin Mohammad Nejad, Masoud Bozorg Bigdeli, Rajat Srivastava and Matteo Fasano. *Heat Transfer at the Interface of Graphene Nanoribbons with Different Relative Orientations and Gaps.* Energies, vol. 12, no. 5, 2019. (Cited on page 63.)

[Munetoh *et al.* 2007] Shinji Munetoh, Teruaki Motooka, Koji Moriguchi and Akira Shintani. *Interatomic potential for Si-O systems using Tersoff parameterization.* Computational Materials Science, vol. 39, no. 2, pages 334–339, 2007. (Cited on pages 22, 27 and 52.)

[Murray & Saviot 2004] Daniel B. Murray and Lucien Saviot. *Phonons in an inhomogeneous continuum: Vibrations of an embedded nanoparticle.* Phys. Rev. B, vol. 69, page 094305, Mar 2004. (Cited on pages 50 and 51.)

[Müller-Plathe 1997] Florian Müller-Plathe. *A simple nonequilibrium molecular dynamics method for calculating the thermal conductivity.* The Journal of Chemical Physics, vol. 106, no. 14, pages 6082–6085, 1997. (Cited on page 38.)

[N. Raja *et al.* 2017] Shyamprasad N. Raja, Reto Rhyner, Kantawong Vuttivorakulchai, Mathieu Luisier and Dimos Poulikakos. *Length Scale of Diffusive Phonon Transport in Suspended Thin Silicon Nanowires.* Nano Letters, vol. 17, no. 1, pages 276–283, 2017. PMID: 28005386. (Cited on page 119.)

[Nabati Shoghl *et al.* 2016] Sina Nabati Shoghl, Jalil Jamali and Mostafa Keshavarz Moraveji. *Electrical conductivity, viscosity, and density of different nanofluids: An experimental study.* Experimental Thermal and Fluid Science, vol. 74, pages 339–346, 2016. (Cited on page 51.)

[Nakamura *et al.* 2015] Yoshiaki Nakamura, Masayuki Isogawa, Tomohiro Ueda, Shuto Yamasaka, Hideki Matsui, Jun Kikkawa, Satoaki Ikeuchi, Takafumi Oyake, Takuma Hori, Junichiro Shiomi and Akira Sakai. *Anomalous reduction of thermal conductivity in coherent nanocrystal architecture for silicon thermoelectric material.* Nano Energy, vol. 12, pages 845–851, 2015. (Cited on pages 77 and 90.)

[Nakamura 2018] Yoshiaki Nakamura. *Nanostructure design for drastic reduction of thermal conductivity while preserving high electrical conductivity.* Science

and Technology of Advanced Materials, vol. 19, no. 1, pages 31–43, 2018. PMID: 29371907. (Cited on page 77.)

[Nasr Esfahani & Jabbari 2020] Mohammad Nasr Esfahani and Masoud Jabbari. *Influence of the surface stress on the size-dependent elastic behavior of silicon nanowires.* Journal of Applied Physics, vol. 127, no. 19, page 195106, 2020. (Cited on page 178.)

[Neogi *et al.* 2015] Sanghamitra Neogi, J. Sebastian Reparaz, Luiz Felipe C. Pereira, Bartlomiej Graczykowski, Markus R. Wagner, Marianna Sledzinska, Andrey Shchepetov, Mika Prunnila, Jouni Ahopelto, Clivia M. Sotomayor-Torres and Davide Donadio. *Tuning Thermal Transport in Ultrathin Silicon Membranes by Surface Nanoscale Engineering.* ACS Nano, vol. 9, no. 4, pages 3820–3828, 2015. PMID: 25827287. (Cited on pages 106 and 119.)

[Nipko *et al.* 1998] J. C. Nipko, C. K. Loong, C. M. Balkas and R. F. Davis. *Phonon density of states of bulk gallium nitride.* Applied Physics Letters, vol. 73, no. 1, pages 34–36, 1998. (Cited on page 56.)

[Nomura *et al.* 2018] Masahiro Nomura, Junichiro Shiomi, Takuma Shiga and Roman Anufriev. *Thermal phonon engineering by tailored nanostructures.* Japanese Journal of Applied Physics, vol. 57, no. 8, page 080101, 2018. (Cited on page 62.)

[Nord *et al.* 2003] J. Nord, K. Albe, P. Erhart and K. Nordlund. *Modelling of compound semiconductors: Analytical bond-order potential for gallium, nitrogen and gallium nitride.* Journal of Physics Condensed Matter, vol. 15, no. 32, pages 5649–5662, 2003. (Cited on page 52.)

[Nosé 1986] Shūichi Nosé. *An extension of the canonical ensemble molecular dynamics method.* Molecular Physics, vol. 57, no. 1, pages 187–191, 1986. (Cited on page 25.)

[Okeke & Lowther 2009] Onyekwelu U. Okeke and J. E. Lowther. *Molecular dynamics of binary metal nitrides and ternary oxynitrides.* Physica B: Condensed Matter, vol. 404, no. 20, pages 3577–3581, 2009. (Cited on page 52.)

[Oltmanns *et al.* 2020] Johannes Oltmanns, David Sauerwein, Frank Dammel, Peter Stephan and Christoph Kuhn. *Potential for waste heat utilization of hot-water-cooled data centers: A case study.* Energy Science & Engineering, vol. 8, no. 5, pages 1793–1810, 2020. (Cited on page 1.)

[Pantha *et al.* 2008] B. N. Pantha, R. Dahal, J. Li, J. Y. Lin, H. X. Jiang and G. Pomrenke. *Thermoelectric properties of InxGa1-xN alloys.* Applied Physics Letters, vol. 92, no. 4, page 042112, 2008. (Cited on page 96.)

[Pei *et al.* 2012] Qing-Xiang Pei, Yong-Wei Zhang, Zhen-Dong Sha and Vivek B. Shenoy. *Carbon isotope doping induced interfacial thermal resistance and*

thermal rectification in graphene. Applied Physics Letters, vol. 100, no. 10, page 101901, 2012. (Cited on pages 138 and 161.)

[Peyrard 2006] M Peyrard. *The design of a thermal rectifier.* Europhysics Letters (EPL), vol. 76, no. 1, pages 49–55, oct 2006. (Cited on pages 138 and 160.)

[Plimpton 1995] Steve Plimpton. *Fast Parallel Algorithms for Short-Range Molecular Dynamics.* Journal of Computational Physics, vol. 117, no. 1, pages 1–19, 1995. (Cited on page 20.)

[Polak & Ribiere 1969] E. Polak and G. Ribiere. *Note sur la convergence de méthodes de directions conjuguées.* ESAIM: Mathematical Modelling and Numerical Analysis - Modélisation Mathématique et Analyse Numérique, vol. 3, no. R1, pages 35–43, 1969. (Cited on page 24.)

[Polian *et al.* 1996] A. Polian, M. Grimsditch and I. Grzegory. *Elastic constants of gallium nitride.* Journal of Applied Physics, vol. 79, no. 6, pages 3343–3344, 1996. (Cited on page 54.)

[Ponomareva *et al.* 2007] Inna Ponomareva, Deepak Srivastava and Madhu Menon. *Thermal Conductivity in Thin Silicon Nanowires: Phonon Confinement Effect.* Nano Letters, vol. 7, no. 5, pages 1155–1159, 2007. PMID: 17394370. (Cited on page 106.)

[Pottier 2007] Noëlle Pottier. Physique statistique hors d'équilibre. EDP Sciences, 2007. (Cited on page 12.)

[Qian *et al.* 2004] Z G Qian, W Z Shen, H Ogawa and Q X Guo. *Experimental studies of lattice dynamical properties in indium nitride.* Journal of Physics: Condensed Matter, vol. 16, no. 12, pages R381–R414, mar 2004. (Cited on page 99.)

[Qiu *et al.* 2020] Lin Qiu, Ning Zhu, Yanhui Feng, Efstathios E. Michaelides, Gaweł Żyła, Dengwei Jing, Xinxin Zhang, Pamela M. Norris, Christos N. Markides and Omid Mahian. *A review of recent advances in thermophysical properties at the nanoscale: From solid state to colloids.* Physics Reports, vol. 843, pages 1–81, 2020. A review of recent advances in thermophysical properties at the nanoscale: From solid state to colloids. (Cited on page 51.)

[Ravichandran *et al.* 2014] Jayakanth Ravichandran, Ajay K Yadav, Ramez Cheaito, Pim B Rossen, Arsen Soukiassian, SJ Suresha, John C Duda, Brian M Foley, Che-Hui Lee, Ye Zhu*et al.* *Crossover from incoherent to coherent phonon scattering in epitaxial oxide superlattices.* Nature materials, vol. 13, no. 2, pages 168–172, 2014. (Cited on page 3.)

[Recoules & Crocombette 2005] Vanina Recoules and Jean-Paul Crocombette. *Ab initio determination of electrical and thermal conductivity of liquid aluminum.* Phys. Rev. B, vol. 72, page 104202, Sep 2005. (Cited on page 45.)

[Riordan 2004] Michael Riordan. *The lost history of the transistor.* IEEE Spectrum, vol. 41, no. 5, pages 44–49, 2004. (Cited on page 1.)

[Roberts & Walker 2011a] N.A. Roberts and D.G. Walker. *A review of thermal rectification observations and models in solid materials.* International Journal of Thermal Sciences, vol. 50, no. 5, pages 648 – 662, 2011. (Cited on pages 137 and 138.)

[Roberts & Walker 2011b] Nick A Roberts and DG Walker. *Phonon transport in asymmetric sawtooth nanowires.* In ASME/JSME Thermal Engineering Joint Conference, volume 38921, page T30053, 2011. (Cited on pages 139 and 161.)

[Rowe 2018] David Michael Rowe. Thermoelectrics handbook: macro to nano. CRC press, 2018. (Cited on page 2.)

[Rurali 2010] Riccardo Rurali. *Colloquium: Structural, electronic, and transport properties of silicon nanowires.* Rev. Mod. Phys., vol. 82, pages 427–449, Feb 2010. (Cited on pages 3 and 152.)

[Rycroft 2007] Christopher Harley Rycroft. *Multiscale modeling in granular flow.* PhD thesis, Massachusetts Institute of Technology, 2007. (Cited on page 32.)

[Sääskilahti *et al.* 2015] K. Sääskilahti, J. Oksanen, S. Volz and J. Tulkki. *Frequency-dependent phonon mean free path in carbon nanotubes from nonequilibrium molecular dynamics.* Phys. Rev. B, vol. 91, page 115426, Mar 2015. (Cited on pages 134 and 166.)

[Sauceda *et al.* 2013] Huziel E. Sauceda, Fernando Salazar, Luis A. Pérez and Ignacio L. Garzón. *Size and shape dependence of the vibrational spectrum and low-temperature specific heat of au nanoparticles.* Journal of Physical Chemistry C, vol. 117, no. 47, pages 25160–25168, 2013. (Cited on page 51.)

[Saviot & Murray 2009] Lucien Saviot and Daniel B. Murray. *Acoustic vibrations of anisotropic nanoparticles.* Phys. Rev. B, vol. 79, no. 21, pages 1–11, 2009. (Cited on page 51.)

[Savitzky & Golay 1964] Abraham Savitzky and Marcel JE Golay. *Smoothing and differentiation of data by simplified least squares procedures.* Analytical chemistry, vol. 36, no. 8, pages 1627–1639, 1964. (Cited on page 31.)

[Schelling *et al.* 2002a] Patrick K. Schelling, Simon R. Phillpot and Pawel Keblinski. *Comparison of atomic-level simulation methods for computing thermal conductivity.* Phys. Rev. B, vol. 65, page 144306, Apr 2002. (Cited on pages 37, 39 and 91.)

[Schelling *et al.* 2002b] Patrick K. Schelling, Simon R. Phillpot and Pawel Keblinski. *Comparison of atomic-level simulation methods for computing thermal conductivity.* Phys. Rev. B, vol. 65, page 144306, Apr 2002. (Cited on pages 38 and 133.)

[Schelling *et al.* 2005] Patrick K. Schelling, Li Shi and Kenneth E. Goodson. *Managing heat for electronics.* Materials Today, vol. 8, no. 6, pages 30–35, 2005. (Cited on page 1.)

[Sen & Youngman 2003] S. Sen and R.E. Youngman. *NMR study of Q-speciation and connectivity in K2O–SiO2 glasses with high silica content.* Journal of Non-Crystalline Solids, vol. 331, no. 1, pages 100–107, 2003. (Cited on pages 30 and 169.)

[Sendra *et al.* 2021] Lluc Sendra, Albert Beardo, Pol Torres, Javier Bafaluy, F. Xavier Alvarez and Juan Camacho. *Derivation of a hydrodynamic heat equation from the phonon Boltzmann equation for general semiconductors.* Phys. Rev. B, vol. 103, page L140301, Apr 2021. (Cited on pages 18, 19, 126, 127 and 132.)

[Seyf & Henry 2016] Hamid Reza Seyf and Asegun Henry. *A method for distinguishing between propagons, diffusions, and locons.* Journal of Applied Physics, vol. 120, no. 2, page 025101, 2016. (Cited on page 16.)

[Shao *et al.* 2018] Cheng Shao, Qingyuan Rong, Nianbei Li and Hua Bao. *Understanding the mechanism of diffuse phonon scattering at disordered surfaces by atomistic wave-packet investigation.* Phys. Rev. B, vol. 98, page 155418, Oct 2018. (Cited on pages 119, 129, 131 and 133.)

[Sklan 2015] Sophia R. Sklan. *Splash, pop, sizzle: Information processing with phononic computing.* AIP Advances, vol. 5, no. 5, page 053302, 2015. (Cited on pages 2 and 138.)

[Slack & Galginaitis 1964] Glen A. Slack and S. Galginaitis. *Thermal Conductivity and Phonon Scattering by Magnetic Impurities in CdTe.* Phys. Rev., vol. 133, pages A253–A268, Jan 1964. (Cited on page 16.)

[Sledzinska *et al.* 2017] Marianna Sledzinska, Romain Quey, Bohayra Mortazavi, Bartlomiej Graczykowski, Marcel Placidi, David Saleta Reig, Daniel Navarro-Urrios, Francesc Alzina, Luciano Colombo, Stephan Roche and Clivia M. Sotomayor Torres. *Record Low Thermal Conductivity of Polycrystalline MoS2 Films: Tuning the Thermal Conductivity by Grain Orientation.* ACS Applied Materials & Interfaces, vol. 9, no. 43, pages 37905–37911, 2017. PMID: 28956443. (Cited on page 63.)

[Sledzinska *et al.* 2020] Marianna Sledzinska, Bartlomiej Graczykowski, Jeremie Maire, Emigdio Chavez-Angel, Clivia M. Sotomayor-Torres and Francesc Alzina. *2D Phononic Crystals: Progress and Prospects in Hypersound and Thermal Transport Engineering.* Advanced Functional Materials, vol. 30, no. 8, page 1904434, 2020. (Cited on page 3.)

[Stillinger & Weber 1985] Frank H. Stillinger and Thomas A. Weber. *Computer simulation of local order in condensed phases of silicon.* Phys. Rev. B, vol. 31, pages 5262–5271, Apr 1985. (Cited on page 21.)

[Stukowski 2009] Alexander Stukowski. *Visualization and analysis of atomistic simulation data with OVITO–the Open Visualization Tool.* Modelling and Simulation in Materials Science and Engineering, vol. 18, no. 1, page 015012, dec 2009. (Cited on pages 27 and 178.)

[Surblys *et al.* 2019] Donatas Surblys, Hiroki Matsubara, Gota Kikugawa and Taku Ohara. *Application of atomic stress to compute heat flux via molecular dynamics for systems with many-body interactions.* Phys. Rev. E, vol. 99, page 051301, May 2019. (Cited on pages 39 and 40.)

[Surender *et al.* 2018] S. Surender, S. Pradeep, K. Prabakaran, S.M. Sumithra, Shubra Singh and K. Baskar. *The role of indium composition on thermoelectric properties of InGaN/GaN heterostructures grown by MOCVD.* Journal of Alloys and Compounds, vol. 734, pages 48–54, 2018. (Cited on page 96.)

[Swope *et al.* 1982] William C. Swope, Hans C. Andersen, Peter H. Berens and Kent R. Wilson. *A computer simulation method for the calculation of equilibrium constants for the formation of physical clusters of molecules: Application to small water clusters.* The Journal of Chemical Physics, vol. 76, no. 1, pages 637–649, 1982. (Cited on page 20.)

[Tang *et al.* 2020] Dao Sheng Tang, Guang Zhao Qin, Ming Hu and Bing Yang Cao. *Thermal transport properties of GaN with biaxial strain and electron-phonon coupling.* Journal of Applied Physics, vol. 127, no. 3, page 035102, 2020. (Cited on pages 56 and 62.)

[Tanguy *et al.* 2002] A Tanguy, J P Wittmer, F Leonforte and J Barrat. *Continuum limit of amorphous elastic bodies : A finite-size study of low-frequency harmonic vibrations.* Phys. Rev. B, vol. 66, no. 17, page 174205, 2002. (Cited on pages 14, 16 and 55.)

[Tanguy *et al.* 2010] A. Tanguy, B. Mantisi and M. Tsamados. *Vibrational modes as a predictor for plasticity in a model glass.* EPL (Europhysics Letters), vol. 90, no. 1, page 16004, apr 2010. (Cited on page 14.)

[Tanguy 2015] Anne Tanguy. *Vibration modes and characteristic length scales in amorphous materials.* JOM, vol. 67, no. 8, pages 1832–1839, 2015. (Cited on page 14.)

[Termentzidis *et al.* 2018a] Konstantinos Termentzidis, V. M. Giordano, Maria Katsikini, Eleni Paloura, Gilles Pernot, Maxime Verdier, David Lacroix, Ioannis Karakostas and Joseph Kioseogloud. *Enhanced thermal conductivity in percolating nanocomposites: a molecular dynamics investigation.* Nanoscale,

vol. 10, no. 46, pages 21732–21741, 2018. (Cited on pages 27, 40, 50, 52, 63, 64, 66, 77, 90, 91 and 163.)

[Termentzidis *et al.* 2018b] Konstantinos Termentzidis, Mykola Isaiev, Anastasiia Salnikova, Imad Belabbas, David Lacroix and Joseph Kioseoglou. *Impact of screw and edge dislocations on the thermal conductivity of individual nanowires and bulk GaN: a molecular dynamics study.* Phys. Chem. Chem. Phys., vol. 20, pages 5159–5172, 2018. (Cited on page 96.)

[Termentzidis 2017] Konstantinos Termentzidis. Nanostructured semiconductors: amorphization and thermal properties. Jenny Stanford Publishing, 2017. (Cited on pages 11 and 17.)

[Terraneo *et al.* 2002] M. Terraneo, M. Peyrard and G. Casati. *Controlling the Energy Flow in Nonlinear Lattices: A Model for a Thermal Rectifier.* Phys. Rev. Lett., vol. 88, page 094302, Feb 2002. (Cited on page 138.)

[Tersoff 1988] J. Tersoff. *Empirical interatomic potential for silicon with improved elastic properties.* Phys. Rev. B, vol. 38, pages 9902–9905, Nov 1988. (Cited on pages 22 and 169.)

[Tian *et al.* 2012] Zhiting Tian, Keivan Esfarjani and Gang Chen. *Enhancing phonon transmission across a Si/Ge interface by atomic roughness: First-principles study with the Green's function method.* Phys. Rev. B, vol. 86, page 235304, Dec 2012. (Cited on page 44.)

[Tlili *et al.* 2019] A. Tlili, V. M. Giordano, Y. M. Beltukov, P. Desmarchelier, S. Merabia and A. Tanguy. *Enhancement and anticipation of the Ioffe–Regel crossover in amorphous/nanocrystalline composites.* Nanoscale, vol. 11, pages 21502–21512, 2019. (Cited on pages 16, 26, 27, 33, 41, 50, 63, 67, 75, 77, 88, 89, 90, 91, 131 and 164.)

[Tong *et al.* 2013] T. Tong, D. Fu, A. X. Levander, W. J. Schaff, B. N. Pantha, N. Lu, B. Liu, I. Ferguson, R. Zhang, J. Y. Lin, H. X. Jiang, J. Wu and David G. Cahill. *Suppression of thermal conductivity in InxGa1-xN alloys by nanometer-scale disorder.* Applied Physics Letters, vol. 102, no. 12, page 121906, 2013. (Cited on page 96.)

[Tong *et al.* 2019] Zi-Xiang Tong, Ya-Ling He and Wen-Quan Tao. *A review of current progress in multiscale simulations for fluid flow and heat transfer problems: The frameworks, coupling techniques and future perspectives.* International Journal of Heat and Mass Transfer, vol. 137, pages 1263–1289, 2019. (Cited on page 3.)

[Tretiakov & Hyżorek 2021] Konstantin V. Tretiakov and Krzysztof Hyżorek. *Role of the phonon confinement effect and boundary scattering in reducing the thermal conductivity of argon nanowire.* The Journal of Chemical Physics, vol. 154, no. 5, page 054702, 2021. (Cited on page 94.)

[Tritt 2005] Terry M Tritt. Thermal conductivity: theory, properties, and applications. Springer Science & Business Media, 2005. (Cited on page 11.)

[Upadhyaya & Aksamija 2016] M. Upadhyaya and Z. Aksamija. *Nondiffusive lattice thermal transport in Si-Ge alloy nanowires.* Phys. Rev. B, vol. 94, page 174303, Nov 2016. (Cited on page 101.)

[van Beest *et al.* 1990] B. W. H. van Beest, G. J. Kramer and R. A. van Santen. *Force fields for silicas and aluminophosphates based on ab initio calculations.* Phys. Rev. Lett., vol. 64, pages 1955–1958, Apr 1990. (Cited on pages 22 and 169.)

[Van Hove 1953] Léon Van Hove. *The occurrence of singularities in the elastic frequency distribution of a crystal.* Physical Review, vol. 89, no. 6, page 1189, 1953. (Cited on page 53.)

[Vasudevan & Fullerton-Shirey 2019] Sandhya Vasudevan and Susan K. Fullerton-Shirey. *Effect of Nanoparticle Shape on the Electrical and Thermal Properties of Solid Polymer Electrolytes.* The Journal of Physical Chemistry C, vol. 123, no. 17, pages 10720–10726, 2019. (Cited on page 77.)

[Verdier *et al.* 2018a] Maxime Verdier, Yang Han, David Lacroix, Pierre-Olivier Chapuis and Konstantinos Termentzidis. *Radial dependence of thermal transport in silicon nanowires.* Journal of Physics: Materials, vol. 2, no. 1, page 015002, nov 2018. (Cited on pages 119, 120, 125, 131 and 164.)

[Verdier *et al.* 2018b] Maxime Verdier, David Lacroix, Stanislav Didenko, Jean-Fran çois Robillard, Evelyne Lampin, Thierno-Moussa Bah and Konstantinos Termentzidis. *Influence of amorphous layers on the thermal conductivity of phononic crystals.* Phys. Rev. B, vol. 97, page 115435, Mar 2018. (Cited on page 106.)

[Verdier *et al.* 2018c] Maxime Verdier, David Lacroix and Konstantinos Termentzidis. *Thermal transport in two- and three-dimensional nanowire networks.* Phys. Rev. B, vol. 98, page 155434, Oct 2018. (Cited on pages 77, 90 and 94.)

[Verdier *et al.* 2019] Maxime Verdier, David Lacroix and Konstantinos Termentzidis. *Roughness and amorphization impact on thermal conductivity of nanofilms and nanowires: Making atomistic modeling more realistic.* Journal of Applied Physics, vol. 126, no. 16, page 164305, 2019. (Cited on pages 119, 125, 133 and 157.)

[Vermeersch *et al.* 2015] Bjorn Vermeersch, Jesús Carrete, Natalio Mingo and Ali Shakouri. *Superdiffusive heat conduction in semiconductor alloys. I. Theoretical foundations.* Phys. Rev. B, vol. 91, page 085202, Feb 2015. (Cited on page 45.)

[Vincent-Dospital *et al.* 2020] Tom Vincent-Dospital, Renaud Toussaint, Stéphane Santucci, Loïc Vanel, Daniel Bonamy, Lamine Hattali, Alain Cochard, Eirik G. Flekkøy and Knut Jørgen Måløy. *How heat controls fracture: the thermodynamics of creeping and avalanching cracks.* Soft Matter, vol. 16, pages 9590–9602, 2020. (Cited on page 1.)

[Vink *et al.* 2001] R.L.C. Vink, G.T. Barkema, W.F. van der Weg and Normand Mousseau. *Fitting the Stillinger–Weber potential to amorphous silicon.* Journal of Non-Crystalline Solids, vol. 282, no. 2, pages 248–255, 2001. (Cited on pages 22, 30, 78 and 108.)

[Virtanen *et al.* 2020] Pauli Virtanen, Ralf Gommers, Travis E. Oliphant, Matt Haberland, Tyler Reddy, David Cournapeau, Evgeni Burovski, Pearu Peterson, Warren Weckesser, Jonathan Bright, Stéfan J. van der Walt, Matthew Brett, Joshua Wilson, K. Jarrod Millman, Nikolay Mayorov, Andrew R. J. Nelson, Eric Jones, Robert Kern, Eric Larson, C J Carey, İlhan Polat, Yu Feng, Eric W. Moore, Jake VanderPlas, Denis Laxalde, Josef Perktold, Robert Cimrman, Ian Henriksen, E. A. Quintero, Charles R. Harris, Anne M. Archibald, Antônio H. Ribeiro, Fabian Pedregosa, Paul van Mulbregt and SciPy 1.0 Contributors. *SciPy 1.0: Fundamental Algorithms for Scientific Computing in Python.* Nature Methods, vol. 17, pages 261–272, 2020. (Cited on page 34.)

[Vollmayr *et al.* 1996] Katharina Vollmayr, Walter Kob and Kurt Binder. *Cooling-rate effects in amorphous silica: A computer-simulation study.* Phys. Rev. B, vol. 54, pages 15808–15827, Dec 1996. (Cited on page 26.)

[Volz & Chen 1999] Sebastian G. Volz and Gang Chen. *Molecular dynamics simulation of thermal conductivity of silicon nanowires.* Applied Physics Letters, vol. 75, no. 14, pages 2056–2058, 1999. (Cited on pages 94, 95 and 119.)

[Volz 2007] Sebastian Volz. Microscale and nanoscale heat transfer, volume 107. Springer-Verlag Berlin Heidelberg, 2007. (Cited on page 7.)

[Wagner & Ellis 1964] R. S. Wagner and W. C. Ellis. *VAPOR-LIQUID-SOLID MECHANISM OF SINGLE CRYSTAL GROWTH.* Applied Physics Letters, vol. 4, no. 5, pages 89–90, 1964. (Cited on page 105.)

[Wang & Li 2007] Lei Wang and Baowen Li. *Thermal Logic Gates: Computation with Phonons.* Phys. Rev. Lett., vol. 99, page 177208, Oct 2007. (Cited on pages 2 and 138.)

[Wang & Pan 2008] Moran Wang and Ning Pan. *Predictions of effective physical properties of complex multiphase materials.* Materials Science and Engineering: R: Reports, vol. 63, no. 1, pages 1–30, 2008. (Cited on pages 90 and 165.)

[Wang *et al.* 2012] Yan Wang, Siyu Chen and Xiulin Ruan. *Tunable thermal rectification in graphene nanoribbons through defect engineering: A molecular*

dynamics study. Applied Physics Letters, vol. 100, no. 16, page 163101, 2012. (Cited on page 160.)

[Wang *et al.* 2013] Yongchun Wang, Baohua Li and Guofeng Xie. *Significant reduction of thermal conductivity in silicon nanowires by shell doping.* RSC Adv., vol. 3, pages 26074–26079, 2013. (Cited on page 106.)

[Wang *et al.* 2014] Yan Wang, Ajit Vallabhaneni, Jiuning Hu, Bo Qiu, Yong P Chen and Xiulin Ruan. *Phonon lateral confinement enables thermal rectification in asymmetric single-material nanostructures.* Nano letters, vol. 14, no. 2, pages 592–596, 2014. (Cited on pages 139, 156, 158 and 161.)

[Wang *et al.* 2017] Haidong Wang, Shiqian Hu, Koji Takahashi, Xing Zhang, Hiroshi Takamatsu and Jie Chen. *Experimental study of thermal rectification in suspended monolayer graphene.* Nature communications, vol. 8, no. 1, pages 1–8, 2017. (Cited on pages 139, 160 and 161.)

[Wehmeyer *et al.* 2017] Geoff Wehmeyer, Tomohide Yabuki, Christian Monachon, Junqiao Wu and Chris Dames. *Thermal diodes, regulators, and switches: Physical mechanisms and potential applications.* Applied Physics Reviews, vol. 4, no. 4, page 041304, 2017. (Cited on pages 2, 138 and 165.)

[Weiße *et al.* 2006] Alexander Weiße, Gerhard Wellein, Andreas Alvermann and Holger Fehske. *The kernel polynomial method.* Reviews of Modern Physics, vol. 78, no. 1, pages 275–306, 2006. (Cited on page 32.)

[Wittmer *et al.* 2002] J. P. Wittmer, A. Tanguy, F. Leonforte and J. L. Barrat. *Vibrations of amorphous nanometric structures: When does the classical continuum theory apply?* Europhysics Letters, vol. 57, no. 3, pages 423–429, 2002. (Cited on page 51.)

[Wong *et al.* 2019] M.Y. Wong, B. Traipattanakul, C.Y. Tso, Christopher Y.H. Chao and Huihe Qiu. *Experimental and theoretical study of a water-vapor chamber thermal diode.* International Journal of Heat and Mass Transfer, vol. 138, pages 173–183, 2019. (Cited on page 137.)

[Wong *et al.* 2021] M.Y. Wong, C.Y. Tso, T.C. Ho and H.H. Lee. *A review of state of the art thermal diodes and their potential applications.* International Journal of Heat and Mass Transfer, vol. 164, page 120607, 2021. (Cited on pages 138 and 159.)

[Wu & Li 2007] Gang Wu and Baowen Li. *Thermal rectification in carbon nanotube intramolecular junctions: Molecular dynamics calculations.* Phys. Rev. B, vol. 76, page 085424, Aug 2007. (Cited on page 139.)

[Wu & Li 2008] Gang Wu and Baowen Li. *Thermal rectifiers from deformed carbon nanohorns.* Journal of Physics: Condensed Matter, vol. 20, no. 17, page 175211, apr 2008. (Cited on page 161.)

[Xie *et al.* 2014] Guofeng Xie, Yuan Guo, Xiaolin Wei, Kaiwang Zhang, Lizhong Sun, Jianxin Zhong, Gang Zhang and Yong-Wei Zhang. *Phonon mean free path spectrum and thermal conductivity for $Si_{1-x}Ge_x$ nanowires.* Applied Physics Letters, vol. 104, no. 23, page 233901, 2014. (Cited on page 117.)

[Xiong *et al.* 2016] Shiyun Xiong, Kimmo Sääskilahti, Yuriy A. Kosevich, Haoxue Han, Davide Donadio and Sebastian Volz. *Blocking Phonon Transport by Structural Resonances in Alloy-Based Nanophononic Metamaterials Leads to Ultralow Thermal Conductivity.* Phys. Rev. Lett., vol. 117, page 025503, Jul 2016. (Cited on page 117.)

[Xu *et al.* 2018] Yuhao Xu, Qing Zhou, Yin Du, Yue Ren, Haimin Zhai, Qiang Li, Jialin Chen and Haifeng Wang. *Modulating mechanical properties of Ti-based bulk metallic glass composites by tailoring dendrite composition with Sn addition.* Journal of Alloys and Compounds, vol. 745, pages 16–25, 2018. (Cited on page 164.)

[Yang & Dames 2013] Fan Yang and Chris Dames. *Mean free path spectra as a tool to understand thermal conductivity in bulk and nanostructures.* Phys. Rev. B, vol. 87, page 035437, Jan 2013. (Cited on pages 16, 43 and 94.)

[Yang & Minnich 2017] Lina Yang and Austin J Minnich. *Thermal transport in nanocrystalline Si and SiGe by ab initio based Monte Carlo simulation.* Scientific reports, vol. 7, no. 1, pages 1–11, 2017. (Cited on page 77.)

[Yang *et al.* 2008] Nuo Yang, Gang Zhang and Baowen Li. *Carbon nanocone: A promising thermal rectifier.* Applied Physics Letters, vol. 93, no. 24, page 243111, 2008. (Cited on pages 159, 160 and 161.)

[Yang *et al.* 2009] Nuo Yang, Gang Zhang and Baowen Li. *Thermal rectification in asymmetric graphene ribbons.* Applied Physics Letters, vol. 95, no. 3, page 033107, 2009. (Cited on pages 139 and 161.)

[Yang *et al.* 2017a] Lin Yang, Qian Zhang, Zhiguang Cui, Matthew Gerboth, Yang Zhao, Terry T. Xu, D. Greg Walker and Deyu Li. *Ballistic Phonon Penetration Depth in Amorphous Silicon Dioxide.* Nano Letters, vol. 17, no. 12, pages 7218–7225, 2017. PMID: 29087722. (Cited on page 92.)

[Yang *et al.* 2017b] Xueming Yang, Dapeng Yu, Bingyang Cao and Albert C To. *Ultrahigh Thermal Rectification in Pillared Graphene Structure with Carbon Nanotube–Graphene Intramolecular Junctions.* ACS applied materials & interfaces, vol. 9, no. 1, pages 29–35, 2017. (Cited on page 161.)

[Yang *et al.* 2018] Lina Yang, Benoit Latour and Austin J. Minnich. *Phonon transmission at crystalline-amorphous interfaces studied using mode-resolved atomistic Green's functions.* Phys. Rev. B, vol. 97, page 205306, May 2018. (Cited on pages 44, 92 and 129.)

[Zaoui *et al.* 2016] Hayat Zaoui, Pier Luca Palla, Fabrizio Cleri and Evelyne Lampin. *Length dependence of thermal conductivity by approach-to-equilibrium molecular dynamics.* Phys. Rev. B, vol. 94, page 054304, Aug 2016. (Cited on pages 40 and 133.)

[Zenji *et al.* 2020] A. Zenji, J. M. Rampnoux, S. Grauby and S. Dilhaire. *Ultimate-resolution thermal spectroscopy in time domain thermoreflectance (TDTR).* Journal of Applied Physics, vol. 128, no. 6, page 065106, 2020. (Cited on page 1.)

[Zhang & Minnich 2015] Hang Zhang and Austin J Minnich. *The best nanoparticle size distribution for minimum thermal conductivity.* Scientific reports, vol. 5, no. 1, pages 1–5, 2015. (Cited on page 50.)

[Zhang *et al.* 2007] W. Zhang, T. S. Fisher and N. Mingo. *The Atomistic Green's Function Method: An Efficient Simulation Approach for Nanoscale Phonon Transport.* Numerical Heat Transfer, Part B: Fundamentals, vol. 51, no. 4, pages 333–349, 2007. (Cited on page 44.)

[Zhang *et al.* 2013] Xiaoliang Zhang, Ming Hu and Dawei Tang. *Thermal rectification at silicon/horizontally aligned carbon nanotube interfaces.* Journal of Applied Physics, vol. 113, no. 19, page 194307, 2013. (Cited on page 138.)

[Zhang *et al.* 2014] Xiaoliang Zhang, Han Xie, Ming Hu, Hua Bao, Shengying Yue, Guangzhao Qin and Gang Su. *Thermal conductivity of silicene calculated using an optimized Stillinger-Weber potential.* Phys. Rev. B, vol. 89, page 054310, Feb 2014. (Cited on page 45.)

[Zhang *et al.* 2016] Zhongwei Zhang, Yuanping Chen, Yuee Xie and Shengbai Zhang. *Transition of thermal rectification in silicon nanocones.* Applied Thermal Engineering, vol. 102, pages 1075–1080, 2016. (Cited on pages 139 and 160.)

[Zheng *et al.* 2021] Qiye Zheng, Menglong Hao, Ruijiao Miao, Joseph Schaadt and Chris Dames. *Advances in thermal conductivity for energy applications: a review.* Progress in Energy, vol. 3, no. 1, page 012002, jan 2021. (Cited on page 1.)

[Zhou & Hu 2016] Yanguang Zhou and Ming Hu. *Record Low Thermal Conductivity of Polycrystalline Si Nanowire: Breaking the Casimir Limit by Severe Suppression of Propagons.* Nano Letters, vol. 16, no. 10, pages 6178–6187, 2016. PMID: 27603153. (Cited on page 129.)

[Zhou *et al.* 2015] Yanguang Zhou, Xiaoliang Zhang and Ming Hu. *Quantitatively analyzing phonon spectral contribution of thermal conductivity based on nonequilibrium molecular dynamics simulations. I. From space Fourier transform.* Phys. Rev. B, vol. 92, page 195204, Nov 2015. (Cited on page 117.)

[Zhou *et al.* 2017] Yanguang Zhou, Xiaoliang Zhang and Ming Hu. *Nonmonotonic Diameter Dependence of Thermal Conductivity of Extremely Thin Si Nanowires: Competition between Hydrodynamic Phonon Flow and Boundary Scattering.* Nano Letters, vol. 17, no. 2, pages 1269–1276, 2017. PMID: 28128960. (Cited on pages 119, 133 and 180.)

[Zhou 2021] Yanguang Zhou. *Assessing the quantum effect in classical thermal conductivity of amorphous silicon.* Journal of Applied Physics, vol. 129, no. 23, page 235104, 2021. (Cited on page 40.)

[Zhu *et al.* 2007] T J Zhu, F Yan, X B Zhao, S N Zhang, Y Chen and S H Yang. *Preparation and thermoelectric properties of bulkin situnanocomposites with amorphous/nanocrystal hybrid structure.* Journal of Physics D: Applied Physics, vol. 40, no. 19, pages 6094–6097, sep 2007. (Cited on page 50.)

[Ziman 1960] John M Ziman. Electrons and phonons: the theory of transport phenomena in solids. Oxford university press, 1960. (Cited on pages 11, 12 and 13.)

[Zou & Balandin 2001] Jie Zou and Alexander Balandin. *Phonon heat conduction in a semiconductor nanowire.* Journal of Applied Physics, vol. 89, no. 5, pages 2932–2938, 2001. (Cited on page 94.)

[Zou *et al.* 2002] J. Zou, D. Kotchetkov, A. A. Balandin, D. I. Florescu and Fred H. Pollak. *Thermal conductivity of GaN films: Effects of impurities and dislocations.* Journal of Applied Physics, vol. 92, no. 5, pages 2534–2539, 2002. (Cited on page 96.)

[Zushi *et al.* 2014] Tomofumi Zushi, Kosuke Shimura, Masanori Tomita, Kenji Ohmori, Keisaku Yamada and Takanobu Watanabe. *Phonon Dispersion in ⟨100⟩ Si Nanowire Covered with SiO2Film Calculated by Molecular Dynamics Simulation.* ECS Journal of Solid State Science and Technology, vol. 3, no. 5, pages P149–P154, 2014. (Cited on pages 111, 115 and 164.)

[Zushi *et al.* 2015] Tomofumi Zushi, Kenji Ohmori, Keisaku Yamada and Takanobu Watanabe. *Effect of a* SiO_2 *layer on the thermal transport properties of* ⟨100⟩ Si *nanowires: A molecular dynamics study.* Phys. Rev. B, vol. 91, page 115308, Mar 2015. (Cited on page 106.)

FOLIO ADMINISTRATIF

THÉSE DE L'UNIVERSITÉ DE LYON OPÉRÉE AU SEIN DE L'INSA LYON

NOM : Desmarchelier

DATE de SOUTENANCE : 06/12/2021

Prénoms : Paul, Matthieu, Alexandre

TITRE : Atomistic Simulations of Nano-Architectured Semiconductors: Thermal and Vibrational Properties / Simulations Atomistiques de Semi-conducteurs Nanoarchitecturés : Propriétés Thermique et Vibratoire

NATURE : Doctorat

Numéro d'ordre : 2021LYSEI081

Ecole doctorale : MECANIQUE, ENERGETIQUE, GENIE CIVIL, ACOUSTIQUE

Spécialité : Thermique Énergétique

RESUME :
À l'échelle nanométrique, les propriétés thermiques et vibratoires sont intimement liées et dépendent de la forme et de la composition des matériaux. Grâce à la nanostructuration, les nanocomposites permettent un meilleur contrôle du transport de chaleur. Elle permet notamment d'améliorer les performances des générateurs thermoélectriques en offrant de meilleurs isolants. Dans ce travail, les propriétés thermiques de quelques nanocomposites sont étudiées en utilisant des calculs à l'échelle atomiques. Dans un premier temps, l'accent est mis sur des nanocomposites constitués d'une matrice amorphe et de nano-inclusions cristallines. L'approche développée pour les verres, séparant la partie balistique et la partie diffusive du transfert thermique est mis à profit. La séparation de ces contributions a montré que si la structuration affecte systématiquement la partie balistique, maîtriser l'impact sur le transport diffusif est plus complexe. Celui-ci peut être réduit, dans des proportions variables, par la présence de pores ou d'inclusions plus molles que la matrice. Une deuxième partie est consacrée à l'étude des nanofils de silicium, et à l'impact de l'amorphisation de ceux-ci. Pour cela, le transport d'énergie en fonction de la fréquence est étudié. La couche amorphe provoque l'apparition d'un transport diffusif et une baisse de transmission aux basses fréquences. La structuration de la couche amorphe en cône est ensuite utilisée pour induire une rectification thermique, c'est-à-dire une asymétrie spatiale dans le transport de chaleur. Finalement, la dynamique moléculaire est couplée aux équations hydrodynamiques du transport de chaleur. Ce couplage est utilisé pour étudier la distribution radiale du flux dans les nanofils cylindriques avec une couche amorphe régulière en régime établie. Cette analyse suggère que la réduction de la conductivité thermique due à l'ajout de la coque n'est pas uniquement liée aux changements des propriétés de l'interface, mais plutôt à un effet global de la coque amorphe sur le libre parcours moyen.

MOTS-CLÉS : Nanocomposite, Nanothermique, Matériaux Amorphe, Transport Balistique, Nanofils, Simulations Atomistiques, Rectification Thermique

Laboratoire (s) de recherche :
Centre d'Énergétique et de Thermique de Lyon
UMR 5008
9, rue de la Physique,
69621 Villeurbanne Cedex FRANCE

Laboratoire de Mécanique des Contacts et des Structures
UMR 5259
20, avenue Albert Einstein
69621 Villeurbanne Cedex FRANCE

Directeur de thèse: Konstantinos TERMENTZIDIS, Anne TANGUY

Président de jury :
Olivier BOURGEOIS

Composition du jury :
Sebastian VOLZ, Evelyne MARTIN, Neophytos NEOPHYTOU, Giorgia FUGALLO, Olivier BOURGEOIS, David LACROIX